

UNIVERSITÀ DEGLI STUDI DI NAPOLI FEDERICO II



PhD IN CHEMICAL SCIENCES

XXXV CYCLE

***FROM POLYOLEFINS TO FUNCTIONAL POLYMERS VIA
INNOVATIVE COORDINATION CATALYSTS***

SUPERVISORS

PROF. ROCCO DI GIROLAMO

PROF. CLAUDIO DE ROSA

COORDINATOR

PROF. ANGELINA LOMBARDI

PhD STUDENT

FABIO DE STEFANO

*To **Giulio Regeni**, a young
researcher who chose to devote
himself to science and whose life
has been taken away too soon
because of a barbaric murder that
remained unpunished until now.
May his rigor, humanity, and
intelligence be an inspiration to
many other future researchers.*

Abstract

The introduction of polar or non-polar functional groups into widely used polyolefins can enhance polymer properties and expand the use of polyolefins for advanced, value-added applications. However, efficient direct copolymerization of α -olefin with functional monomers to give functional copolymers with both high molecular weight and tacticity remains a big challenge.

The developed research activity was aimed at synthesizing these new classes of polymers (functional and functionalizable polyolefins) with potentially new microstructures and enhanced properties by using innovative catalysts based on different transition metals. All the obtained polymers were carefully characterized with different techniques, in order to study the structure-property relationships.

Ethylene, propylene and 5-ethylidene-2-norbornene terpolymers with high ethylene and diene contents were obtained from catalytic terpolymerization promoted by different vanadium based catalysts. The synthesized terpolymers behave as thermoplastic elastomers with enhanced mechanical properties, excellent elastic properties and remelting processability with no failure in properties for recycle use.

Chromium complexes were investigated as precatalysts for the polymerization of ethylene using different aluminum cocatalysts and Lewis base NEt_3 as additive. We demonstrated that with a simple and cheap additive, NEt_3 , is possible to produce ultra-high-molecular-weight polyethylene (UHMWPE) that is an engineering and smart polymer used in different application fields. In addition, the synthesis of some poly(cyclic olefin)s and polyesters, obtained with novel chromium complexes, were also explored.

An extensive part of the project was devoted to the synthesis and characterization of new stereoregular crystalline polyolefins incorporating functional or functionalizable groups, produced by using an Hf-based catalytic system. In particular, it has been demonstrated that through the incorporation of allyltrimethylsilane and methylene-1,3-cyclopentane units into isotactic polypropylene and isotactic poly(4-methyl-1-pentene), respectively, it is possible to achieve improved mechanical properties of the original homopolymers and to induce the formation of new crystalline modifications under specific conditions, which have never been described in the literature.

Furthermore, the effect of the presence of two α,ω -non conjugated dienes (1,5-hexadiene and 1,7-octadiene) on the polymorphic behaviour and on all the other properties of isotactic polybutene (iPB) was investigated. The study revealed that in butene/1,5-hexadiene

copolymers the presence of methylene-1,3-cyclopentane units into iPB main chain accelerates the transformation from the metastable form II to the thermodynamically stable form I crystals, whereas in butene/1,7-octadiene copolymers the co-presence of both cyclic and linear co-units significantly stabilize the form II, slowing down the II – I phase transition.

Several catalysts based on Nd, Co, Cu and Fe complexes have been used to synthesize poly(isoprene)s with different molecular structures and configurations. The study showed that the mechanical and the physical properties strictly depend on the concentration of different constitutional units. In particular poly(isoprene)s with almost regular *cis*-1,4 and alternating *cis*-1,4-*alt*-3,4 structures are amorphous with low glass transition temperatures (T_g) and mechanical properties characterized by viscous flow. By contrast, poly(isoprene)s with prevalent 3,4 syndiotactic structure are crystalline materials with higher T_g s, better mechanical properties and remarkable elastic behavior.

Novel ethylene, CO and norbornene terpolymers were synthesized with two advanced Ni and Pd complexes, obtaining linear functional polyethylenes characterized by physical and mechanical properties that depend on crystallinity, which in turn depends on the concentration of the two comonomers. Finally, we also synthesized polyethylenes with combined in-chain and side-chain functional groups formed by catalytic terpolymerization of ethylene, CO, and methyl-5-norbornene-2-carboxylate achieving interesting polymers characterized by the presence of small amounts of polar co-units that impart photodegradability to the material and do not alter the desirable properties of polyethylene.

This study is an example of how different classes of polymers with well controlled molecular structure and completely different properties can be obtained through the rational choice of catalysts and the optimization of polymerization conditions.

Description of thesis work	1
References	5
1. Vanadium	6
1.1 Vanadium-based catalysts for polyolefins: the state of the art	6
1.1.1 Vanadium (V) complexes	7
1.1.2 Vanadium (IV) complexes	8
1.1.3 Vanadium (III) complexes	9
1.2 Synthesis and characterization of Ethylene-Rich EPDM Thermoplastic Elastomers	10
1.2.1 Materials and Methods	10
1.2.2 General Introduction	13
1.2.3 Polymerization – First Screening	16
1.2.4 Catalyst 1a	18
1.2.5 Thermal and Structural Characterization of EPDMs synthesized using Catalyst 1a	20
1.2.6 Mechanical Properties of EPDMs synthesized using Catalysts 1a	26
1.2.7 Fiber diffraction analysis and strain-induced crystallization of EPDMs Synthesized using Catalyst 1a	28
1.2.8 Catalyst 2a	36
1.2.9 Thermal and Structural Characterization of EPDMs synthesized using Catalyst 2a	38
1.2.10 Mechanical Properties of EPDMs synthesized using Catalyst 2a	44
1.2.11 Fiber diffraction analysis and strain-induced crystallization of EPDMs Synthesized using Catalyst 2a	46
1.2.12 Catalyst 2b	59
1.2.13 Thermal and Structural Characterization of EPDMs synthesized using Catalyst 2b	60
1.2.14 Mechanical Properties of EPDMs synthesized using Catalyst 2b	66
1.2.15 Fiber diffraction analysis and strain-induced crystallization of EPDMs Synthesized using Catalyst 2b	69
1.2.16 Study of EPDMs morphology by Atomic Force Microscopy (AFM)	82
1.2.17 Conclusion Chapter 1	83

References	85
2. Chromium	89
2.1 Chromium The state of the art	89
2.1.1 Heterogeneous Cr-based Catalysts	89
2.1.2 Homogenous Cr-based Catalysts	90
2.2 Synthesis and characterization of Ultra High Molecular Weight Polyethylene (UHMWPE) by using Iminopyridine Chromium Complexes	91
2.2.1 Materials and Methods	91
2.2.2 General Introduction	91
2.2.3 Catalytic Screening – Selection of the Aluminum Activator	93
2.2.4 Effect of Lewis Base NEt ₃ Additive on the Catalytic Performance	95
2.2.5 Polymerization of Ethylene by Cr1/MAO/NEt ₃ at Different Temperatures	99
2.2.6 What is the role of NEt ₃ ? A spectroscopic study	103
2.2.7 Cr1 + NEt ₃	105
2.2.8 Cr1 + TEAl	106
2.2.9 NEt ₃ + TEAl	108
2.2.10 Cr1 + NEt ₃ + TEAl	110
2.2.11 NEt ₃ and its role behind the scenes	112
2.3 Cr (III) Complexes Bearing β-Ketoimine Ligand for Cyclic Olefins Polymerization	113
2.3.1 Materials and Methods	113
2.3.2 General Introduction	114
2.3.3 Synthesis of the complexes	115
2.3.4 Polymerization tests	116
2.3.5 Cyclic Olefin Oligomers Characterization	121
2.4 Copolymerization of cyclohexene oxide (CHO) and phthalic anhydride (PA)	131
2.4.1 Materials and Methods	131
2.4.2 General Introduction	132
2.4.3 Polymerization	133
2.4.4 Structural and Thermal Characterization	134
2.4.5 Conclusions Chapter 2	139
References	140

3. Hafnium	144
3.1 Hafnium: The state of the art	144
3.2 Synthesis and characterization of functional copolymers of isotactic polypropylene with allyltrimethylsilane	147
3.2.1 Materials and Methods	147
3.2.2 General Introduction	150
3.2.3 Polymerization	152
3.2.4 Structural and thermal properties	154
3.2.5 Mechanical properties	164
3.2.6 Stretching-induced phase transition	169
3.2.7 Self-Nucleation (SN) study	181
3.2.8 Morphology by POM	195
3.3 Synthesis and characterization of isotactic 4-methyl-1-pentene/1,5-hexadiene copolymers from post-metallocene catalyst	197
3.3.1 Materials and Methods	197
3.3.2 General Introduction	199
3.3.3 Polymerization	200
3.3.4 Structural and thermal properties	204
3.3.5 Mechanical properties	209
3.3.6 Stretching-induced phase transition	214
3.3.7 Morphology by AFM	226
3.4 Synthesis and characterization of post-metallocene made 1-butene/ α,ω -non conjugated dienes isotactic copolymers	232
3.4.1 Materials and Methods	232
3.4.2 General Introduction	235
3.4.3 1-Butene/1,5-Hexadiene isotactic copolymers - Polymerization	237
3.4.4 Structural and thermal properties	239
3.4.5 Mechanical Properties	247
3.4.6 Kinetics of nucleation and growth of form II – form I transition	252
3.4.7 1-Butene/1,7-Octadiene isotactic copolymers - Polymerization	271
3.4.8 Structural and thermal properties	274
3.4.9 Mechanical Properties	282
3.4.10 Stretching-induced phase transition	287

3.4.11 Conclusion Chapter 3	311
References	314
4. Cobalt, Iron, Copper, Neodymium	322
4.1 Catalytic systems for the stereospecific polymerization of 1,3-dienes	323
4.1.1 Cobalt Catalysts	323
4.1.2 Iron Catalysts	324
4.1.3 Copper Catalysts	326
4.1.4 Neodymium Catalysts	326
4.2 Synthesis and characterization of Poly(isoprene)s of different molecular structure prepared with different catalysts based on complexes of Co, Fe, Cu and Nd	328
4.2.1 Materials and Methods	328
4.2.2 General Introduction	330
4.2.3 Polymerization	331
4.2.4 <i>cis</i> -1,4 poly(isoprene) from Neodymium catalysts	333
4.2.5 <i>cis</i> -1,4- <i>alt</i> -3,4 alternating poly(isoprene)s from Fe and Cu based catalysts	335
4.2.6 Regular <i>cis</i> -1,4- <i>alt</i> -3,4 alternating poly(isoprene)s from Co based catalysts	341
4.2.7 Random <i>cis</i> -1,4/3,4 poly(isoprene)s with prevailing 3,4 syndiotactic structure from Cu based catalysts	343
4.2.8 Regular 3,4 syndiotactic poly(isoprene)s from Fe based catalysts	347
4.3 Synthesis and characterization of Stereoregular poly(isoprene)s by Iron and Neodymium-based Catalysts	358
4.3.1 Materials and Methods	358
4.3.2 General Introduction	359
4.3.3 Polymerization	360
4.3.4 Structural and thermal characterization	362
4.3.5 Mechanical properties	365
4.3.6 Conclusion Chapter 4	370
References	372
5. Nickel, Palladium	377
5.1 Catalytic systems for copolymerization of olefins with polar monomer	377
5.2 Synthesis and characterization of novel polyethylene-based terpolymers with	

non-alternating in-chain keto groups	379
5.2.1 Materials and Methods	379
5.2.2 General Introduction	382
5.2.3 Ethylene-CO-Norbornene Terpolymers – Synthesis and Characterization	384
5.2.4 Ethylene-CO-methyl-5-Norbornene-2-Carboxylate Terpolymers Synthesis and Characterization	397
5.2.5 Conclusions Chapter 5	409
References	411

Annex	413
--------------	------------

From polyolefins to functional polymers via Innovative coordination catalysts

Description of the thesis work

The development of synthetic polymers is one of the topmost achievements of the 20th Century. Polymers are hardly replaceable materials that have changed modern society and revolutionized everyday life, combining unrivalled physical and mechanical properties with low cost, low weight and versatility in terms of applications. Over the past 50 years, the importance of plastics in our life and economy has consistently grown. The global production of plastics has increased twentyfold since the 1960s, reaching more than 320 million tonnes in 2015, and in the years to come it is expected to grow at a steady step of 34% per year.^{1,2}

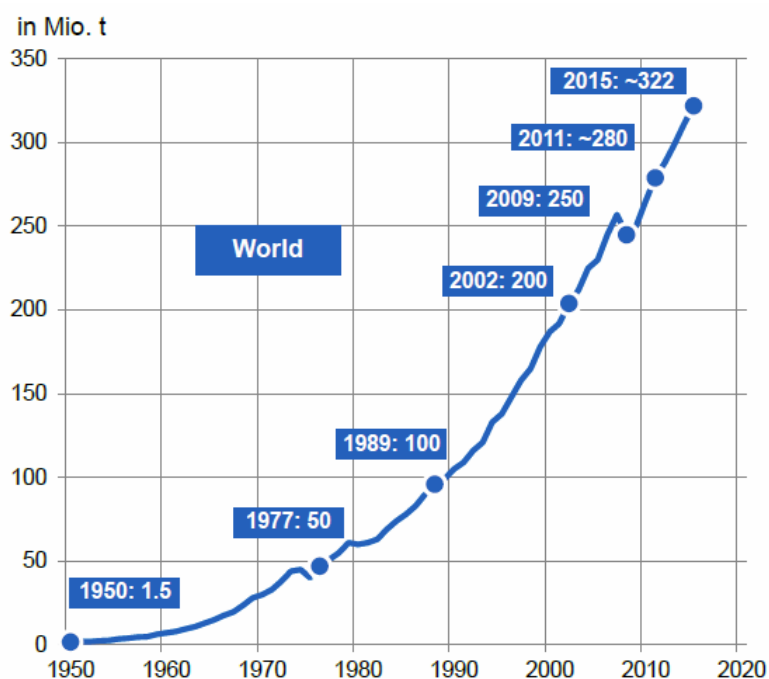


Figure 1. Plastic global production (Source: Plastic Europe Market Research Group).²

However, the general perception of plastics is rather negative because they generate significant externalities along their whole life-cycle. In particular: 1) plastics production still relies on the use of fossil resources and is responsible for the emission of large amounts of greenhouse gases; 2) plastics have usually a lifetime shorter than one year, and after that only ca. 20% of plastic wastes are recycled, while the remaining are often dispersed in the environment with the consequent degradation of natural systems. According to the “European Strategy for Plastics

in a Circular Economy”, launched at the beginning of 2018, the whole plastics value-chain has to be rethought and improved in order to create a new plastic economy. Relevant actions would involve the use of renewable resources to address point (1), and an elongation of the plastics lifetime (that means a valorization of plastics) coupled with an intelligent recycling policy to address point (2). The extraordinarily success in plastics story in the last century was driven by the innovations in catalysis, engineering and processing. In the same way it is expected that catalysis will play a major role also in the modern economy, providing many new opportunities in polymer science and plastics upcycling.

This PhD project is placed in the context of improving the value-chain of plastic and aims at synthesizing functional and durable aliphatic polyolefins prepared by innovative catalysts (based on Hf, Cr, Zr, V etc.).

As well known, polyolefins bearing functional side groups are highly desired materials, due to their unique and rapidly expanding range of material properties such as enhanced stiffness, adhesion, toughness, print/paintability, miscibility, rheological properties and many others.^{3,4} The current state of the art with respect to controlled synthesis of functional polyolefins includes (a) direct copolymerization of α -olefin with a functional monomer, (b) chemical modification of the preformed polyolefin, and (c) a reactive polymer intermediate that can be effectively prepared and then selectively interconverted to functional groups under mild reaction conditions.⁴⁻¹³

Despite the many advances in this field over little more than a half century, the chemical modification and functionalization of polyolefins still remains a challenge. The design of new catalysts and the optimization of new synthetic strategies play a central role in the obtainment of functional polymers under mild conditions in a precise manner.³ Olefin polymerization catalysts can be broadly classified into four categories: Phillips catalysts, Ziegler-Natta catalysts, metallocene catalysts and late transition metal catalysts.

Homogeneous metallocene and late transition metal catalysts (also known as post-metallocenes) were introduced in the 1980s and 1990s, respectively, whereas the discovery of heterogeneous Ziegler-Natta and Phillips catalysts marked the beginning of a paradigm shift in olefin polymerization methods in the early 1950s. As is well known, because of their intrinsic multi-site nature due to the presence of various active catalytic sites on the surface of catalyst particles, heterogeneous catalysts produce polyolefin samples characterized by complicated mixtures of macromolecules characterized by different stereoregularities, molecular weights and, in the case of olefin copolymers a non-random distribution of the monomeric units along the polymer chain resulting in a non-uniform composition.¹⁴ On the other hand, single-center

homogeneous catalysts allow a precise control of microstructure and all other molecular properties of polymer chains and, consequently, provide the opportunity to obtain polymeric materials with the desired properties.¹⁵

In this context, the main goal of this project consists in the development and characterization of these new classes of polymers (functional and functionalizable polyolefins) with potentially new microstructures and enhanced properties by using different classes of homogeneous catalysts based on various transition metals.

The work carried out within this PhD project is hereafter presented as follows:

- **Chapter 1** reports the synthesis and the characterization of ethylene, propylene and 5-ethylidene-2-norbornene terpolymers (EPDM) with high ethylene and diene contents obtained by using three novel imido Vanadium (IV) complexes. We will show that through the use of these new catalytic systems it is possible to obtain interesting materials that behave as thermoplastic elastomers (TPEs) without the need of polymers blending and reinforcement through the addition of active fillers. All the obtained polymers will be characterized at all length scales to study of structure-properties relationships.
- **Chapter 2** is focused on chromium, in particular on the study of some homogeneous chromium complexes used for the polymerization of ethylene and cyclic olefins. We will show that by using an iminopyridine chromium complex in combination with a simple and cheap additive, NEt_3 , is possible to produce ultra-high-molecular-weight polyethylene (UHMWPE) that is an engineering and smart polymer characterized by high wear-resistance, toughness, durability, and biocompatibility that make it useful in many fields such as chemical, machinery, joint replacement, and other fields.
- **Chapter 3** is dedicated to the synthesis and characterization of new semicrystalline copolymers based on stereoregular polyolefins of relatively high crystallinity and melting temperatures, incorporating functional group or reactive sites that can be quantitatively interconverted into the desirable functional (polar) groups. Specifically, four different series of functional or functionalizable stereoregular copolymers, obtained by using a hafnium-based catalytic system, will be presented and investigated in detail.

- **Chapter 4** describes the study of poly(isoprene) and poly(myrcene) samples of different molecular structures, synthesized with different catalysts based on complexes of different metals, such as Nd, Co, Cu and Fe, and various ligands based on pyridylimine, phosphines and bipyridine. We will report the characterization of the structure and of the thermal and mechanical properties of these novel polymers and the study of the relationships between properties and molecular structures determined by the different used catalyst.

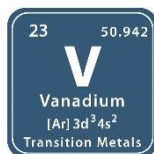
- **Chapter 5** reports the catalytic terpolymerization, performed with two advanced nickel and palladium complexes, of ethylene, carbon monoxide and norbornene under mild reaction conditions that yield linear functional polyethylene with tunable crystallinity. In addition, we will also show the synthesis of polyethylenes with combined in-chain and side-chain functional groups formed by Pd(II)-catalyzed terpolymerization of ethylene, carbon monoxide, and methyl-5-norbornene-2-carboxylate. We obtained very interesting polymers characterized by the presence of small amounts of polar co-units (<1 mol%) that impart photodegradability to the material and at the same time do not compromise the desirable properties of polyethylene such as crystallinity, melting temperature and mechanical behavior.

References

- 1) World Economic Forum, Ellen MacArthur Foundation and McKinsey & Company, The New Plastics Economy — Rethinking the future of plastics (2016, <http://www.ellenmacarthurfoundation.org/publications>).
- 2) “Plastics – the Facts 2017” PlasticsEurope, www.plasticseurope.org
- 3) N. M. G. Franssen, J. t N. H. Reek, B, de Bruin *Chem. Soc. Rev.* **2013**, *42*, 5809.
- 4) A. Nakamura, S. Ito, K. Nozaki *Chem. Rev.* **2009**, *11*, 5215.
- 5) A. Keyes, H. E. Basbug Alhan, E. Ordonez, U. Ha, D. B. Beezer, H. Dau, Y. S. Liu, E. Tsogtgerel, G. R. Jones, E. Harth *Angew. Chem., Int. Ed.* **2019**, *58*, 12370.
- 6) D. J. Walsh, M. G. Hyatt, S. A. Miller, D. Guironnet *ACS Catal.* **2019**, *9*, 11153.
- 7) C. Tan, C. Chen *Angew. Chem., Int. Ed.* **2019**, *58*, 7192.
- 8) A. Nakamura, T. M. J. Anselment, J. Claverie, B. Goodall, R. F. Jordan, S. Mecking, B. Rieger, A. Sen, P. W. N. M. van Leeuwen, K. Nozaki *Acc. Chem. Res.* **2013**, *46*, 1438.
- 9) S. Mecking, L. K. Johnson, L. Wang, M. Brookhart *J. Am. Chem. Soc.* **1998**, *120*, 888.
- 10) J. B. Williamson, S. E. Lewis, R. R. Johnson, I. M. Manning, F. A. Leibfarth *Angew. Chem., Int. Ed.* **2019**, *58*, 8654.
- 11) L. Chen, K. G. Malollari, A. Uliana, D. Sanchez, P. B. Messersmith, J. F. Hartwig *Chem.* **2021**, *7*, 137.
- 12) T. J. Marks, J. Chen, Y. Gao *Angew. Chem. Int. Ed.* **2020**, *24*, 14834.
- 13) T. C. M. Chung *Macromolecules* **2013**, *46*, 6671.
- 14) C. De Rosa, O. R. de Ballesteros, R. Di Girolamo, A. Malafrente, F. Auriemma, G. Talarico, M. Scoti *Polymer Chemistry* **2020**, *11*, 34.
- 15) D. Fischer, R. Mülhaupt *Macromol. Chem. Phys.* **1994**, *195*, 1433.

Chapter 1

Vanadium



-Parts of this chapter have been published and are reproduced here from:

- 1) G. Leone, G. Zanchin, R. Di Girolamo, **F. De Stefano**, C. Lorber,
C. De Rosa, G. Ricci, F. Bertini *Macromolecules*
2020, 53, 5881

Vanadium is the element of the periodic table with atomic number 23 belonging to the Group 5 of the transition series. The chemistry of vanadium is noteworthy for the accessibility of the four adjacent oxidation states (II)–(V). Vanadium is an important element for many catalytic applications.¹ The most commercially important compound is vanadium pentoxide (V_2O_5), used as a catalyst for the production of sulfuric acid.

In the world of catalysis for olefins polymerization, the combination of VCl_4 or $V(acac)_3$ with aluminum alkyl compounds is among the first catalysts reported for the copolymerization of cyclic olefins.²

1.1 Vanadium-based catalysts for polyolefins: the state of the art

Natta established the ability of trivalent and tetravalent vanadium salts to encourage olefin copolymerization from the beginning of his research.³ Vanadium catalysts have shown to be able to produce polymers with unique features, including synthetic rubber and elastomers, although having low catalytic activity. For instance, the combination of VCl_4 with Et_2AlCl and anisole produced high molecular weight amorphous ethylene/propylene copolymers⁴ and ethylene/cyclic olefin copolymers, while the system $VCl_4-AlBr_3-AlPh_3$ allowed the synthesis of linear polyethylenes with excellent catalytic activity.⁵

Despite the fact that vanadium-based Ziegler-Natta technology is well known and frequently used in the industrialized world [for instance, the commercially used trivalent $V(acac)_3$ ($acac$ = acetylacetonate) for the production of ethylene/propylene/diene elastomers (EPDM)],⁶ Group 5 metals were largely ignored, and until the late 1990s.

This is due to the inherent instability of the V-C bond as well as the low activity of vanadium catalysts, which is related to their propensity to undergo reductive elimination towards inert divalent species.⁷ The use of moderate oxidizing agents (such as chlorinated esters or halocarbons) that can restore the trivalent state is typically used to avoid the reduction to inactive V(II) species,⁸ even if their precise function and mode of action are still up for discussion in the most current research.

Many ancillary ligands with different denticities and containing various combinations of donor atoms, such as N, O, P, and S, have been developed and used in the synthesis of vanadium complexes in different oxidation states, from (III) to (VI), with the goal of controlling the oxidation state (stabilization of the oxidation state, catalytically active species), thereby extending the catalyst's lifetime.

The majority of these complexes are generated from V(V) complexes with arylimido-aryloxo,⁹ amine pyridine(s) phenolate,¹⁰ and tetradentate amine trihydroxy ligands,¹¹ and V(III) complexes supported by multidentate ligands with N and O hard donor atoms in various combinations.^{7,8,12,13}

One of the earliest catalysts described for the copolymerization of cyclic olefins was obtained from the combination of these complexes with aluminum alkyl compounds.²

Specifically, ethylene was copolymerized with numerous cyclic olefins, including cyclopentene, cycloheptene, cyclooctene, and cyclohexene, using the $VCl_4/Al(C_6H_{13})_3$ and $V(acac)_3/Et_2AlCl$ systems.¹⁴ As a result, several vanadium-based systems were synthesized and employed as pre-catalysts for the copolymerization of cyclic olefins.^{7,8,12,13}

According to their oxidation states, some of them are reported in the following section.

1.1.1 Vanadium(V) complexes

The V(V) complex-based catalysts with the highest activity include those with arylimido-aryloxo,⁹ amine pyridine(s) phenolate,¹⁰ and tetradentate amine trihydroxy ligands.¹¹ A lot of research has been done on the E/NB copolymerization using the (arylimido)(aryloxo)V(V) complexes $VCl_2(2,6-Me_2C_6H_3N)(2,6-R_2C_6H_3O)$ (R= Me, *i*Pr, Ph) (complex **V-1** of Figure 1.1).

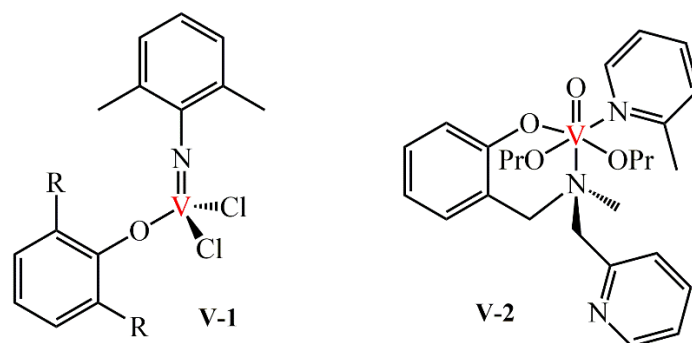


Figure 1.1. (arylimido)(aryloxo) (**V-1**) and amine pyridine phenolate (**V-2**) V(V) complexes.

When combined with MAO or Et_2AlCl , these complexes exhibit strong catalytic activity and produce atactic, alternating copolymers.

Despite having a minimal impact on the incorporation of NB and the microstructure of the resulting copolymers, the substituents on the aryloxo ligand have a large impact on the catalytic activity and molecular weight of the resulting copolymers.⁹

When combined with Me_2AlCl , the bis(benzimidazole)amino V(V) complexes exhibited extremely high activity ($11250 \text{ kg}_{\text{pol}} \text{ mol}_V^{-1} \text{ h}^{-1}$) and high NB incorporation (up to 33 mol%)¹⁵ for the E/NB copolymerization even at 50 °C. Li et al. reported V(V) complexes with amine, pyridine, and phenolate ligands for the first time (complex **V-2** of Figure 1.1).¹⁰

These novel complexes exhibited very high catalytic activities for the E/NB copolymerization in the presence of Et_2AlCl as cocatalyst and ETA (ethyltrichloro acetate, Cl_3CCOOEt) as reactivating agent even at high temperatures, affording high molecular weight copolymers with unimodal molecular weight distribution. Both the polymer properties as well as the copolymerization behavior were both considerably influenced by the substituents in the aryloxo group and N-bridge fragment. In fact, the incorporation of NB into the copolymer increased as the steric congestion around the metal center decreased, while the measured catalytic activity was less than that of the more hindered complexes.

1.1.2 Vanadium(IV) complexes

Complexes of vanadium in the (IV) oxidation state are quite uncommon compared to V(V). Ligands that have been employed with V(IV) are aryl(imido) ligands (complex **V-3** of Figure 1.2),^{16,17,18,19,20} bis(amide) ligands (complex **V-4** of Figure 1.2),²¹ O,N-chelating aminophenolate ligands (complex **V-5** of Figure 1.2),²² and among them also salen-type tetradentate ligands (complex **V-6** of Figure 1.2).²³

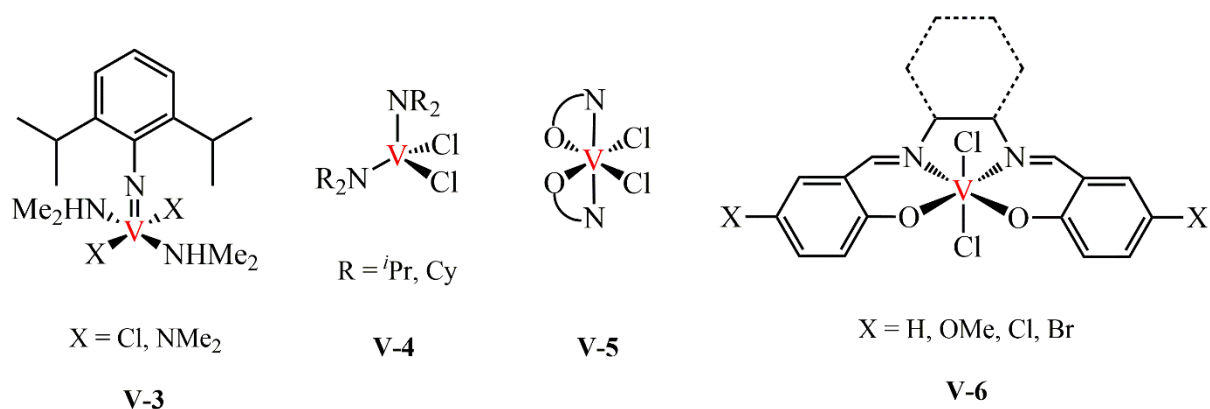


Figure 1.2. V(IV) complexes bearing different N and O donor atom ligands.

For instance, the complex **V-3** of Figure 1.2 by Lorber *et al.* was one example of numerous (arylimido)vanadium(IV) dichloride complexes that demonstrated strong catalytic activity for ethylene polymerization in the presence of Et_2AlCl cocatalyst.²⁰

When Et_2AlCl was present, the activity of **V-3** was higher ($120 \text{ kg}_{\text{PE}} \text{ molV}^{-1} \text{ h}^{-1}$; $\text{Al/V} = 10$; ethylene 1 atm, 20°C in toluene, 2 or 10 min) than when MAO was present ($59 \text{ kg}_{\text{PE}} \text{ molV}^{-1} \text{ h}^{-1}$; $\text{Al/V} = 500$). Uniform molecular weight distributions were seen in the resulting polymers. In this regard, they discovered that adding a 2,6-disubstituted aryylimido moiety appeared to be useful in stabilizing the catalytically active species. Recently, novel methylamine–imido $\text{V}(=\text{NR})\text{Cl}_2 (\text{NHMe}_2)_2$ [$\text{R} = \textit{t}\text{Bu}$] and pyridine–imido $\text{V}(=\text{NR})\text{Cl}_2 (\text{Py})_3$ [$\text{R} = \textit{t}\text{Bu}, \text{CPh}_3$] complexes were synthesized and such complexes have been shown to be efficient precatalysts in the copolymerization of ethylene with α -olefins²⁴ and cyclic olefins.²⁵ These type of complexes were used in the present PhD work to synthesise ethylene-propylene-5-ethylidene-2-norbornene terpolymers, which will be described in detail in the section 1.2.

1.1.3 Vanadium(III) complexes

In 2005, Lorber *et al.*²⁶ presented a few novel amine bis(phenolate) complexes of V(III) (Figure 1.3), demonstrating that the complex **V-7**, in ethylene/norbornene copolymerization, showed an NB incorporation ranging from 14 to 29 mol%, substantially dependent on the polymerization conditions.

Successively, multidentate ligands with N and O hard donor atoms in various combinations led to catalysts with good activity and high NB incorporation.²⁷

In fact, the productivity was increased overall by using mono(β -enaminoketonato) $\text{N}^{\wedge}\text{O}$ ligands, and mostly alternating copolymers were produced.

Later, it was discovered that a number of catalytic systems that are similar to **V-8** (Figure 1.3) are effective catalysts for the (co)polymerization of olefins.

They exhibited activity in the range 1500 and 6800 kg_{pol} mol_V⁻¹ h⁻¹ when combined with Et₂AlCl and in the presence of ETA, and NB incorporation between 32.6 and 42.7 mol%.²⁷

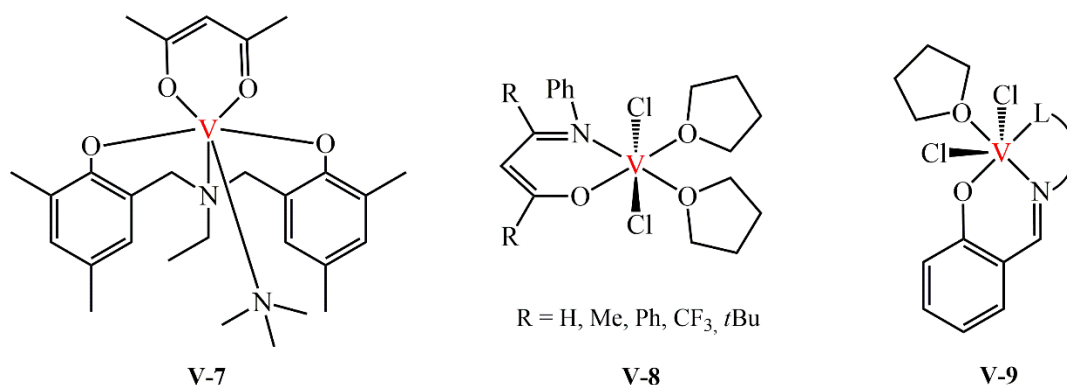


Figure 1.3. V(III) complexes bearing different N[^]O and N[^]O[^]L ligands.

Furthermore, the introduction of a pendant L heteroatom in the bidentate N[^]O Schiff base ligand gave V(III) complexes (complex **V-9** of Figure 1.3) which exhibited the highest activity for the E/NB copolymerization (17300 kg_{pol} mol_V⁻¹ h⁻¹ with L = phosphorus donor). As a matter of fact, N[^]O ligands with pendant phosphine groups, in which the nitrogen and phosphorous atoms are connected by a stiff phenylene bridge, aid in strengthening the phosphine coordination and stabilizing the V(III) species.²⁸

1.2 Synthesis and characterization of Ethylene-Rich EPDM Thermoplastic Elastomers

1.2.1 Materials and Methods

EPDMs samples (characterized with 1H- and 13C analysis) were synthesized and supplied by Dr. Giuseppe Leone (CNR-ISMAL Milano) within a collaborative project “Chromium catalysis: from fundamental understanding to functional aliphatic polymers (Cr4FUN)” (PRIN-MIUR DD 3402 del 21/12/2018). The details about synthesis of EPDMs samples and their molecular characteristics are discussed in the following paragraphs and in Ref 29.

The calorimetric measurements were performed with a Mettler-DSC822 operating in N₂ atmosphere. The sample, typically 5 mg, was placed in a sealed aluminum pan, and the measurement was carried out from -70 to 180°C using a heating and cooling rate of 10 °C min⁻¹.

X-ray diffraction patterns have been recorded at room temperature with Ni filtered Cu K α radiation (wavelength $\lambda=0.15418$ nm). The powder diffraction profiles have been obtained with an automatic PANalytical Empyrean diffractometer operating in the reflection geometry.

The index of crystallinity (x_c) was evaluated from the X-ray powder diffraction profiles by the ratio between the crystalline diffraction area (A_c) and the total area of the diffraction profile (A_t), $x_c = A_c/A_t$. The crystalline diffraction area was obtained from the total area of the diffraction profile by subtracting the amorphous halo. The diffraction profiles of the amorphous phase of samples were obtained from the X-ray diffraction profile of the amorphous sample 7 obtained by compression molding. In fact, this sample does not crystallize by cooling the melt to room temperature, and the amorphous film is obtained by compression molding.

Small Angle X-ray scattering measurements have been collected at room temperature using a Kratky compact camera SAXSess (Anton Paar, Graz, Austria) in the slit collimation configuration, attached to a conventional X-ray source (CuK α , wavelength $\lambda = 1.5418$ Å). The scattered radiation was recorded on a BAS-MS imaging plate (FUJIFILM) and processed with a digital imaging reader Perkin Elmer Cyclone Plus (storage phosphor system). In particular, both WAXS and SAXS measurements were performed on samples crystallized from the melt obtained using two different crystallization protocols. In the first case, samples have been heated up to melting between flat Teflon plates under an hydraulics press at very low pressure (< 1 bar), kept at high temperature for 5 min, and slowly cooled to room temperature (≈ 15 °C/min). In the second case, in order to enhance the crystallinity, samples were cooled from the melt to -50 °C at 2.5 °C/min using a Linkam hot stage.

The materials for the mechanical characterization were molded in a press at 80–120 °C and 50 bar for 5 min; then the press plates were cooled to 20 °C min $^{-1}$ to room temperature. Films with a thickness of about 150 μ m were produced. Tensile dog-bone-shaped specimens (length overall 75 mm, gauge length 25 mm, and width of narrow section 4 mm) were analyzed at 20 °C by using a Zwick Roell ProLine Z010 mechanical tester equipped with a XforceP (50 N) load cell at a constant crosshead rate of 15 mm min $^{-1}$. In the hysteresis experiments performed at the fixed strain of 300% (cyclic test 1) or a gradually increased strain between 30 and 1460% (cyclic test 2), the specimens were cyclically loaded and unloaded in uniaxial tension.

The strain recovery (SR) was calculated as $SR = 100(\varepsilon_a - \varepsilon_r)/\varepsilon_a$, where ε_a is the applied strain and ε_r is the strain in the cycle at zero load after the applied strain. For each material, at least five samples were tested for extension experiments and two samples for strain recovery tests. Possible occurrence of stress-induced crystallization (SIC) has been analyzed by recording the two dimensional WAXS patterns during stretching and after relaxation of the specimens to

verify whether crystals formed at high deformations melt during elastic recovery (reversible SIC). elastic recovery (reversible SIC). X-ray fiber diffraction patterns have been collected with Ni-filtered $\text{CuK}\alpha$ radiation and recorded on a BAS-MS imaging plate (FUJIFILM) using a cylindrical camera and processed with a digital imaging reader Perkin Elmer Cyclone Plus (storage phosphor system).

For each deformation of all samples the bidimensional X-ray diffraction pattern and the equatorial profile are reported. Equatorial profiles have been evaluated reading the intensity along the equatorial line of the bidimensional patterns with the digital imaging reader. In addition, for samples in the undeformed state, stretched to the maximum investigated deformation and after removal of tension the bidimensional X-ray diffraction pattern, the equatorial profile integrated over the azimuthal coordinate are reported. Equatorial profiles have been evaluated reading the intensity along the equatorial line of the bidimensional patterns with the digital imaging reader. The integrated profiles have been calculated integrating the intensity along the azimuthal coordinate χ of the bidimensional patterns by using the software FIT2D (Figure 2.56). On samples stretched at the maximum deformation and relaxed an evaluation of the variation in degree of crystallinity (Δx_c) has been made by comparing the crystallinity achieved upon stretching and after relaxation with respect to the crystallinity visible in the same unoriented sample before stretching. The evaluation of Δx_c has been made by comparing integrated profiles of stretched and relaxed samples instead of the corresponding equatorial profiles.

Atomic force microscopy (AFM) measurements were carried on a Bruker Multimode 8, in tapping mode, using a silicon cantilever RTESTPA-300 tip with radius of about 8 nm, at resonance frequency and force constant in the range 200–400 kHz and 40 N m^{-1} , respectively. For AFM measurements, polymer films (with a thickness of 50–100 nm) have been prepared via drop-casting from 0.05 wt% p-xylene solution on a glass slide. Thus, the obtained films were heated at temperature 20–30 °C higher than the melting temperature of the sample at $40 \text{ }^\circ\text{C min}^{-1}$ and held 5 min, then cooled at $2.5 \text{ }^\circ\text{C min}^{-1}$ to $-50 \text{ }^\circ\text{C}$, and reheated to room temperature (for AFM imaging) with a rate of $50 \text{ }^\circ\text{C min}^{-1}$ in a Linkam hot stage. AFM images were processed with Gwyddion software.

1.2.2 General Introduction

EPDM denotes a synthetic rubber produced from a terpolymer of ethylene, propylene and a non-conjugated diene, usually 5-ethylidene-2-norbornene (ENB).^{30,31} EPDM market has grown tremendously, and today EPDM is the largest synthetic non-tire rubber with a volume of about 1200 kton/yr for application in the automotive components, building packing, and electrical cable. EPDM combines a saturated polymer backbone with residual unsaturations as side groups. As a consequence, EPDM is more resistant to oxygen, ozone, UV, and heat than commodity rubbers.^{32,33} However, EPDMs have quite poor mechanical properties: most of EPDM applications requires reinforcement in blends to improve, as an example, the tensile strengths, or cross-linking by using sulfur or peroxides. Sulphur vulcanization leads to a dramatic improvement in the thermal stability, and mechanical properties, but irreversible permanent cross-link is a disadvantage to the recyclability nature of the rubber.³⁴

EPDMs are designed according to the following criteria: (i) ethylene/propylene ratio, (ii) diene content, and (iii) viscosity, which in turn strongly affects the properties of raw EPDM rubbers as well as those of the corresponding vulcanizates. The ethylene/propylene ratio is thought to have the greatest effect on EPDM properties, and applications. At high propylene level (above 50 wt%), only short ethylene sequences exist in the terpolymer chain so crystallinity is absent, while a small amount of crystallinity is present at low propylene level (below 35 wt%). If ethylene and propylene contents are approximately equal, both the (co)monomers are evenly distributed, meaning the rubber is amorphous with low glass transition temperature (T_g even lower than -60°C) and remarkably superior cold resistance for outdoor applications (*e.g.*, automotive and construction).³⁵

EPDM are manufactured commercially in solution and slurry processes using Ziegler–Natta (ZN) catalysts based on group 4 metals and vanadium. Among them, homogeneous vanadium catalysts are of great importance. The main difference between ZN catalysts and homogeneous vanadium-based ones consists in the fact that the heterogeneous Ziegler-Natta catalyst's surfaces contain a variety of catalyst sites, resulting in a mixture of macromolecules with varying molecular masses, stereoregularities, and non-random distributions of comonomeric units. Consequently, these EPDM samples can be fractionated by traditional extraction techniques using boiling solvents into various fractions distinguished by macromolecules having different compositions, which are characterized by different crystallinities and melting behavior.

Concerning homogenous vanadium-based catalytic systems, they are made up of the combination of vanadium compounds (*e.g.*, VCl_4 , VOCl_3 , $\text{VO}(\text{OR})_3$, $\text{V}(\text{acac})_3$, R = alkyl group,

acac = acetylacetonate) and alkyl aluminum halide (typically Et_2AlCl) or aluminum hydride derivatives, and a Lewis base (*e.g.*, anisole).³⁶⁻⁴³

As already mentioned, concerning crystallinity and physical properties, commercial EPDM rubbers are usually amorphous or low crystalline materials depending on their composition. EPDM terpolymers characterized by an ethylene concentration higher than 65% are semi-crystalline at room temperature and crystallize in the orthorhombic and pseudo-hexagonal form of polyethylene (PE) at high and low ethylene content, respectively.⁴⁴⁻⁶⁰ The bulky diene units are expelled from the crystals and reduce the length of the crystallizable ethylene sequences. On the other hand, propene units are easily incorporated in the PE unit cell promoting the crystallization of the pseudo-hexagonal form. As a result, the size of the *a*-axis of the orthorhombic unit cell of PE linearly increases as the concentration of propene units rises, whereas the size of the *b*- and *c*-axes do not significantly change. In particular, the formation of the pseudo-hexagonal form is obtained when the propene concentration is around 20 wt%. For these compositions the crystals include a significant amount of structural disorder and the ratio between the *a* and *b* axes reaches a threshold value ($\sqrt{3}$) that leads to the formation of the pseudo-hexagonal form.^{44,46,47,52-60} Figure 1.4 shows the model of the crystal structure of the orthorhombic form of PE (lattice parameters $a = 7.42 \text{ \AA}$, $b = 4.95 \text{ \AA}$, and c (chain axis) = 2.54 \AA) while Figure 1.5 shows the relationship between orthorhombic (a_o , b_o) and hexagonal (a_h , b_h) unit cell parameters.

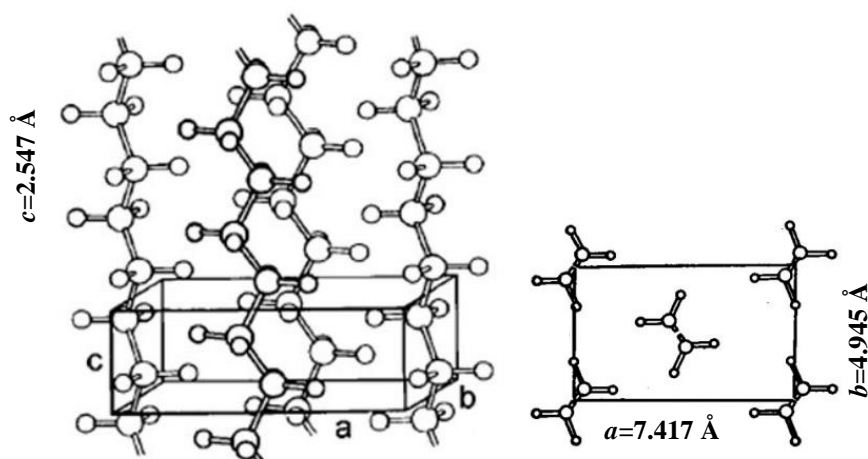


Figure 1.4. Model of the crystal structure of the orthorhombic form of PE.

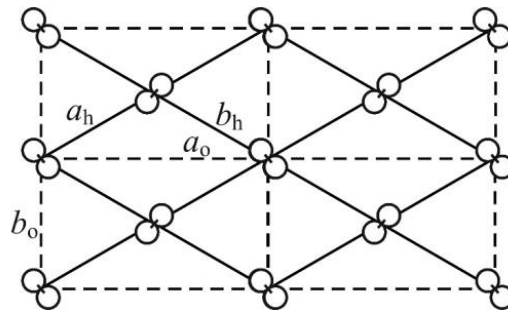


Figure 1.5. Relationship between orthorhombic (a_o , b_o) and hexagonal (a_h , b_h) unit cell parameters in the structure of polyethylene. Chains of ethylene–propylene copolymers for propylene content close to 25% pack in a pseudo-hexagonal unit cell, with orthorhombic lattice parameters in the ratio $a_o/b_o = \sqrt{3}$.

Energetic considerations and structural studies have indicated that the structural organisation in EPM copolymers can be described in terms of a mosaic model (Figure 1.6) in which the chains are organised as in the orthorhombic form of PE only locally.⁶¹ However, at long range, the relative orientation of the chains around their own axis and the relative position of the chains parallel to their axis deviate from that typical of PE in the orthorhombic form, resulting in a high degree of structural disorder, and only the positional order of the chain axes at the nodes of a hexagonal lattice is preserved (Figure 1.6).

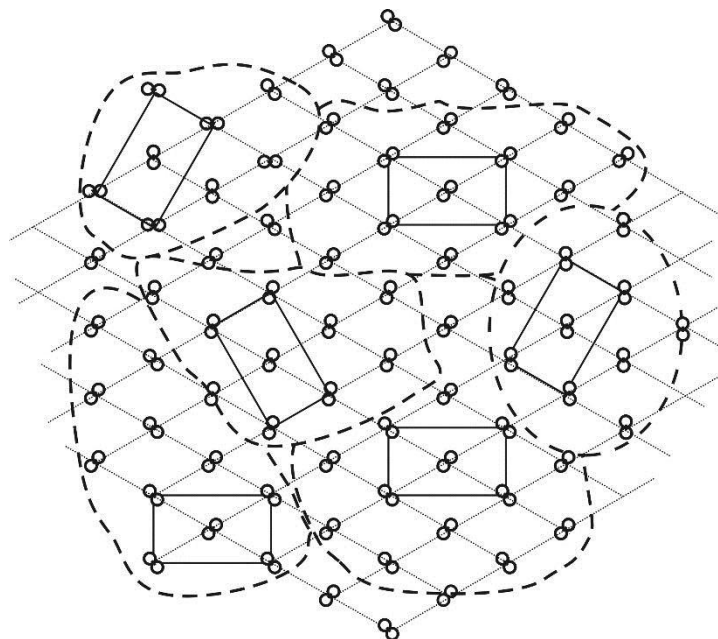


Figure 1.6. Mosaiclike structure of crystalline microaggregates of EP copolymer chains in the pseudo-hexagonal form. In the different ordered domains, enclosed in the dashed lines, the chains are locally packed as in the orthorhombic structure of PE. The different domains are arranged in a mosaic structure so that long-range positional order of chain axes placed at nodes of a pseudo-hexagonal lattice is maintained. The unit cells of orthorhombic model is shown as continuous lines, whereas the hexagonal lattice is shown as dotted lines.⁶¹

1.2.3 Polymerization – First Screening

Ethylene, propylene and 5-ethylidene-2-norbornene (ENB) terpolymers (EPDM) have been synthesized using three imido vanadium(IV) complexes reported in Figure 1.7.

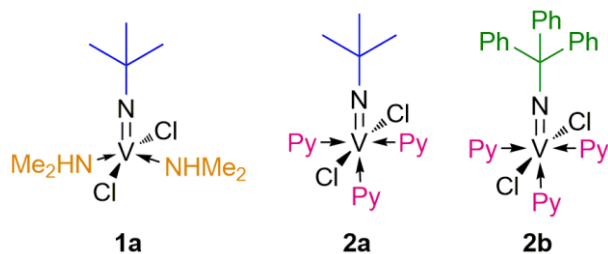
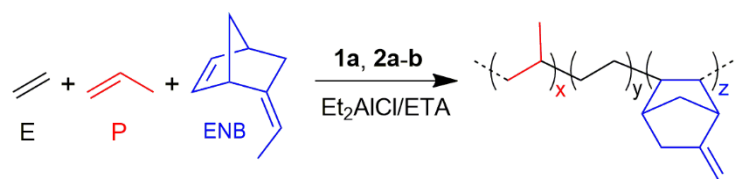


Figure 1.7. V(IV) complexes used for the synthesis of EPDM terpolymers.

Two of used complexes have the *tert*-butyl imido substituent but differ in the nature of coligand, *i.e.*, pyridine (Py) vs dimethylamine (NHMe₂). They are V(=N^tBu)Cl₂(NHMe₂)₂ (**1a**), and V(=N^tBu)Cl₂(Py)₃ (**2a**). The third one has the pyridine coligand as **2a** but a different imido substituent, *i.e.*, V(=NCPH₃)Cl₂(Py)₃ (**2b**) (Figure 1.7). These same complexes have been used in literature for the synthesis of ethylene copolymers with α -olefins²⁴ and cyclic olefins²⁵ but have never been tested in terpolymerization experiments. Therefore, at an early screening stage, the catalytic utility of these known imido V(IV) complexes has been investigated in the terpolymerization of ethylene with propylene and ENB.

The polymerizations were carried out in a semi-batch mode, at an ethylene pressure of 1 atm, at room temperature, and by using only 2.5 μ mol of vanadium precursor to easily maintain the temperature throughout the polymerization without cooling in the early stages. The ethylene gaseous monomer was replenished by maintaining a constant gas pressure during the reaction timecourse, while all the liquid comonomers were placed in the reactor at the beginning. In all three cases, Et₂AlCl was used as activator, and the polymerizations were conducted in the presence of ETA, which acts as reoxidant.⁶² This first screening was performed with a fixed comonomer feedstock ratio P/E/ENB of 4/1/0.5. The results are summarized in Table 1.1.

Table 1.1. Terpolymerization of ethylene with propylene and ENB by **1a**, **2a–b** in combination with Et₂AlCl and ETA.^a



entry	cat	yield (mg)	Activity ^b	terpolymer composition (mol%) ^c			(co)monomer conversion (%) ^d		M _w ^e ×10 ³	M _w /M _n ^e
				E	P	ENB	P	ENB		
1	1a	72	433	92.5	2.5	5.0	0.2	3.0	193	1.9
2	2a	263	1578	83.6	6.4	10.0	1.6	19.3	143	2.0
3	2b	501	3006	80.3	6.5	13.2	2.8	44.9	112	1.9

^a polymerization conditions: ethylene pressure, 1.01 bar; total volume, 50 mL (toluene); V complex, 2.5 μmol; Al/V = 500; ETA/V = 10; temperature, 20 °C; time, 2 min; P/E/ENB feed ratio = 4/1/0.5 (mol/mol) in liquid phase; ^b activity in kg_{pol}×(mol_V×h)⁻¹; ^c determined by NMR; ^d the comonomer conversion was calculated by combining the NMR data, comonomer feed, and weight of the obtained terpolymer; ^e determined by SEC.

With the exception of the complex **1a**, complexes **2a** and **2b** showed very high activity, producing high-ethylene (>80 mol%), high-molecular-weight EPDMs with unimodal and moderately narrow molecular weight distribution ($M_w/M_n = 1.9–2.0$, Table 1.1).

One plausible explanation for the low initiation rate of **1a** would be that NHMe₂ remains closer to the active center than the pyridine due to its stronger Lewis base character, thus limiting the approach of the (co)monomers. The involvement of a deleterious interaction between the amine and the aluminum alkyl, leading to the deprotonation of dimethylamine or preventing catalyst formation in terms of efficient alkylation may also account for.⁶³

From the data reported in Table 1.1 is evident that all the catalysts under study exhibit a preference for introducing ENB to propylene, which is in line with the fact that they are more active when copolymerizing ethylene with cyclic olefins²⁵ than when by using α-olefins.²⁴

The ligand set had an impact on the comonomer incorporation; it increased in the following order: **1a** (P = 2.5 mol%; ENB = 5.0 mol%) ≪ **2a** (P = 6.4 mol%; ENB = 10.0 mol%) < **2b** (P = 6.5 mol%; ENB = 13.2 mol%). Furthermore, it should be noted that the conversion of comonomers is very high and, in particular, reaches 45% in the case of ENB (entry 3, Table 1.1). Such high consumption of comonomers, since ethylene is fed continuously, causes strong variation in the instantaneous comonomer feed composition with conversion, thus altering the composition of the terpolymer over the period of conversion. The comonomer feed changes in composition as one of the comonomer preferentially enters the terpolymer chain, thus resulting in a *composition drift* towards the less reactive comonomer over time. This drift in composition

implies the formation of heterogeneous terpolymers with a broad chemical composition distribution. At least in principle, the chains formed at the reaction start, when the comonomer concentration is at the maximum, should have the highest fraction of comonomers. As propylene and ENB are consumed, both the two comonomers will enter the chain occasionally and with decreasing frequency. At the end of the terpolymerization, with very little comonomer left in the reactor flask, the formed chains should have the highest fraction of ethylene (Figure 1.8). If the comonomer feed composition changes significantly, then the properties of the resultant EPDM should become conversion dependent.

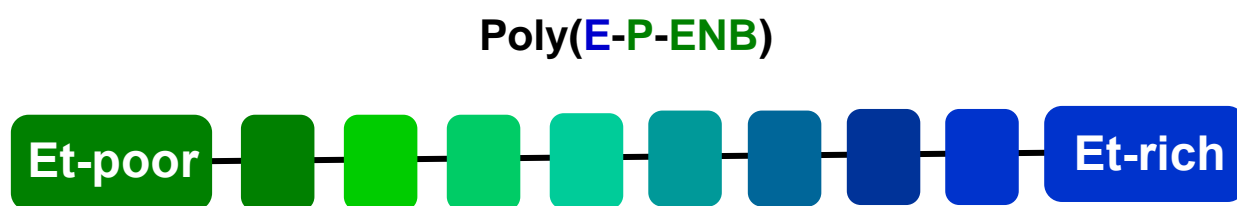


Figure 1.8. Schematic representation of the compositional drift in an E/P/ENB terpolymers.

In order to study the properties of these heterogeneous EPDMs, several samples were synthesized using the catalysts shown in Figure 1.7 and varying the polymerization conditions in order to accentuate the just described compositional drift in the various cases.

The results obtained with the three different employed catalysts will be discussed separately in the next paragraphs for clarity's sake.

1.2.4 Catalyst 1a

The terpolymerization behavior of **1a**/Et₂AlCl/ETA was investigated for a reaction time between 2 and 6 min in steps of 1 or 2 min, and at P/E/ENB = 4/1/0.5.

Details of the reaction conditions and polymerization results are summarized in Table 1.2.

All the obtained terpolymers have high molecular weight ($100 < M_w \times 10^3 \text{ g/mol} < 197$), and narrow molecular weight distribution ($1.9 < M_w/M_n < 2.3$). As shown in Figure 1.9A, both the yield and the activity linearly increase with the polymerization time. Likewise, Figure 1.9B shows that there is a continuous increase in the comonomer conversion over time, and that ENB always preferentially incorporates into the terpolymer by a higher rate than propylene, reaching a conversion of 51.7% vs 2.2% for propylene. The comonomers are consumed at different rates in the terpolymerizations, and consequently the comonomer feed composition changes in the course of the reaction. As chains are created and terminate continuously in chain-

growth polymerization, the variation in comonomer feed ratio results in a broad chemical composition distribution. This results in fluctuations in the terpolymer composition with conversion, as shown in Table 1.2 and in Figure 1.9C. The content of ENB in the terpolymer increases quickly up to 11.5 % of conversion, while for the next two minutes of reaction the increase is much slower (Table 1.2 and Figure 1.9C). This behavior is consistent with a rapid exhaustion of ENB at the beginning of the terpolymerization.

Table 1.2. Terpolymerization of ethylene with propylene and ENB by **1a**/Et₂AlCl/ETA at different polymerization time.^a

entry	time (min)	yield (mg)	activity ^b	terpolymer composition (mol%) ^c			(co)monomer conversion (%) ^d		M_w^e ×10 ³	M_w/M_n^e
				E	P	ENB	P	ENB		
1 ^f	2	72	433	92.5	2.5	5.0	0.2	3.0	193	1.9
4	3	170	680	88.0	3.1	8.9	0.5	11.5	197	2.0
5	5	474	1139	85.8	4.2	9.9	1.8	34.5	136	1.9
6	6	721	1442	87.1	3.3	9.6	2.2	51.7	100	2.3

^a polymerization conditions: ethylene pressure, 1.01 bar; total volume, 50 mL (toluene); V complex, 2.5 μmol; Al/V = 500; ETA/V = 10; temperature, 20 °C; P/E/ENB feed ratio = 4/1/0.5 (mol/mol) in liquid phase; ^b activity in kg_{pol}×(mol_v×h)⁻¹; ^c determined by NMR; ^d the comonomer conversion was calculated by combining the NMR data, comonomer feed, and weight of the obtained terpolymer; ^e determined by SEC; ^f first reported in Table 1.1.

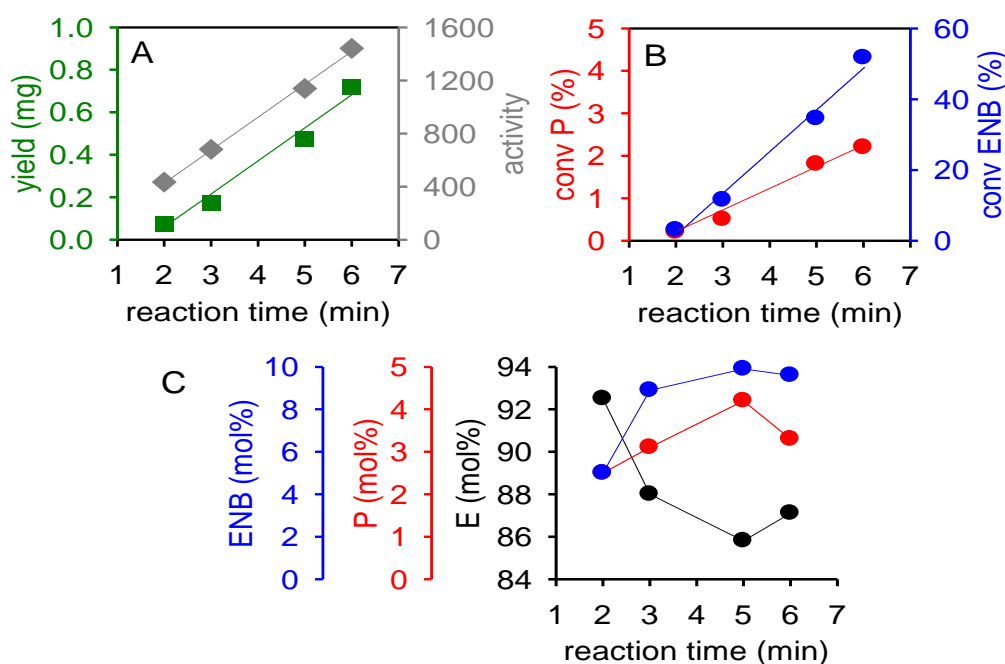


Figure 1.9. (A) Plot of yield and activity vs reaction time, (B) Plot of propylene and ENB conversion vs reaction time. (C) Plot of ethylene, propylene and ENB content in the terpolymer vs reaction time.

However, since **1a** has a low initiation rate, it can be inferred that a more pronounced composition drift likely occurs for the experiment 6 min long (sample **6**). At this time, the ethylene content increases to 87.1 mol% with respect to the same data of 85.8 mol% for the

experiment 5 min long. This increase in the ethylene content together with the increase in the comonomer consumption (Figures 1.9B and 1.9C) indicates that, when the reaction bath is severely and increasingly depauperated in the comonomers, and most of ENB is consumed, the rate of ethylene homopolymerization is accelerated with respect to the (co)polymerization rate, thus increasing the chance of forming longer ethylene sequences.

1.2.5 Thermal and Structural Characterization of EPDMs synthesized using Catalyst 1a

The DSC curves of EPDM terpolymer samples reported in Table 1.2, recorded during first heating from -70°C to 180°C , successive cooling from the melt to -70°C , and second heating of the melt crystallized samples up to 180°C , all recorded at $10^{\circ}\text{C}/\text{min}$, are reported in Figure 1.10A-C. The values of glass transition temperatures and melting and crystallization temperatures with corresponding enthalpies are reported in Table 1.3. Because of the broad melting and crystallization peaks and the overlapping with the glass transition, the exact determination of the beginning of the melting endotherm and of the crystallization exotherm is not immediate. As extensively reported in literature,⁶⁶ the extrapolation of the DSC curve to lower temperature from the melt has been used as the baseline for melting and crystallization peaks. This curve also corresponds to the tangent for the glass transition evaluation. For all samples, melting (ΔH_m^I , ΔH_m^{II}) and crystallization (ΔH_c) enthalpies has been evaluated by integrating the area below the melting and the crystallization peaks.

From the data reported in Figure 1.10, it is evident that all 4 samples show similar DSC thermograms despite differences in composition. The DSC cooling curves show well defined exothermic peaks that indicate crystallization from the melt at low temperatures in the range $4^{\circ}\text{C} - 10^{\circ}\text{C}$ (Figure 1.10B).

Glass transition at low temperature, followed by cold crystallization and broad melting at higher temperature can be observed during second heating scans in all four cases (Figure 1.10C). The glass transition temperature (T_g) and the melting temperature (T_m) of the obtained terpolymers ranges from -6 to -4°C , and from 40 to 46°C , respectively (Table 1.3). These data do not appear to be closely related to the terpolymer composition, and it could be inferred that composition drift may have an unpredictable effect on thermal properties. Indeed, random (co)polymers with an ethylene content as high as 85 mol% usually are semicrystalline materials with T_m higher than those of terpolymers under investigation.⁶⁴ At least in principle, the presence of ENB-rich segments and chains, formed at the beginning of the reaction, may hinders the crystallization of those chains having longer methylene sequences and contribute

to lowering the T_m . Besides, it is worth of note that T_g and T_m of these terpolymers are comparable.

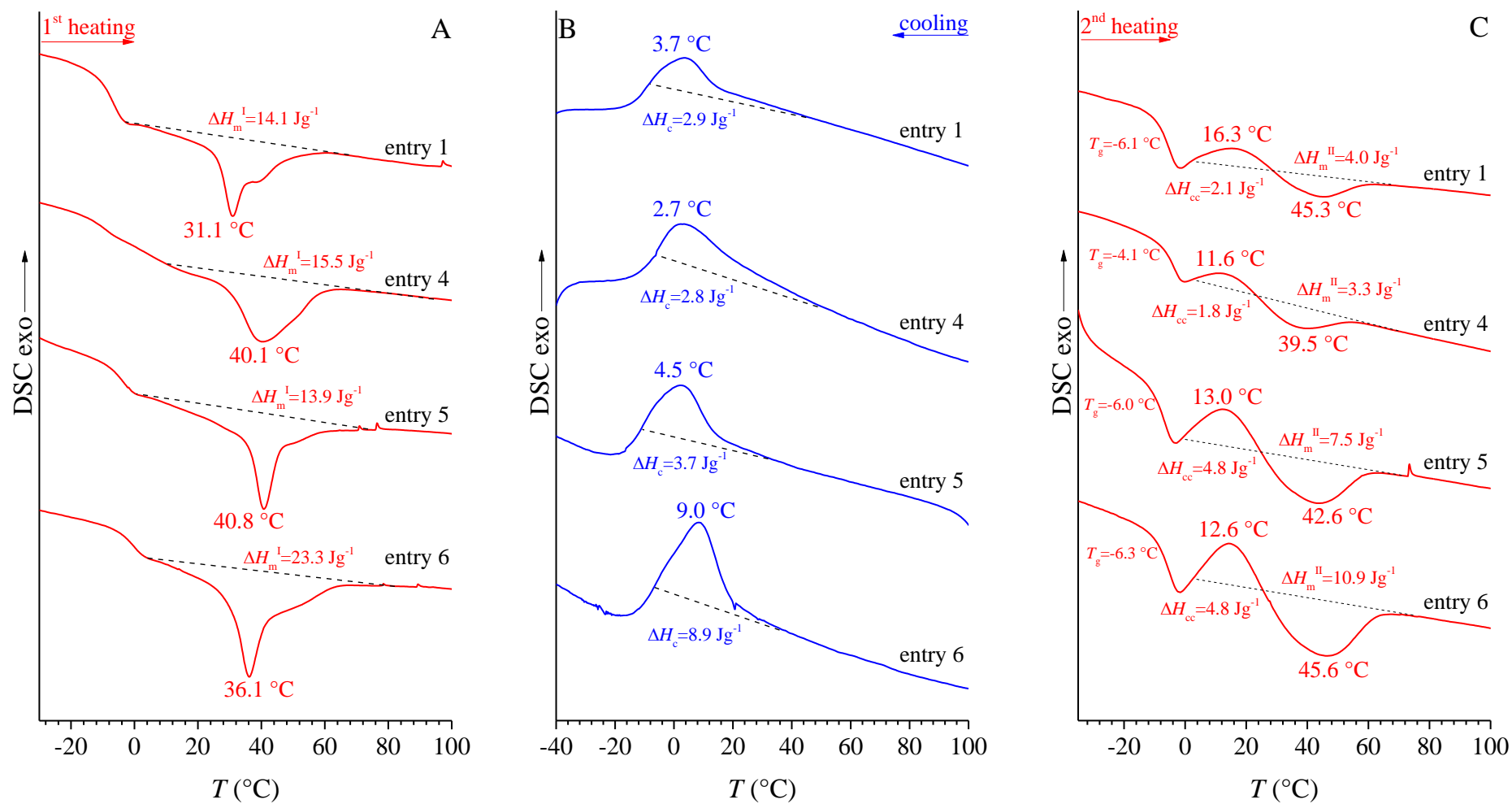


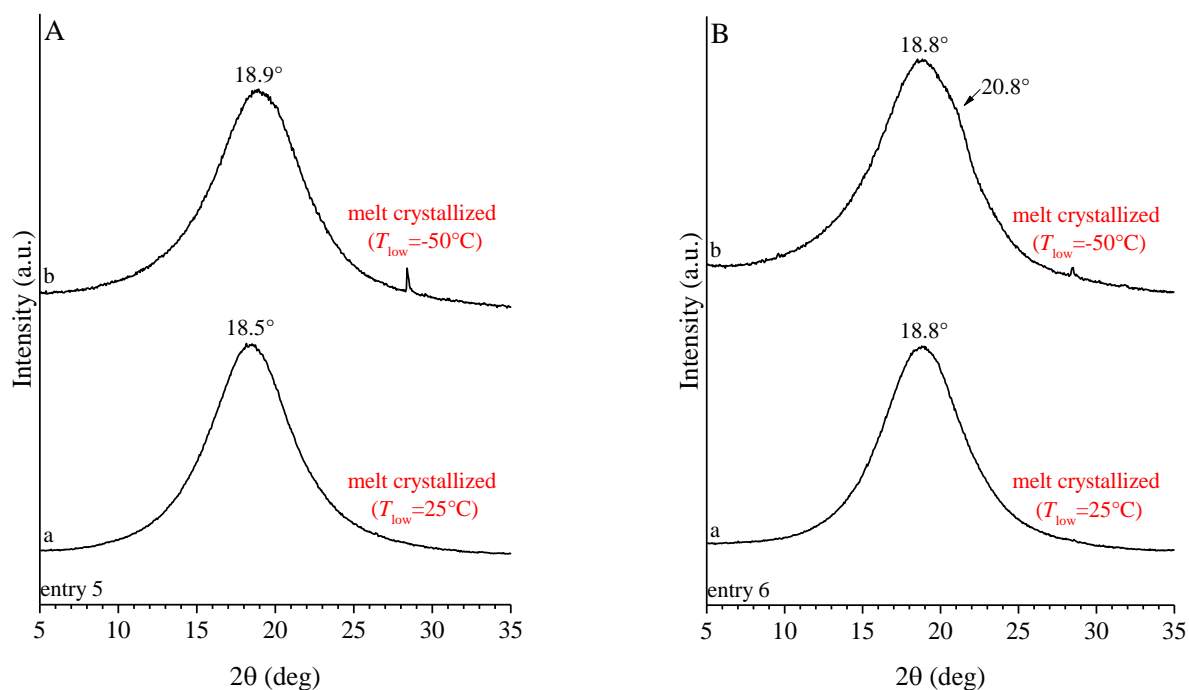
Figure 1.10. DSC curves recorded during heating of the as-prepared sample (A), cooling (B) and successive second heating (C) at scanning rate of 10 °C/min, of E/P/ENB terpolymers obtained by **1a**/Et₂AlCl/ETA.

Table 1.3. Thermal Properties of E/P/ENB terpolymers obtained by **1a**/Et₂AlCl/ETA.

entry	time (min)	terpolymer composition (mol%)			T_m^I (°C) ^a	T_c (°C) ^{ab}	T_m^{II} (°C) ^a	T_g (°C) ^c	ΔH_m^I (J g ⁻¹) ^a	ΔH_c (J g ⁻¹) ^{ab}	ΔH_m^{II} (J g ⁻¹) ^a
		E	P	ENB							
1	2	92.5	2.5	5.0	31.1	3.7 (16.3)	45.3	-6.1	14.1	2.9 (2.1)	4.0
4	3	88.0	3.1	8.9	40.1	2.7 (11.6)	39.5	-4.1	15.5	2.8 (1.8)	3.3
5	5	85.8	4.2	9.9	40.8	4.5 (13.0)	42.6	-6.0	13.9	3.7 (4.8)	7.5
6	6	87.1	3.3	9.6	36.1	9.0 (12.6)	45.6	-6.3	23.3	8.9 (4.8)	10.9

^a From DSC of Figure 1.10; ^b The temperatures and enthalpies of crystallization shown in brackets corresponds to the cold-crystallization peak observed in the second heating scan; ^cevaluated from the second heating curves of Figure 1.10C.

The X-ray powder diffraction profiles of compression molded films of samples 5 and 6 (Table 1.2), prepared as described in the section 1.2.1, are reported in Figure 1.10. Both samples, even when cooled to -50°C, show quite similar WAXS profiles with a broad halo centered at $2\theta \approx 19^\circ$ typical of amorphous EP copolymers.⁶⁵ It is worth noting that both samples show clear melting and crystallization peaks in the DSC curves of Figure 1.10 notwithstanding they seem amorphous from the WAXS analysis because of the absence of sharp diffraction peaks (Figure 1.10). Thus, the data from thermal analysis are in contrast with the data from diffraction analysis, as the former reveal the presence of crystallinity, which is not detected by WAXS. This kind of “hidden crystallinity” has already been observed in commercial EPDM samples and has been named *cryptocrystallinity*.⁶⁶

**Figure 1.11.** WAXS profiles of EPDM terpolymer samples 5 (A) and 6 (B) crystallized by cooling from the melt to 25°C (a) and -50°C (b). In both cases, the WAXS spectra were collected at room temperature.

In order to confirm the existence of the cryptocrystallinity found by DSC measurements and to verify that these small crystals are able to arrange in ordered entities on the nanometer scale, Small Angle X-ray Scattering (SAXS) measurements were performed. SAXS profiles of compression molded films, prepared as described in the section 1.1.1, have been collected at room temperature.

The desmeared SAXS profiles of samples 5 and 6 of Table 2 and the corresponding Lorentz corrected profiles are shown in Figure 1.12.

SAXS profiles of both samples, when the compression-molded films have been prepared by cooling the melt to room temperature, do not show any correlation peak (Figure 1.12A,A'). In contrast, when the samples are cooled from the melt to -50°C in order to enhance the crystallization, while the SAXS profile of sample 5 remains almost unchanged (profiles *a* of Figure 1.12B,B'), that of sample 6 show a broad and weak correlation peaks centered at $q^* \approx 0.5 \text{ nm}^{-1}$ (profiles *b* of Figure 1.12B,B')

The presence of a correlation peak in the SAXS profile of the sample 6 (profiles *b* of Figure 1.12B,B'), that appear amorphous from the WAXS, is quite surprising and may be attributed to the presence of crystallinity. However, it is important to remember that for these samples the presence of crystallinity has been revealed by the presence of endothermic and exothermic peaks in the DSC thermograms of Figure 1.10B. The data reported in Figure 1.12 indicate that the cryptocrystallinity revealed by DSC analysis and not detected by WAXS is, at least for the sample 5, confirmed by SAXS. In this regard, it is worth remembering that the SAXS data can be interpreted in terms of a crystalline lamellar morphology that presents large imperfections due to the presence of the propene and diene units. The formation of distorted lamellar morphologies is, indeed, typical of copolymers.⁶⁷ Distorted lamellae having small lateral dimensions, large distributions of the thicknesses of the crystalline and amorphous layers in the lamellar stacks, the presence of single lamellar entities besides a population of periodic arrays of parallel lamellae are typical defects, in particular for copolymers.⁶⁸ The small intensity of SAXS scattering observed in the SAXS profile of sample 6 may be associated with the small lateral dimensions of the crystallites and the presence of non-negligible amount of extra-lamellar amorphous phase.

The fact that the presence of crystallinity can only be detected in sample 6 by SAXS is probably related to the higher degree of composition drift, and consequent higher heterogeneity, that characterize this sample compared to sample 5. Indeed, as described in the paragraph 1.2.3, since sample 6 was polymerized for the longer investigated time (see Table 1.2), it is very likely to contain a higher concentration of crystallizable ethylene-rich chains, formed at the

end of the polymerization when a very low amount of comonomers is left in the reaction mixture, compared to all the other samples in the series.

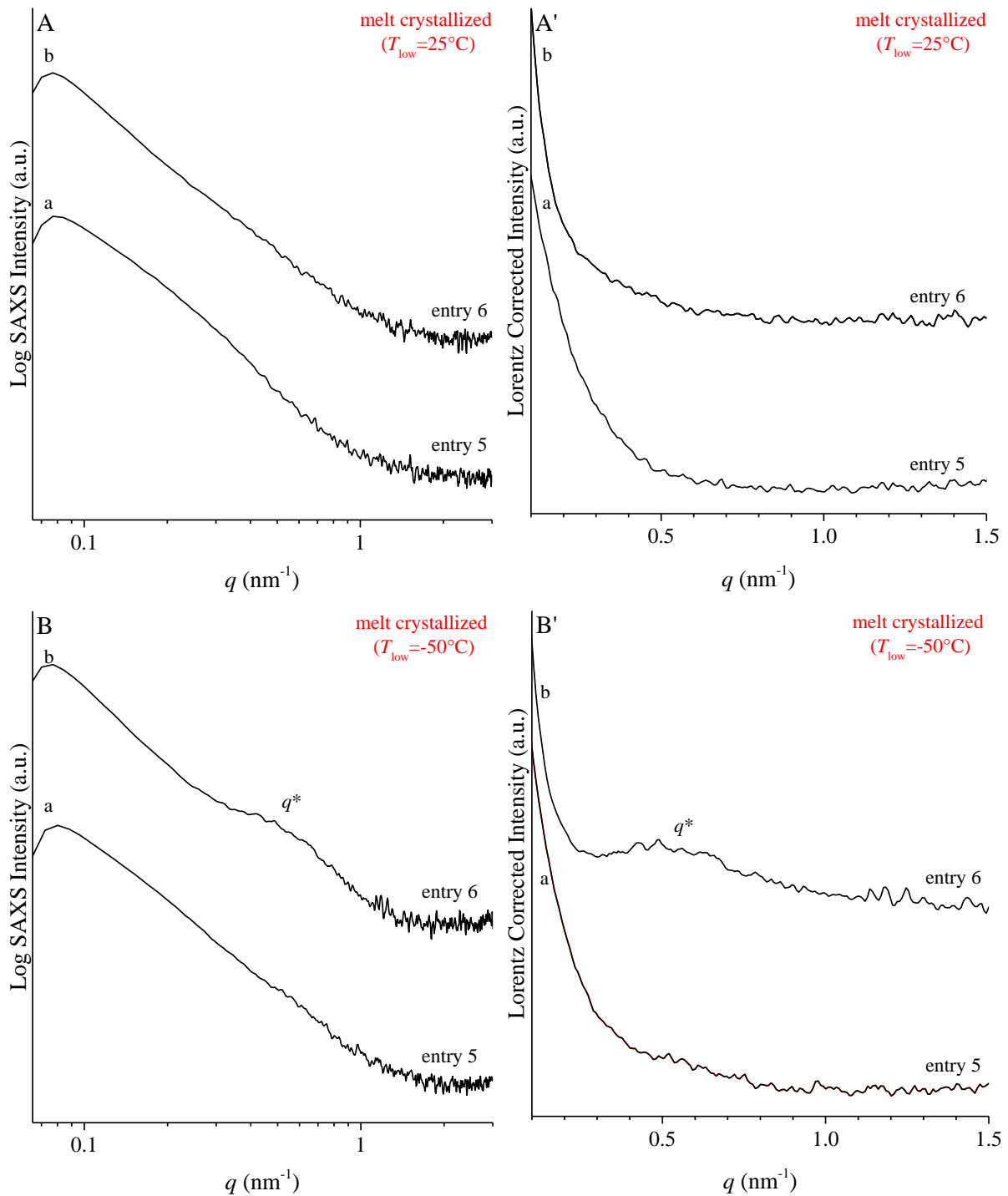


Figure 1.12. SAXS intensity profiles (A,A') and Lorentz-corrected SAXS profiles (B,B') measured at room temperature of EPDM terpolymer samples 5 and 6 crystallized by cooling from the melt to 25°C (A,A') and -50°C (B,B').

1.2.6 Mechanical Properties of EPDMs synthesized using Catalyst 1a

The stress strain curves of compression-molded films of samples 5 and 6 (Table 1.2) are displayed in Figure 1.13. The mechanical parameters obtained from the stress-strain data are summarized in Table 1.3. The compression molded films are prepared by rapid cooling from the melt, at cooling rate of nearly 20-40 °C/min as described in the Section 1.2.1. Both the samples show a mechanical behavior with typical features of elastomers characterized by low Young's modulus, uniform deformation to high strain, high values of deformation at break, and strain hardening at the late stage of deformation. It is worth remembering that in these crystallization conditions, where the samples are compression molded from the melt and cooled to room temperature, crystallization does not occur (Figure 1.10B and profiles *a* of Figure 1.11). Thus, the low values of Young's modulus and the high deformability could be associated with the fact that both samples are amorphous in the unstretched state. Strain hardening phenomenon at the late stage of deformation evident for both samples, as will be shown in paragraph 1.2.7, is associated with the crystallization of ethylene sequences induced by stretching. Small crystals can form upon stretching, acting as physical knots in the elastomeric network, resulting in increase of tensile strength of the rubber.^{65,69}

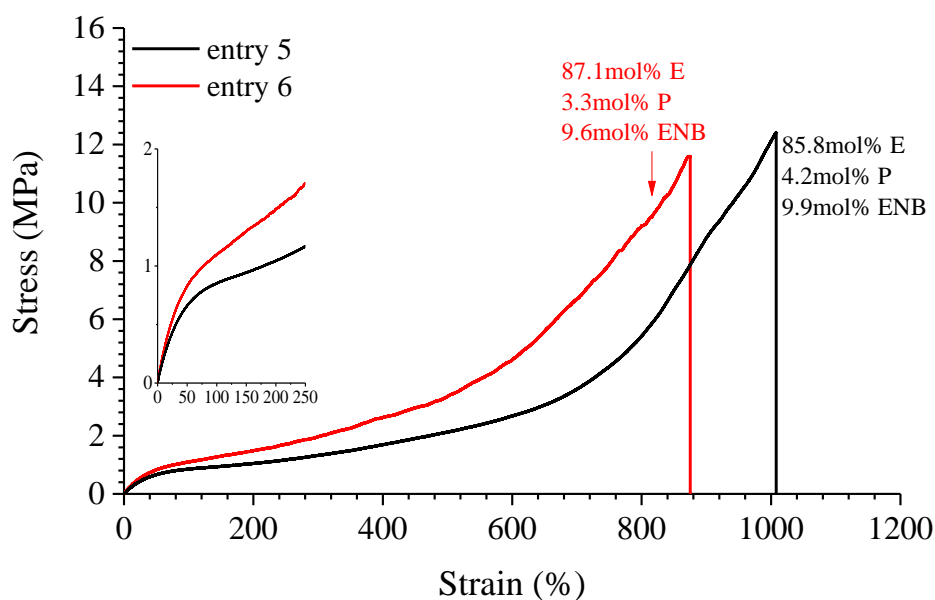


Figure 1.13. Stress-strain curves of compression molded films of samples 5 and 6.

Table 1.3. Mechanical properties of EPDMs obtained with **1a**/Et₂AlCl/ETA.

entry	E ^a (MPa)	σ _b ^b (MPa)	ε _b ^c (%)	σ _y ^d (MPa)	ε _y ^e (%)	t _b ^f (%)	cycle 1		cycle 2	
							SR ₁ ^d	SR _x ^e	SR _{420%} ^f	SR _{810%} ^g
5	2.4±0.1	12.1±1.1	968±75	0.6±0.1	23±2	80±2	84	71	83	81
6	3.0±0.1	11.9±0.3	878±55	0.9±0.1	24±3	85±5	87	76	85	81

^a Young's modulus; ^b stress at break; ^c strain at break; ^d stress at yield; ^e strain at yield; ^f tension set at break; ^g strain recovery measured after the first step in a step cycle test type at 300% strain; ^h strain recovery measured after the last step in a step cycle test type at 300% strain; ⁱ strain recovery measured after the strain at 420% in a step cycle test type at increasing strains; ^l strain recovery measured after the strain at 810% in a step cycle test type at increasing strains.

From Figure 1.13 it can be observed some changes in the onset of strain hardening and yield stress between the two investigated samples. Sample 6 has a significantly higher yield stress than sample 5, although both samples are amorphous with a comparable composition. It is worth noting that both samples present a diffuse yielding around 40–60% of deformation. At deformation higher than 100%, it is likely that both samples start to experience progressively strain-induced crystallization that is enhanced in sample 6. In fact, sample 6 shows higher stress values at any strain compared to those of sample 5. The higher degree of composition drift, and consequent higher heterogeneity, for sample 6 may account for this phenomenon.

The elastic behavior of both the terpolymers was evaluated performing two different cycle tensile tests: hysteresis and step cycle experiments. All the parameters obtained from the hysteresis experiments and from the step cycle tensile tests are also reported in Table 1.3.

In the first set of experiments, the samples were cyclically loaded and unloaded ten times to 300% strain, and the percent recovery in specimen length was measured after removal of the strain for each cycle. In Figure 1.14A, as representative, are shown the cyclic curves obtained for the sample 6. The first cycle results in the most significant amount of permanent deformation, followed by minimal increase in the unrecovered strain on subsequent cycles.

The recovery strain after the first load cycle is 84% for sample 5 and 87% for sample 6, while 71% and 76% after the last load cycle, respectively (Table 1.3).

In the second set of hysteresis experiments, the samples were extended step by step up to different strains (Figure 1.14B). The hysteresis loop enlarged only gradually as the applied strain increased, both samples giving remarkable and almost stable strain recovery in the range from 85 to 81% when the applied strain goes from 420 to 810%, respectively (Table 1.3). The elastic behavior is slightly improved in sample 6 which presumably presents a more effective crystalline network that acts as physical nodes during stretching and successive release of the tension.

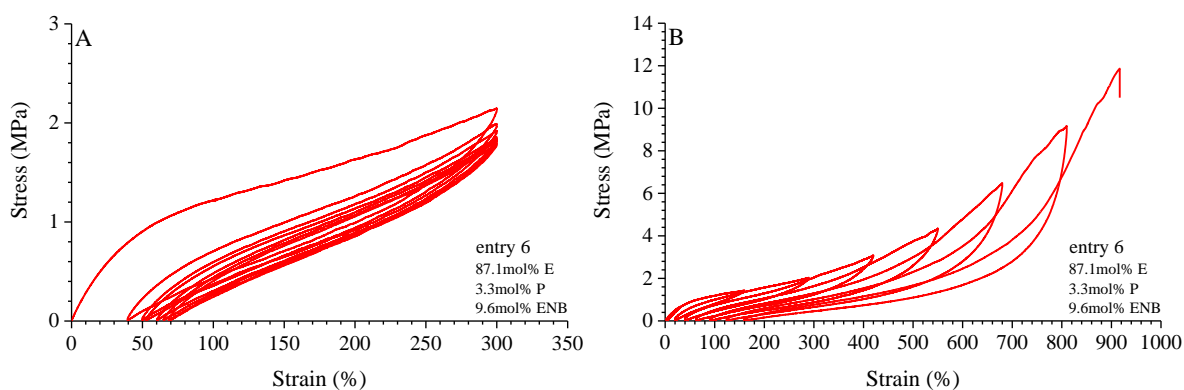


Figure 1.14. (A) stress-strain curve of sample 6 in the hysteresis experiments for a strain of 300%, and (B) stress-strain curve of sample 6 during step cycle tensile deformation at different strain.

1.2.7 Fiber diffraction analysis and strain-induced crystallization of EPDMs synthesized using Catalyst 1a

In order to reveal the possible occurrence of stress induced crystallization (SIC) during the stretching of the studied terpolymer samples, Wide Angle X-ray Diffraction measurements have been performed. In particular, X-ray fiber diffraction patterns have been collected during deformation and after releasing the tension of samples 5 and 6. Measurements have been performed on compression molded films before stretching and after stretching at different degrees of deformation. Finally, the diffraction pattern has been recorded on the relaxed fiber upon removing the tension from the maximum deformation. For each investigated deformation of both samples, the bidimensional X-ray diffraction pattern and the corresponding profile read along the equatorial layer line is reported. Furthermore, in order to evaluate the variation of the degree of crystallinity, from the X-ray diffraction patterns of the undeformed samples, of the samples stretched at maximum deformation and after removal of tension, the equatorial profiles integrated over the azimuthal coordinate have also been calculated. Details about the method used for the calculation of the integrated profiles are shown in section 1.2.1.

The bidimensional X-ray diffraction patterns, and the corresponding equatorial and integrated profiles, of the unstretched samples and of fibers stretched at different degrees of deformation and after releasing the tension, of samples 5 and 6 are reported in Figures 1.15 and 1.16. Both samples in the undeformed state appear amorphous as indicated by the presence of the broad halo at $2\theta \approx 18-19^\circ$ in the diffraction patterns and in the equatorial profiles of Figures 1.15A and 1.16A. The equatorial profiles are in agreement with the WAXS profiles recorded at room temperature of compression-molded sample (profiles *a* of Figures 1.11A,B).

The diffraction patterns of both stretched samples of Figures 1.15 and 1.16 show, already at low degrees of deformation, the appearance of a sharp peak at $2\theta \approx 20^\circ$, corresponding to the

(110)_o/(100)_h reflection of the orthorhombic/pseudo-hexagonal forms of PE, and its polarization on the equator. This indicates that in both cases SIC occurs by stretching already in the early stages of the deformation ($\epsilon = 300\%$). This is also in agreement with recently published findings on ethylene/propylene(/diene) (EP(D)M) co- (and ter-)polymers characterized by low level of crystallinity.⁶⁵

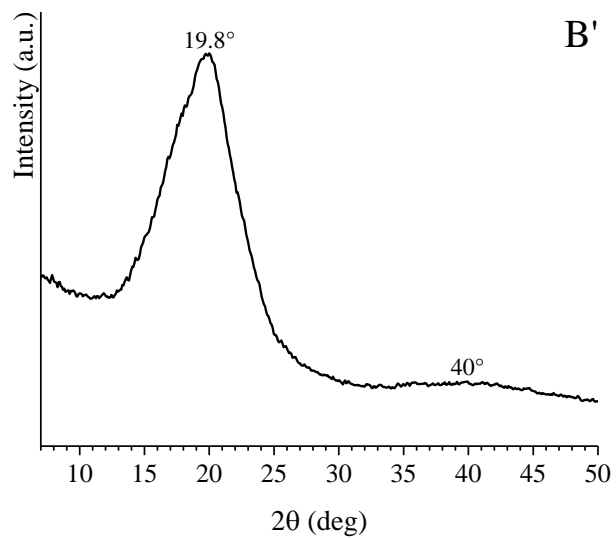
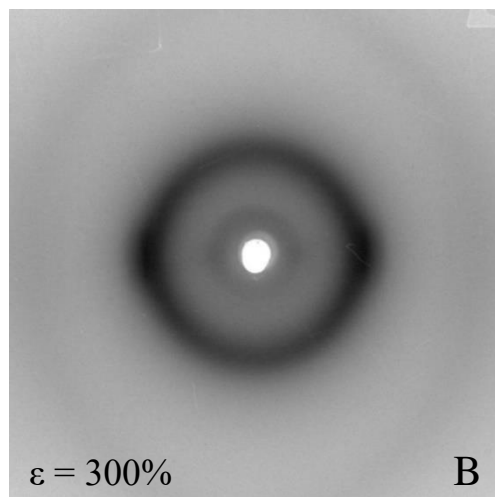
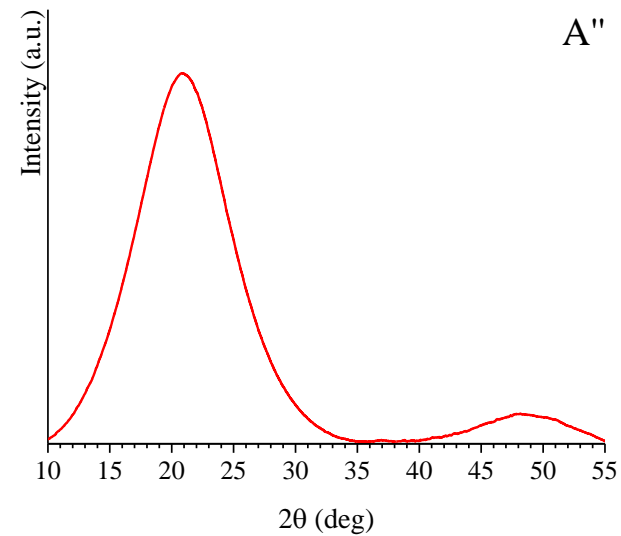
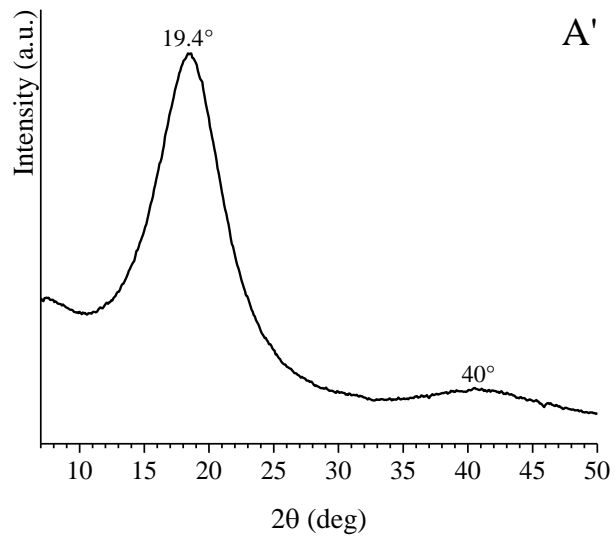
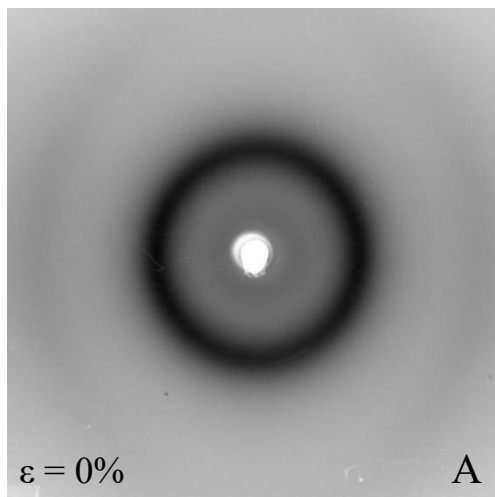
With the progressive increase of the deformation, improvement of orientation of crystals is observed with increase of polarization of equatorial reflections and increase of the intensity and sharpness of the reflection at $2\theta \approx 20^\circ$. At the same time, a decrease of the amorphous halo intensity at $2\theta = 18-19^\circ$ and its polarization on the equator is observed. When the tension is released, the broad amorphous halo at $2\theta \approx 18-19^\circ$ becomes more intense and reemerges as the main peak's shoulder in the equatorial profiles of Figures 1.15E and 1.16E.

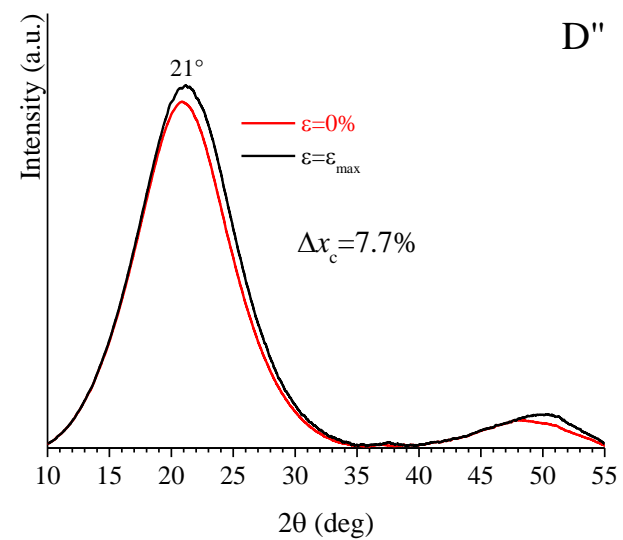
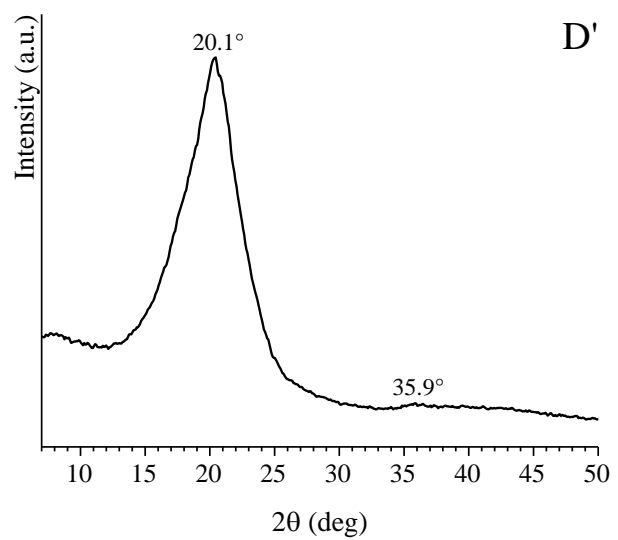
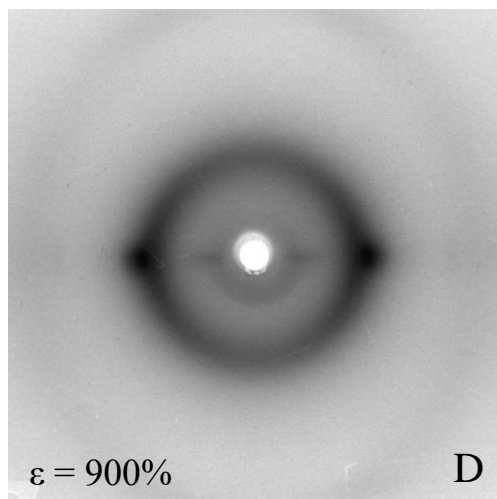
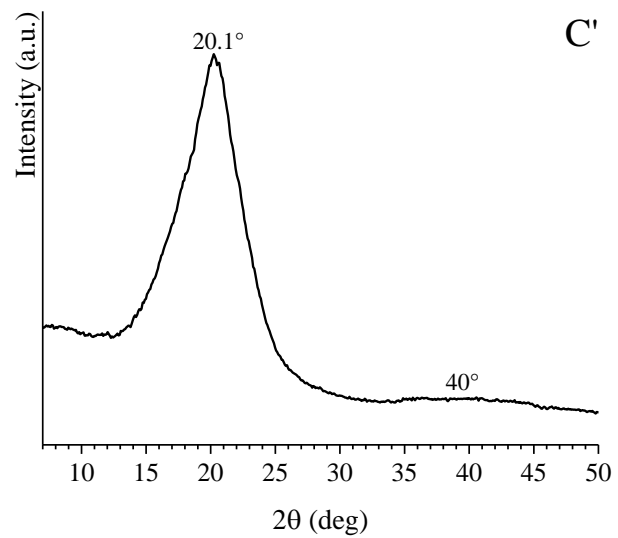
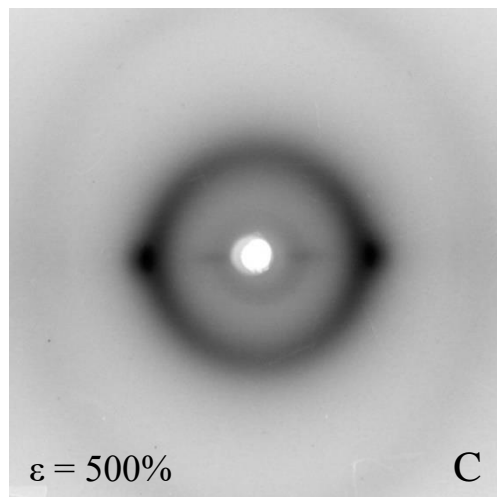
This indicates that after the release of the tension and the relaxation of the fibers, a partial melting of the crystals formed during stretching occurs, as well as a decrease in the orientation of the remaining crystals.

The value of the calculated crystallinity increment Δx_c with respect to crystallinity eventually present in the unstretched samples, evaluated from the integrated profiles, is $\Delta x_c \approx 8\%$ for sample 5 (Figure 1.15D'') and $\approx 13\%$ for sample 6 (Figure 1.16D'') whereas the value of the residual crystallinity increment after tension release is similar between the two samples and around 6% (Figures 1.15E'' and 1.16E'').

Considering that the two investigated samples have a similar composition (Table 1.2), it is likely that the differences observed in terms of the crystallinity they are able to develop under stretching, are strictly dependent on the different distribution of comonomeric units along the polymer chains and on the lengths of crystallizable ethylene sequences which, in turn, depend on the different degree of compositional drift that characterize the two samples. As already discussed, sample 6, synthesized by using more pronounced compositional drift conditions, is probably characterized by chains with ethylene sequences longer than those in the chains of samples 5. This results in higher amount of SIC in sample 6 compared to sample 5, even though the ethylene content is almost the same in the two samples.

entry 5 (85.8mol% E, 4.2mol% P, 9.9mol% ENB) (Table 1.2)





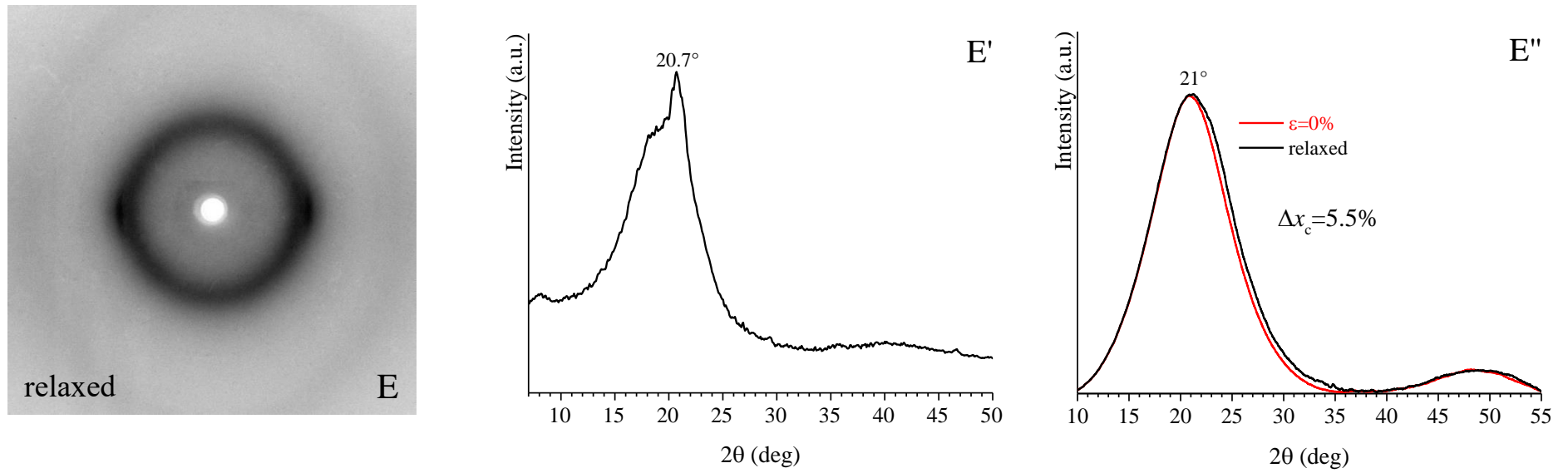
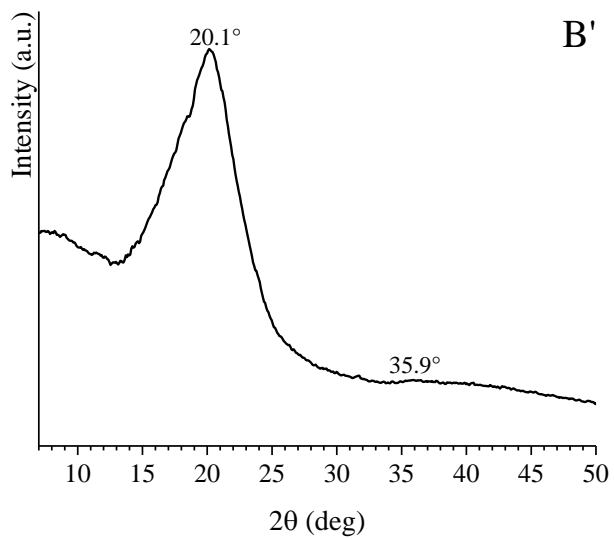
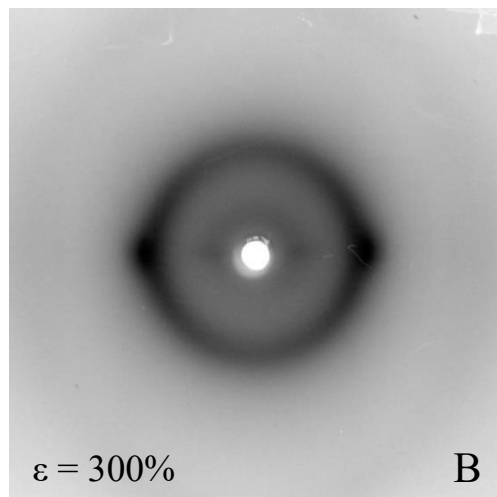
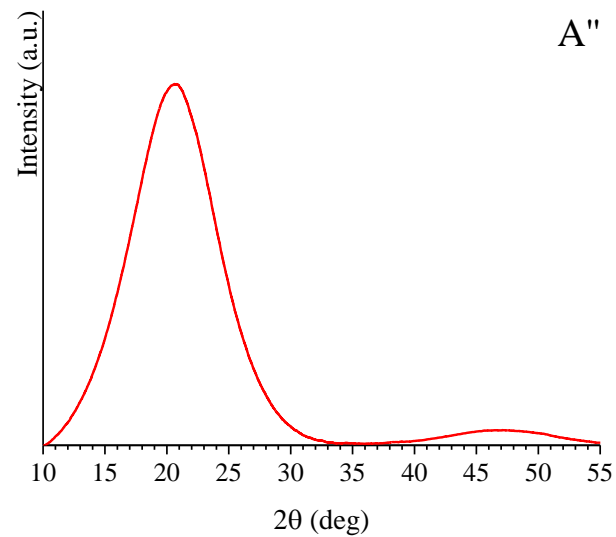
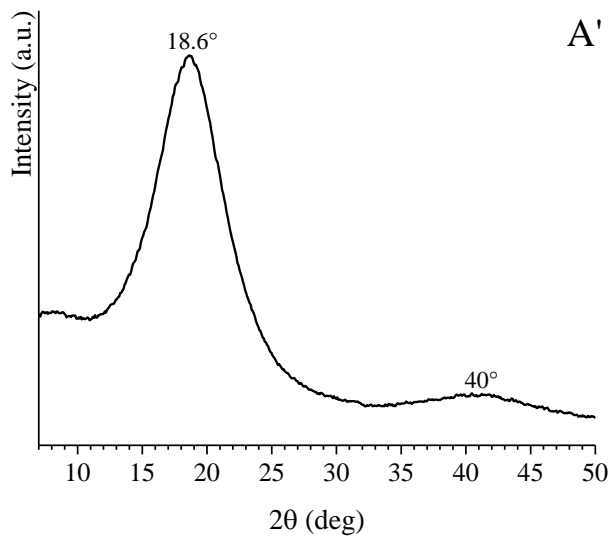
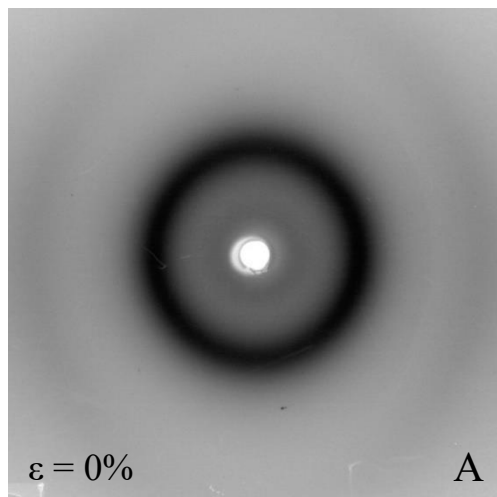
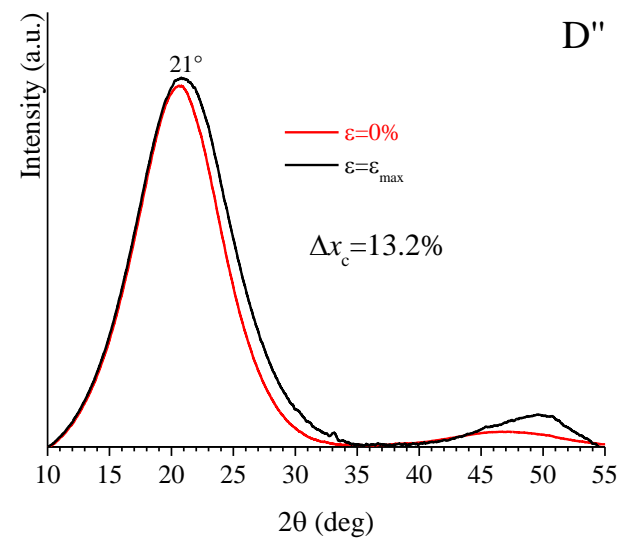
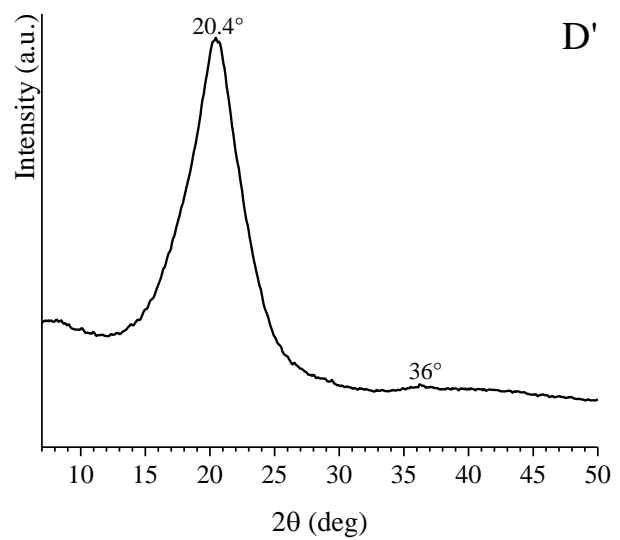
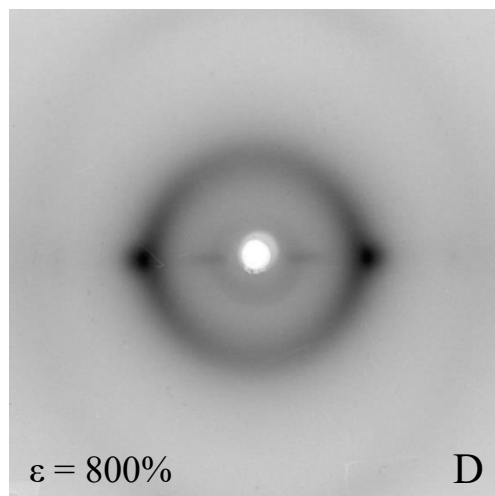
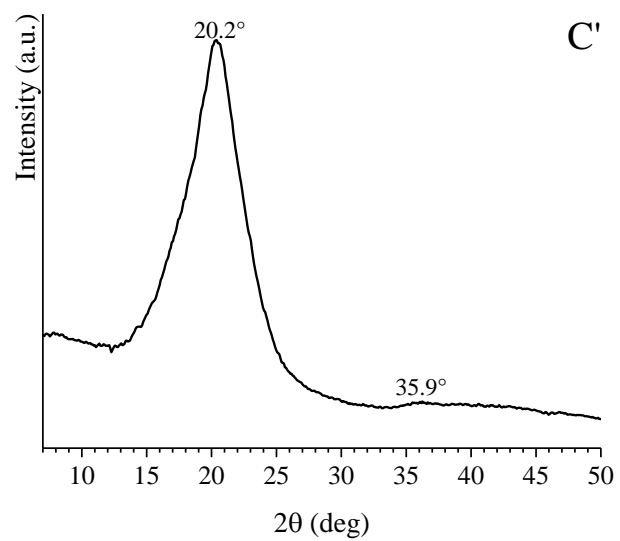
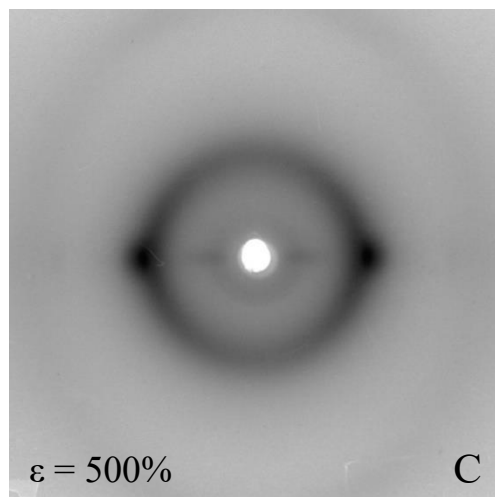


Figure 1.15. X-ray fiber diffraction patterns (A-E), and corresponding equatorial (A' - E') and integrated (A'' - E'') profiles, of the sample 5 recorded at $\epsilon = 0\%$ (A,A'), $\epsilon = 300\%$ (B,B'), $\epsilon = 500\%$ (C,C'), $\epsilon = 900\%$ (D,D') and after releasing the tension (E,E').

entry 6 (87.1mol% E, 3.3mol% P, 9.6mol% ENB) (Table 1.2)





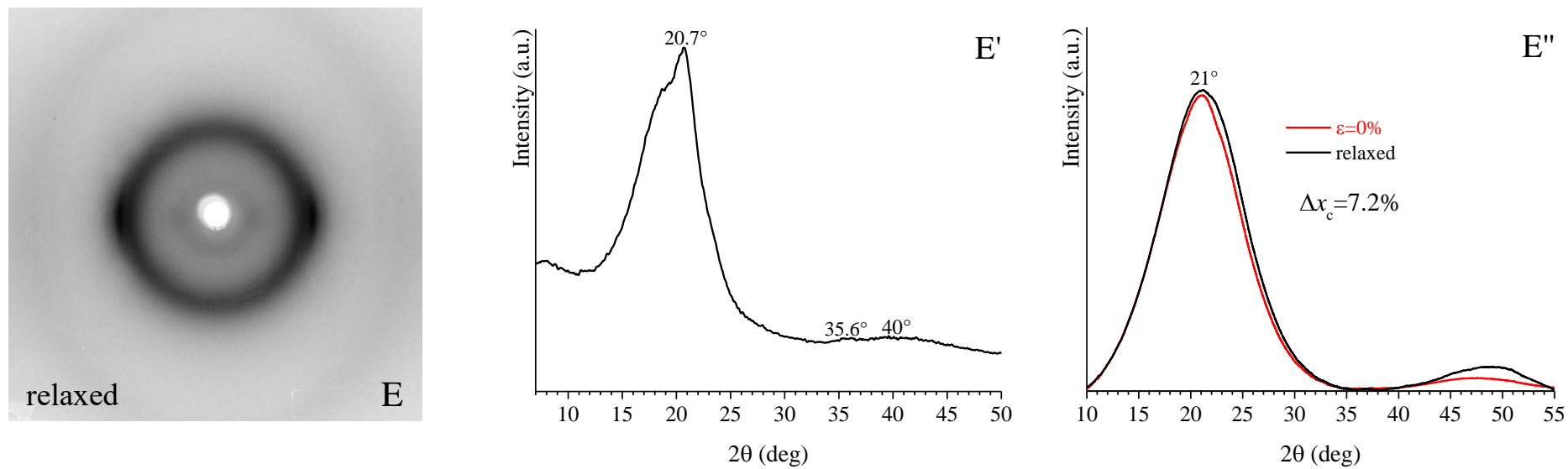


Figure 1.16. X-ray fiber diffraction patterns (A-E), and corresponding equatorial (A' - E') and integrated (A'' - E'') profiles, of the sample 6 recorded at $\epsilon = 0\%$ (A,A'), $\epsilon = 300\%$ (B,B'), $\epsilon = 500\%$ (C,C'), $\epsilon = 800\%$ (D,D') and after releasing the tension (E,E').

1.2.8 Catalyst 2a

Terpolymerization experiments with complex **2a** in combination with Et₂AlCl and ETA were carried out by varying the reaction time between 2 and 6 min in steps of 2 min fixing the ratio of the monomers in the feed at P/E/ENB = 4/1/0.5. In addition, further experiments were carried out by decreasing the feed concentration of ENB (P/E/ENB = 4/1/0.25) and polymerizing for 2 and 4 minutes. In the latter case, it is not possible to extend the experiments for more than 4 minutes since complex **2a** is very active (see Table 1.4) and, therefore, working with a low concentration of ENB in the feed would completely lose control of the reaction, producing highly heterogeneous terpolymers.

Details of the reaction conditions and polymerization results are summarized in Table 1.4.

Table 1.4. Terpolymerization of ethylene with propylene and ENB by **2a**/Et₂AlCl/ETA.^a

entry	P/E/ENB ^b	time (min)	yield (mg)	activity ^c	terpolymer composition (mol%) ^d			(co)monomer conversion (%) ^e		M_w^f ×10 ³	M_w/M_n^f
					E	P	ENB	P	ENB		
2 ^g	4/1/0.5	2	263	1578	83.6	6.4	10.0	1.6	19.3	143	2.0
7	4/1/0.5	4	516	1548	76.8	11.4	11.8	5.1	42.0	96	2.1
8	4/1/0.5	6	1160	2320	85.3	5.4	9.2	5.9	80.1	102	2.1
9	4/1/0.25	2	326	1956	83.7	9.9	6.4	3.2	32.9	127	2.1
10	4/1/0.25	4	765	2295	89.2	4.7	6.1	3.7	76.1	109	2.4

^a polymerization conditions: ethylene pressure, 1.01 bar; total volume, 50 mL (toluene); V complex, 2.5 μmol; Al/V = 500; ETA/V = 10; temperature, 20 °C; ^b P/E/ENB feed ratio (mol/mol) in liquid phase; ^c activity in kg_{pol}×(mol_v×h)⁻¹; ^d determined by NMR; ^e the comonomer conversion was calculated by combining the NMR data, comonomer feed, and weight of the obtained terpolymer; ^f determined by SEC; ^g first reported in Table 1.

Figure 1.17 shows the composition of the obtained terpolymers (A, B) and the conversion of the two comonomers (C, D) as a function of polymerisation time for the two different feed composition ratios investigated (1.17A,C for P/E/ENB = 4/1/0.5 and 1.17B,D for P/E/ENB = 4/1/0.25).

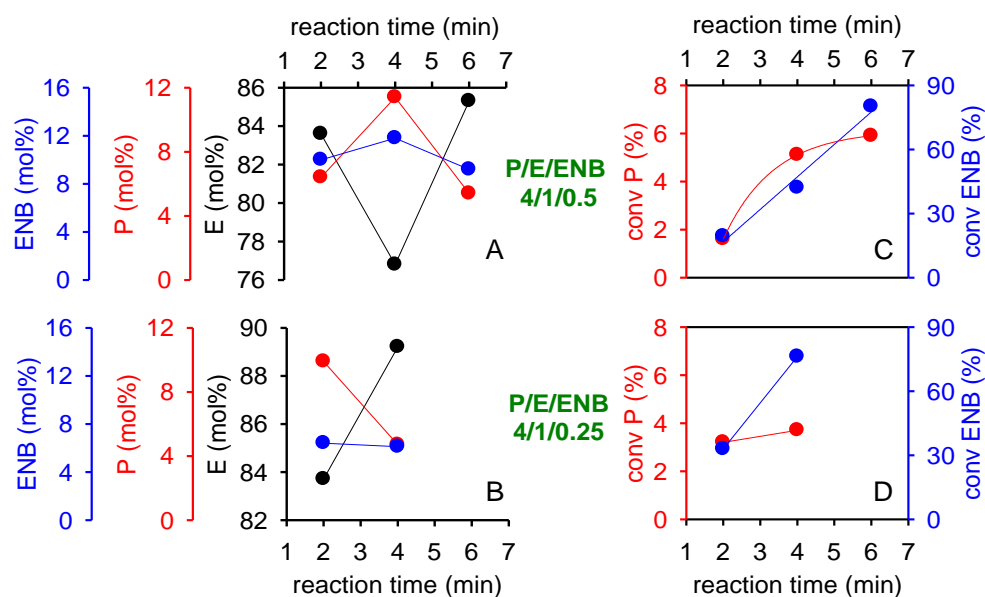


Figure 1.17. (A, B) Plot of ethylene, propylene and ENB content in the terpolymer vs reaction time. (C, D) Plot of propylene and ENB conversion vs reaction time.

For the experiments at P/E/ENB = 4/1/0.5, when the polymerization was stopped after 2 min (entry 2), a terpolymer with a propylene content of 6.4 mol% (1.6% conversion of propylene) and ENB content of 10.0 mol% (19.3% conversion of ENB) was obtained. When the polymerization time was extended to 4 min (entry 7), the yields doubled and the activity remained almost constant. With these reaction conditions a terpolymer with a propylene content of 11.4 mol % (5.1% conversion of propylene) and ENB content of 11.8 mol% (42.0% conversion of ENB) was obtained. When the polymerization time was extended to 6 min (entry 8), the yield more than doubled, and the activity significantly increased. The increase in activity could be related to the fact that the rate of the homopolymerization of ethylene is accelerated with respect to the (co)polymerization rate since the reaction mixture is strongly depauperated in the comonomers (the conversion of ENB reaches 80%). Thus, in these conditions, significant composition drift occurs, and the ethylene content in the terpolymer increases from 76.8 to 85.3 mol %, even though the conversion of the comonomers still grows. If we compare the results obtained at P/E/ENB = 4/1/0.5 with those at P/E/ENB = 4/1/0.25, on the same time scale, large differences can be observed. Indeed, at low concentration of ENB in feed (entries 9 and 10), the activity of **2a** is considerably higher compared to the same experiments performed with a higher concentration of ENB in feed (entries 2 and 7). When the polymerization was stopped after 2 min (entry 9), a terpolymer with a propylene content of 9.9 mol % (3.2% conversion of propylene) and ENB content of 6.4 mol % (32.9% conversion of ENB) was obtained. When the polymerization was quenched after 4 min (entry 10), a terpolymer with a propylene content

of 4.7 mol % (3.7% conversion of propylene) and ENB content of 6.1 mol % (72.1% conversion of ENB) was obtained. The fast depletion of comonomers already in the first 2 min of the reaction determines a significant composition drift over time. Indeed, the content of ethylene increases up to 89.2 mol % with respect to the same data of 76.8 mol % for the experiment 4 min long performed using a less concentration of ENB in feed (entry 7), consistent with a more pronounced composition drift, and hence with an higher incorporation of ethylene during the late stage of the polymerization when working with a lower initial concentration of ENB.

1.2.9 Thermal and Structural Characterization of EPDMs synthesized using Catalyst 2a

The DSC curves of EPDM terpolymer samples synthesized with **2a**, reported in Table 1.4, recorded during first heating from -70°C to 180°C , successive cooling from the melt to -70°C , and second heating of the melt crystallized samples up to 180°C , all recorded at $10^{\circ}\text{C}/\text{min}$, are reported in Figure 1.18A-C. The values of glass transition temperatures and melting and crystallization temperatures with corresponding enthalpies are reported in Table 1.5.

From the data reported in Figure 1.18 it can be observed that samples 2 and 7, which were polymerized for a short time and, thus, are characterized by low compositional drift, do not crystallize by cooling from the melt at the rate of $10^{\circ}\text{C}/\text{min}$. In particular, they exhibit a T_g of about -10°C , and while sample 7 shows no thermal phenomenon during subsequent heating, sample 2 is characterized by a cold crystallization event followed by a melting at about 40°C . Since both samples are characterized by a slight compositional drift, it is likely that the higher tendency to crystallize of sample 2 compared to sample 7 is due to the higher ethylene content present in the first sample (see Table 1.4). Consistent with a more pronounced composition drift, and hence with a formation of longer ethylene sequences, the DSC thermogram of sample 8 shows, in addition to the T_g at -9°C , a clear crystallization event during the cooling from the melt and a broad and multimodal melting endotherm during the subsequent heating with a melting point of around 70°C . The broad shape of the melting event could originate from the non-homogeneous distribution of crystallizable units along the polymer chains which leads to the formation of different crystal families characterised by different lamellar thicknesses and, therefore, melting at different temperatures.

Concerning synthesized samples by decreasing the feed concentration of ENB (P/E/ENB = 4/1/0.25), the low amount of ENB in the feed led to a more propylene incorporation in the terpolymer, and consistent with the high propylene content, sample 9 has a T_g as low as -21°C (Figure 1.18C). In addition, the DSC thermogram of sample 9 also shows a broad melting endotherm with T_m at about 50°C . Finally, sample 10 exhibits a distinct crystallization peak in

the cooling scan and a broader melting endotherm during the successive heating shifted to higher temperature (Figure 1.18C), in accordance with the strong compositional drift that characterizes this sample. Indeed, it is worth noting that the presence of a higher melting peak in this sample obtained at longer reaction time, provides indirect evidence for long crystallizable methylene segments formed at the late stage of the reaction.

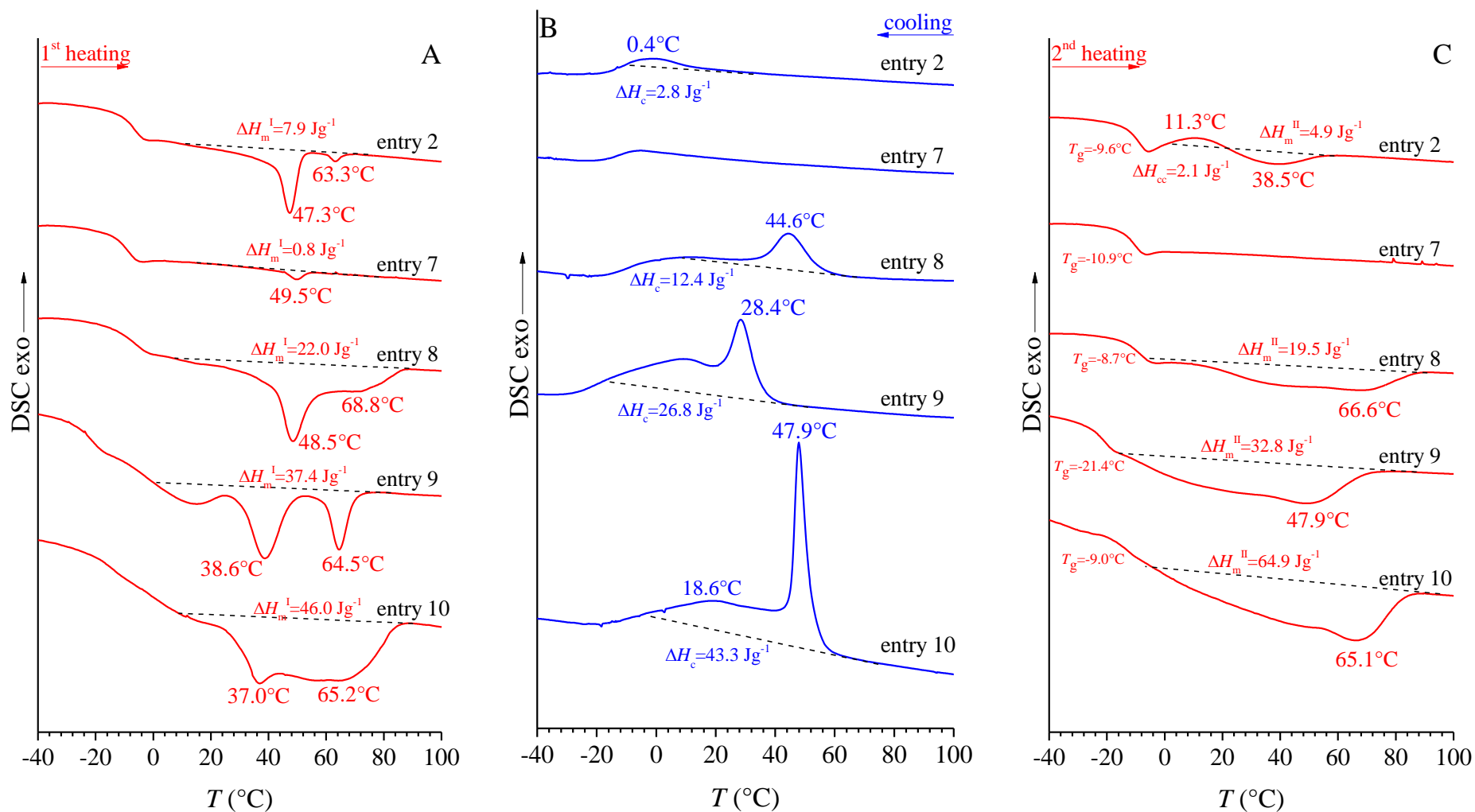


Figure 1.18. DSC curves recorded during heating of the as-prepared sample (A), cooling (B) and successive second heating (C) at scanning rate of 10 °C/min, of E/PENB terpolymers obtained by **2a**/Et₂AlCl/ETA.

Table 1.5. Thermal Properties of E/P/ENB terpolymers obtained by **2a**/Et₂AlCl/ETA.

entry	time (min)	terpolymer composition (mol%)			T_m^I (°C) ^a	T_c (°C) ^{a,b}	T_m^{II} (°C) ^a	T_g (°C) ^c	ΔH_m^I (J g ⁻¹) ^a	ΔH_c (J g ⁻¹) ^{a,b}	ΔH_m^{II} (J g ⁻¹) ^a
		E	P	ENB							
2	2	83.6	6.4	10.0	47.3, 63.3	0.4 (11.3)	38.5	-9.6	7.9	2.8 (2.1)	4.9
7	4	76.8	11.4	11.8	49.5	-	-	-10.9	0.8	-	-
8	6	85.3	5.4	9.2	48.5, 68.8	28.4	66.6	-8.7	22.0	12.4	19.5
9	2	83.7	9.9	6.4	38.6, 64.5	44.6	47.9	-21.4	37.4	26.8	32.8
10	4	89.2	4.7	6.1	37.0, 65.2	18.6, 47.9	65.1	-9.0	46.0	43.3	64.9

^aFrom DSC of Figure 1.18; ^b The temperatures and enthalpies of crystallization shown in brackets corresponds to the cold-crystallization peak observed in the second heating scan; ^cevaluated from the second heating curves of Figure 1.18C.

The X-ray powder diffraction profiles of compression molded films of samples reported in Table 1.4, prepared by cooling from the melt to room temperature and to -50°C, are reported in Figure 1.19A and 1.19B, respectively. For sample 7, WAXS and SAXS measurement were performed only on the sample cooled from the melt to room temperature since exothermic phenomena are completely absent from the DSC curves even at low temperature (Figure 1.18B).

According to the DSC data, samples 7 is amorphous at WAXS (profile b of Figure 1.19A), while the diffraction profiles of melt crystallized sample 8 shows the presence of slight PE crystallinity (profile c of Figure 1.19A). In contrast, although sample 7 shows very low crystallinity at DSC, it appears amorphous at WAXS, even when cooled from the melt to -50°C (profiles a of Figure 1.19A,B).

Regarding samples obtained at low concentration of ENB in the feed (samples 9 and 10), both are semicrystalline by WAXS as confirmed by the presence of a diffraction peak at $2\theta \approx 21^\circ$ corresponding to the (110) reflection of the orthorhombic form and/or (100) reflection of the pseudo-hexagonal form of PE (profiles d, e of Figure 1.19A). In particular, sample 10 exhibits the higher degree of crystallinity ($\approx 9\%$). The WAXS profiles of the various samples collected on the films prepared by cooling the melt to room temperature and to -50°C are very similar to each other. Only an increase in crystallinity for samples 8, 9 and 10 is observed when they are cooled to low temperature (-50°C) in agreement with the fact that from the DSC data (Figure 1.18B) the crystallization of these samples is complete at temperature lower than room temperature.

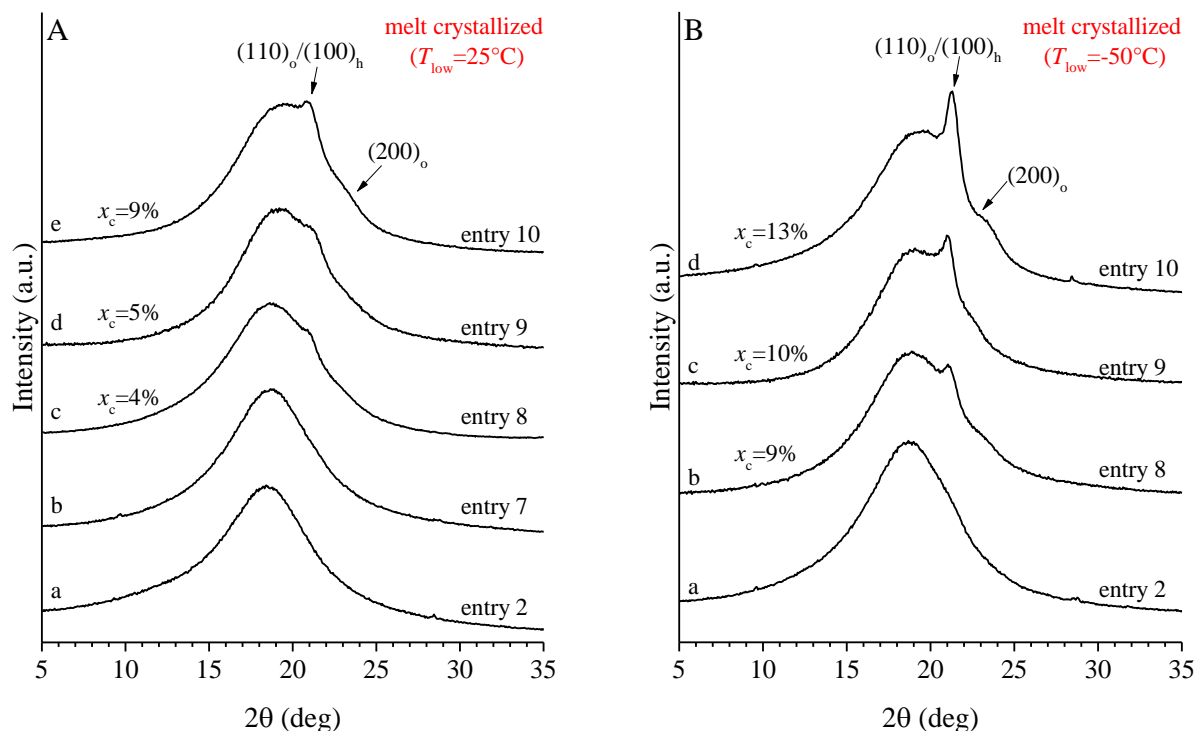


Figure 1.19. WAXS profiles of EPDM terpolymer samples of Table 1.4 crystallized by cooling from the melt to 25°C (A) and -50°C (B). In both cases, the WAXS spectra were collected at room temperature.

The desmeared SAXS profiles of samples of Table 1.4 and the corresponding Lorentz corrected profiles are shown in Figure 1.20A,B and 1.20A',B' respectively.

Samples 2 and 7 do not show any correlation peak confirming their amorphous character already highlighted by WAXS (profiles a,b of Figure 1.20A,A'). In addition, for sample 2, no crystallinity emerges in the SAXS profile even when obtained by cooling from the melt to -50°C, although a slight crystallinity was revealed by the DSC curves (Figure 1.18C).

On the other hand, the SAXS profiles of samples 8, 9 and 10, recorded both on samples cooled by the melt at room temperature and at -50°C, confirm the presence of a broad correlation peak for crystalline samples generated by the broad distribution of defective crystals (profiles c-e of Figure 1.20A,A' and profiles b-d of Figure 1.20B,B'). In particular, moving from sample 8 to sample 10 the correlation peak observed at SAXS becomes more defined in accordance with the increase in crystallinity. While the intensity of the correlation peaks increases when samples are obtained by cooling at low temperature, the position does not change and, specifically, they are centered at $q^* = 0.43, 0.47$ and 0.55 nm^{-1} for samples 8, 9 and 10, respectively.

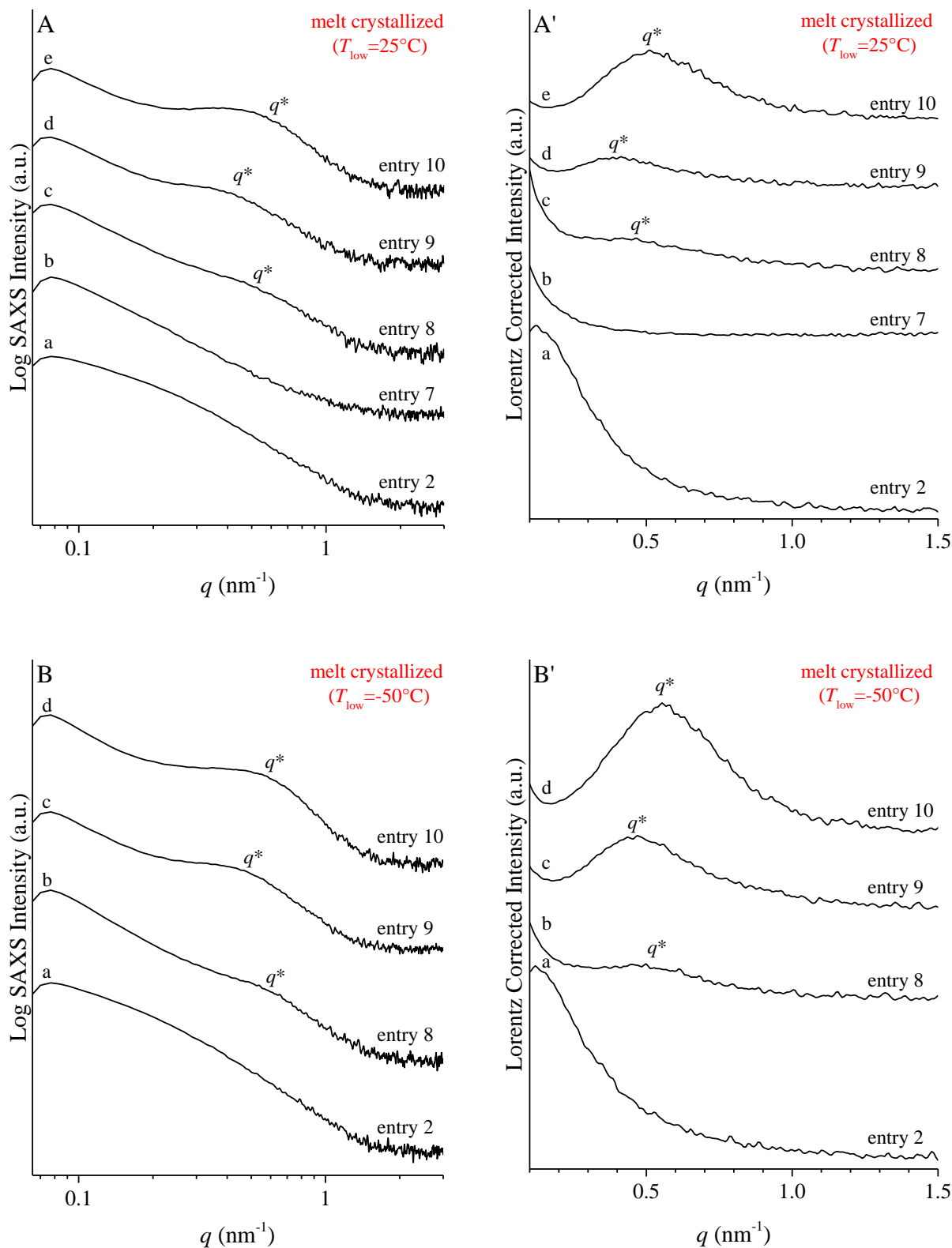


Figure 1.20. SAXS intensity profiles (A,B) and Lorentz-corrected SAXS profiles (A',B') measured at room temperature of EPDM terpolymer samples reported in Table 1.4 crystallized by cooling from the melt to 25°C (A,A') and -50°C (B,B').

1.2.10 Mechanical Properties of EPDMs synthesized using Catalyst 2a

The stress strain curves of compression-molded films of samples reported in Table 1.4 are shown in Figure 1.21, and the tensile parameters extracted from the curves are listed in Table 1.6. The observed different behavior may be also rationalized on the basis of the abovementioned structural data by WAXS (Figure 1.19A). The amorphous sample 7 has low modulus ($E = 1.2$ MPa), and it is highly ductile with an elongation at break higher than 1500% and stress at break close to 0.2 MPa. Sample 7 starts to behave like a viscous liquid at higher elongation. The material is amorphous with a T_g of -7°C , and high contribution of stress strain-induced crystallization is not expected in this sample containing 23.2 mol% of comonomers (P+ENB). On the contrary, sample 8, semicrystalline ($x_c = 4\%$) in the unstretched state when prepared by cooling from the melt to room temperature, has a higher modulus ($E = 3.9$ MPa), a significant increased strength, an elongation at break of 1250%, and it exhibits strain hardening at the late stage of deformation.

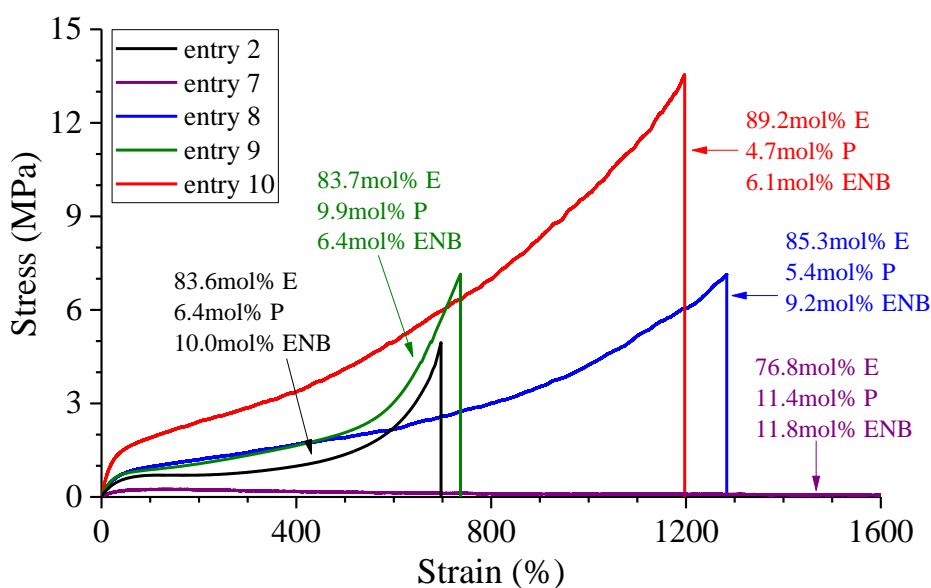


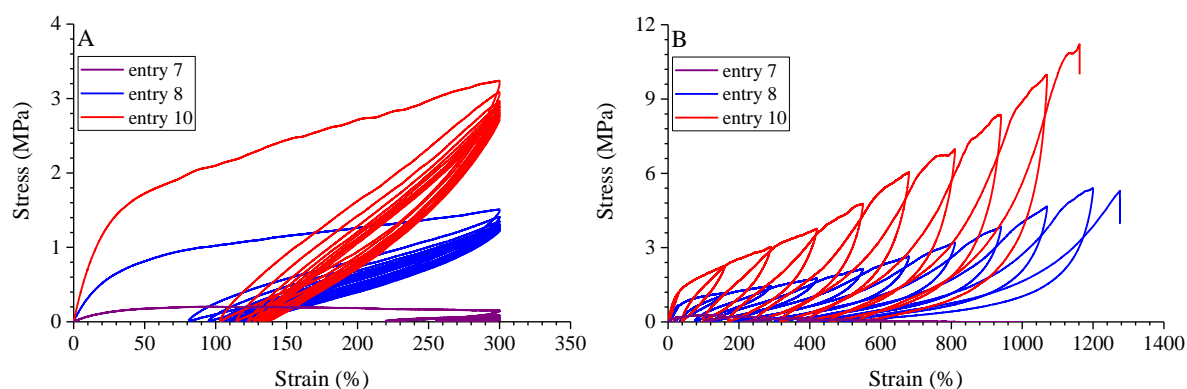
Figure 1.21. Stress-strain curves of compression molded films of samples reported in Table 1.4.

Table 1.6. Mechanical properties of EPDMs obtained with **2a**/Et₂AlCl/ETA.

entry	E ^a (MPa)	σ _b ^b (MPa)	ε _b ^c (%)	σ _y ^d (MPa)	ε _y ^e (%)	t _b ^f (%)	cycle 1		cycle 2	
							SR ₁ ^g	SR _x ^h	SR _{420%} ⁱ	SR _{810%} ^l
2	2.3±0.2	5.0±1.0	697±40	0.5±0.1	18±2	35±3	-	-	-	-
7	1.2±0.2	0.2±0.02	1587±267	0.10±0.02	11±1	30±5	29	3	12	break
8	3.9±0.4	6.8±0.5	1250±47	0.6±0.1	15±3	70±2	73	58	70	63
9	2.6±0.4	7.1±1.0	737±7	0.6±0.1	17±1	90±10	-	-	-	-
10	8.3±0.3	14.7±1.2	1194±58	1.5±0.2	18±2	65±5	66	54	60	52

^a Young's modulus; ^b stress at break; ^c strain at break; ^d stress at yield; ^e strain at yield; ^f tension set at break; ^g strain recovery measured after the first step in a step cycle test type at 300% strain; ^h strain recovery measured after the last step in a step cycle test type at 300% strain; ⁱ strain recovery measured after the strain at 420% in a step cycle test type at increasing strains; ^l strain recovery measured after the strain at 810% in a step cycle test type at increasing strains.

Sample 8 was found to have better elasticity than sample 7, as demonstrated by both the cyclic experiments (Table 1.6, and Figure 1.22). The difference in tensile properties between sample 7 and 8 is the results a reflection of the change in crystallinity level, which in turn strong depends on the extent of composition drift. On the contrary, sample 10, obtained by using a lower amount of ENB in the feed, exhibits the highest modulus ($E = 8.3$ MPa), and remarkable strain hardening with ultimate tensile strength of 14.7 MPa. These data may be due to the highest crystallinity of sample 10 in the unstretched state, i.e., 9% (compared to 4% for entry 8) and to the presence of longer ethylene-rich chain segments formed at the late stage of the reaction when the reaction mixture is strongly depauperated in the comonomers. Besides, sample 10 exhibits more plastic deformation with lower strain recoveries than sample 8 (Table 1.6, and Figure 1.22).

**Figure 1.22.** (A) stress-strain curves of some samples reported in Table 1.4 in the hysteresis experiments for a strain of 300%, and (B) during step cycle tensile deformation at different strain.

1.2.11 Fiber diffraction analysis and strain-induced crystallization of EPDMs synthesized using Catalyst 2a

Figures 1.23 – 1.27 show the X-ray fiber diffraction patterns, and the equatorial and integrated profiles of samples synthesized with the complex **2a** obtained by using a feed composition of P/E/ENB = 4/1/0.5. According to the X-ray diffraction profiles of the compression molded samples obtained by cooling from the melt to room temperature shown in Figure 1.19A, samples 2, 7 and 8 appear basically amorphous in the undeformed state from the analysis of the diffraction patterns reported in Figure 1.23A – 1.27A. As previously discussed, since samples 2 and 7 were polymerised under conditions of slight compositional drift, they can be considered almost homogeneous terpolymers. Thus, the differences observed between these two samples are essentially related to their differences in terms of composition. In fact, whereas for sample 7, with a lower ethylene content, no SIC is observed, sample 2 with a higher ethylene concentration is able to crystallise under stretching, as evidenced by the presence of the $(110)_o/(100)_h$ reflection of the orthorhombic/pseudo-hexagonal forms of PE at $2\theta \approx 20^\circ$. In particular, when stretched to the maximum strain investigated (650%), sample 2 shows an increase in crystallinity of around 6.5%. Sample 8 also develops crystallinity under stretching already for low strains as evident from the X-ray diffraction patterns shown in Figure 1.25. In this case, the calculated increase in crystallinity is about 13%. The fact that sample 8 develops a higher crystallinity than sample 2, despite its similar composition, can still be attributed to the fact that whereas in sample 2, the ethylene units are randomly distributed along the polymer chains, in sample 8, they are likely to be segregated in chain segments, forming a kind of multi-block structure. Thus, since in the latter case (sample 8), the average length of the methylene units is higher, the sample is more likely to crystallise in a greater extent. From the data in Figure 1.26, it is evident that sample 9 shows very similar behaviour to that observed in sample 8 (Figure 1.25). In fact, even in this case, the sample is amorphous in the undeformed state but crystallizes under stretching reaching an Δx_c value of about 12%. It is worth to remind that samples 2 and 9 were synthesized by using the same reaction time but different content of ENB in the feed, lower in the case of sample 9. As mentioned in the section 1.2.8, the lower diene content in feed, for the same polymerization time, determines a significant composition drift and, hence, a higher amount of ethylene rich chains.

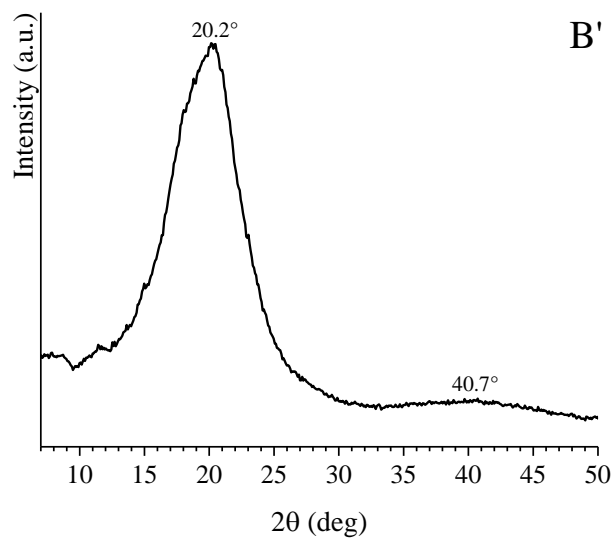
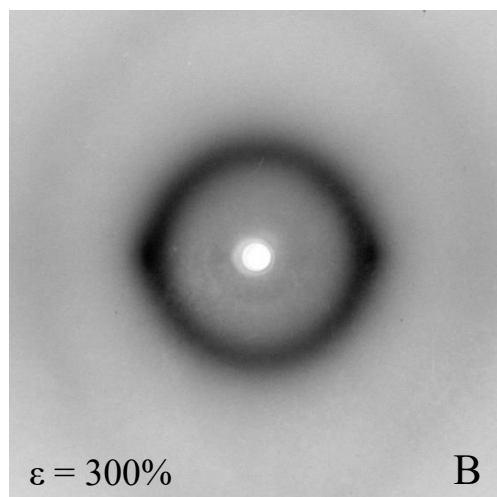
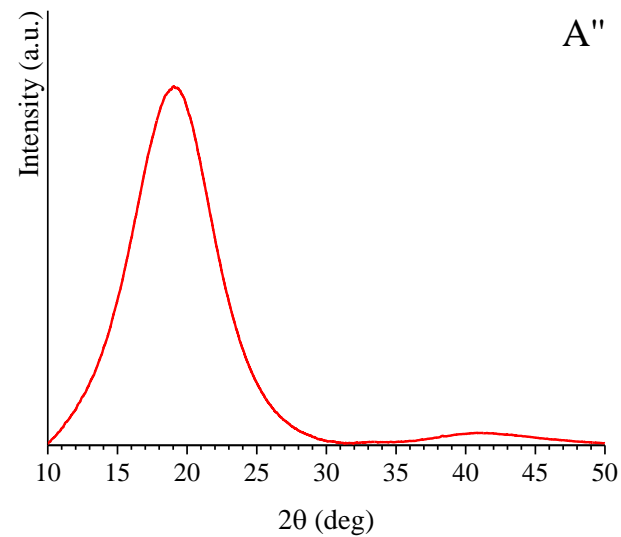
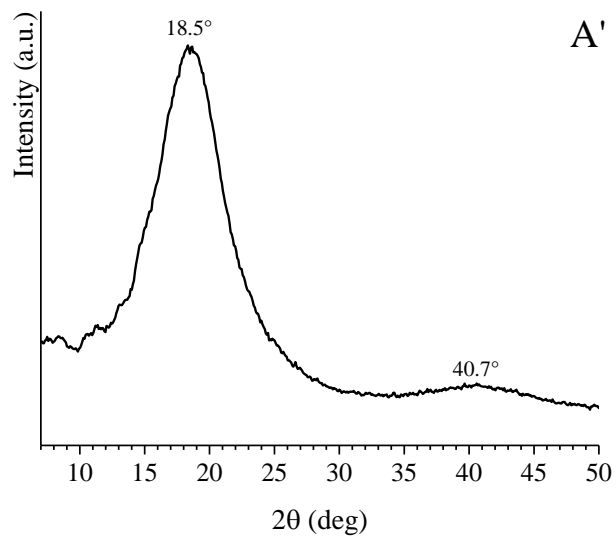
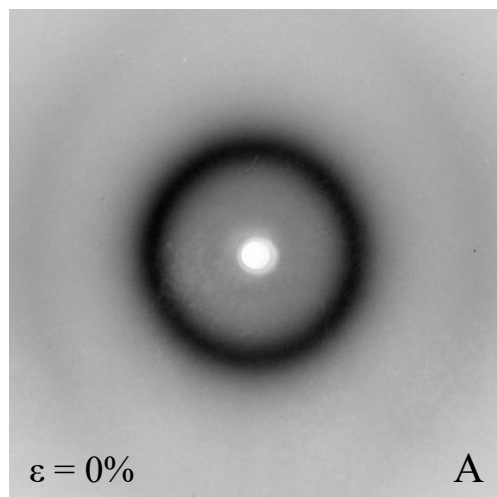
This may explain the higher crystallinity values that sample 9 achieves under stretching if compared to sample 2.

Concerning the sample 10, synthesised under conditions of highest compositional drift (P/E/ENB = 4/1/0.25 and long polymerization time), from the X-ray pattern reported in Figure

1.27, it is evident that this is already crystalline in the undeformed state, in agreement with the diffraction profile of the compression molded sample shown in Figure 1.19A. In particular, the X-ray diffraction pattern of the sample in the undeformed state exhibits the classical reflection of the orthorhombic/pseudo-hexagonal forms of PE at $2\theta = 21^\circ$ that emerges on the amorphous halo. By stretching the sample, the orientation of the orthorhombic/pseudo-hexagonal form crystals is observed, as demonstrated by the polarization of the reflection $2\theta = 21^\circ$ on the equator already for low strain values ($\epsilon = 200\%$). In addition, in the diffraction patterns of the deformed sample, it is also possible to observe other weak reflections on the equator at $2\theta = 37^\circ$, corresponding to the hexagonal form of PE, and on the first layer line correlated to the transplanar periodicity of PE. Improvements in crystal orientation are evident as deformation increases up to 1000%, as indicated by the strong polarization of equatorial reflections. Accordingly, as the applied deformation increases, the intensity and polarization on the equator of the amorphous halo is also observed. This shows that stretching improves the orthorhombic/pseudo-hexagonal PE crystals that were already present in the unstretched sample, and that crystallization may continue under stretching at high deformation. The broadening of the equatorial reflections along the azimuthal coordinate after the tension has been released shows that the degree of orientation of the crystals acquired during stretching has only slightly decreased. Furthermore, the intensity of the amorphous halo does not seem to increase after relaxation. This, in addition to the fact that all equatorial reflections visible in the diffraction patterns of the stretched sample are present in the patterns of Figure 1.27F', may indicate PE crystals do not tend to melt upon relaxation.

It is clear that the observed differences in SIC can be related to the different mechanical behaviour of the various samples. In fact, all the samples that showed crystallisation under stretching exhibit stress-strain curves characterised by a more or less pronounced strain-hardening phenomenon depending on the extent of SIC. For instance, among the samples that in the undeformed state are amorphous, samples 8 and 9 are those that show more pronounced strain hardening and higher tensile strength values, in agreement with the high SIC they develop under stretching.

entry 2 (83.6mol% E, 6.4mol% P, 10.0mol% ENB) (Table 1.4)



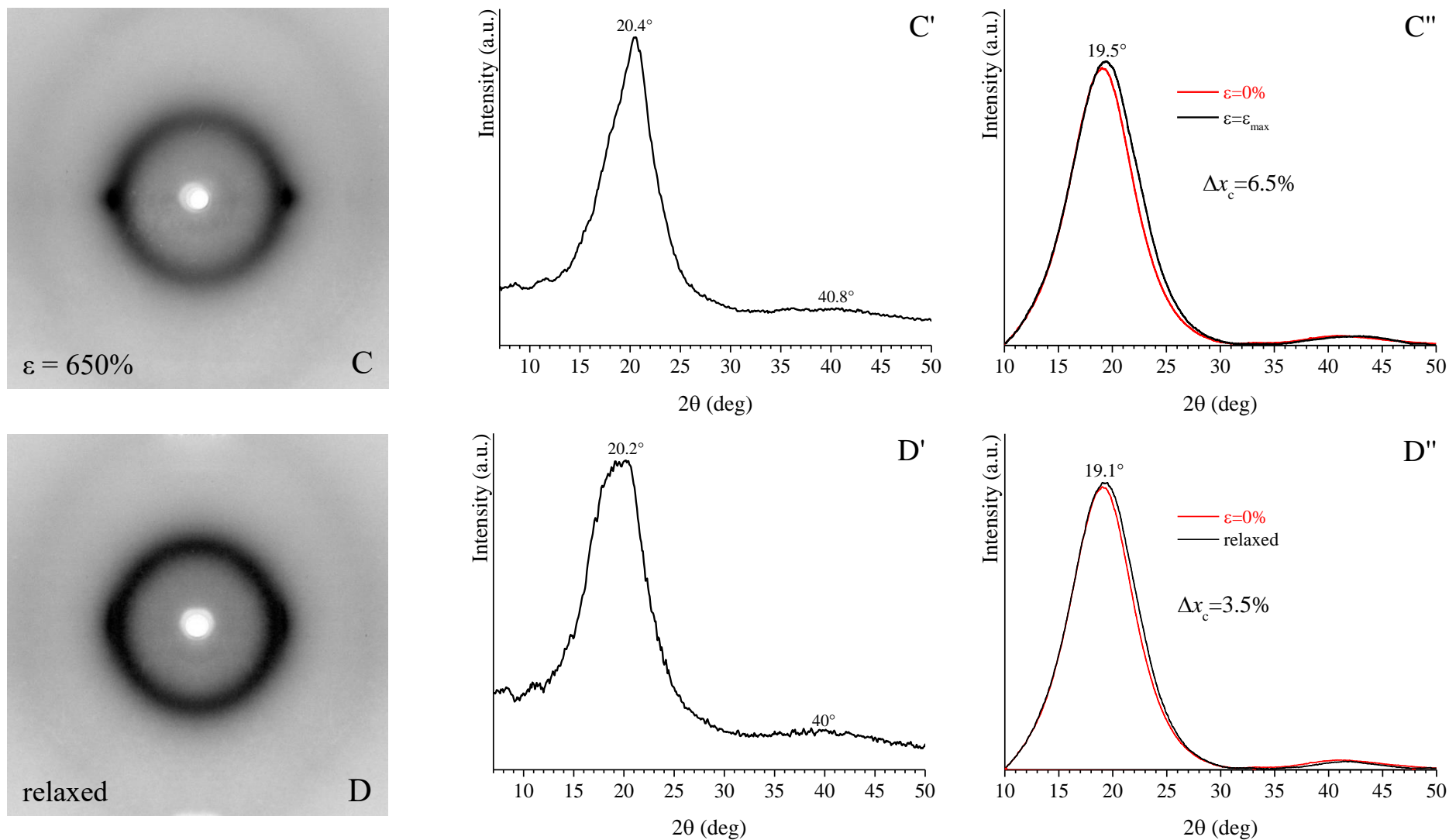


Figure 1.23. X-ray fiber diffraction patterns (A-D), and corresponding equatorial (A'- D') and integrated (A'' - D'') profiles, of the sample 2 recorded at $\varepsilon = 0\%$ (A,A'), $\varepsilon = 300\%$ (B,B'), $\varepsilon = 650\%$ (C,C') and after releasing the tension (D,D').

entry 7 (76.8mol% E, 11.4mol% P, 11.8mol% ENB) (Table 1.4)

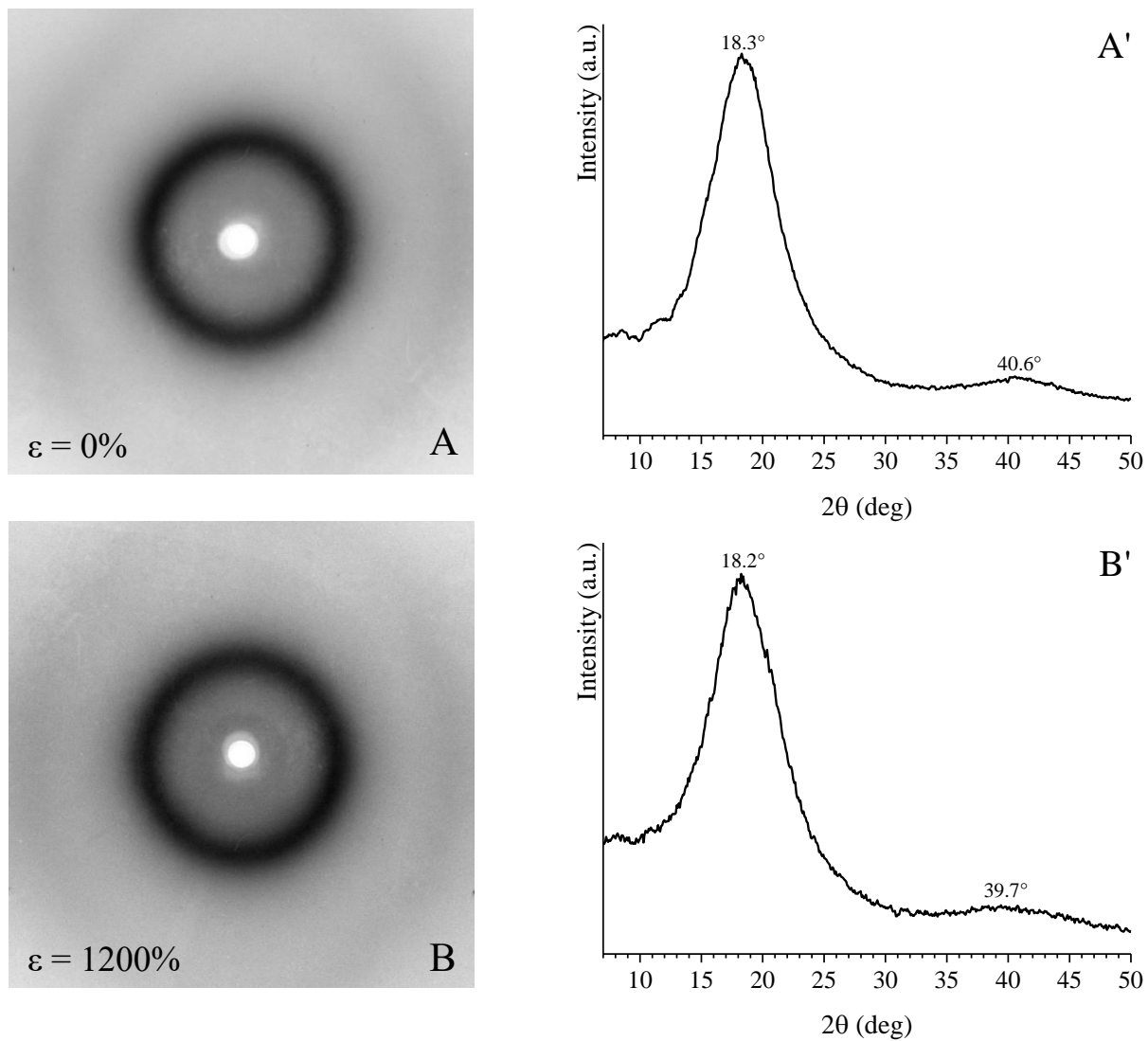
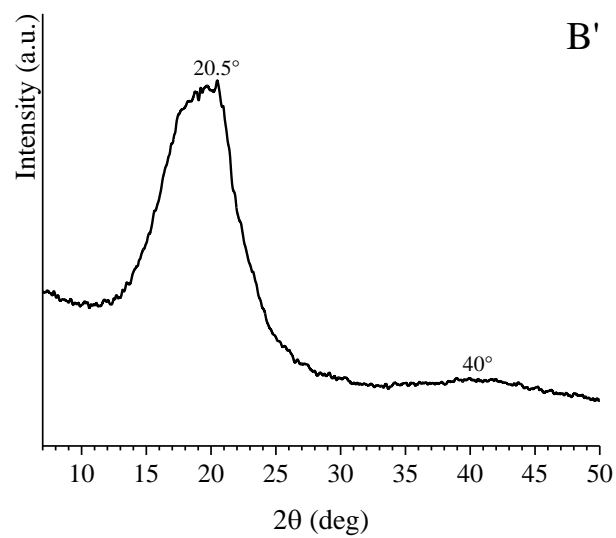
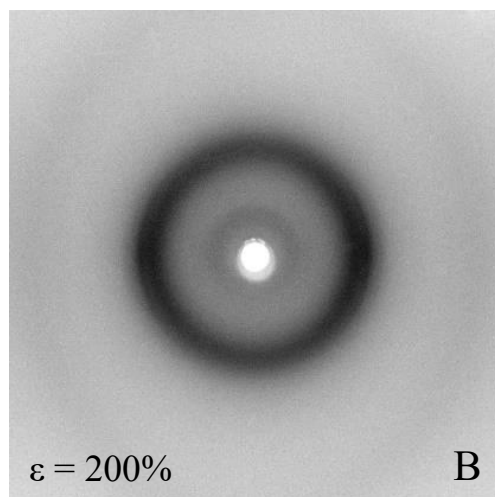
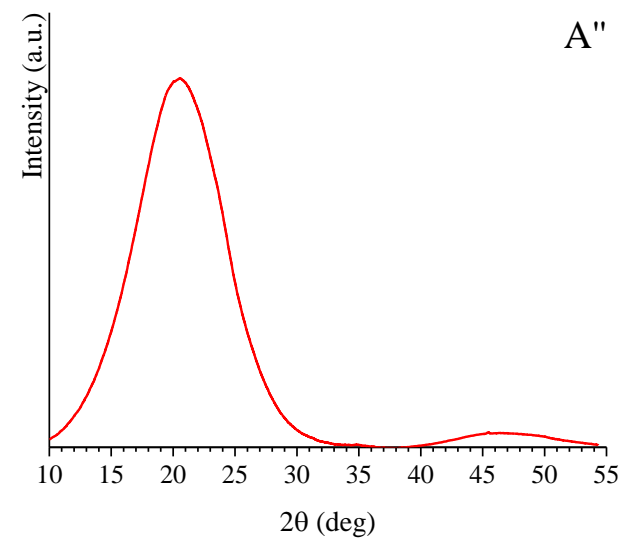
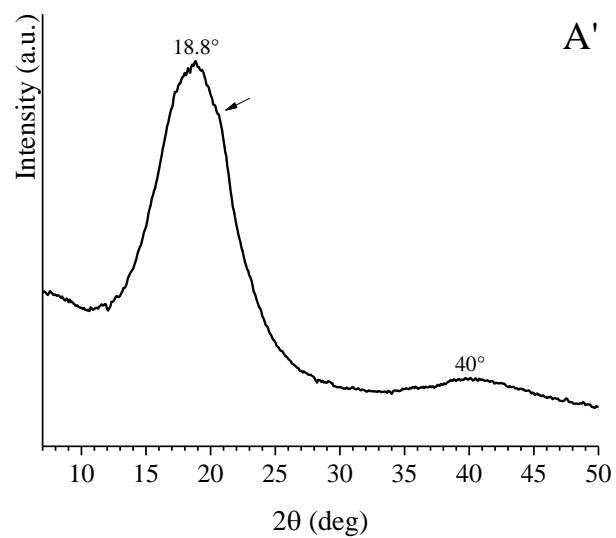
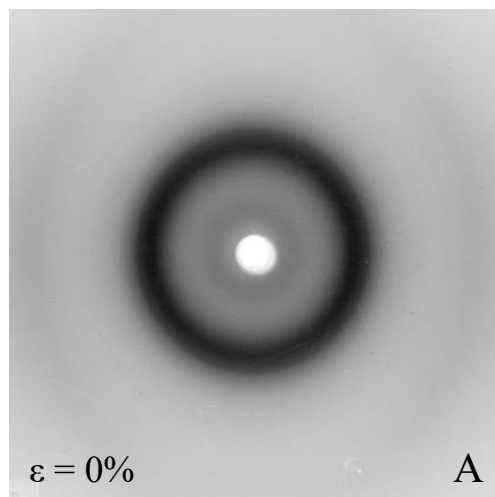
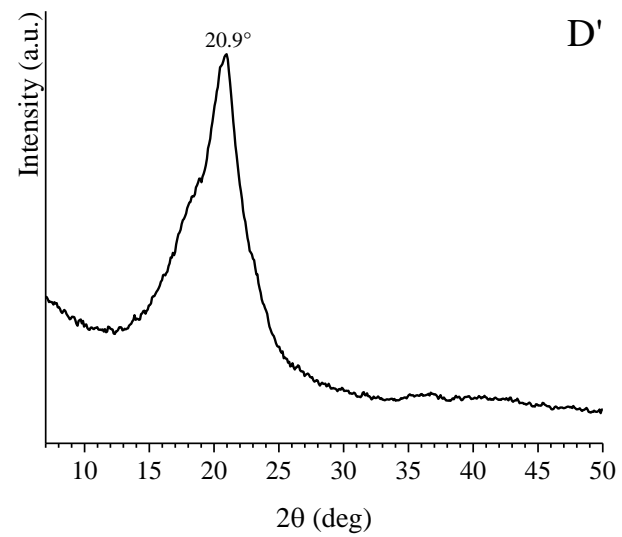
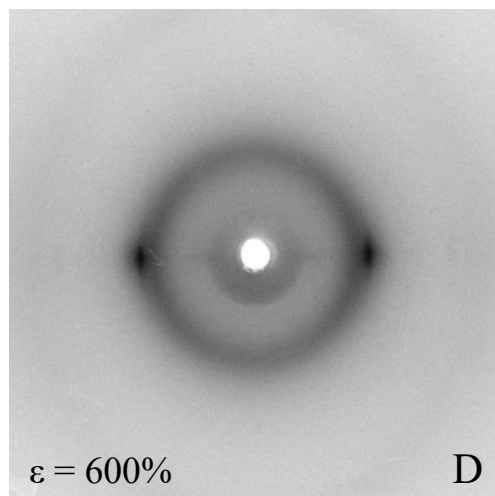
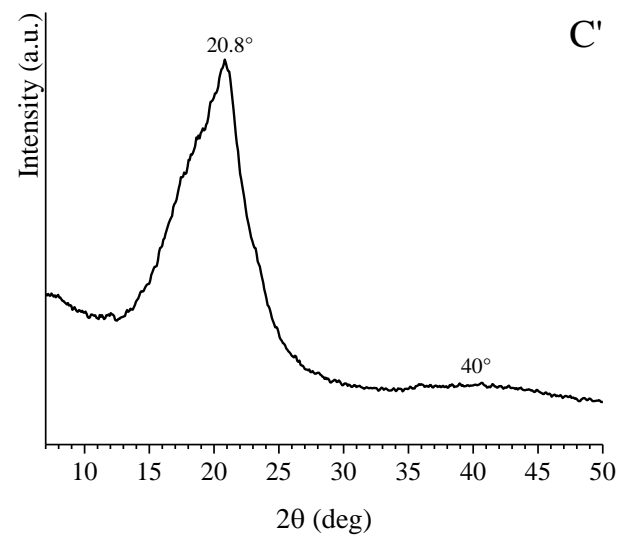
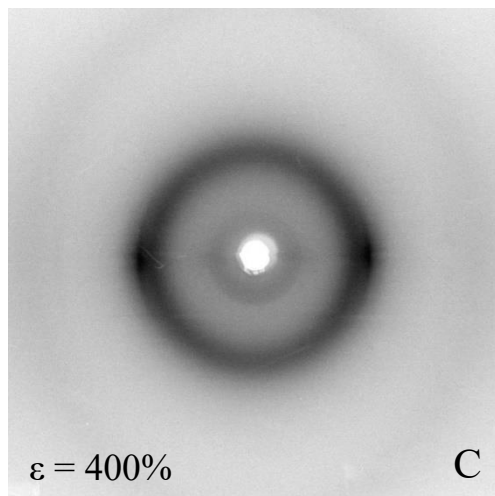


Figure 1.24. X-ray fiber diffraction patterns (A,B), and corresponding equatorial (A',B') profiles, of the sample 7 recorded at $\epsilon = 0\%$ (A,A') and $\epsilon = 1200\%$ (B,B').

entry 8 (85.3mol% E, 5.4mol% P, 9.2mol% ENB) (Table 1.4)





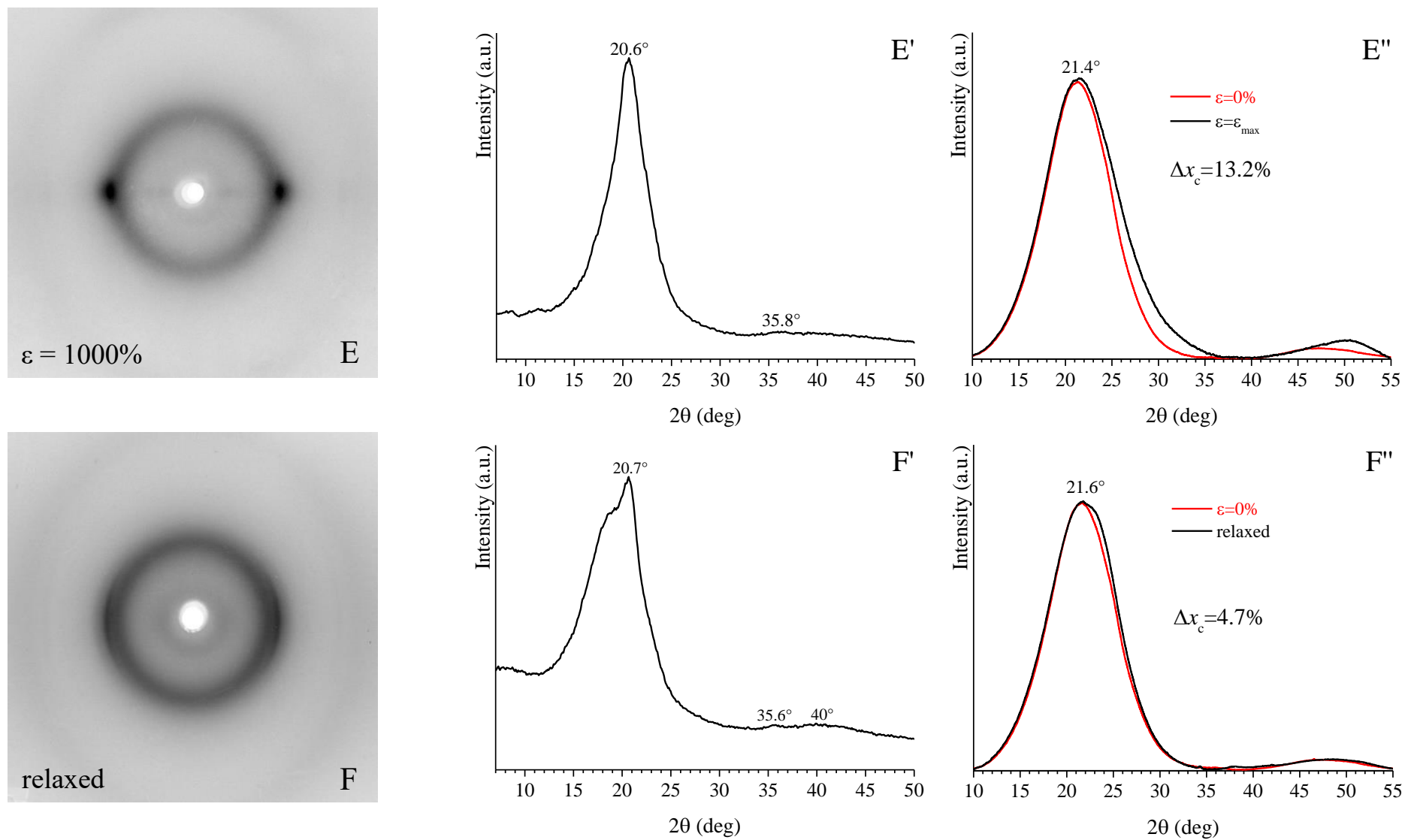
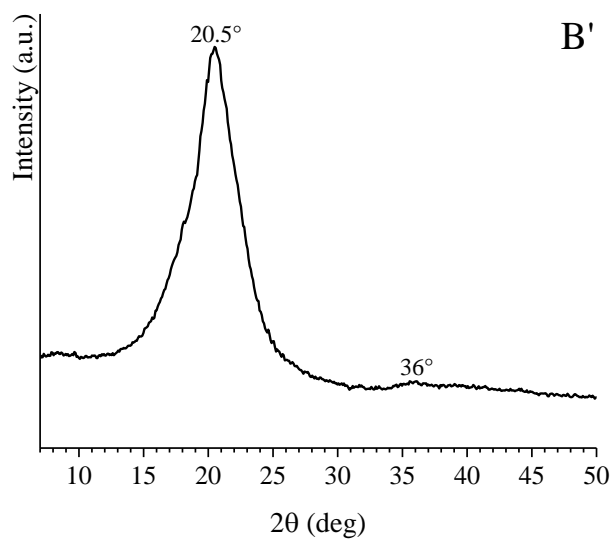
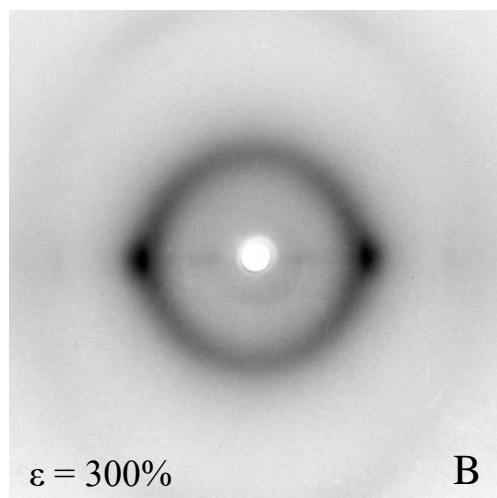
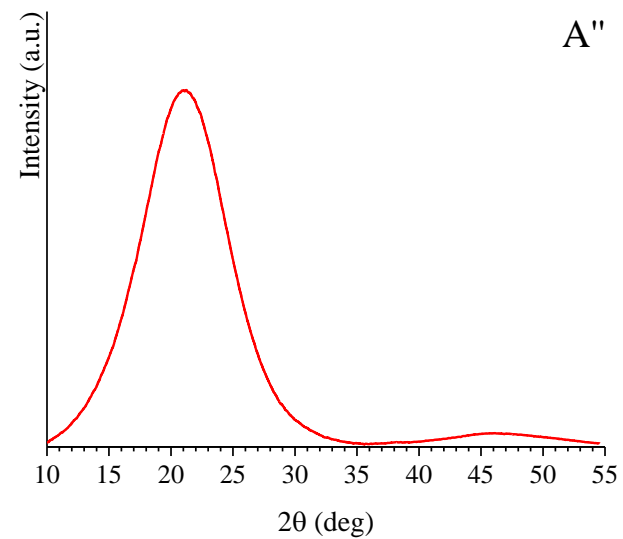
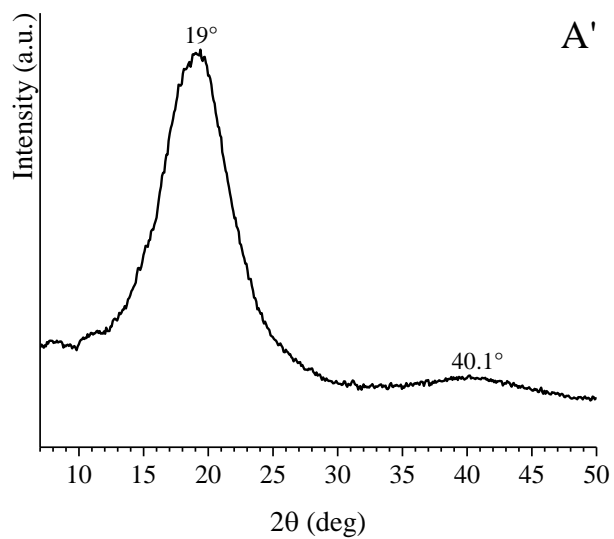
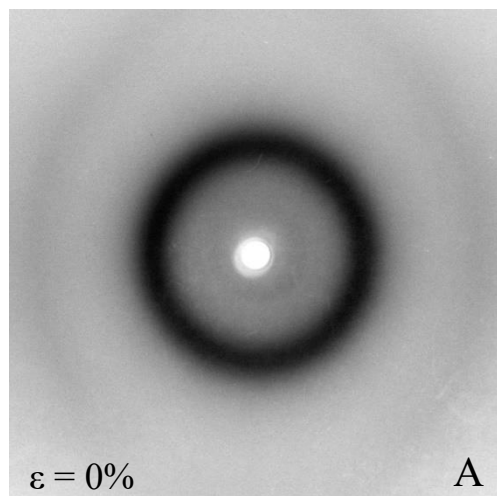


Figure 1.25. X-ray fiber diffraction patterns (A-F), and corresponding equatorial (A'-F') and integrated (A''-F'') profiles, of the sample 8 recorded at $\varepsilon = 0\%$ (A,A'), $\varepsilon = 200\%$ (B,B'), $\varepsilon = 400\%$ (C,C'), $\varepsilon = 600\%$ (D,D'), $\varepsilon = 1000\%$ (E,E') and after releasing the tension (F,F')

entry 9 (83.7mol% E, 9.9mol% P, 6.4mol% ENB) (Table 1.4)



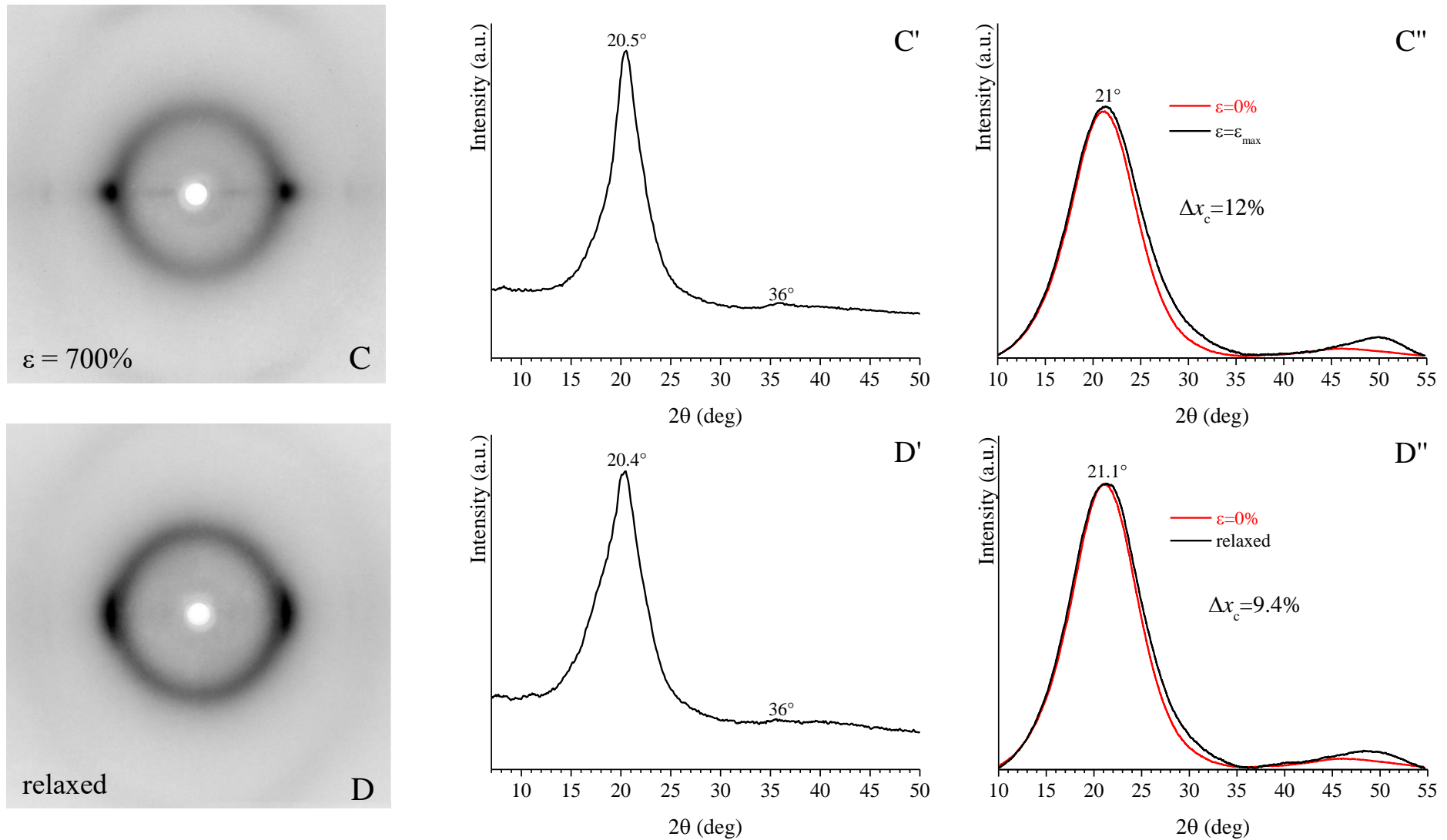
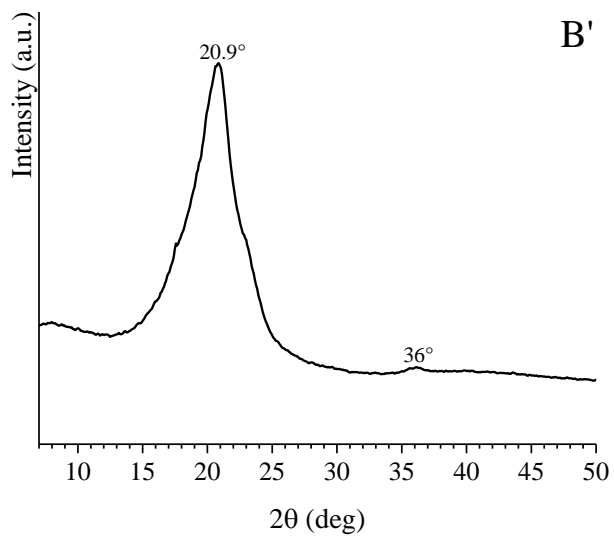
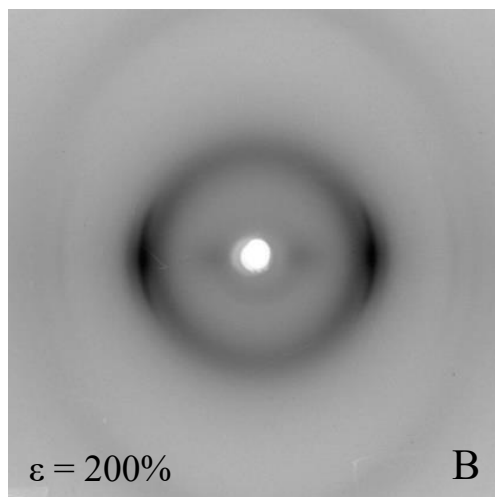
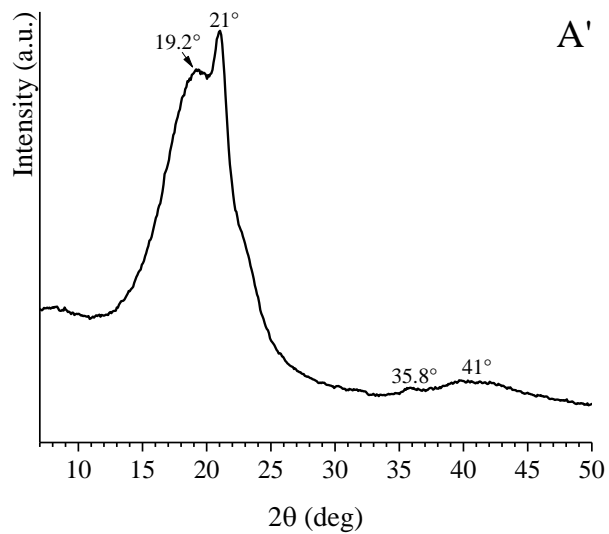
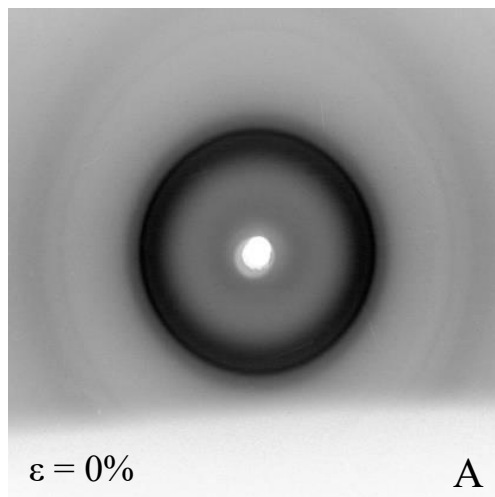
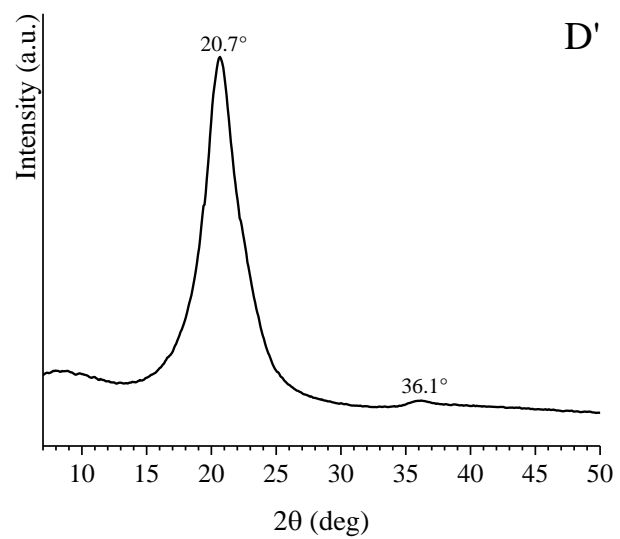
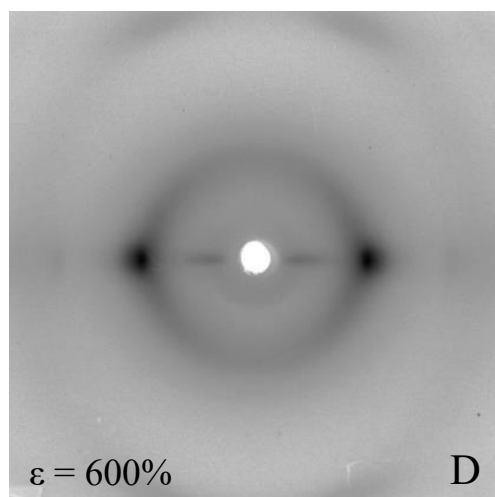
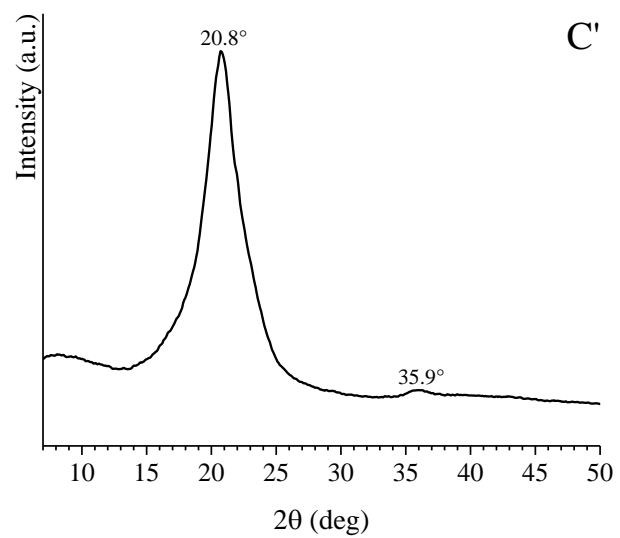
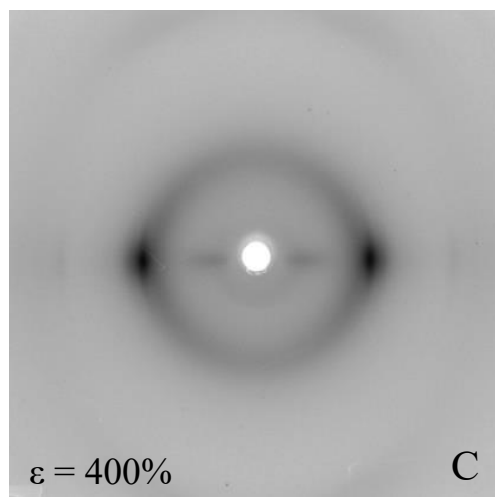


Figure 1.26. X-ray fiber diffraction patterns (A-D), and corresponding equatorial (A'-D') and integrated (A''-D'') profiles, of the sample 9 recorded at $\epsilon = 0\%$ (A,A'), $\epsilon = 300\%$ (B,B'), $\epsilon = 700\%$ (C,C') and after releasing the tension (D,D').

entry 10 (83.7mol% E, 9.9mol% P, 6.4mol% ENB) (Table 1.4)





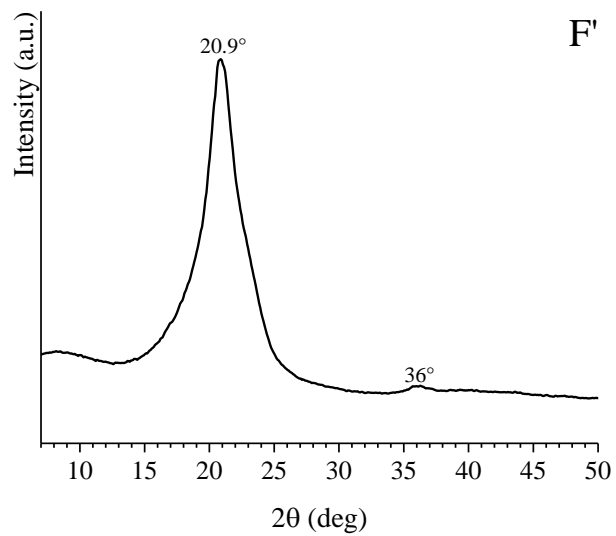
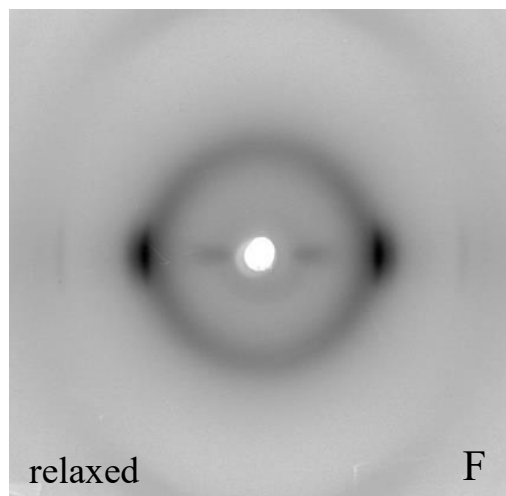
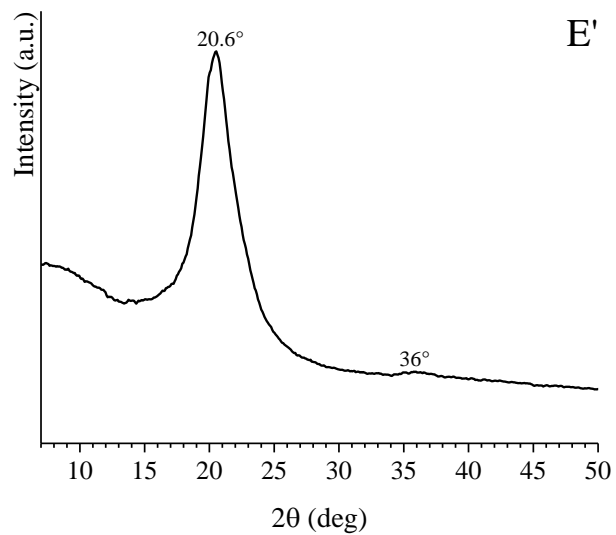
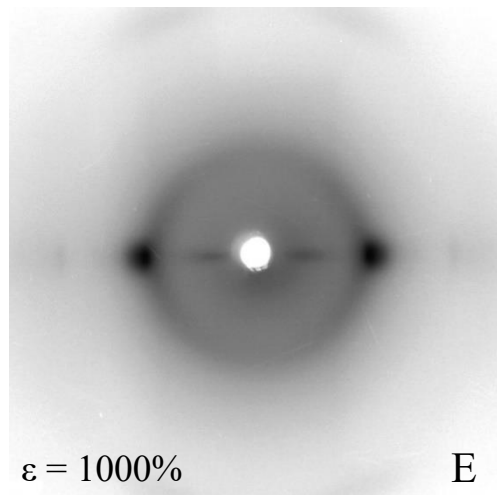


Figure 1.27. X-ray fiber diffraction patterns (A-F), and corresponding equatorial (A' - F') and integrated (A'' - F'') profiles, of the sample 10 recorded at $\varepsilon = 0\%$ (A,A'), $\varepsilon = 200\%$ (B,B'), $\varepsilon = 400\%$ (C,C'), $\varepsilon = 600\%$ (D,D'), $\varepsilon = 1000\%$ (E,E') and after releasing the tension (F,F')

1.2.12 Catalyst 2b

The catalytic behavior of the complex **2b** was explored for the same reaction time of 4 min at the same comonomer feed ratio (P/E/ENB = 4/1/0.5), and at different ENB concentration in the feed between 0.035 and 0.14 mol L⁻¹. Details of the reaction conditions and polymerization results are summarized in Table 1.7.

Table 1.7. Terpolymerization of ethylene with propylene and ENB by **2b**/Et₂AlCl/ETA.^a

entry	[ENB] ₀	P/E/ENB ^b	time (min)	yield (mg)	activity ^c	terpolymer composition (mol%) ^d			(co)monomer conversion (%) ^e		M _w ^f ×10 ³	M _w /M _n ^f
	mol/L					E	P	ENB	P	ENB		
12	0.07	4/1/0.5	4	833	2499	84.8	4.5	10.7	3.4	64.4	102	2.2
13	0.035	4/1/0.25	4	860	2580	89.8	4.2	6.0	3.7	84.0	93	2.0
14	0.11	4/1/0.75	4	897	2691	84.7	2.2	13.1	1.7	52.5	154	2.3
15	0.14	4/1/1	4	625	1875	81.9	2.6	15.5	1.3	31.0	132	2.2

^a polymerization conditions: ethylene pressure, 1.01 bar; total volume, 50 mL (toluene); V complex, 2.5 μmol; Al/V = 500; ETA/V = 10; temperature, 20 °C; ^b P/E/ENB feed ratio (mol/mol) in liquid phase; ^c activity in kg_{pol}×(mol_V×h)⁻¹; ^d determined by NMR; ^e the comonomer conversion was calculated by combining the NMR data, comonomer feed, and weight of the obtained terpolymer.; ^f determined by SEC.

Comparing the data reported in Tables 1.7 and 1.4, it is evident that the complex **2b** shows higher affinity for ENB incorporation than its homolog **2a**.

Furthermore, it is worth noting that keeping the polymerization time constant (4 min) but increasing the diene content of the feed from 0.035 up to 0.11 mol L⁻¹, the activity does not change significantly. However, a further increase in the concentration of ENB in the feed resulted in a loss in activity likely due to a favored ENB coordination/insertion, which competes with the homopolymerization of ethylene and propylene insertion, and contributes to slow down the rate of terpolymerization.

In this series, it is clear that since all samples were polymerized for the same time (4 min), the more pronounced composition drift likely occurs for the experiment performed by using the less amount of diene in feed (sample 13). Working with a low concentration of ENB in the feed, in fact, it is rapidly consumed and consequently the reaction bath is enriched in ethylene. At this time, the rate of ethylene homopolymerization is accelerated with respect to the (co)polymerization rate, thus increasing the chance of forming longer ethylene sequences. Thus, it is possible to infer that the compositional heterogeneity of the various samples is in the order: 13 > 12 > 14 > 15.

Despite the large differences in terms of incorporated diene, it is important to note that all terpolymers have high molecular masses and polydispersity in the range 2.0–2.3, consistent with single homogeneous catalytic species. The ENB content in the terpolymers as a function of the diene concentration in the feed is shown in Figure 1.28. From the data reported in Figure 1.28, it is evident that increasing the ENB concentration in feed, its content in the terpolymer increase linearly up to 15.5 mol% for the synthesis performed by using the highest amount of ENB in feed (0.14 mol L⁻¹).

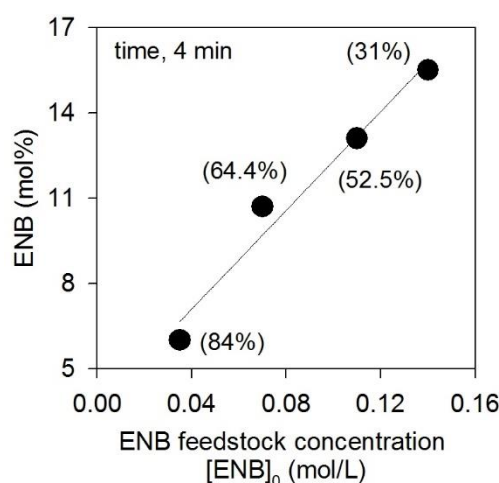


Figure 1.28. Plot of ENB incorporated in the terpolymer vs concentration of ENB in the feed. In brackets the conversion of ENB.

1.2.13 Thermal and Structural Characterization of EPDMs synthesized using Catalyst 2b

The DSC curves of EPDM terpolymer samples synthesized with **2b**, reported in Table 1.8, recorded during first heating from -70°C to 180°C, successive cooling from the melt to -70°C, and second heating of the melt crystallized samples up to 180°C, all recorded at 10 °C/min, are reported in Figure 1.29A-C. The values of melting and crystallization temperatures and enthalpies are reported in Table 1.8.

From the data reported in Figure 1.29 and in Tale 1.8 it is evident that the diene content has a large effect on T_g , which increases from -6 to 17 °C with the increase in the incorporation of ENB from 6.0 to 15.5 mol%, respectively. Considering that ENB is bulkier than ethylene and propylene and reduces the rotational movement of the polymer chains, this result is rather expected.

Furthermore, samples 13 and 12, synthesized by using a low content of ENB in feed, also show broad exothermic and endothermic phenomena, in contrast to samples 14 and 15 obtained at higher concentration of diene, which only display a T_g .

In particular, for sample 13, the melting endotherm is shifted to higher temperatures compared to sample 12. Also in this case, the presence of a multimodal endothermic phenomena may suggest the presence of crystallizable segments with different lengths of methylene sequences that melt at different temperatures. In other words, it is likely that the macromolecules in these samples consist of chain segments with high propylene and ENB content, formed in the early stages of the polymerization that melt at low temperature, and polyethylene-like blocks with low comonomers content, formed in the late stages of the process, that melt at high temperature.

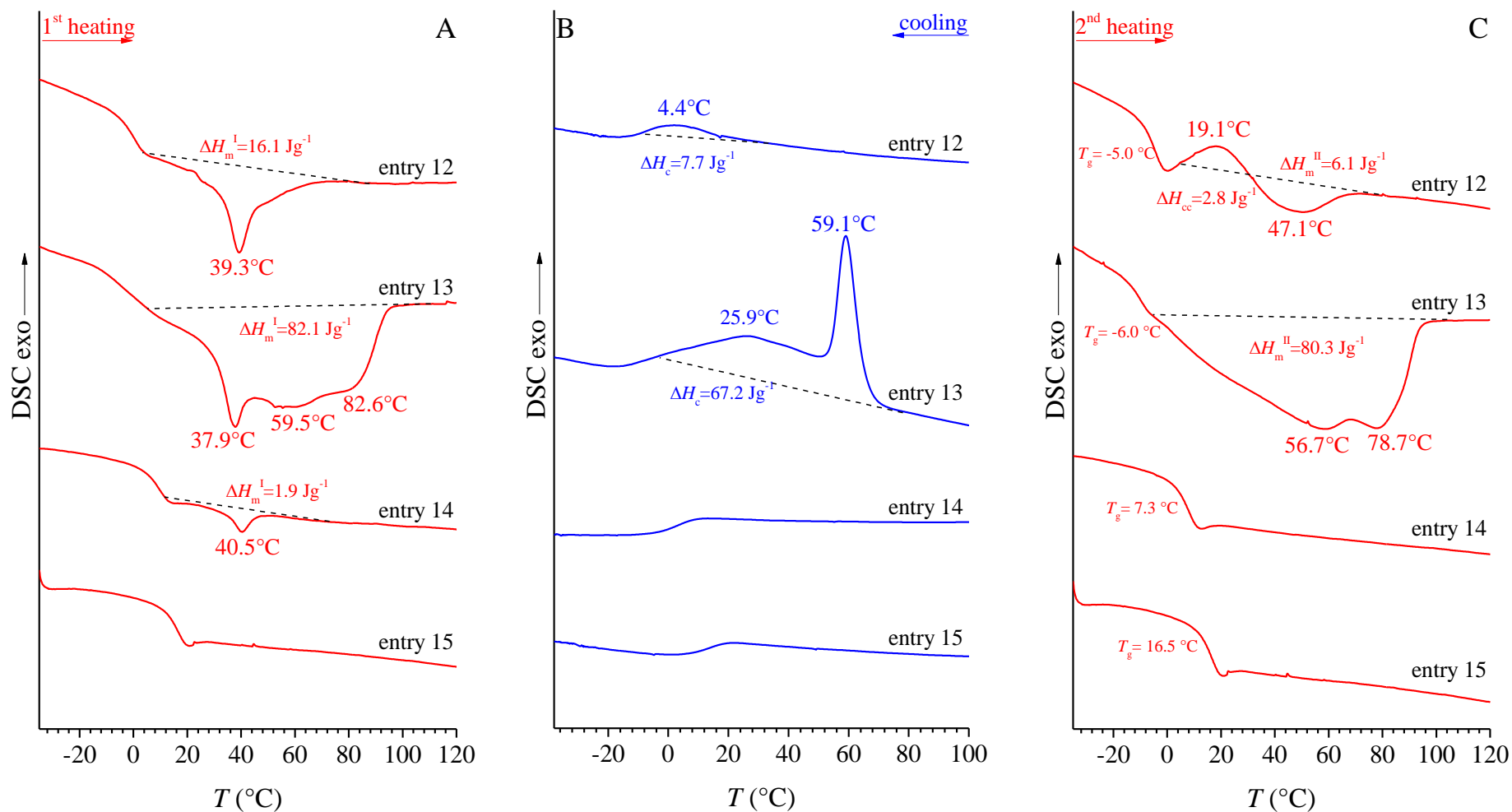


Figure 1.29. DSC curves recorded during heating of the as-prepared sample (A), cooling (B) and successive second heating (C) at scanning rate of 10 °C/min, of E/P/ENB terpolymers obtained by **2b**/Et₂AlCl/ETA.

Table 1.8. Thermal Properties of E/P/ENB terpolymers obtained by **2b**/Et₂AlCl/ETA.

entry	time (min)	terpolymer composition (mol%)			T_m^I (°C) ^a	T_c (°C) ^{a,b}	T_m^{II} (°C) ^a	T_g (°C)	ΔH_m^I (J g ⁻¹) ^a	ΔH_c (J g ⁻¹) ^{a,b}	ΔH_m^{II} (J g ⁻¹) ^a
		E	P	ENB							
12	4	84.8	4.5	10.7	39.3	4.4 (19.1)	47.1	16.1	7.7 (2.8)	6.1	
13	4	89.8	4.2	6.0	37.9, 82.6	25.9, 59.1	56.7, 78.7	82.1	67.2	80.3	
14	4	84.7	2.2	13.1	40.5	-	-	1.9	-	-	
15	4	81.9	2.6	15.5	-	-	-	-	-	-	

^a From DSC of Figure 1.29; ^b The temperatures and enthalpies of crystallization shown in brackets corresponds to the cold-crystallization peak observed in the second heating scan.

X-ray diffraction profiles of compression molded samples reported in Table 1.7, obtained by cooling from the melt to room temperature and to -50°C, are shown in Figure 1.30. Sample 13 crystallizes in the orthorhombic/pseudo-hexagonal forms of PE, which is consistent with DSC results, as shown by the (110)_o/(100)_h and (200)_o reflections at $2\theta \approx 21$ and 24° , respectively (profile b of Figures 1.30), with a moderate level of crystallinity (13%). On the other hand, after cooling from the melt samples 12, 14, and 15 are unable to crystallize. Also in this case, WAXS and SAXS measurement of samples 14 and 15 were collected only on samples cooled from the melt to room temperature since exothermic phenomena are completely absent from the DSC curves both during colling from the melt and during the second heating (Figure 1.29B,C).

While for samples 14 and 15 this is in agreement with the DSC analysis, the WAXS data of sample 12 are in contrast to the thermal data, which, on the other hand, revealed the presence of crystallinity (entry 12 of Figure 1.29B,C).

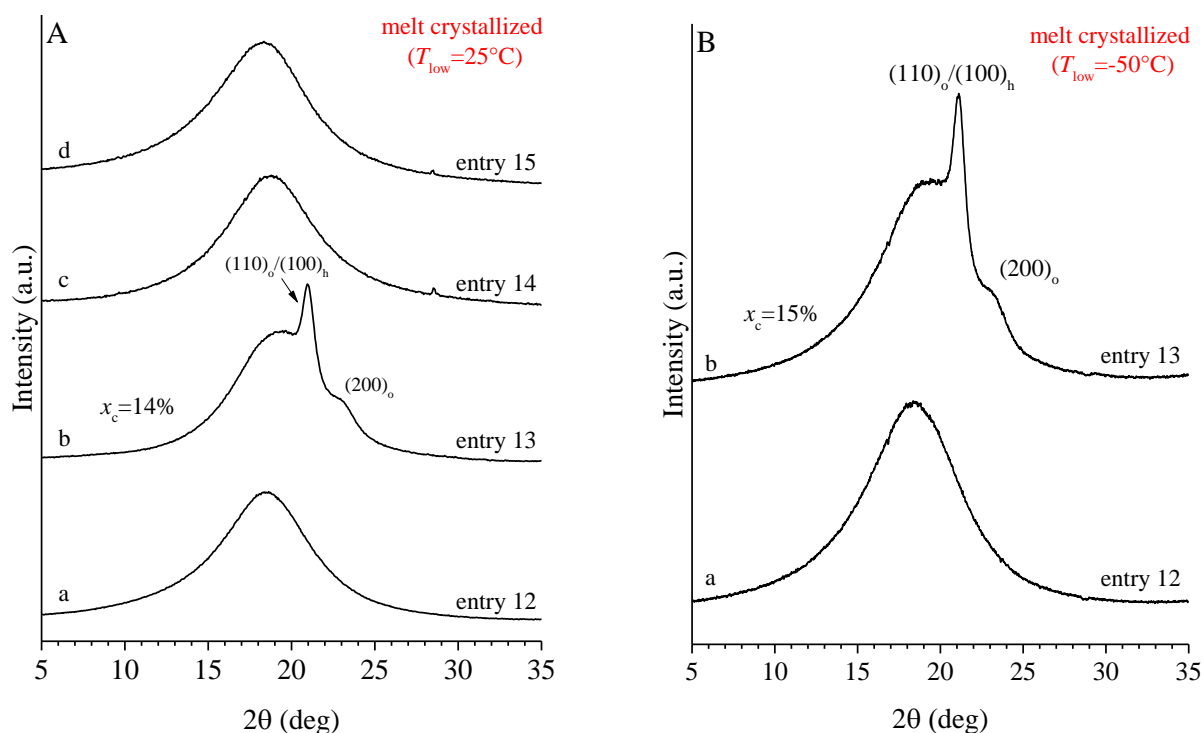


Figure 1.30. WAXS profiles of EPDM terpolymer samples of Table 1.8 crystallized by cooling from the melt to 25°C (A) and -50°C (B). In both cases, the WAXS spectra were collected at room temperature.

The desmeared SAXS profiles and the corresponding Lorentz corrected profiles of samples reported in Table 1.7 are shown in Figure 1.31A,B and 1.31A'B', respectively. As in the case of the WAXS experiments, the SAXS measurements were also collected at room temperature on compression molded samples, obtained by cooling from the melt at both 25°C (Figure 1.31A,A') and -50°C (Figure 1.31B,B'). As expected, SAXS profiles of samples 14 and 15, do not show any correlation peak (profiles c,d of Figure 1.31A,A')

The presence of crystallinity in sample 13 is also confirmed by the SAXS profiles which, in both cases, show a broad correlation peak, centered at $q \approx 0.55 \text{ nm}^{-1}$ (profile b of Figure 1.31A,A'), indicating a large thicknesses distribution of crystalline and amorphous layers. The SAXS profile of sample 12 collected on the sample prepared by cooling the melt to room temperature, in agreement with the WAXS data, shows no correlation peaks (profile a of Figure 1.31A,A'). On the contrary, in Figure 1.31B,B', it can be seen that cooling the sample 12 from the melt to -50°C, results in a SAXS profile characterized by the presence of a very broad, low intensity correlation peak. Therefore, also for this sample, the cryptocrystallinity revealed by DSC analysis and not detected by WAXS is confirmed by SAXS.

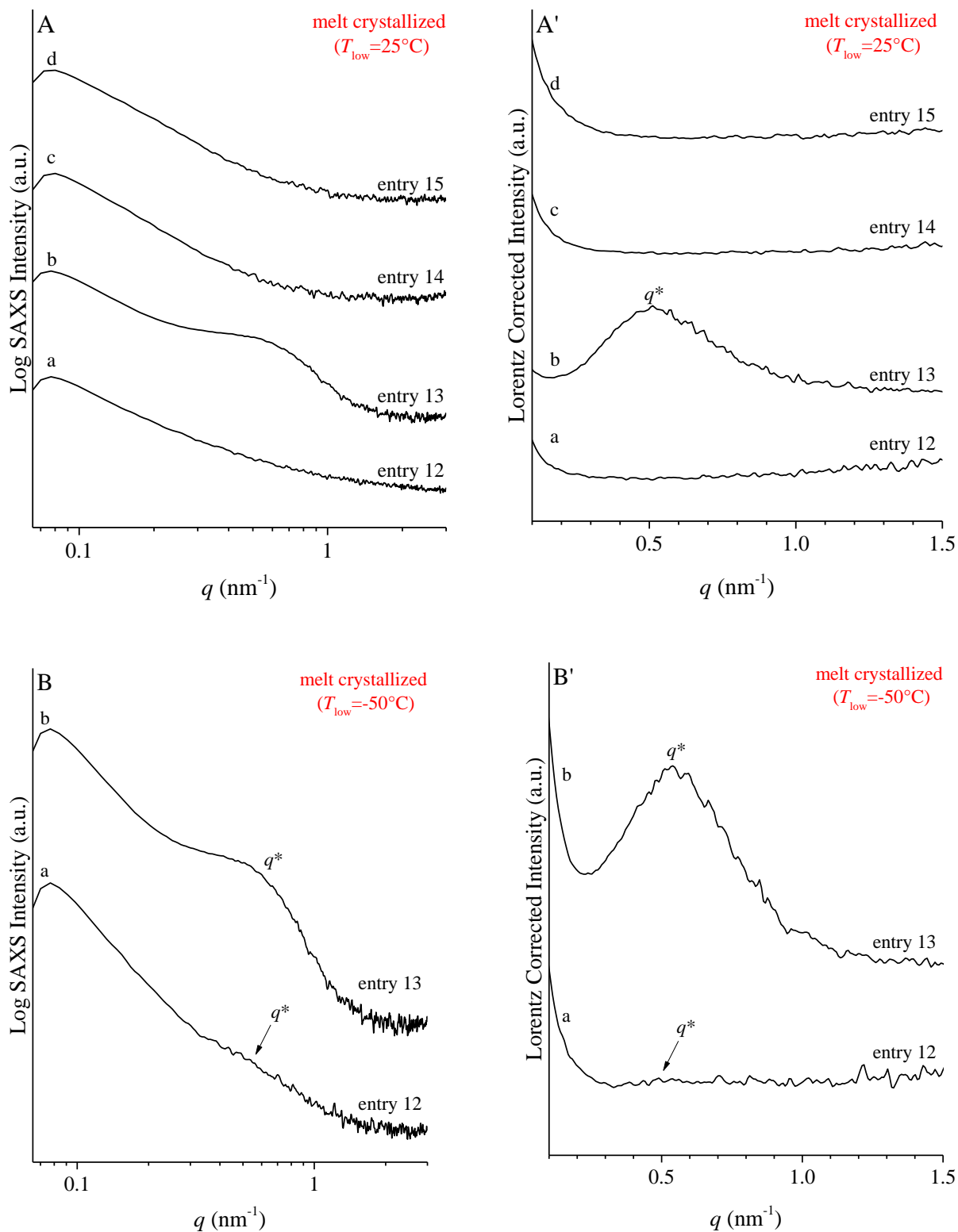


Figure 1.31. SAXS intensity profiles (A,B) and Lorentz-corrected SAXS profiles (A',B') measured at room temperature of EPDM terpolymer samples reported in Table 1.7 crystallized by cooling from the melt to 25°C (A,A') and -50°C (B,B').

1.2.14 Mechanical Properties of EPDMs synthesized using Catalyst 2b

The stress-strain curves measured by stretching compression molded films of the terpolymer samples reported in Table 1.7 are shown in Figure 1.32. The average values of the mechanical parameters obtained from stress-strain curves are reported in Table 1.9. From the data reported in Figure 1.32 it is evident that the various samples, synthesized by using different concentration of ENB in the feed, present a very different mechanical behavior. In particular, they exhibit mechanical properties ranging from thermoplastic to elastomer. These different mechanical features are probably due to the different chemical composition distribution of the various samples, resulting from the synthetic approach used, which in turn have a significant impact on the crystallinity and the glass transition temperature. Sample 15, with the highest content of ENB (15.5 mol%), exhibits the mechanical behavior of a strong thermoplastic characterized by a reasonably high modulus (95 MPa), high tensile strength (20.5 MPa), and moderate strain at break (400%). It is worth noting that the sample 15 is amorphous in the undeformed state, hence its mechanical behaviour appears quite unexpected. It is likely that the tensile properties of sample 15 are strongly influenced by the high content of diene (15.5 mol%), and its high glass transition temperature (19°C) which is close to the temperature at which the sample was tested. Samples synthesized using less diene in feed and, thus, with a higher ethylene content in chains are characterized by higher ductility, lower mechanical resistance and tensile strength.

In particular, samples 12 and 14 show a typical elastomeric stress-strain curve with a very low modulus (about 2 MPa) and high values of strain at break of ≈ 1200 and $\approx 700\%$, respectively. Sample 13, already crystalline in the undeformed state, exhibits higher values of the Young modulus, tensile stress and tensile strength if compared to samples 12 and 14.

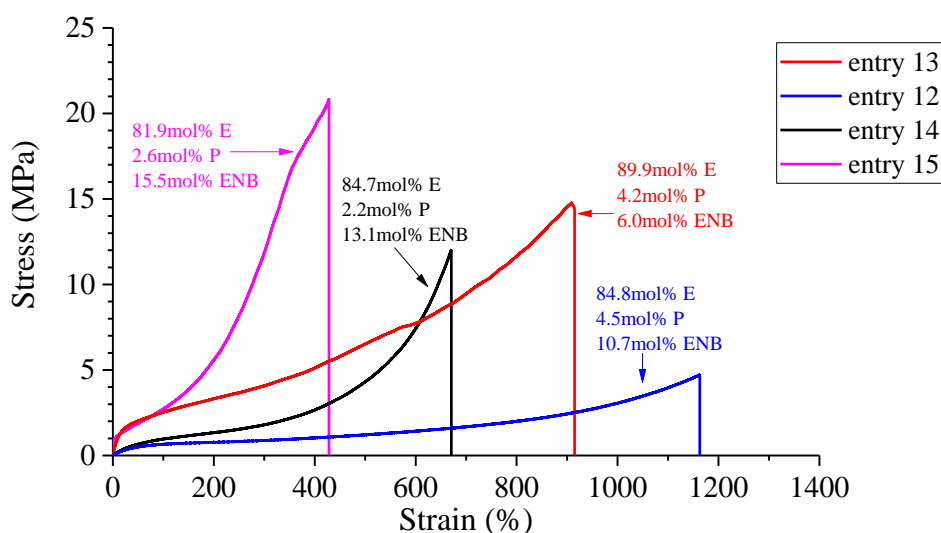


Figure 1.32. Stress-strain curves of compression molded films of samples reported in Table 1.7.

Table 1.9. Mechanical properties of EPDMs obtained with **2a**/Et₂AlCl/ETA.

entry	E ^a (MPa)	σ _b ^b (MPa)	ε _b ^c (%)	σ _y ^d (MPa)	ε _y ^e (%)	t _b ^f (%)	cycle 1		cycle 2	
							SR ₁ ^g	SR _x ^h	SR _{420%} ⁱ	SR _{810%} ^l
12	2.2±0.1	4.8±0.1	1124±54	0.5±0.1	29±2	75±5	79	62	73	71
13	13.5±0.7	14.0±3.5	888±82	1.6±0.2	12±1	58±3	66	54	64	51
14	2.5±0.1	12.0±2.8	657±31	0.7±0.1	37±3	85±4	88	72	87	break ^h
15	95±20	20.5±1.5	444±27	1.1±0.1	4±1	63±2	68	67	62	break ^h

^a Young's modulus; ^b stress at break; ^c strain at break; ^d stress at yield; ^e strain at yield; ^f tension set at break; ^g strain recovery measured after the first step in a step cycle test type at 300% strain; ^h strain recovery measured after the last step in a step cycle test type at 300% strain; ⁱ strain recovery measured after the strain at 420% in a step cycle test type at increasing strains; ^l strain recovery measured after the strain at 810% in a step cycle test type at increasing strains.

The elastomeric behavior of all the samples synthesized with **2b** was investigated performing 10 successive mechanical cycles of stretching and compression at fixed strain of 300% and also recording stress-strain curves during step cycle deformation at different strain. As an example, the results obtained for samples 14 and 15 in both experiments are shown in Figure 1.33. The mechanical parameters extracted from these experiments are shown in Table 1.9.

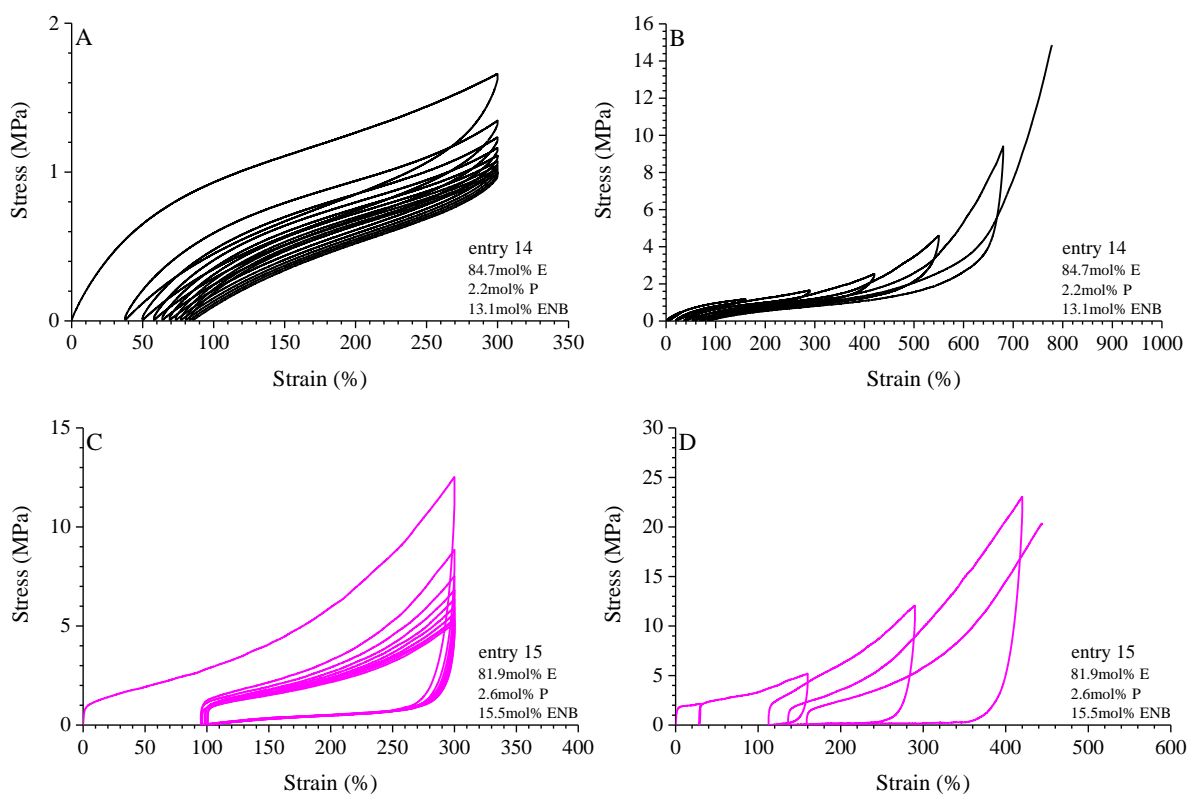


Figure 1.33. (A) stress-strain curves of sample 14 in the hysteresis experiments for a strain of 300%, (B) stress-strain curves of sample 14 during step cycle tensile deformation at different strain, (C) stress-strain curves of sample 15 in the hysteresis experiments for a strain of 300%, (D) stress-strain curves of sample 15 during step cycle tensile deformation at different strain.

The measured elastic recovery after each hysteresis cycle and each step of deformation as a function of the applied strain is reported in Figure 1.34A and 1.34B, respectively.

Concerning the data reported in Figure 1.34A, all samples display values of the strain recovery after the first cycle in the range 66 – 88% which slightly decrease in subsequent stretching cycles. In particular, the elasticity of the various samples is in the order: $13 < 12 < 15 < 14$. The lower elastic performance of sample 13, compared to the other samples in the series, could be attributed to its moderate level of crystallinity which derives from the pronounced compositional drift that characterize this sample. By contrast, for sample 14 it is demonstrated that a minor, but still significant, composition drift is beneficial to impart excellent elasticity to the material.

From the data shown in Figure 1.34B it is evident that as the applied strain increases, the elastic recovery for samples 14 and 12 remains stable at around 87 and 73%, respectively. On the contrary, for sample 13 the recovery decreases as the applied strain increases (Figure 1.34B). In this regard, it is worth noting that the sample 15 exhibits a completely different behavior: the elastic recovery values progressively increase with increasing the applied strain. Once

again, this unusual result may be explained by recalling that sample 15 has a T_g very close to room temperature and, thus, close to the temperature at which the experiments were performed. This probably plays a strong role in the mechanical behaviour of this sample.

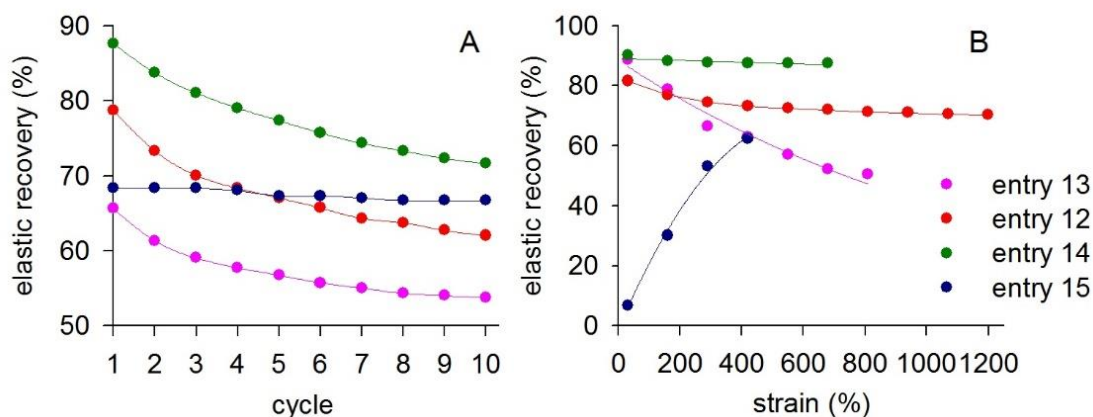


Figure 1.34. (A) strain recovery as a function of cycle number at 300% of strain; (B) strain recovery as a function of the applied strain.

1.2.15 Fiber diffraction analysis and strain-induced crystallization of EPDMs synthesized using Catalyst 2b

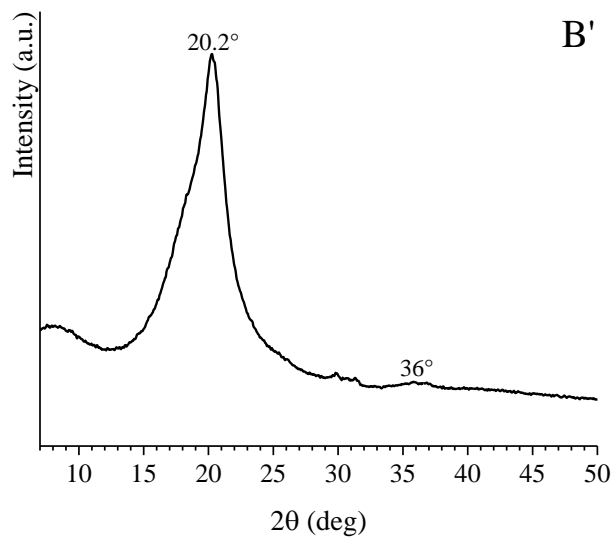
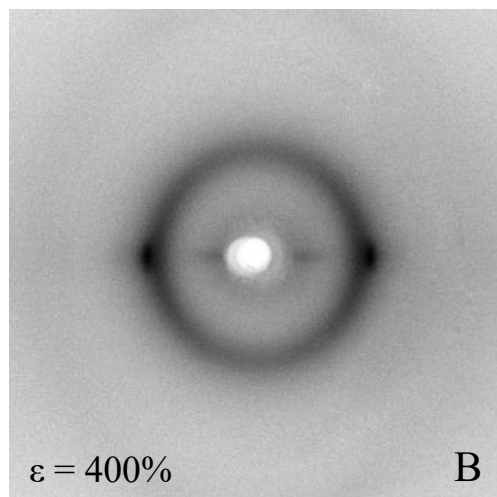
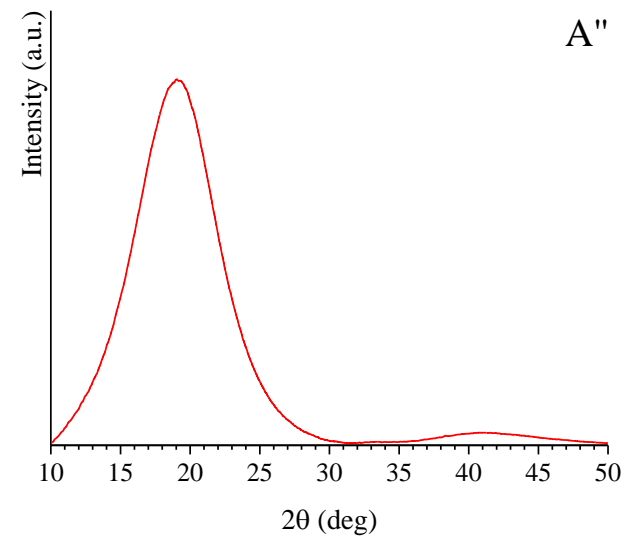
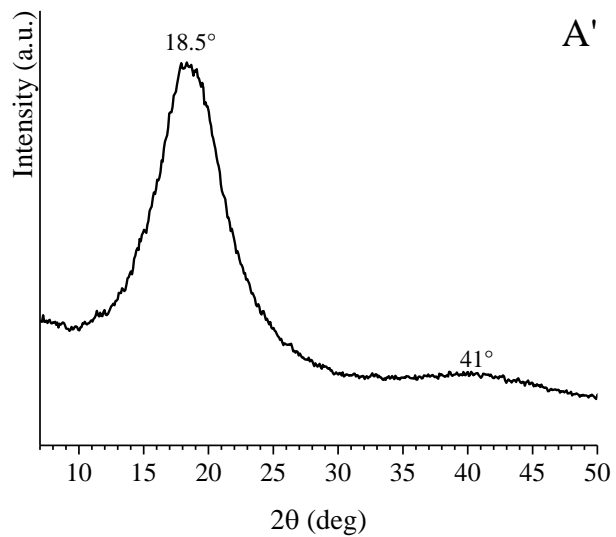
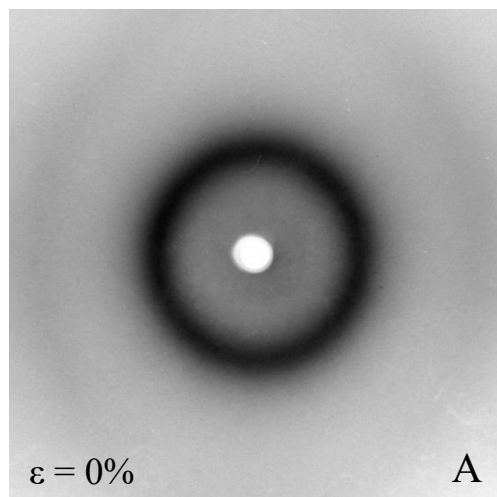
Figures 1.35-1.38 show the X-ray fiber diffraction patterns, and the equatorial and integrated profiles of samples synthesized with the complex **2b** reported in Table 1.7. From the diffraction patterns shown in Figure 1.38A, it can be observed that sample 15, with the highest diene content (15.5 mol%) in the series, is initially amorphous and does not develop crystallinity under stretching even at strains close to the strain at break (400%) (Figure 1.38E). In fact, from the diffraction patterns recorded at the maximum investigated strain, no diffraction spots are observed but only the polarization of the amorphous halo at $2\theta = 18-19^\circ$ close to the equator. This demonstrates that the strong strain-hardening that characterizes the stress-strain curves of this sample (Figure 1.32), is not related to any stress induced crystallisation phenomenon but, is probably linked to both its high T_g and the possible presence of glassy domains of ENB that increase the mechanical strength of the material.

Sample 14, with 13.2mol% of ENB, exhibits similar behaviour to sample 15 even if, for deformations close to breaking, it seems to develop a hint of crystallinity. In fact, from the diffraction pattern reported in Figure 1.37D, it can be noticed that on the equator, close to the amorphous halo, seems to appear a faint reflection which, however, does not resolve as a peak in the corresponding equatorial profile (Figure 1.37D'). Sample 12, also initially amorphous (Figure 1.35A), crystallizes under stretching as is evident from the diffraction patterns shown

in Figure 1.35B,C. In fact, starting from 400% strain, the reflection at $2\theta \approx 20^\circ$ of the orthorhombic/pseudo-hexagonal forms of PE appears. At the highest achievable strain (1100%), the sample develops an increase in crystallinity Δx_c , evaluated from the integrated profiles, of around 10% (Figure 1.35C''). After releasing the tension from the maximum deformation, the intensity of the broad amorphous halo at $2\theta \approx 18-19^\circ$ increases (Figure 1.38D,D') while the reflection at $2\theta \approx 20^\circ$ seems to disappear almost completely. This indicates that the crystals formed under stretching essentially melt after removing the tension and upon relaxation of the fibers. It is worth noting that samples 12 and 14 have almost the same ethylene content but, as just shown, only the former exhibits an appreciable increase in crystallinity under stretching. This difference can be explained on the basis of two factors. Firstly, sample 12 was synthesised with less norbornene in feed, so it probably has longer ethylene sequences able to crystallize formed as a result of the pronounced compositional drift. Secondly, it should be noted that sample 12 has a higher ENB content than sample 14. Since ENB is a very bulky comonomeric unit, it probably contributes to hinder the crystallization of sample 12, even under stretching.

As shown by the WAXS profile reported in Figure 1.30, sample 13 is the only one sample in the series that exhibits crystallinity when obtained by cooling from the melt. This has previously been attributed to the high ethylene content and strong compositional drift that characterizes this sample. Indeed, it is important to remember that since the synthesis of sample 12 was carried out using the lowest concentration of ENB in the feed, this is depleted within the first few minutes of reaction, allowing for high ethylene incorporation during the remaining polymerization time. The crystallinity of the sample 12 is confirmed by the X-ray diffraction pattern collected in the undeformed state reported in Figure 1.36A. From the data shown in Figures 1.36B-E, it is observed that as the applied strain increases, there is a progressive orientation of both the amorphous and crystalline phases, as demonstrated by the polarization on the equator of the reflection at $2\theta \approx 20^\circ$ and the amorphous halo at $2\theta \approx 18-19^\circ$, respectively. Only a slight reduction in the degree of orientation of the crystals achieved during stretching is observed after the tension has been released (Figure 1.36F), as seen by the broadening of the equatorial reflections along the azimuthal coordinate.

entry 12 (84.8mol% E, 4.5mol% P, 10.7mol% ENB) (Table 1.7)



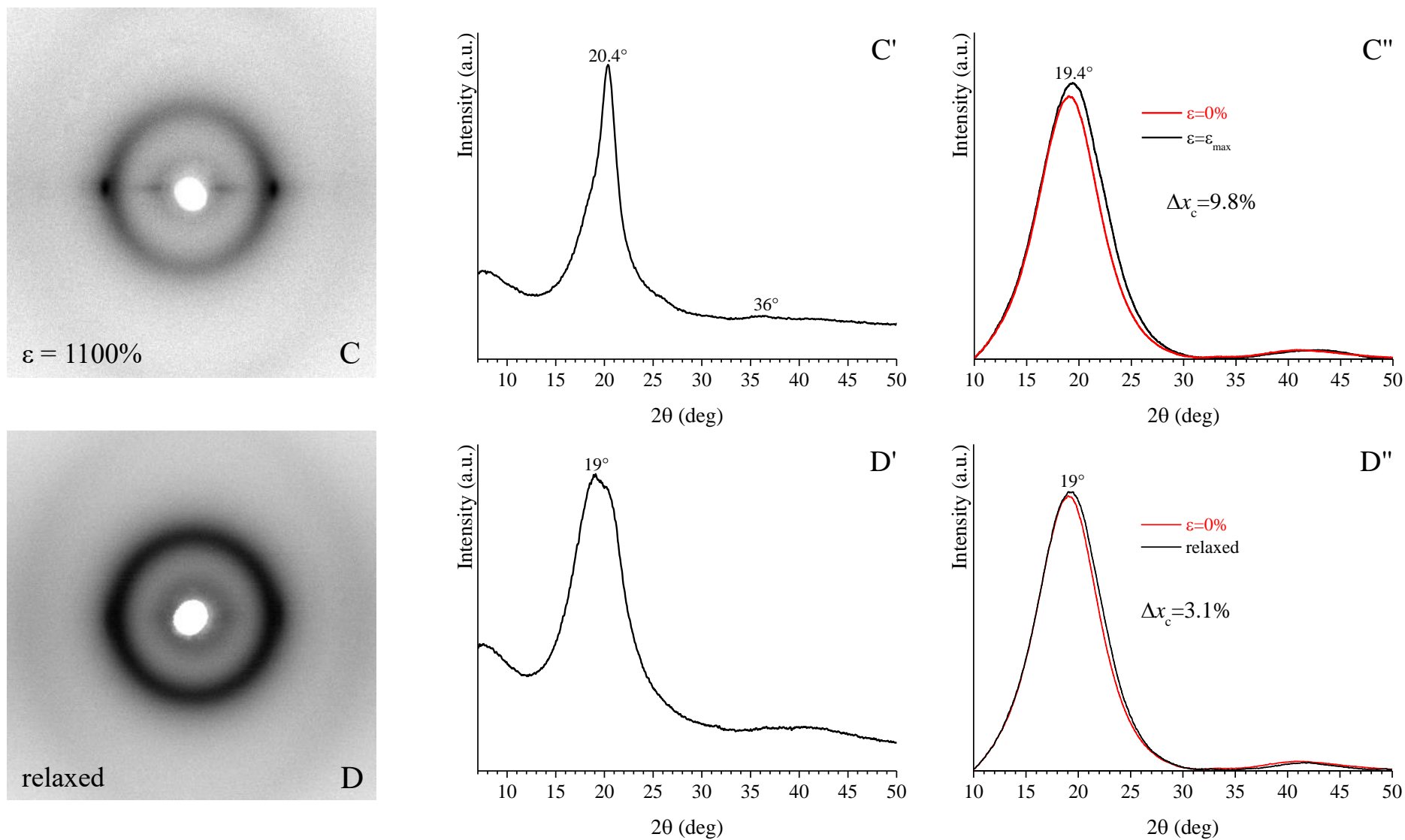
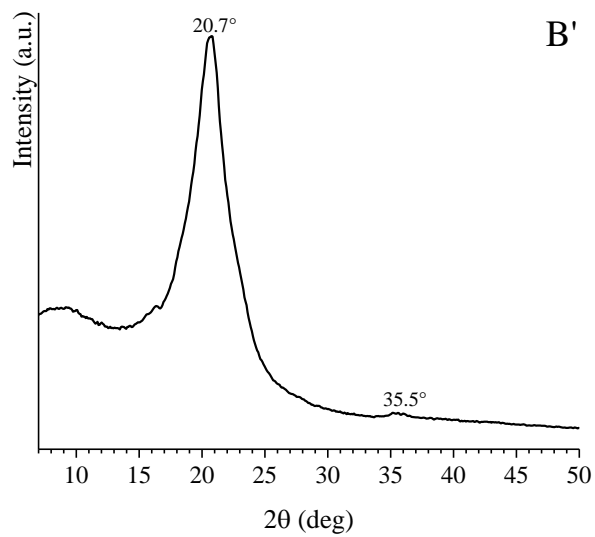
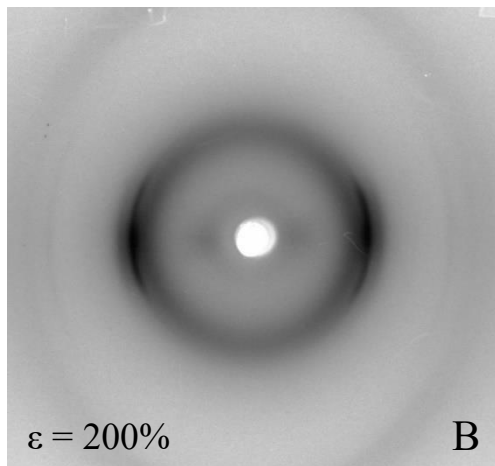
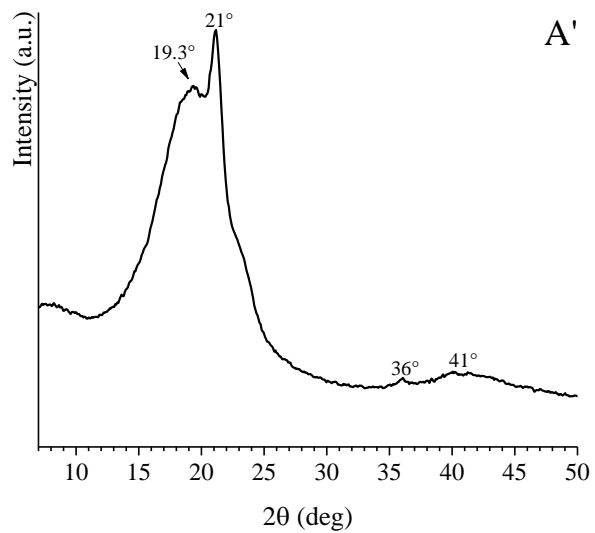
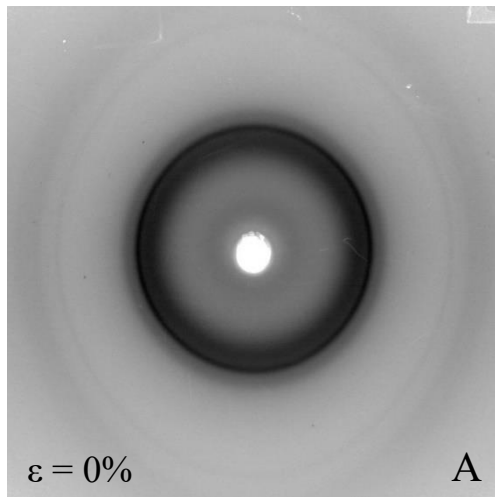
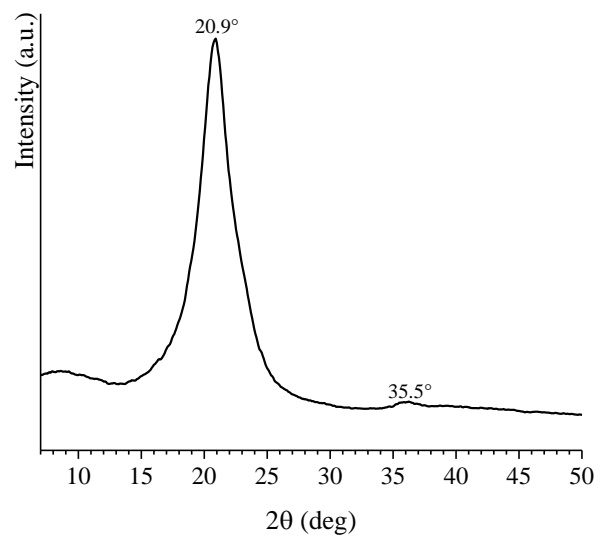
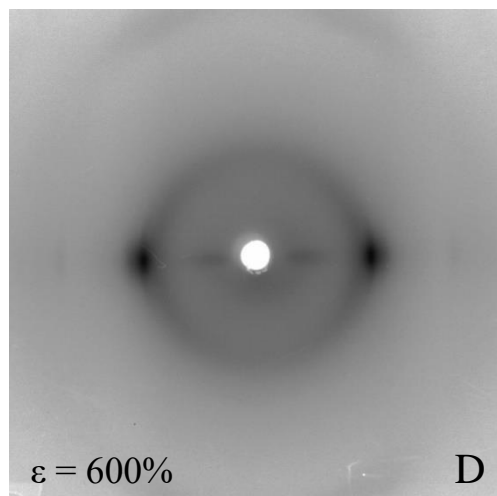
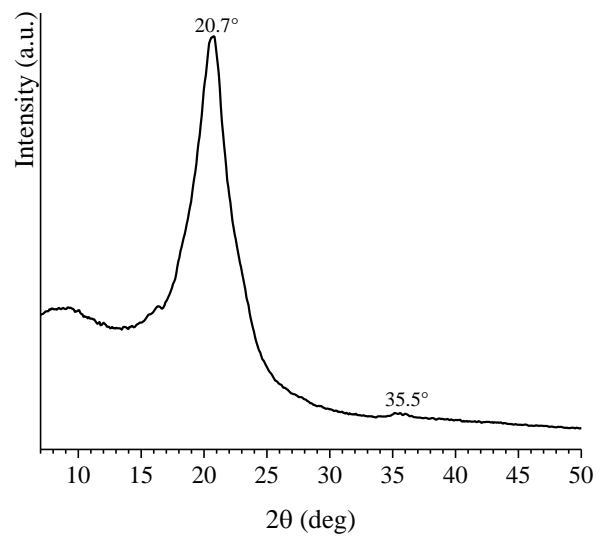
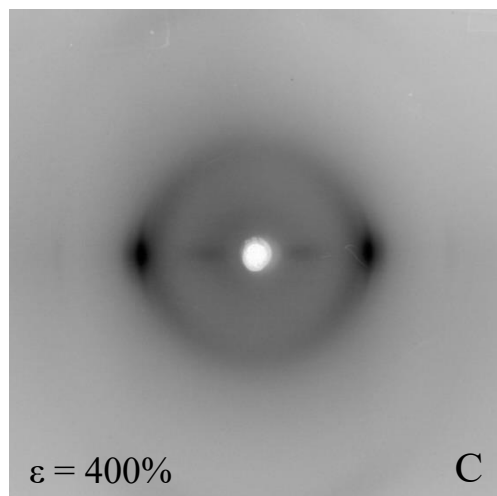


Figure 1.35. X-ray fiber diffraction patterns (A-D), and corresponding equatorial (A' - D') and integrated (A'' - D'') profiles, of the sample 12 recorded at $\epsilon = 0\%$ (A,A'), $\epsilon = 400\%$ (B,B'), $\epsilon = 1100\%$ (C,C'), and after releasing the tension (D,D').

entry 13 (89.8mol% E, 4.2mol% P, 6.0mol% ENB) (Table 1.7)





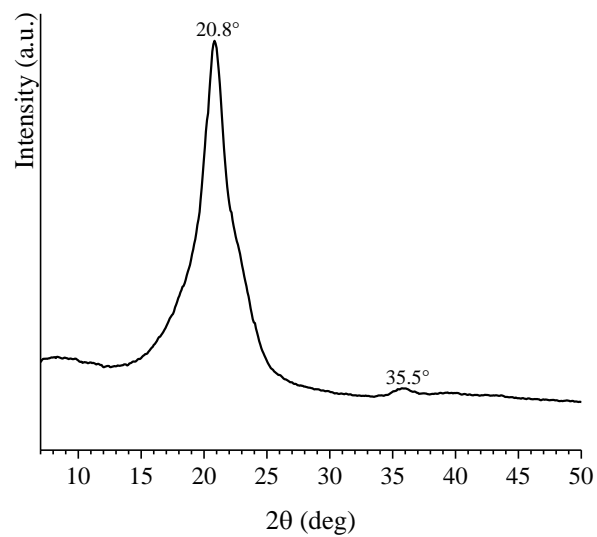
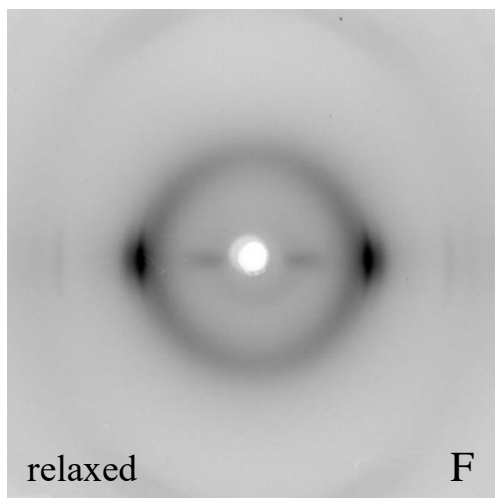
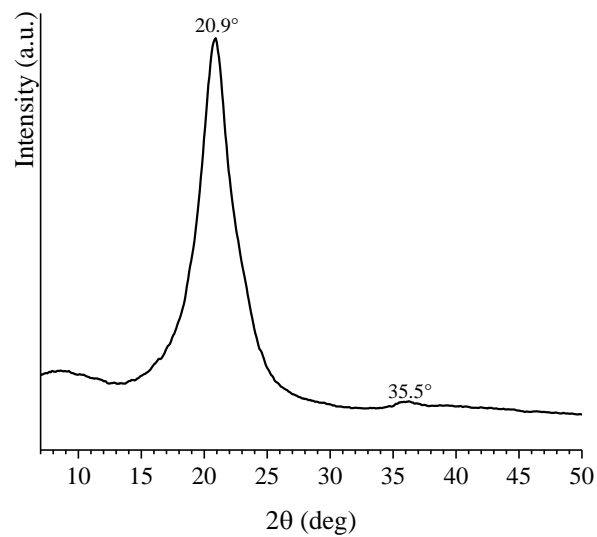
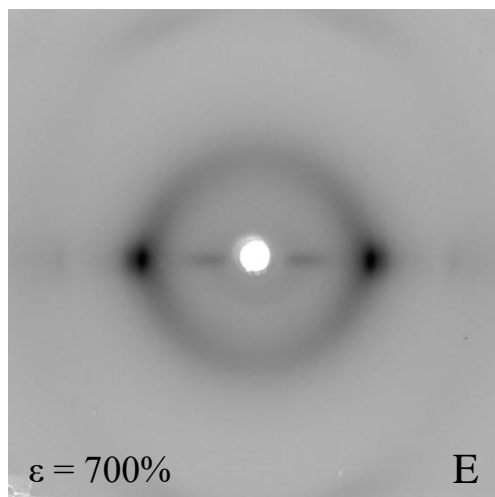
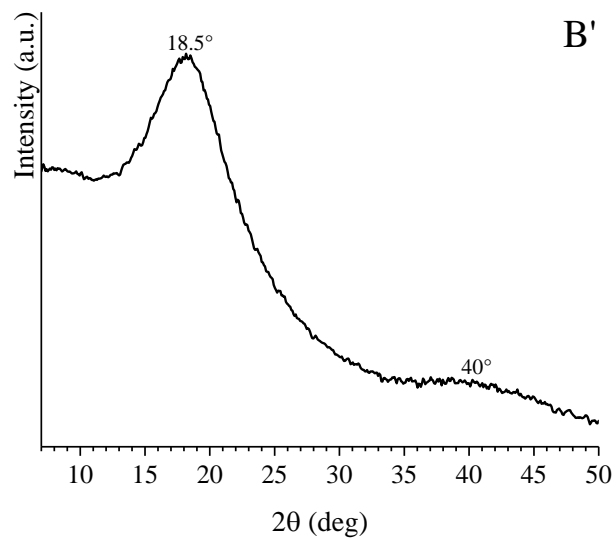
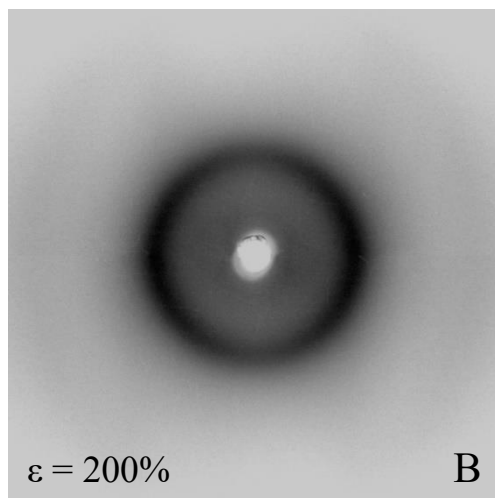
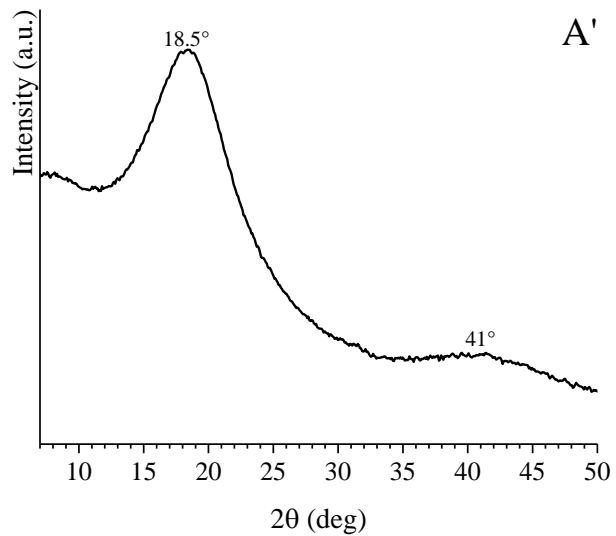
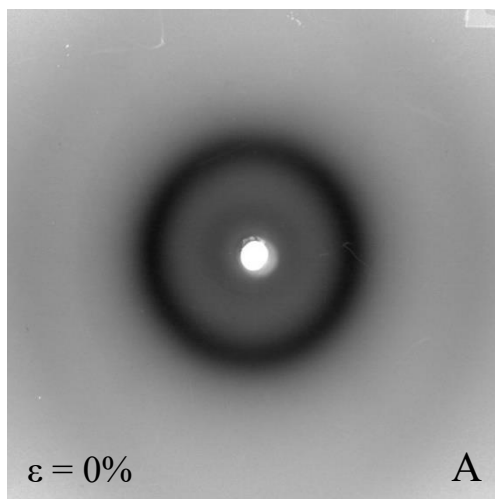
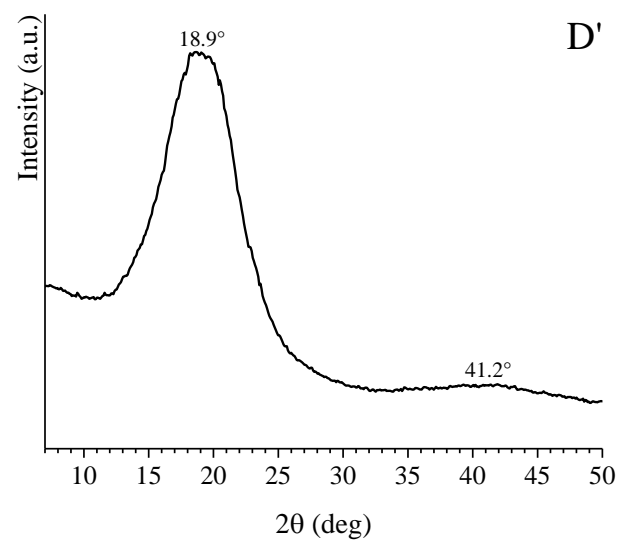
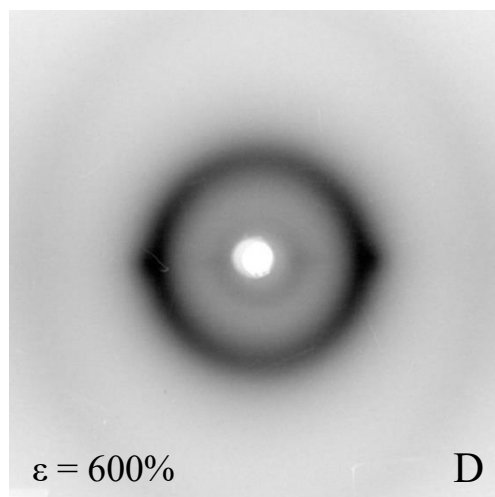
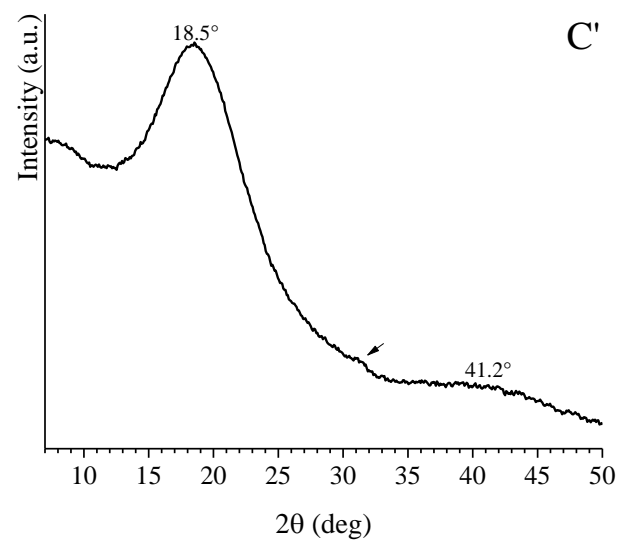
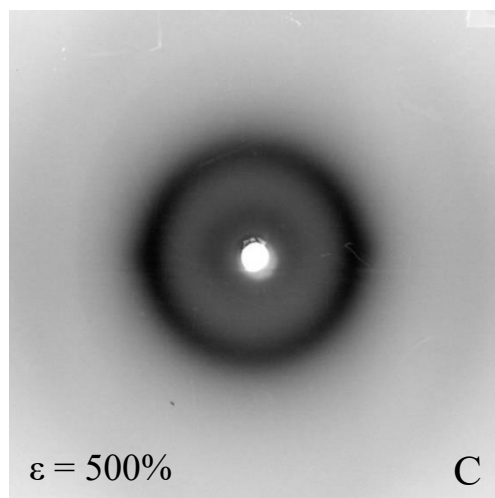


Figure 1.36. X-ray fiber diffraction patterns (A-F), and corresponding equatorial (A' - F') profiles, of the sample 13 recorded at $\varepsilon = 0\%$ (A,A'), $\varepsilon = 200\%$ (B,B'), $\varepsilon = 400\%$ (C,C'), $\varepsilon = 600\%$ (D,D'), $\varepsilon = 700\%$ (E,E') and after releasing the tension (F,F').

entry 14 (84.7mol% E, 2.2mol% P, 13.1mol% ENB) (Table 1.7)





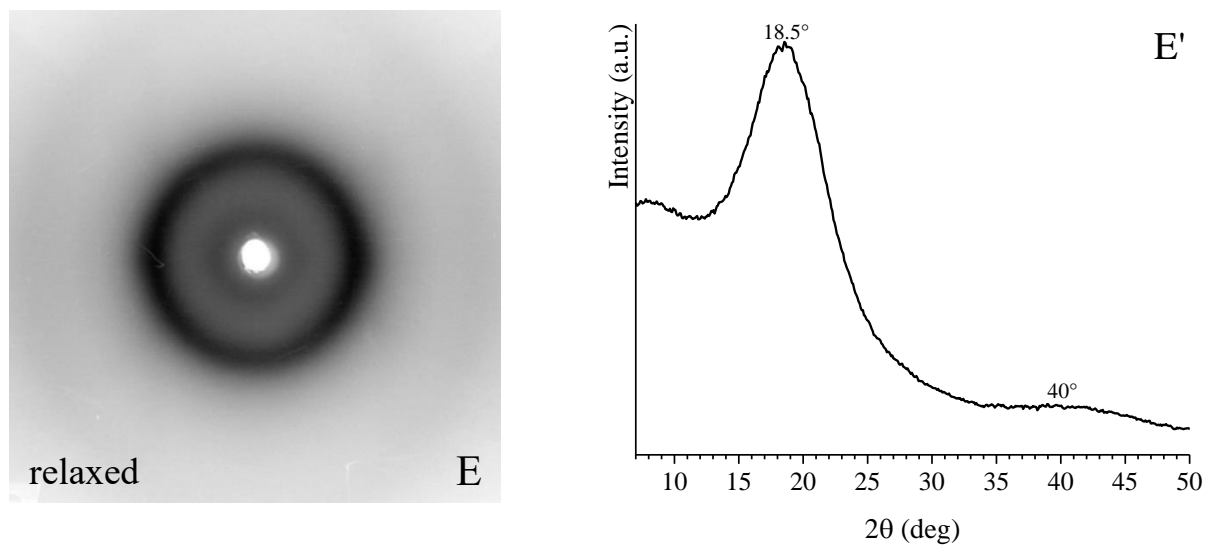
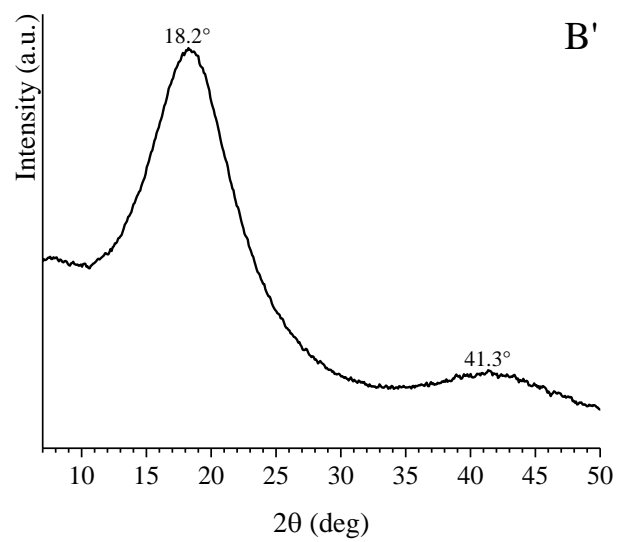
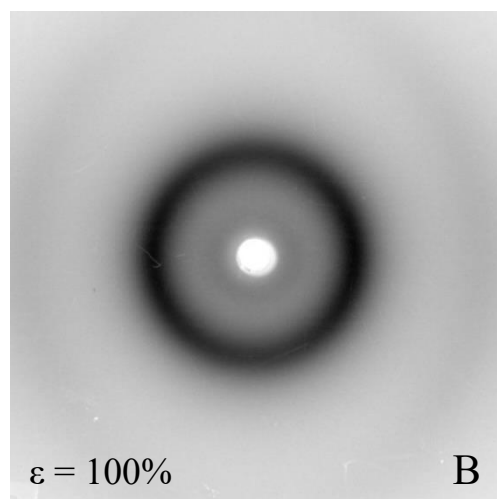
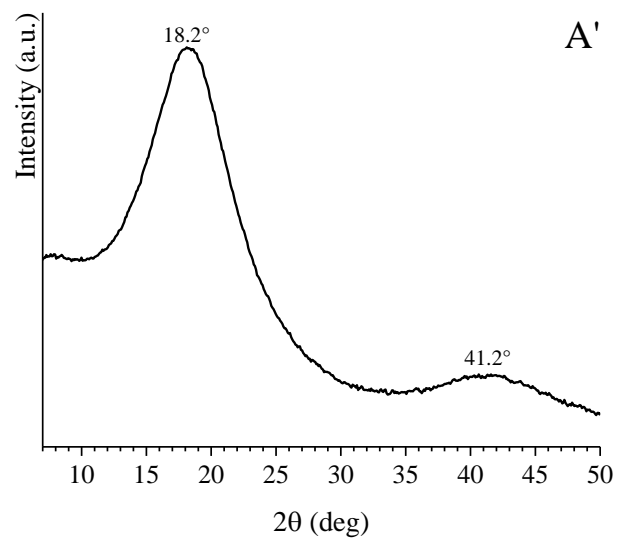
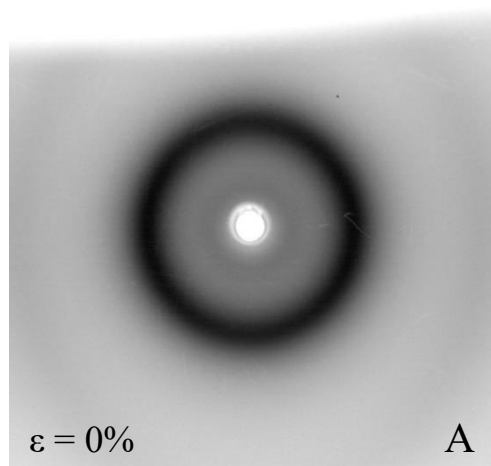
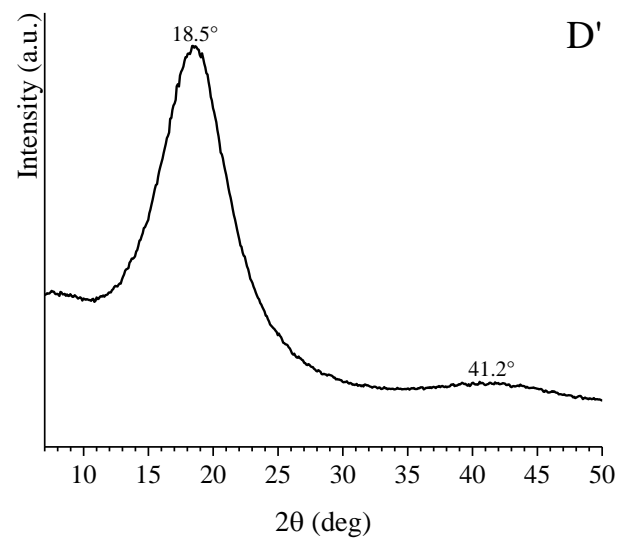
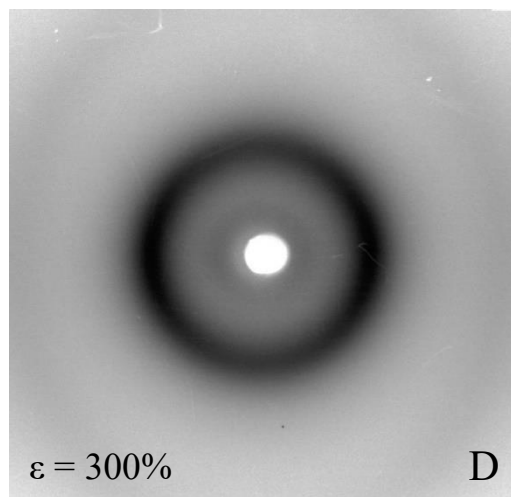
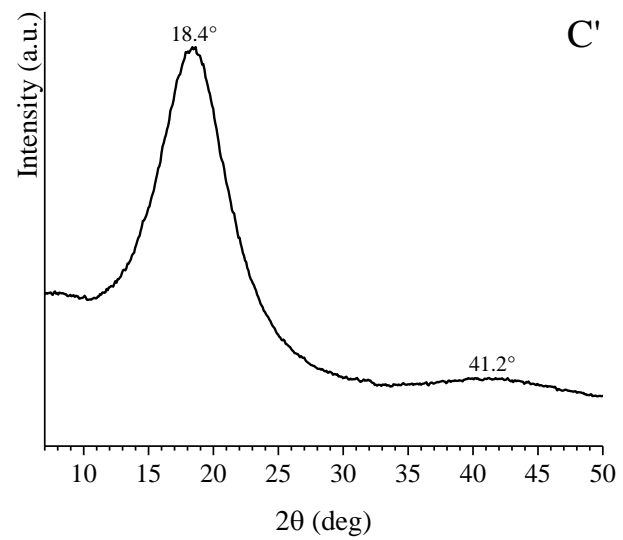
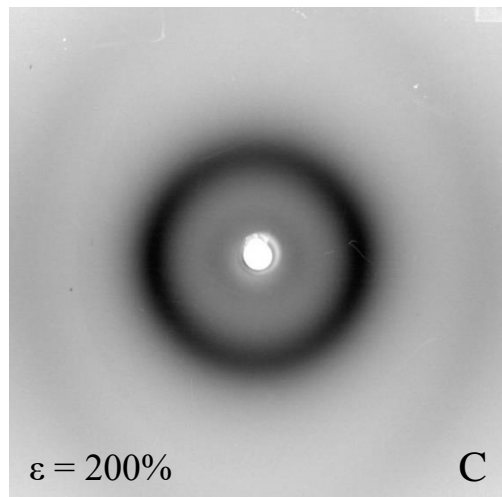


Figure 1.37. X-ray fiber diffraction patterns (A-F), and corresponding equatorial (A' - F') profiles, of the sample 14 recorded at $\epsilon = 0\%$ (A,A'), $\epsilon = 200\%$ (B,B'), $\epsilon = 500\%$ (C,C'), $\epsilon = 600\%$ (D,D') and after releasing the tension (E,E').

entry 15 (81.9mol% E, 2.6mol% P, 15.5mol% ENB) (Table 1.7)





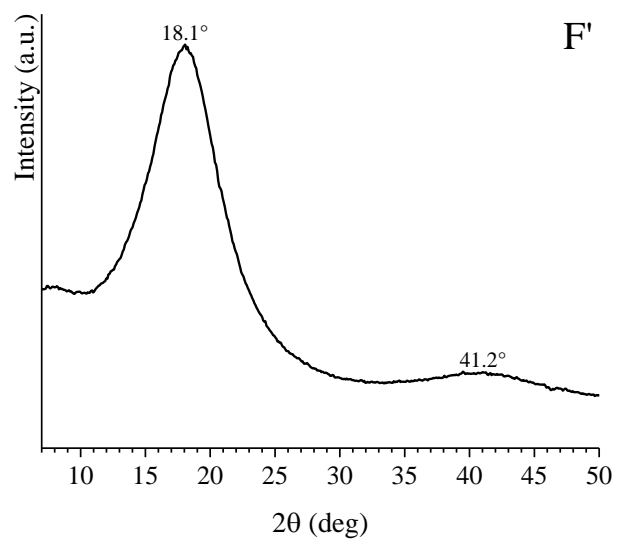
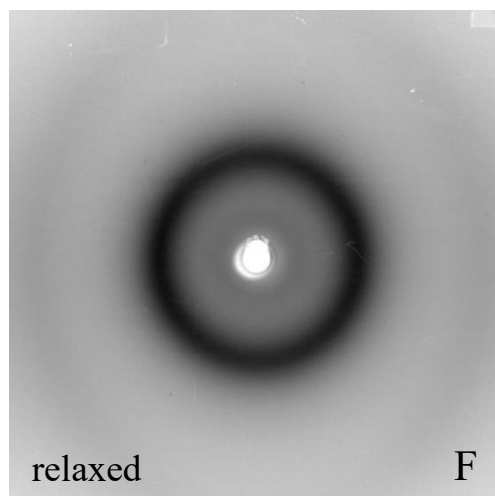
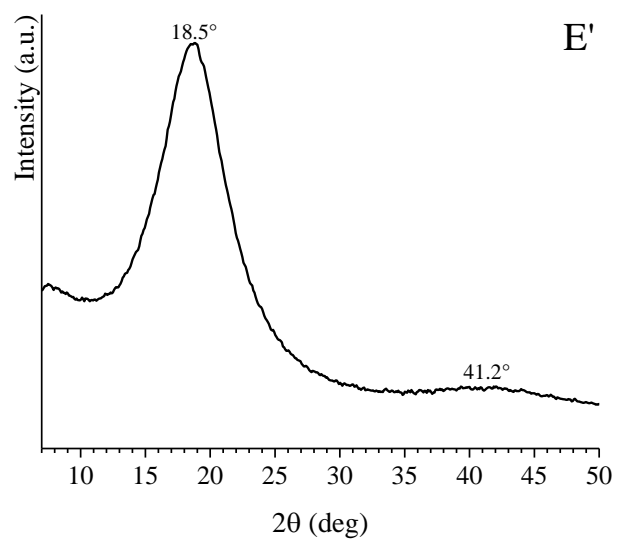
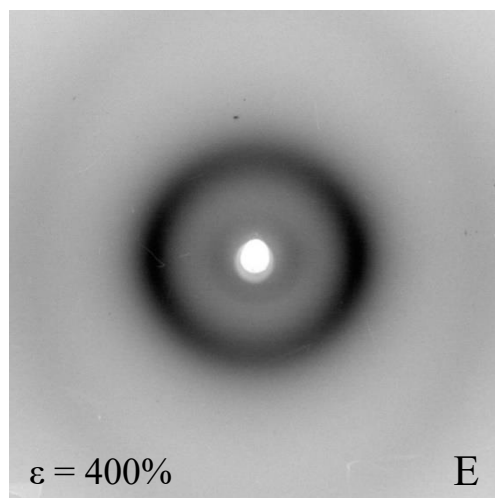


Figure 1.38. X-ray fiber diffraction patterns (A-F), and corresponding equatorial (A' - F') profiles, of the sample 15 recorded at $\epsilon = 0\%$ (A,A'), $\epsilon = 100\%$ (B,B'), $\epsilon = 200\%$ (C,C'), $\epsilon = 300\%$ (D,D'), $\epsilon = 400\%$ (E,E') and after releasing the tension (F,F').

1.2.16 Study of EPDMs morphology by Atomic Force Microscopy (AFM)

AFM height contrast images collected on samples 8, 10 and 13 are shown in Figure 1.39. The study focused only on these three samples as they show moderate crystallinity when cooled by the melt and, therefore, it is possible to appreciate their morphology while avoiding artifacts related to the AFM tip radius and the small crystal size. Furthermore, it is important to note that samples for AFM characterization were prepared using a crystallization procedure different to that applied for obtaining compression-molded films used for mechanical and structural studies. Specifically, the samples were cooled from the melt to -50°C at $2.5^{\circ}\text{C}/\text{min}$ in order to enhance the crystallization and to ensure the formation of crystalline aggregates of sufficient size to be easily detected by AFM. From the images reported in Figures 1.39A,B, it can be seen that samples 8 and 10 are characterised by a bundle-like morphology. Furthermore, a small amount of granular texture is also evident in sample 8, whereas sample 10, which has a higher degree of crystallinity, develop larger superstructures (average diameter 100–200 nm). Sample 13 exhibits a well-organized morphology (Figure 1.39C) characterized by small, starfish-like spherulites and a bundle-like structures.

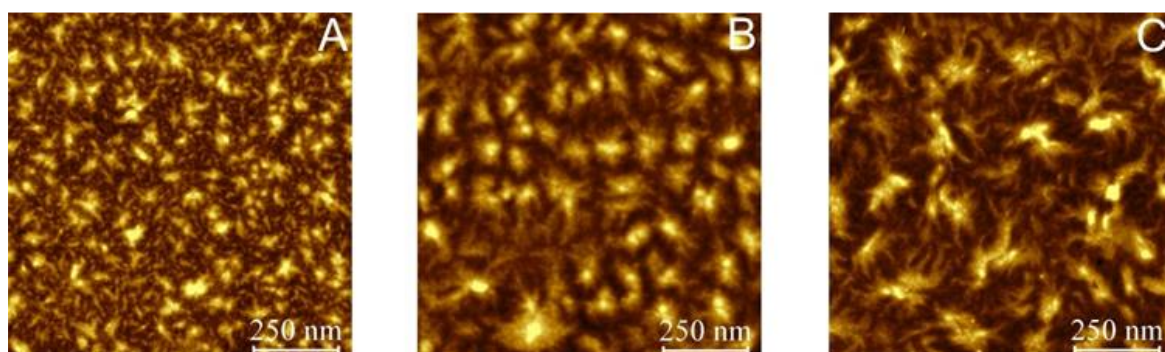


Figure 1.39. AFM height images showing $1\mu\text{m} \times 1\mu\text{m}$ scans of sample **8** (A), **10** (B), and **13** (C).

Figure 1.40 show AFM images acquired on the same samples at smaller scan sizes. From these images it is possible to appreciate the lamellar details and calculate their average thickness, which is approximately 2 nm for samples 10 and 13. Data concerning the morphological study of EPDM samples with similar composition to those studied in this project are not available in the literature. However, if the morphology of these samples is compared with that of other systems exhibiting similar crystallinity and elastic properties, such as ethylene-octene copolymers,⁷⁰⁻⁷² these EPDMs crystallize into well-organized crystalline structures. This is probably due to the compositional drift of these EPDMs, which leads to the formation of long

chain segments with consecutive ethylene units that determine the development of the displayed morphologies.

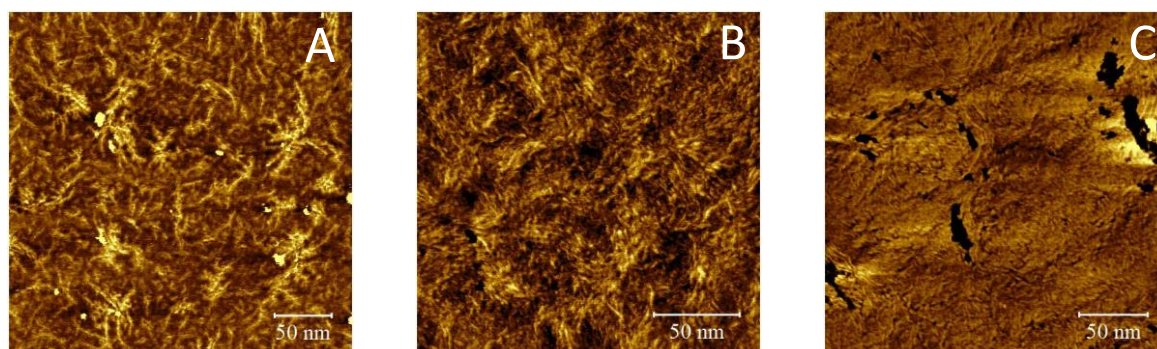


Figure 1.40. AFM height images showing $0.2\mu\text{m} \times 0.2\mu\text{m}$ scans of sample **8** (A), **10** (B), and **13** (C).

1.2.17 Conclusions Chapter 1

In this chapter the synthesis and characterization of ethylene, propylene and 5-ethylidene-2-norbornene terpolymers (EPDM) with high ethylene and diene contents were illustrated. Different sets of EPDM terpolymers were prepared by using three known imido vanadium(IV) complexes, differing in the imido substituent and coligand, in combination with Et_2AlCl and $\text{Cl}_3\text{CCO}_2\text{Et}$ as cocatalysts. Through an in-depth study and by using different characterization techniques, it has been shown that the obtained EPDMs are presumably a mixture of macromolecules, each of them featuring a nonrandom comonomer distribution and nonuniform composition. Each chain is like having a multiblocks where the comonomers are segmented, *i.e.*, blocks with high ethylene content that may crystallize and blocks with high propylene and ENB content that may not crystallize. This broad chemical composition distribution is due to time drift that occurs during the polymerization, which in turn depends on the experimental conditions and ligand set. Composition drift causes variation in the instantaneous feed comonomer ratio and hence in the chemical composition of the terpolymer over the period of conversion. It is worth noting that the molecular architecture of these heterogeneous EPDMs, qualitatively investigated by all the experimental techniques presented in the chapter (DSC, WAXS, SAXS, 2D-WAXS and mechanical tests), will be further investigated by SSA thermal fractionation techniques and TREF-NMR in order to obtain quantitatively information about the molecular structure and to clarify the comonomer distribution.

In proper experimental conditions, EPDMs behave as thermoplastic elastomers (TPEs) without the need of vulcanization, polymer blending, and reinforcement through the addition of fillers. They exhibit high elasticity, strain hardening at large deformation, excellent shape retention

properties, and remelting processability with no fall in properties. Examination of tensile behavior demonstrates the needful presence of ethylene sequences, long enough to crystallize during deformation and to act as physical knots in the elastomeric network, to ensure high elasticity and desired recovery. In addition, the high ENB content makes such EPDMs potentially functionalizable since the double bonds of the diene side chain could be selectively interconverted to a specific functional group extending the application fields of these materials.

References

- 1) R.R. Langeslay, D.M. Kaphan, C.L. Marshall, P.C. Stair, A.P. Sattelberger, M. Delferro *Chem. Rev.* **2019**, *119*, 2128.
- 2) (a) G. Natta, G. Dall'Asta, G. Mazzanti, I. Pasquon, A. Valvassori, A. Zambelli *Makromol. Chem.* **1962**, *54*, 95; (b) G. Natta, G. Dall'Asta, G. Mazzanti *Angew. Chem., Int. Ed.* **1964**, *3*, 723.
- 3) G. Natta, P. Pino, P. Corradini, F. Gianrusso, E. Mantica, G. Mazzanti, G. Moraglio *J. Am. Chem. Soc.* **1955**, *77*, 1708.
- 4) (a) E. Junghanns, O. Gumboldt, G. Bier *Makromol. Chem.* **1962**, *58*, 18; (b) G. Natta, G. Mazzanti, A. Valvassori, G. Sartori, D. Fiumani *J. Polym. Sci.* **1961**, *51*, 411.
- 5) W.L. Carrick *J. Am. Chem. Soc.* **1958**, *80*, 6455.
- 6) S.C. Davis, W. von Hellens, H. Zahalka *Polymer Material Encyclopedia* **1996**, Vol. 3 Salamone, J.C. Ed.; CRC Press Inc., Boca Raton, FL.
- 7) S. Gambarotta *Coord. Chem. Rev.* **2003**, *237*, 229.
- 8) K. Nomura, S. Zhang *Chem. Rev.* **2011**, *111*, 2342.
- 9) (a) W. Wang, K. Nomura *Adv. Synth. Catal.* **2006**, *348*, 743; (b) W. Wang, K. Nomura *Macromolecules* **2005**, *38*, 5905.
- 10) J. B. Wang, L. P. Lu, J. Y. Liu, Y. S. Li *Dalton Trans.* **2014**, *43*, 12926.
- 11) J. Q. Wu, J. S. Mu, S. W. Zhang, Y.S. Li *J. Polym. Sci. A: Polym. Chem.* **2010**, *48*, 1122.
- 12) C. Lorber "Vanadium Organometallics" **2007**, Elsevier Ltd.
- 13) J.Q. Wu, Y.S. Li *Coord. Chem. Rev.* **2011**, *255*, 2303.
- 14) G. Dall'Asta, G. Mazzanti, *Makromol. Chem.* **1963**, *61*, 178.
- 15) A.K. Tomov, V.C. Gibson, D. Zaher, M.R.J. Elsegood, S.H. Dale *Chem. Commun.* **2004**, 1956.
- 16) A.Y. Khalimon, E. Peterson, C. Lorber, L.G. Kuzmina, J.A.K. Howard, A. van der Est, G.I. Nikonov *J. Inorg. Chem.* **2013**, *12*, 2205.
- 17) C. Lorber, R. Choukroun, L. Vendier *Inorg. Chem.* **2007**, *46*, 3192.
- 18) C. Lorber, R. Choukroun, B. Donnadiou *Inorg Chem.* **2003**, *42*, 673.
- 19) C. Lorber, R. Choukroun, B. Donnadiou *Inorg. Chem.* **2002**, *41*, 4216.
- 20) C. Lorber, B. Donnadiou, R. Choukroun *Dalton Trans.* **2000**, 4497.
- 21) (a) N. Desmangles, S. Gambarotta, C. Bensimon, S. Davis, H.J. Zahalka *Organomet. Chem.* **1998**, *562*, 53; (b) C. Cuomo, A. Milione, A. Grassi *J. Polym. Sci., Part A: Polym. Chem.* **2006**, *44*, 3279; (c) C. Lorber, B. Donnadiou, R. Choukroun *Organometallics* **2000**, *19*, 1963.

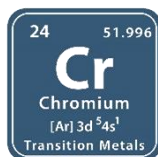
- 22) H. Hagen, J. Boersma, M. Lutz, A.L. Spek, G. van Koten *Eur. J. Inorg. Chem.* **2001**, 117.
- 23) (a) M. Biazek, K. Czaja *J. Polym. Sci., Part A: Polym. Chem.* **2008**, *46*, 6940; (b) M. Biazek, K. Czaja *Polimery* **2008**, *53*, 364.
- 24) G. Zanchin, F. Bertini, L. Vendier, G. Ricci, C. Lorber, G. Leone *Polym. Chem.* **2019**, *10*, 6200.
- 25) G. Zanchin, L. Vendier, I. Pierro, F. Bertini, G. Ricci, C. Lorber, G. Leone *Organometallics* **2018**, *37*, 3181.
- 26) C. Lorber, F. Wolff, R. Choukroun, L. Vendier *Eur. J. Inorg. Chem.* **2005**, 2850.
- 27) L.M. Tang, J.Q. Wu, Y.Q. Duan, L. Pan, Y.G. Li, Y.S. Li *J. Polym. Sci., Part A: Polym. Chem.* **2007**, *19*, 2038.
- 28) (a) J. Burt, W. Levason, G. Reid *Coord. Chem. Rev.* **2014**, *260*, 65-115; (b) C. Cheng, J. F. Hartwig *Science* **2014**, *343*, 853-857.
- 29) G. Leone, G. Zanchin, R. Di Girolamo, F. De Stefano, C. Lorber, C. De Rosa, G. Ricci, F. Bertini *Macromolecules* **2020**, *53*, 5881–5894.
- 30) N. P. Cheremisinoff *Polym. Plast. Technol. Eng.* **1992**, *31*, 713–744.
- 31) G. van Doremale, M. M. van Duin, M. Valla, A. Berthoud *J. Polym. Sci., Part A: Polym. Chem.* **2017**, *55*, 2877–2891.
- 32) P. S. Ravishankar *Rubber Chem. Technol.* **2012**, *85*, 327–349.
- 33) E. N. Kresge *Rubber Chem. Technol.* **2010**, *83*, 227–234.
- 34) G. Zhang, X. Zhou, K. Liang, B. Guo, X. Li, Z. Wang, L. Zhang *ACS Sustainable Chem. Eng.* **2019**, *7*, 11712–11720.
- 35) A. O. Starzewski, N. Steinhauser, B. .S Xin *Macromolecules* **2008**, *41*, 4095–4101.
- 36) V. Thakur, C. L. P. Shan, G. Li *Plast., Rubber Compos.* **2019**, *48*, 32–41.
- 37) G. Ver Strate In *Encyclopedia of Polymer Science and Engineering*; John Wiley and Sons: New York, **1986**, *6*, 522–564.
- 38) G. Natta, I. Pasquon, A. Zambelli *J. Am. Chem. Soc.* **1962**, *84*, 1488–1490.
- 39) E. Giannetti, R. Mazzocchi, E. Albizzati, T. Fiorani, F. Milani *Makromol. Chem.* **1984**, *185*, 2133–2151.
- 40) S. Cesca *Macromol. Rev.* **1975**, *10*, 1–230.
- 41) E. Giannetti, R. Mazzocchi, E. Albizzati, T. Fiorani, F. Milani *Makromol. Chem.* **1984**, *185*, 2133–2151.
- 44) P.R. Swann *J. Polym. Sci.* **1962**, *56*, 409.
- 45) R.B. Richards *J. Appl. Chem.* **1951**, *1*, 370.
- 46) B. Wunderlich, D. Poland *J. Polym. Sci., Part A* **1963**, *1*, 357.

- 47) C. H Baker, L. Mandelkern *Polymer* **1965**, 7, 71.
- 48) G. Ver Strate, Z.W. Wilchinsky *J. Polym. Sci., Part A* **1971**, 2, 9.
- 49) F.P. Baldwin, G. Ver Strate *Chem. Technol.* **1972**, 45, 709.
- 50) B.J.R. Scholtens *Rubber Chem. Tech.* **1984**, 57, 703.
- 51) B.J.R. Scholtens, E. Riande, J. E Mark *J. Polym. Sci., Polym. Phys.* **1984**, 22, 1223.
- 52) E.R. Walter, F.P. Reding *J. Polym. Sci.* **1956**, 21, 561.
- 53) E.A. Cole, D.R. Holmes *J. Polym. Sci.* **1960**, 46, 245.
- 54) R.M. Eichorn *J. Polym. Sci.* **1958**, 31, 197.
- 55) J.E. Preedy *Polym. J.* **1973**, 5, 13.
- 56) W. Bassi, P. Corradini, G. Fagherazzi, A. Valvassori *Eur. Polym. J.* **1970**, 6, 709.
- 57) G. Crespi, A. Valvassori, V. Zamboni, U. Flisi *Chim. Ind.* **1973**, 55, 130.
- 58) G. Guerra, M. Ilavsky, J. Biros, K. Dusek *Polym. Sci.* **1981**, 259, 1190.
- 59) G. Guerra, O. Ruiz de Ballesteros, V. Venditto, M. Galimberti, F. Sartori, R. Pucciarello *J. Polym. Sci., Part B: Polym. Phys.* **1999**, 37, 1095.
- 60) O. Ruiz de Ballesteros, F. Auriemma, G. Guerra, P. Corradini *Macromolecules* **1996**, 29, 7141.
- 61) F. Auriemma, P. Corradini, C. De Rosa, *Adv. Polym. Sci.* **2005**, 181, 1.
- 62) G. Leone, I. Pierro, G. Zanchin, A. Forni, F. Bertini, A. Rapallo, G. Ricci *J. Mol. Catal. A: Chem.* **2016**, 424, 220.
- 63) C. Lorber, L. Vendier *Dalton Trans.* **2013**, 42, 12203.
- 64) G. Leone, M. Mauri, S. Losio, F. Bertini, G. Ricci, L. Porri *Polym. Chem.* **2014**, 5, 3412.
- 65) F. Auriemma, M. Scoti, R. Di Girolamo, A. Malafrente, C. De Rosa, M. Van Duin *Polymer* **2020**, 199, 122540.
- 66) M. Scoti PhD Thesis, University of Naples Federico II, **2018**.
- 67) (a) F. J. Balta-Calleja, C. G. Vonk *X Ray Scattering of Synthetic Polymers*. Elsevier: Amsterdam, **1989**. (b) I. G. Voigt-Martin, R. Alamo, L. Mandelkern *J. Polym. Sci., Part B: Polym. Phys.* **1986**, 24, 1283. R. Alamo, R. H. Glaser, L. Mandelkern *J. Polym. Sci., Part B: Polym. Phys.* **1988**, 26, 2169. R. Alamo, L. Mandelkern *Macromolecules* **1989**, 22, 1273. R. Alamo, R. B. D. Viers, L. Mandelkern *Macromolecules* **1993**, 26, 5740. J. R. Isasi, J. A. Haigh, J. T. Graham, L. Mandelkern, R. Alamo *Polymer* **2000**, 41, 8813.
- 68) B. Poon, M. Rogunova, A. Hiltner, E. Baer, S. P. Chum, A. Galeski, E. Piorkowska *Macromolecules* **2005**, 38, 1232.
- 69) K. S. O'Connor, A. Watts, T. Vaidya, A. M. LaPointe, M. A. Hillmyer, G. W. Coates *Macromolecules* **2016**, 49, 6743.

- 70) J. Minick, A. Moet, A. Hiltner, E. Baer, S. P. Chum *J. Appl. Polym. Sci.* **1995**, 58, 1371.
- 71) S. Bensason, J. Minick, A. Moet, S Chum, A. Hiltner, E. Baer *J. Polym. Sci., Part B: Polym. Phys.* **1996**, 34, 1301.
- 72) S. Holzer, M. Menzel, Q. Zia, U. S. Schubert, M. Beiner, R. Weidisch *Polymer* **2013**, 54, 5207.

Chapter 2

Chromium



-Parts of this chapter have been published and are reproduced here from:

- 1) G. Zanchin, A. Piovano, A. Amodio, **F. De Stefano**, R. Di Girolamo, E. Groppo, G. Leone *Macromolecules* **2021**, 54, 1243.
- 2) A. Amodio, G. Zanchin, **F. De Stefano**, A. Piovano, B. Palucci, V. Guiotto, R. Di Girolamo, G. Leone, E. Groppo *Catalysts* **2022**, 12, 119.

Chromium is the first element in Group 6 of the transition series and has atomic number 24. It can exist in a variety of oxidation states, with (III) being the most stable. Stainless steel and chrome plating are the two principal uses, making up 85% of all commercial use.

Chromium and titanium reclaim a leading position in the field of olefin polymerization catalysis. In fact, chromium oxides are used in the Phillips catalysts, which are used to produce about half of the PE in the world, as will be described in detail later.

2.1 Chromium: the state of the art

2.1.1 Heterogeneous Cr-based Catalysts

Heterogeneous Cr-based catalysts account for the production of large volumes of polyolefins (POs) commodities.¹ The Phillips-type catalysts – where the active metal is Cr grafted on the surface of porous silica – supply almost 40% of the high density polyethylene (HDPE) total world demand. They are specific to produce a HDPE having a very broad molecular weight (M_w) distribution (i.e., M_w/M_n), which confers characteristic rheological properties useful for specific applications.

Despite its industrial relevance and the fact that the Philips catalysts are largely investigated, they are poorly understood from a fundamental point of view.^{2,3} In fact, although sixty years passed from the first patent of this kind of catalyst,⁴ the structure and oxidation state of the Cr active sites and the exact mechanism of ethylene polymerization are still debated.^{2,3,5} Contrary to other olefin polymerization catalysts, it does not need any activator to develop activity, a

fact that raises the question on the origin of the first Cr-C bond. Recent works⁶⁻⁹ have suggested some possible routes for Cr alkylation in the presence of ethylene, but experimental evidences are still missing. Depending on the choice of the support and on the chemical composition, the Phillips catalysts can produce from liquid oligomers to the ultrahigh- M_w PE grades (UHMWPE), with M_w/M_n varying from narrow ($M_w/M_n < 4$ as in Ziegler polymers) to extremely broad ($M_w/M_n > 100$).¹ This indicates that the properties of the Cr sites can be fine-tuned for obtaining specific products, but so far a clear correlation between the structure of the Cr active sites and their catalytic performances has not been established yet.

Therefore, developing homogenous molecular chromium catalysts is crucial because they may help with understanding how supported chromium catalysts work and open up new possibilities for adjusting activity and selectivity.

2.1.2 Homogeneous Cr-based Catalysts

From the year 2000 onward, numerous studies have recently been published in the literature with the goal of producing homogeneous single-site chromium catalysts.¹⁰⁻¹³ Several Cr-based catalysts have been developed and utilized to selectively oligomerize and polymerize ethylene using a variety of molecular chromium complexes.¹⁰⁻¹³ Due to the ease with which their steric and electrical characteristics may be tuned,¹⁴ the majority of the recently discovered chromium complexes are characterized by non-cyclopentadienyl ligands,¹⁵ specifically multidentate ligands with phosphine, amine, ether, and thioether donors.

In addition to ethylene polymerization, chromium catalysts have attracted interest and have also been used to synthesize other types of polyolefins characterized by different molecular structures. In this context, for example, Cr(II) complexes with bidentate phosphines in combination with methylaluminoxane (MAO), were extremely active, giving highly syndiotactic and predominantly isotactic 1,2-poly(butadiene)s, depending on the type of phosphine.

Similarly, for homogenous Cr catalysts employed for the olefin (co)polymerization, many questions are still open, especially those concerning the Cr oxidation state in the actual active species, and the possibility of efficiently producing high- M_w PEs.

2.2 Synthesis and Characterization of Ultra High Molecular Weight Polyethylene (UHMWPE) by using Iminopyridine Chromium Complexes

2.2.1 Materials and Methods

Catalysts and polyethylene samples were synthesized and supplied by Dr. Giuseppe Leone (CNR-ISMAR Milan) within a collaborative project “Chromium catalysis: from fundamental understanding to functional aliphatic polymers (Cr4FUN)” (PRIN -MIUR DD 3402 del 21/12/2018). The details about synthesis of complexes and PEs are discussed in a Ref 16.

Molecular weight (M_w) and molecular weight distribution (M_w/M_n) were obtained by a high-temperature Waters GPCV2000 size exclusion chromatography (SEC) system using an online refractometer detector. The experimental conditions consisted of three PL Gel Olexis columns, *o*-dichlorobenzene as the mobile phase, 0.8 mL min⁻¹ flow rate, and 145 °C temperature. The calibration of the SEC system was constructed using 18 narrow M_w/M_n PS standards with M_w values ranging from 162 to 5.6×10^6 g mol⁻¹. For SEC analysis, about 12 mg of polymer was dissolved in 5 mL of *o*-dichlorobenzene.

The calorimetric measurements were performed with a Mettler-DSC822 operating in N₂ atmosphere. The sample, typically 5 mg, was placed in a sealed aluminum pan, and the measurement was carried out from -70 to 180 °C using a heating and cooling rate of 10 °C min⁻¹.

The X-ray powder diffraction profiles of the as-prepared samples were obtained with Ni filtered Cu K α radiation (wavelength $\lambda=0.15418$ nm) by using an Empyrean diffractometer by Panalytical operating in the reflection geometry.

FT-IR and UV-Vis-NIR measurements were carried out by the research group of Prof. Elena Groppo (University of Turin – Department of Chemistry). Experimental details and procedures about these experiments are reported in Ref 16.

2.2.2 General Introduction

As mentioned in the paragraph 2.1.2, homogeneous chromium-based catalysts are of great interest for the polymerization of ethylene. In particular, the peculiarity of homogeneous molecular organochromium complexes is the ability to promote the polymerization of ethylene to give from linear α -olefins (selective tri- and tetramerization) to high-density PE (HDPE), and even ultrahigh-molecular weight PE (UHMWPE), depending on the ligand set. The selectivity originates from either ligand steric and electronic tuning or the presence of covalently linked neutral donor modifiers. However, generally, chromium complexes are

intended for the oligomerization of ethylene,¹⁷ while examples of UHMWPE are rare. These include chromium complexes bearing β -ketoimines and β -diketimines,¹⁸ half-metallocene Cr(III) complexes bearing a N[^]O ligand,¹⁹ and salicylaldiminate Cr(III) complexes.²⁰

Beyond the modification of ligand steric and electronic features, alternative strategies to effectively tune the molecular weight of the resultant PEs involve the addition of external electron additive donors (or modifiers) to existing chromium compounds have been demonstrated to be effective to tune the molecular weight of the resultant PEs.^{21,22}

The additives act by selectively disadvantaging β -hydrogen chain-transfer and subsequent chain-termination with respect to chain-propagation. Rastogi *et al.* used 2,6-di-*tert*-butylphenol (BHT) to trap free-AlMe₃, present in commercially available MAO and responsible of fast chain-termination, to synthesize UHMWPE from a hemi-metallocene chromium catalyst.²¹ Enders *et al.* demonstrated that the addition of a 9-borabicyclo[3.3.1]nonane enables the synthesis of UHMWPE from half-metallocene organochromium catalysts.²²

Generally, the modifiers are small organic molecules having heteroatoms (N, O, and P) or metal salts (*e.g.*, ZnCl₂, AlCl₃, and BF₃), and they can be classified as Lewis acids or Lewis bases. Lewis acids are used to electronically depauperate the active site, favoring olefin coordination and insertion, and thereby increasing the rate of polymerization and productivity. Lewis base additives (*e.g.*, THF, ethyl benzoate, acetonitrile, PPh₃) coordinate to the most acidic species over the course of the polymerization, namely the complex in its activated form and/or the Al-cocatalyst (*i.e.*, MAO or AlR₃). By steric shielding or electron density modification, the Lewis base additives modify the ratio between the rate constants of chain-propagation and chain-termination. Most of these modifiers have been previously reported to afford enhancements in the oligomerization and polymerization of ethylene catalyzed by zirconium,²³⁻²⁵ cobalt,^{26,27} vanadium,²⁸ tungsten²⁹ and late transition metal based catalysts.³⁰⁻³² Despite the important beneficial effects in the use of additives to design competitive catalysts, the full potential of additives in selective polymerization of ethylene has not been investigated as well as their “activation” path remains elusive in many cases.

In this context, it has been recently reported in the literature the polymerization of ethylene catalyzed by simple and readily accessible iminopyridine chromium complexes in the formal oxidation state +2 (**Cr1**–**Cr3**) and +3 (**Cr4**) (Figure 2.1).³³ The four different chromium complexes differ in the nature of the substituents at the iminic carbon and at the *ortho*-aryl positions. In the same work, it has been demonstrated that a concerted Cr-to-ligand electron transfer, coupled with a good stability of the [(L[•])Cr^{III}]⁻ intermediate with the ligand in the monoanionic radical form (L[•])⁻, fulfilled only for **Cr1**, providing an unexpected utility in the

polymerization of ethylene. This result is rather counterintuitive since iminopyridines are expected to provide a less efficient shielding to stabilize the chromium active species, and thereby they are believed to have the right “structural” motif to generate catalysts for the oligomerization of ethylene but not for its polymerization.

Since these chromium catalysts showed all these special features, the same complexes were chosen for the study reported in this chapter. In particular, they were investigated as precatalysts for the polymerization of ethylene using different aluminum cocatalysts and Lewis base NEt_3 as additive.

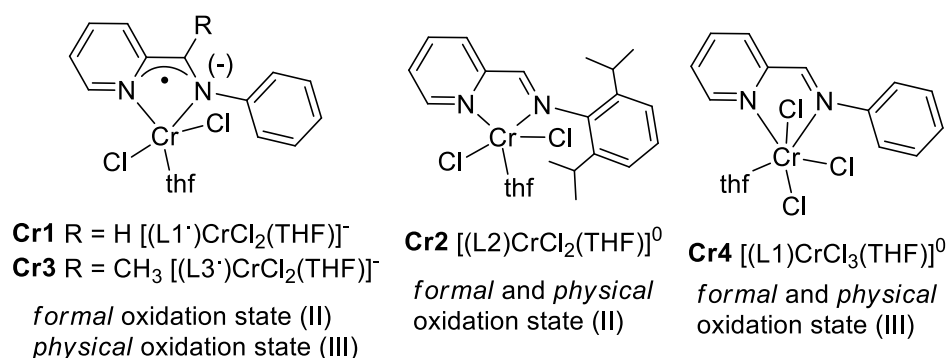


Figure 2.1. Iminopyridine chromium pre-catalysts **Cr1–Cr4**.

2.2.3 Catalytic Screening – Selection of the Aluminum Activator

A baseline catalytic behavior of **Cr1** activated with various aluminoxanes and aluminum alkyls was first established. In this regard, it is important to remember that homogeneous chromium-based complexes, unlike the Philips catalyst, require an activator to be active in polymerization. The results are shown in Table 2.1. The selected Al-activators were methylaluminoxane (MAO), TMA-depleted MAO (dMAO; TMA stands for AlMe_3), diethylaluminum chloride (DEAC), triisobutylaluminum (TIBA) and diisobutylaluminum hydride (DIBALH). The polymerizations were performed in toluene at an ethylene pressure of 1 atm, room temperature, and 250 equiv. of Al to Cr. Low chromium catalyst loading and short reaction time were employed to easily keep constant the temperature throughout the polymerization without cooling in the early stages, to maintain physical homogeneous conditions and to avoid side reactions caused by gel effect and high mixture viscosities.

The use of different Al-cocatalysts had a considerable effect on the catalytic behavior. The only productive run was obtained with MAO (Table 2.1), whereas dMAO and all the aluminum alkyls entirely stop the catalysis, resulting in a loss of activity for **Cr1**. The basis of our interpretation of the positive effect of MAO is its ability of generating large counterions around

the active species (sharply simplified with the formula $L_nMtMe^+ \cdots ClMAO^-$), less coordinating than R_3AlCl^- , generated with the other Al-cocatalysts.³⁵⁻³⁷ It can be inferred that the formation of a looser ion pair, as the one formed with **Cr1**/MAO, is fundamental to exhibit ethylene polymerization activity. Conversely, the formation of a tight ion pair in the presence of DEAC, TIBA, and DIBALH may inhibit subsequent insertions of ethylene and somehow facilitates a faster chain-termination over chain-propagation. This is in line with earlier results reported by Nomura and Zhang, who described a high tendency for β -hydride elimination and subsequent chain-termination with aluminum alkyls.³⁸ Furthermore, modification of the ligand skeleton may be an alternative scenario to explain the lack of activity of **Cr1**/AlR₃. A reduction of the iminic C=N bond in phenoxyimine Group 4 complexes by DIBALH and TIBA is documented.^{39,40}

Meanwhile, we were puzzled by the inactivity of **Cr1** when dMAO was employed as cocatalyst, since it is well established and documented that oligomeric (AlOMe)_n cages possess intrinsic alkylating capabilities and likely play a prominent role over TMA.^{41,42} In such an event, we therefore speculate that the presence of free-TMA in commercial MAO solution is somehow essential for polymerization activity. Given the monoanionic radical (L[•])⁻ state of **L1** (Figure 2.1) and the highly sensitivity of chromium, it can be inferred that the TMA plays a fundamental role by acting as oxygen and impurities scavenger that otherwise would poison the catalytic system.

Table 2.1. Polymerization of ethylene catalyzed by **Cr1** with different aluminum co-catalysts.^a

entry	co-cat	t (min)	yield (mg)	act ^b	M_w^e (g mol ⁻¹)	M_w/M_n
1	MAO	2	183	2290	1.0×10^4	4.8
15	DEAC	5	-			
16	dMAO ^d	5	-			
17	DIBALH	5	-			
18	TIBA	5	-			

^a polymerization conditions: ethylene pressure, 1.01 bar; total volume, 25 mL (toluene); Cr complex, 2.4 μ mol, complex solution in dry dichloromethane; Al/Cr = 250, Al = MAOs; time, 2 min. ^b activity in kg_{pol} mol_{Cr}⁻¹ h⁻¹; ^c determined by SEC; ^d d-MAO was prepared removing toluene and free-AlMe₃ from commercially available MAO.

2.2.4 Effect of Lewis Base NEt₃ Additive on the Catalytic Performance

Subsequently, it has been investigated the effect of the addition of NEt₃ on the catalytic behavior of **Cr1**/MAO. A solution of **Cr1** was treated with NEt₃ prior to activation with MAO and ethylene injection. A first screening was performed at room temperature, at atmospheric ethylene pressure and by varying the NEt₃ concentration while [Cr] was maintained constant. Polymerization conditions and results are summarized in Table 2.2. **Cr2–Cr4** were also investigated for comparison.

Table 2.2. Polymerization of ethylene catalyzed by **Cr1–Cr4**/MAOs and with the addition of NEt₃.^a

entry	Cr	NEt ₃ (μmol)	NEt ₃ (equiv. to Cr)	yield (mg)	activity ^b	M _w ^c (g mol ⁻¹)	M _w /M _n ^c	T _m ^{II d} (°C)	ΔH _m ^{II d} (J g ⁻¹)
1	Cr1			183	2290	1.0×10 ⁵	4.8	131.9	252.4
4	Cr1	25	10	192	2400	4.5×10 ⁵	10.4	134.4	230
5	Cr1	37.5	15	234	2925	1.2×10 ⁶	7.5	137.0	204
6	Cr1	50	20	235	2940	> 2×10 ⁶	5.3	137.6	159
7	Cr1	125	50	115	1440	> 2×10 ⁶	6.1	139.7	167
8	Cr2	50	20	–					
9	Cr3	50	20	–					
10	Cr4	50	20	–					

^a polymerization conditions: ethylene pressure, 1.01 bar; total volume, 25 mL (toluene); Cr complex, 2.4 μmol, complex solution in dry dichloromethane; Al/Cr = 250, Al = MAOs; time, 2 min; temperature, 20 °C. ^b activity in kg_{pol} mol_{Cr}⁻¹ h⁻¹; ^c determined by SEC; ^d determined from the DSC curves of second heating. NEt₃ was stirred with the solution of pre-catalyst for 1 min before they were charged in the reaction flask.

The data in Table 2.2 reveal that the addition of NEt₃ leads to significant changes in the catalysis employing **Cr1**. As a matter of fact, the catalytic activities for **Cr1** in the presence of the additive are all very high and even higher than in the absence of the additive when 15 and 20 equiv of NEt₃ were used. The test with a large excess of the additive (50 equiv to Cr, entry 7) is an exception. At NEt₃/Cr = 50, the activity strongly decreases, suggesting that a higher concentration of NEt₃ may interfere with the ethylene coordination/insertion or in any case poison the chromium precatalyst, resulting in a significant reduction in activity.

An even more interesting result is the molecular weight of the obtained polymers. The addition of NEt₃ leads to an increase of the PE molecular weight, while keeping the molecular weight distribution unimodal, in the range from 5.3 to 10.4. Addition of 10 equiv of NEt₃ gave rise to a fourfold increase of the molecular weight. The increase in the polymer molecular weight is

especially significant when 20 and more equivalents of NEt_3 were employed: in these cases, the obtained polymers are UHMWPEs, where the number average molar mass determined by GPC exceeds $2 \times 10^6 \text{ g mol}^{-1}$ (entries 6 and 7 in Table 2.2). The obtained findings are of relevance because they show that it is possible to tune the molecular weight over a broad range by using different amounts of NEt_3 , without changing the reaction conditions and/or the ligand set.

Overall, the addition of NEt_3 has a positive influence on both the catalytic activity and the polymer molecular weight. This effect is correlated to the amount of NEt_3 added, the optimal conditions identified being at $\text{NEt}_3/\text{Cr1} = 20$, while a further increase to $\text{NEt}_3/\text{Cr1} = 50$ is detrimental for the activity. This might be due to (i) a sort of drowning of the catalytically active species by the additive, resulting in inhibition of monomer coordination, and (ii) a possible “degradation” of MAO through adduct formation, which disrupts dative $\text{Al}\cdots\text{O}$ bonding. This last scenario has been documented for pyridine and bipyridine;⁴⁴ hence, it is plausible that NEt_3 behaves analogously.

The DSC curves of polyethylene samples reported in Table 2.2, recorded during first heating from -70°C to 180°C , successive cooling from the melt to -70°C , and second heating of the melt crystallized samples up to 180°C , all recorded at $10^\circ\text{C}/\text{min}$, are reported in Figure 2.2. The values of the second melting temperatures and associated enthalpy evaluated from the DSC curves of second heating are listed in Table 2.2.

From the data reported in Figure 2.3 is clear that the molecular weight strongly affects the thermal properties of the obtained PEs. DSC second heating scans reported in Figure 2.2C indicate that all samples present a single melting temperature (T_m^{II}) with a melting peak that increases with increasing molecular weight. In particular, the melting temperature ranges from 131.9°C (entry 1 in the absence of the additive) to 139.7°C (entry 7 at $\text{NEt}_3/\text{Cr} = 50$).

In Figure 2.3 are reported the WAXS patterns collected on as-prepared samples shown in Table 2.2. From the diffraction spectra reported in Figure 2.3 is evident that all PE samples crystallize in the orthorhombic form with a small amount of the monoclinic form.

Finally, **Cr2–Cr4**, not active in the absence of the additive, show no activity even in the presence of NEt_3 (Table 2.2, entries 8–10). The additive has no effect on the activation path of **Cr2–Cr4**. It is therefore reasonable to ascertain definitively that the nature of the iminopyridine substituents plays a fundamental role in the catalytic transformation of ethylene regardless of the presence of the additive. Necessary conditions for ethylene polymerization are the Cr-to-ligand synergy (*i.e.*, the tendency of chromium to undergo one-electron transfer

to the ligand) and the good stability of the active intermediate in the presence of the Al activator, both conditions fulfilled only by **Cr1**.

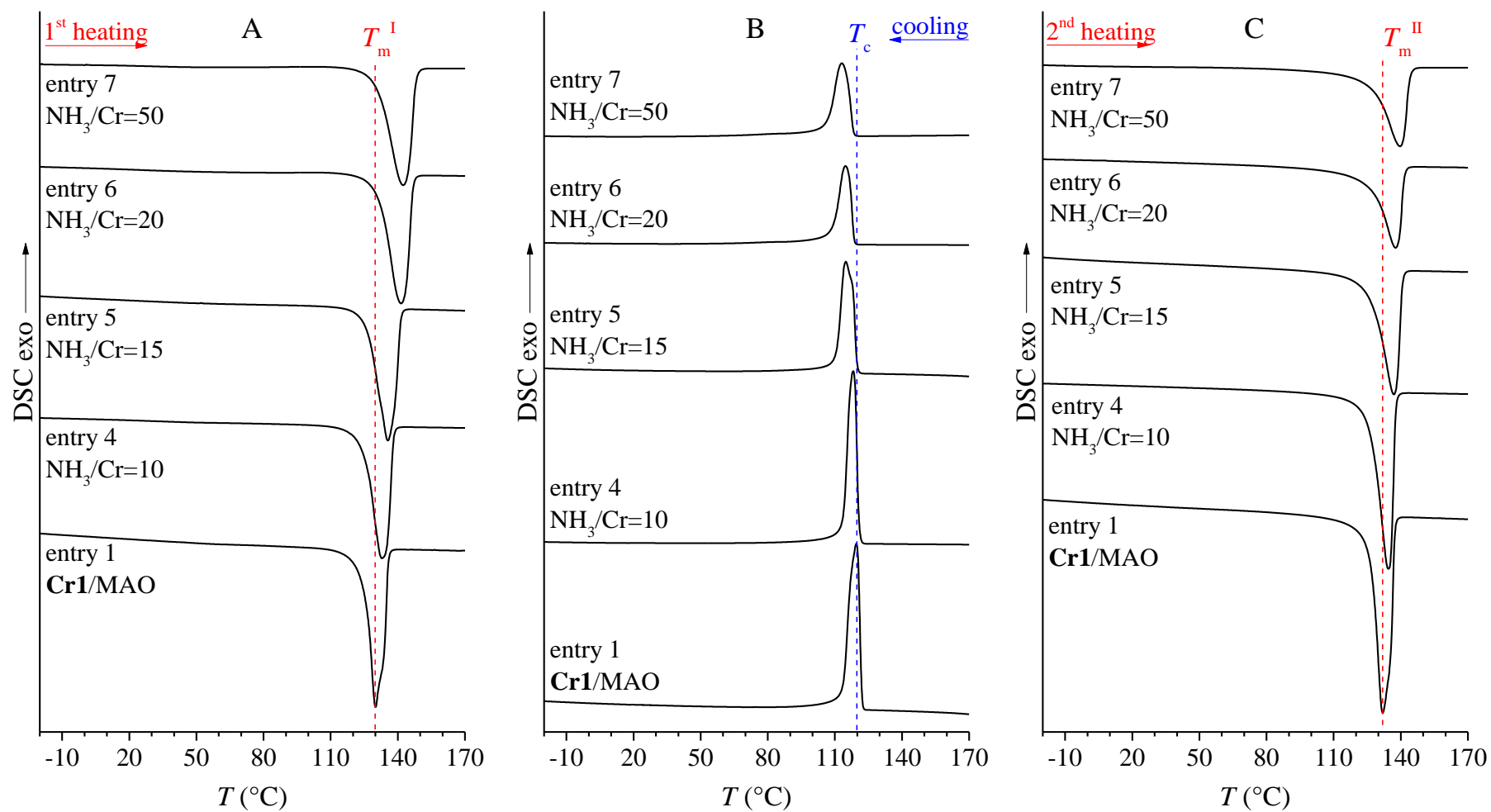


Figure 2.2. DSC thermograms of PE samples reported in Table 2.2 recorded at 10 °C/min during heating of as-polymerized samples (A), cooling from the melt (B) and successive heating (C).

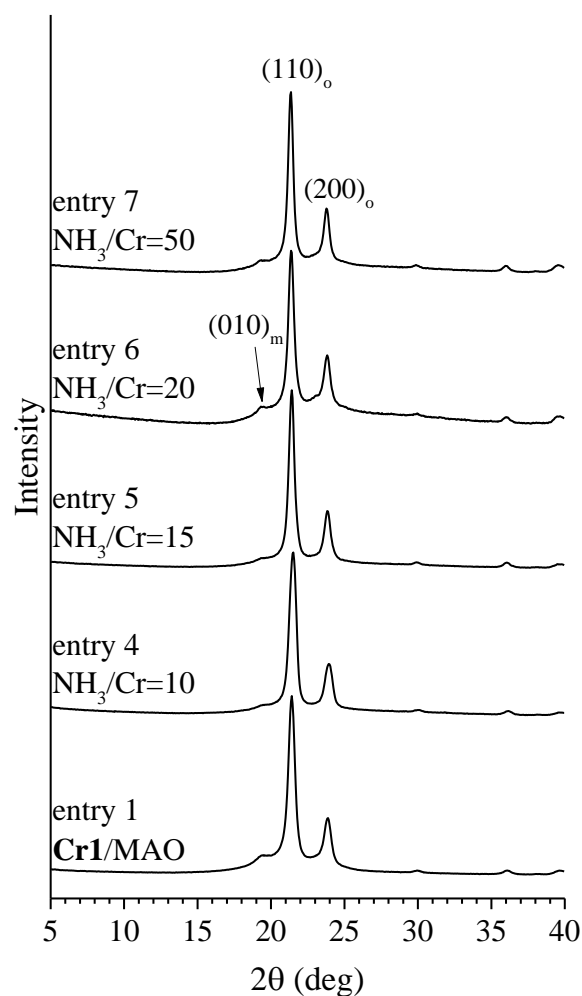


Figure 2.3. WAXS profiles of as-polymerized PE samples reported in Table 2.2.

2.2.5 Polymerization of Ethylene by Cr1/MAO/ NEt_3 at Different Temperatures

A series of polymerization were performed at different temperature with a feed of 250 equiv. of MAO and 20 equiv. of NEt_3 . The aim is to investigate whether the presence of the amine has a favorable effect on the thermal stability of **Cr1**. The same tests in the absence of NEt_3 were performed for comparison. Polymerization conditions and results are summarized in Table 2.3.

Table 2.3. Polymerization of ethylene catalyzed by **Cr1**/MAOs and with the addition of NEt_3 .^a

entry	NEt_3 (equiv. to Cr)	T (°C)	yield (mg)	activity ^b	M_w^c (g mol ⁻¹)	M_w/M_n^c	$T_m^{\text{II}d}$ (°C)	$\Delta H_m^{\text{II}d}$ (J g ⁻¹)
1		20	183	2288	1.0×10^5	4.8	131.9	252.4
11		40	160	2000	7.7×10^4	13.0	130.8	222.5
12		60	167	2090	1.2×10^5	17.4	130.1	218.6
6	20	20	235	2940	$> 2 \times 10^6$	5.3	137.6	158.5
13	20	40	192	2400	1.4×10^6	1.6	137.9	164.8
14	20	60	189	2360	6.6×10^4	4.4	131.6	250.3

^a polymerization conditions: ethylene pressure, 1.01 bar; total volume, 25 mL (toluene); Cr complex, 2.4 μmol , complex solution in dry dichloromethane; Al/Cr = 250, Al = MAOs; time, 2 min. ^b activity in $\text{kg}_{\text{pol}} \text{mol}_{\text{Cr}}^{-1} \text{h}^{-1}$; ^c determined by SEC; ^d determined from the DSC curves of second heating.

Generally, when the temperature was enhanced a smooth decrease in the activity was observed. While a decrease in ethylene solubility at elevated temperatures may play a key role, a major effect on the activity should be attributed to increased instability of the Cr–alkyl bond and catalyst decay, which both correlate with dominant chain-transfer.⁴³

In Figure 2.4, SEC traces of PE samples reported in Table 2.3 are shown.

From the data of Table 2.3 and Figure 2.4, is clear that in the absence of the additive, the properties of the resulting PEs resemble those of PEs by heterogeneous chromium-silica catalysts with M_w/M_n in the range 4.8–17.4 (M_w of about 1.0×10^5 g mol⁻¹). Increasing the reaction temperature, the chain transfer becomes predominant, the shape of the SEC curves strongly depending on the polymerization temperature (black curves of Figure 2.4).

Particularly at 60 °C, the SEC curve is dominated by two components with a low- M_w and a high- M_w fraction centered at 7000 and 1×10^5 g mol⁻¹, respectively (black curve of Figure 2.4c). This uniquely indicates the presence of several active species under certain polymerization conditions. On the opposite, the catalytic system **Cr1**/MAO/ NEt_3 exhibits good performance in terms of selectivity toward nearly monodisperse UHMWPE even at 40 °C (green curve of Figure 2.4b). Indeed, the net effect of the additive is that **Cr1**/MAO/ NEt_3 produces more polymer chains of comparable molecular weights ($1.6 < M_w/M_n < 5.3$) than **Cr1**/MAO.

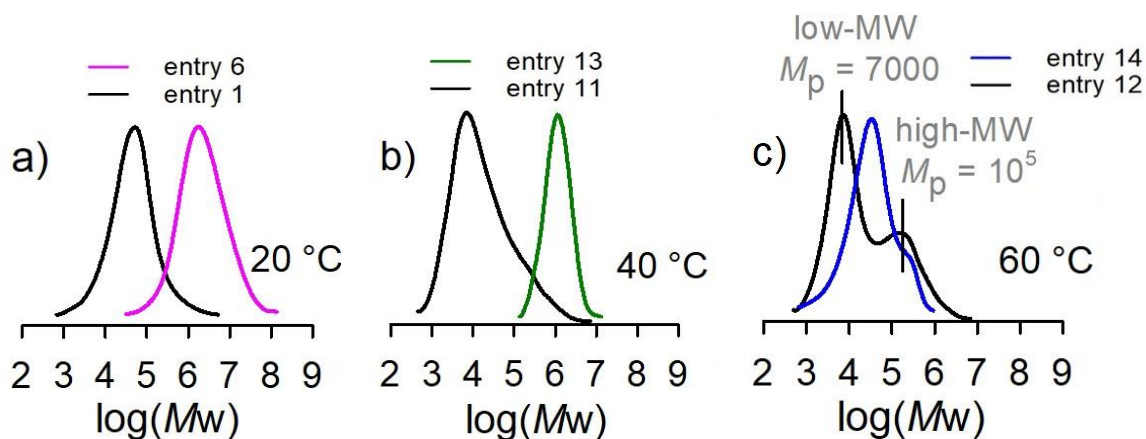


figure 2.4. SEC traces of PEs obtained by Cr1/MAO (black) and Cr1/MAO/NEt₃ (pink) at 20 °C (a). SEC traces of PEs obtained by Cr1/MAO (black) and Cr1/MAO/NEt₃ (green) at 40 °C (b). SEC traces of PEs obtained by Cr1/MAO (black) and Cr1/MAO/NEt₃ (blue) at 60 °C (M_p is the peak molecular weight in g mol⁻¹) (c).

The effect of polymerization temperature and additive loading on the molecular weight is confirmed by the DSC thermograms shown in Figure 2.5. In fact, samples synthesized at low temperature with high NEt₃ loading are characterized by the highest molecular weight thus showing high melting temperature (entries 6 and 13) in respect to those obtained at high temperature and low NEt₃ loading that present lower melting temperature as in the case of sample 12 synthesized at 60 °C in absence of NEt₃. Moreover, samples 11 and 12 presenting very broad or bimodal MWD, (13 and 17.4 respectively) show a shoulder in the DSC endotherms of Figure 2.5C at temperature lower than that of the main peak presumably due to the melting of PE crystals originated from PE fractions with low molecular weight that are present in these samples. These data show that controlling additive loading and polymerization temperature is possible to tune molecular weight, MWD and therefore thermal properties.

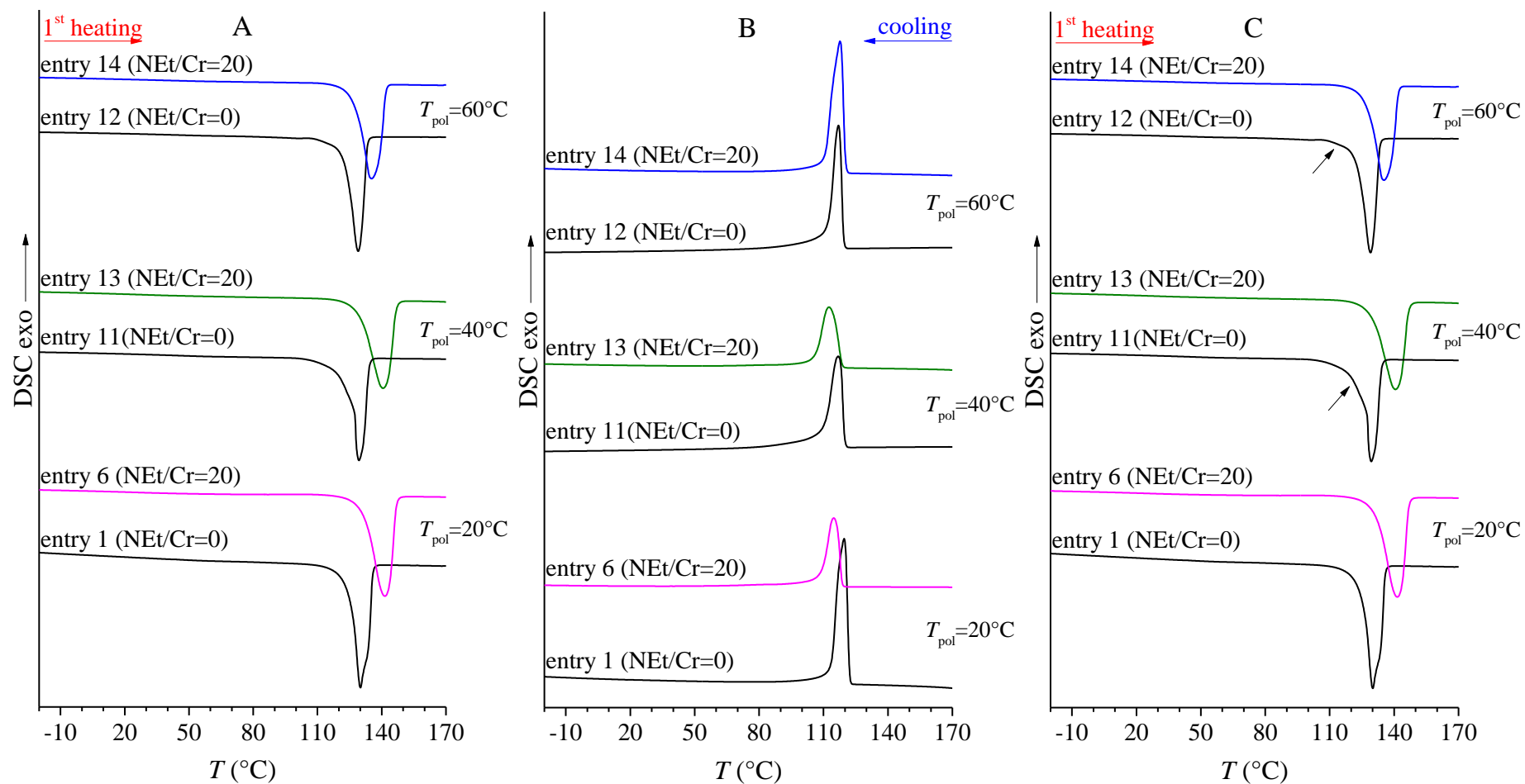


Figure 2.5. DSC thermograms of PE samples reported in Table 2.3 recorded at 10 °C/min during heating of as-polymerized samples (A), cooling from the melt (B) and successive heating (C).

WAXS patterns performed on as-prepared samples of Tables 2.3 show also in this case the presence of PE crystals in the orthorhombic form with a small amount of the monoclinic form (Figure 2.6).

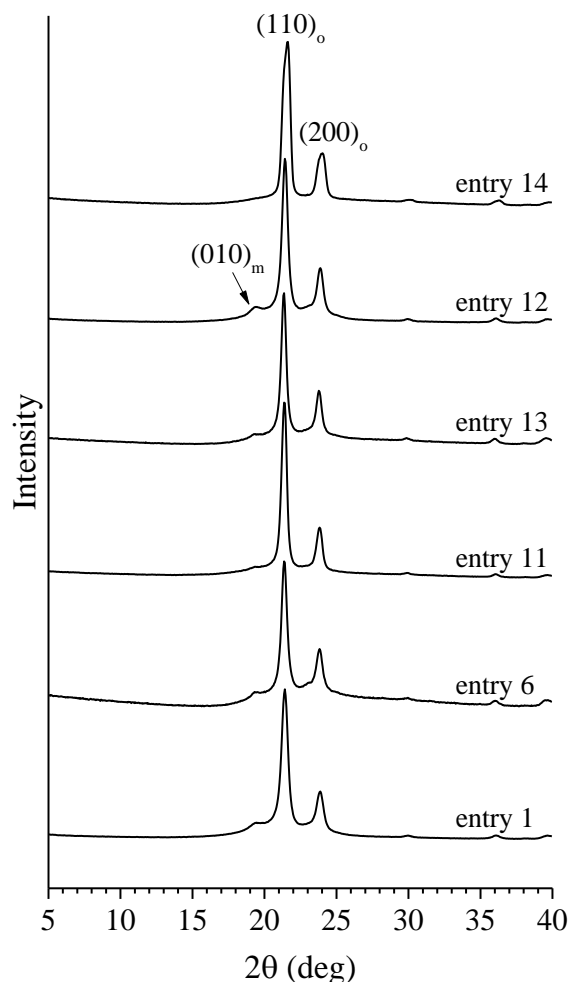


Figure 2.6. WAXS profiles of as-polymerized PE samples reported in Table 2.3.

2.2.6 What is the role of NEt₃? A spectroscopic study

To sum up the experimental results presented so far, the presence of NEt₃ has a remarkable and beneficial effect on the polymerization of ethylene by **Cr1**, mitigating the chain transfer and favoring the growth of the macromolecular chain over the side reactions that bring to chain “release”. To formulate some mechanistic hypotheses, however, it is necessary to understand how NEt₃ interacts with all of the components in the system. Considering that NEt₃ is a Lewis base, it can potentially interact with all of the inorganic and organometallic compounds in the system that have a Lewis acidic character, namely, the Al cocatalyst, the chromium complex, and the cationic active species generated by the interaction of **Cr1** with the aluminum cocatalyst. All these interactions are expected to be weak Coulomb interactions rather than

covalent bonding, but which interaction(s) actually take place is not known a priori. To answer this question, we performed a series of experiments by UV–vis–NIR and FT-IR spectroscopy techniques, whose use in the field of Cr-based catalysts for olefin polymerization is well assessed.⁴⁴⁻⁴⁶

Figure 2.7a shows the UV–vis–NIR spectra of **Cr1** and the **Cr1**/NEt₃/MAO system. The spectrum of **Cr1** is characterized by well-defined bands at 30200, 20000, 16500, 14000, 10500, and 5500 cm⁻¹, which were previously assigned to the π – π^* transitions of the ligand in the π -radical monoanionic (L•)⁻ form (being the spectrum of the neutral ligand L characterized only by bands above 24000 cm⁻¹).³³ After contact with NEt₃ and MAO, the band at 30200 cm⁻¹ decreases in intensity and slightly downward shifts, while all of the others disappear. The same behavior was observed upon contacting **Cr1** with NEt₃ and TEAl, as shown in Figure 4.7b. In both cases, a much weaker band seems to appear at ~23000 cm⁻¹, more evident for TEAl than for MAO. These results indicate that after contact with NEt₃ and the aluminum activator, the electronic properties of **Cr1** dramatically change. In particular, the disappearance of the bands diagnostic for the (L•)⁻ ligand univocally indicates that the ligand goes back to its neutral (L) form. This is independent from the type of aluminum activator, corroborating the hypothesis that all of the aluminum cocatalysts generate chromium active sites with the same electronic properties, even though only MAO activates **Cr1** for ethylene polymerization. For this reason, we decided to perform the spectroscopic study by using TEAl since its spectroscopic features are much simpler than those of MAO. The interpretation of the UV–vis–NIR spectra of the ternary **Cr1**/NEt₃/TEAl system (and even more of the IR spectra) is not straightforward and requires to know not only which are the spectroscopic fingerprints of each component alone but also which are the spectroscopic manifestations of all of the possible binary systems, namely, **Cr1**/NEt₃, **Cr1**/TEAl, and NEt₃/TEAl.

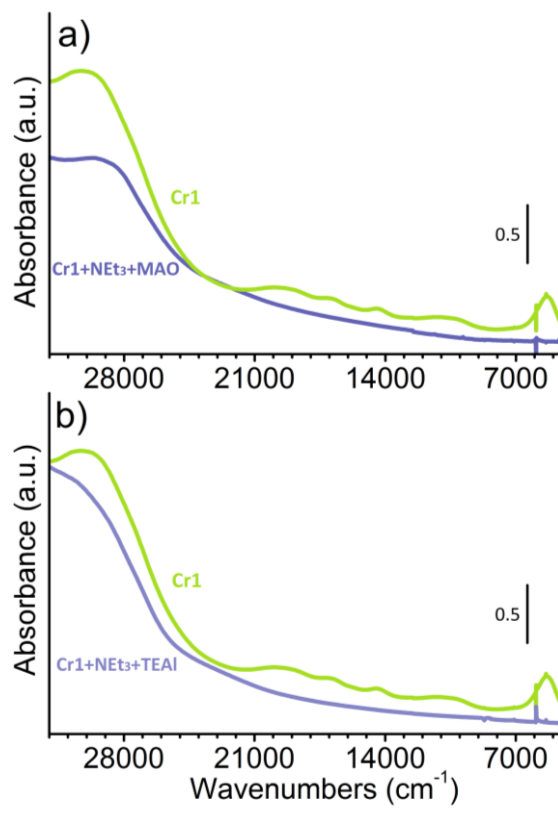


Figure 2.7. UV-vis-NIR spectra of **Cr1** and **Cr1/NET₃/MAO** (a) and **Cr1/NET₃/TEAL** (b) ($Cr = 10^{-3}M$ in $CHCl_3$, $Al/Cr = 10$, $N/Cr = 20$).

2.2.7 Cr1 + NET₃

Figure 2.8 shows the UV-Vis-NIR and FT-IR spectra of **Cr1**, NET_3 and their mixture. The UV-Vis spectrum of **Cr1** was already commented above, that of NET_3 does not show any absorption band in the investigated spectral range, and that of **Cr1/NET₃** is almost the same as that of **Cr1**. The FT-IR spectrum is the bare sum of those of **Cr1** and NET_3 . Both evidences univocally indicate that NET_3 does not interact with **Cr1**, even though there are a few cases in the literature reporting interactions between a pre-catalyst and a Lewis base.^{24,25,47}

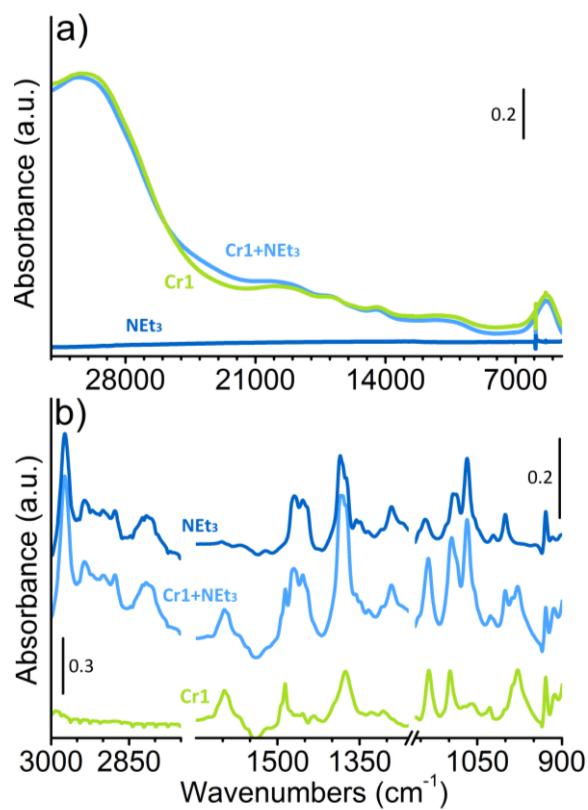


Figure 2.8. UV-Vis-NIR (part a) and FT-IR (part b) spectra of **Cr1**, NEt₃ and **Cr1**+NEt₃ in chloroform (Cr = 10⁻³ M in CHCl₃, N/Cr=20).

2.2.8 Cr1 + TEAl

A different spectral behavior is observed when contacting **Cr1** with TEAl, as reported in Figure 2.9. The UV-Vis-NIR spectrum of **Cr1**/TEAl (Figure 2.9a) is very similar to that of the Cr1/TEAl/NEt₃ discussed above (Figure 2.7b). Upon interaction of **Cr1** with TEAl, the absorption bands due to the π - π^* transitions of the ligand in its (L[•])⁻ radical form disappear, indicating that upon **Cr1** activation the ligand goes back to its neutral L form.³³

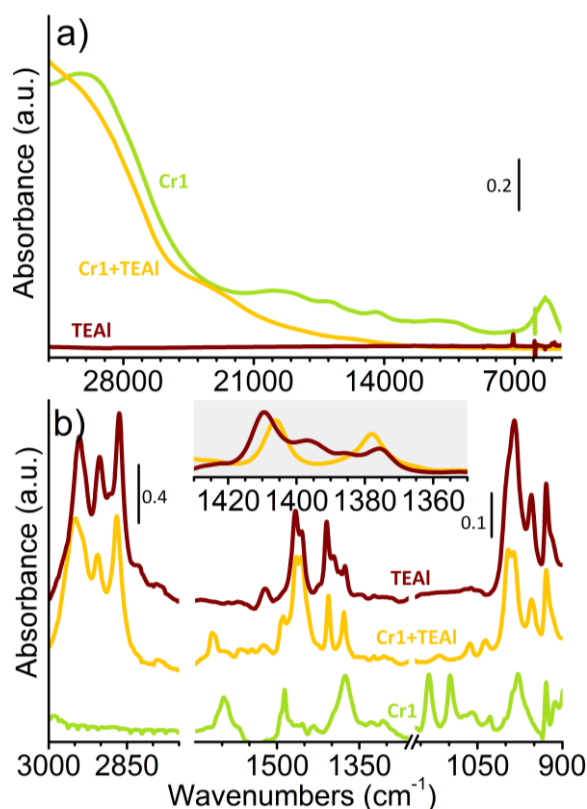


Figure 2.9. UV-Vis-NIR (part a) and FT-IR (part b) spectra of **Cr1**, TEAl and **Cr1**+TEAl ($\text{Cr} = 10^{-3} \text{ M}$ in CHCl_3 , $\text{Al}/\text{Cr}=10$). The inset in part b) shows a magnification of the $1430 - 1360 \text{ cm}^{-1}$ region, which contains the absorption bands due to the $\delta(\text{CH}_2)$ and $\delta_{\text{sym}}(\text{CH}_3)$ vibrational modes.

FT-IR spectroscopy (Figure 2.9b) confirms that **Cr1** and TEAl interact together. The IR spectrum of **Cr1** shows a series of absorption bands in the $1700\text{--}900 \text{ cm}^{-1}$ region, which are due to the vibrations of the $(\text{L}^\bullet)^-$ radical anionic ligand. These bands are still visible in the spectrum of **Cr1**/TEAl, but shifted in different positions and much less intense, as expected if $(\text{L}^\bullet)^-$ is transformed into L. Indeed, the absorption bands due to the vibrations of the radical anion of a conjugated molecule are strongly enhanced in intensity in comparison to the corresponding neutral form. For example, the band at 1597 cm^{-1} in the spectrum of **Cr1** is observed at 1618 cm^{-1} in the spectrum of **Cr1**/TEAl, while the doublet at $1135\text{--}1098 \text{ cm}^{-1}$ shifts at $1062\text{--}1035 \text{ cm}^{-1}$. As far as the spectrum of TEAl is concerned, characteristic bands are observed in the ranges $3000\text{--}2800 \text{ cm}^{-1}$ (CH_x stretching modes), $1500\text{--}1300 \text{ cm}^{-1}$ (CH_x bending modes) and $1000\text{--}900 \text{ cm}^{-1}$ (C-C stretching modes). All these bands are observed in the spectrum of **Cr1**/TEAl but shifted. The most informative region is the $1430\text{--}1360 \text{ cm}^{-1}$ one, which contains the absorption bands due to the $\delta(\text{CH}_2)$ and $\delta_{\text{sym}}(\text{CH}_3)$ vibrational modes. The spectrum of TEAl shows four bands at $1410, 1397, 1385$ and 1375 cm^{-1} , which are specific for TEAl in the dimeric form.⁴⁸ This explains why both the $\delta(\text{CH}_2)$ and $\delta_{\text{sym}}(\text{CH}_3)$ vibrational

modes are split in two bands: the ethyl groups bridging the two Al cations behave differently from the others, and are responsible for the two bands at 1397 cm^{-1} , $\delta(\text{CH}_2)$, and 1385 cm^{-1} , $\delta_{\text{sym}}(\text{CH}_3)$. The spectrum of **Cr1**/TEAl is much simpler in this region, where only two bands are observed at 1406 and 1377 cm^{-1} , which are attributed to the $\delta(\text{CH}_2)$ and $\delta_{\text{sym}}(\text{CH}_3)$ vibrational modes of TEAl in its monomeric form. This observation indicates that TEAl dimers are dissociated upon reaction with **Cr1**.

All in all, UV-vis-NIR and FT-IR spectroscopic techniques allow us to formulate a plausible mechanism for the interaction between **Cr1** and dimeric TEAl, as sketched in Figure 2.10: (1) a Cl^- ligand is substituted by an alkyl group, with the consequent release of AlR_2Cl ; (2) a second Cl^- ligand is removed by coordinated AlR_3 with the subsequent creation of the coordination vacancy and the generation of an ion pair between the cationic chromium complex and the anionic Al-alkyl moiety; and (3) a further electronic rearrangement occurs, whereby the unpaired electron of the $(\text{L}\cdot)^-$ ligand drains onto the chromium ion, leading to a cationic Cr(II) complex, which has all of the elements to be active in ethylene polymerization, *i.e.*, an alkyl ligand, a coordination vacancy, and an effective positive charge, in agreement with the most accepted theory for homogeneous polymerization catalysis.

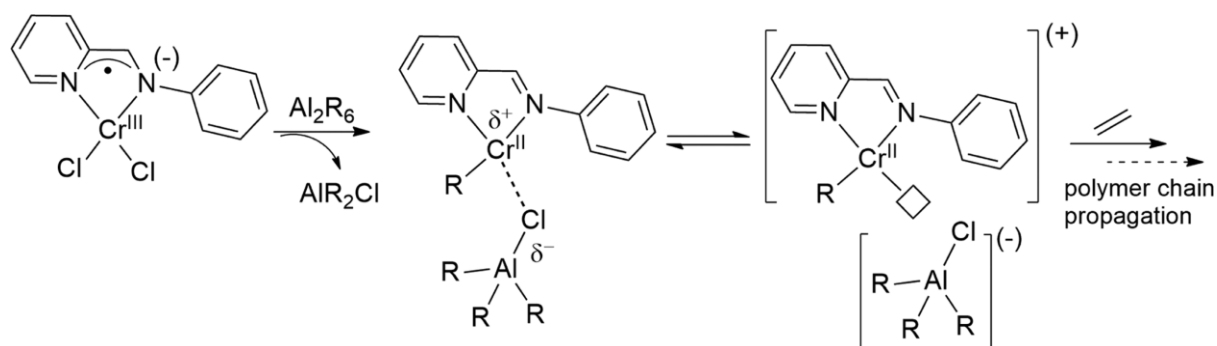


Figure 2.10. Mechanistic hypothesis for the interaction between **Cr1** and TEAl, as derived from the spectroscopic data.

2.2.9 NEt_3 + TEAl

The interaction between aluminum compounds and amines is well accepted in the literature. In the field of olefin polymerization, the complexation of free- AlMe_3 in commercial MAO solution with aromatic amines (namely pyridine and bipyridine) is one of the possible strategies for determining its amount.⁴⁹ Spectroscopy may help in understanding the kind of interaction. In this case, UV-Vis-NIR spectroscopy is not useful, since both TEAl and NEt_3 have no absorptions in the investigated region. In contrast, FT-IR spectroscopy does help.

Figure 2.11 shows the FT-IR spectra of NEt_3 +TEAl and of the two compounds alone. The spectrum of NEt_3 shows absorption bands in three main ranges: in the $3000\text{--}2800\text{ cm}^{-1}$ ($\nu(\text{CH}_x)$ modes), in the $1500\text{--}1300\text{ cm}^{-1}$ ($\delta(\text{CH}_2)$ and $\delta(\text{CH}_3)$), and in the $1100\text{--}1000\text{ cm}^{-1}$ ($\nu(\text{C-N})$ and $\nu(\text{C-C})$). In particular, the band of $\nu(\text{C-N})$ at 1067 cm^{-1} is the most sensitive to the interaction with NEt_3 . In the spectrum of NEt_3 +TEAl this band shifts down to 1046 cm^{-1} , indicating that the two compounds combine together. An analogous shift was observed for the interaction between the tertiary amine NMe_3 in adduct with the Lewis acid BH_3 .⁵⁰ Even more informative is the $1430\text{--}1360\text{ cm}^{-1}$ region, which is highlighted in the inset of Figure 2.11. The spectrum of NEt_3 shows only two bands at 1385 and 1374 cm^{-1} , which are assigned to $\delta(\text{CH}_2)$ and $\delta(\text{CH}_3)$ modes, opposite to the case of TEAl where four bands are observed due to its dimeric form. Interestingly, the spectrum of NEt_3 /TEAl is characterized by two very intense bands at 1395 and 1385 cm^{-1} , which are specific for the bending modes of bridging ethyl groups. These bands are remarkably more intense than in the spectrum of TEAl and indicate that a strong interaction is taking place between NEt_3 and TEAl. This is in agreement with the literature reporting that many Lewis bases (B) reversibly interact with aluminum alkyls,⁵¹ cleaving the alkyl-bridged dimers to form new adducts, according to the equation $(\text{AlR}_3)_2 + 2\text{B} \rightleftharpoons 2(\text{B}^*\text{AlR}_3)$.⁵² Each $\text{NEt}_3^*\text{TEAl}$ adduct bears two bridging ethyl groups as depicted in Figure 2.12, thus roughly doubling their total amount.

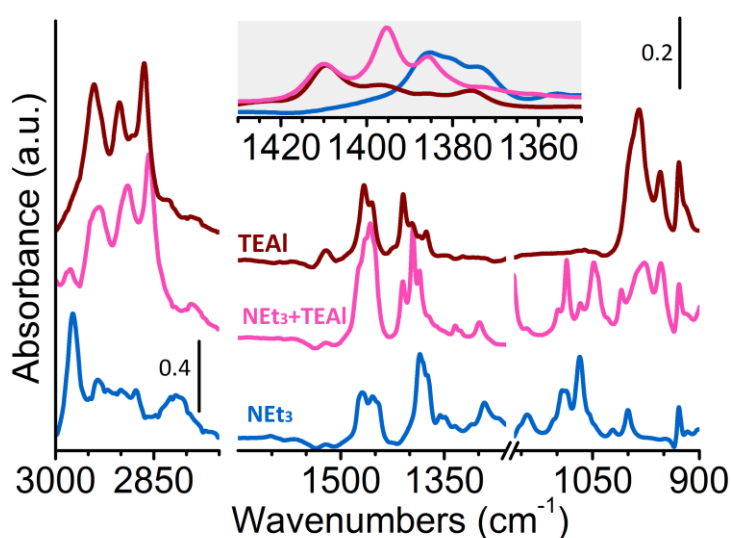


Figure 2.11. FT-IR spectra of NEt_3 , TEAl and TEAl+ NEt_3 (in CHCl_3). The inset shows a magnification of the $1430\text{--}1360\text{ cm}^{-1}$ region, which contains the absorption bands due to the $\delta(\text{CH}_2)$ and $\delta_{\text{sym}}(\text{CH}_3)$ vibrational modes.

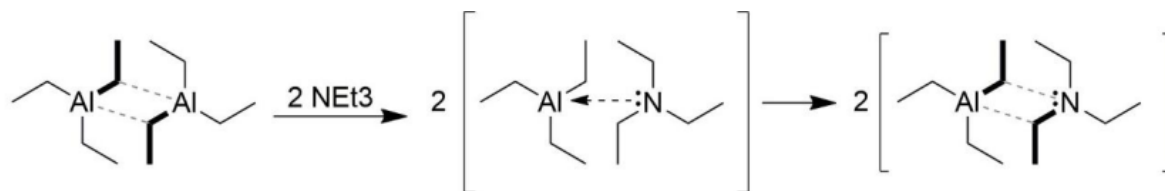


Figure 2.12. Mechanism of reaction between TEAl dimer and NEt_3 to form $\text{NEt}_3^*\text{TEAl}$ adduct.

2.2.10 Cr1 + NEt_3 + TEAl

When all the three actors are mixed the situation is more complex and requires the complementarity of the characterization techniques to get a unified picture. From the electronic point of view (Figure 2.13a), the effect of the activation of **Cr1**+ NEt_3 by TEAl on the UV–Vis spectrum is analogous to that observed upon the activation of **Cr1** alone. The spectroscopic manifestations of the ligand in its radical anionic form disappear. FT–IR spectroscopy indicates the presence of $\text{NEt}_3^*\text{TEAl}$ adducts, as revealed by the $\nu(\text{C-N})$ band at 1046 cm^{-1} and the two intense bands at 1395 and 1385 cm^{-1} due to the $\delta(\text{CH}_2)$ and $\delta(\text{CH}_3)$ modes of bridging ethyl groups.

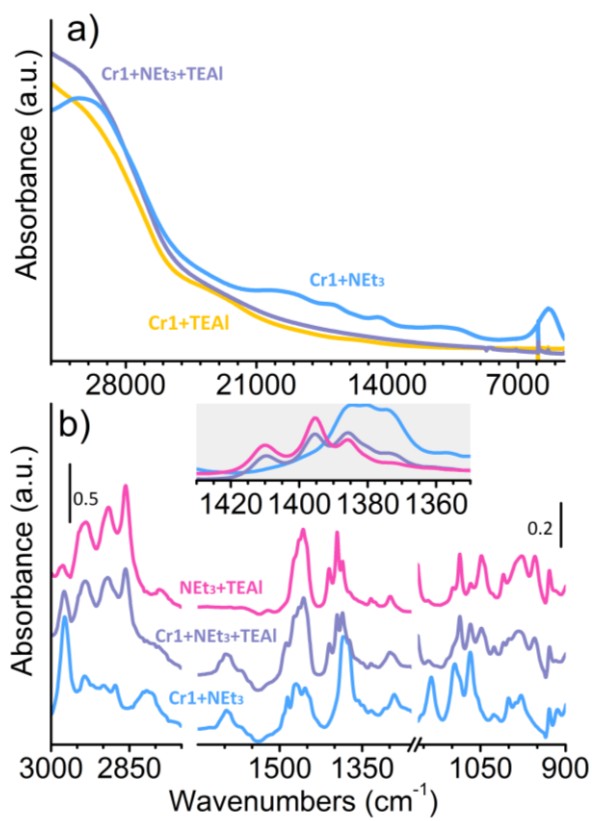


Figure 2.13. Part a): UV-Vis-NIR spectra of **Cr1**+NEt₃, **Cr1**+TEAl, and **Cr1**+NEt₃+TEAl (Cr = 10⁻³ M in CHCl₃, Al/Cr = 10, N/Cr = 20). Part b) FT-IR spectra of **Cr1**+NEt₃, NEt₃+TEAl and **Cr1**+NEt₃+TEAl (Cr = 10⁻³ mol L⁻¹ in CHCl₃, Al/Cr = 10, N/Cr = 20). The inset in part b) shows a magnification of the 1430–1360 cm⁻¹ region, which contains the absorption bands due to the $\delta(\text{CH}_2)$ and $\delta_{\text{sym}}(\text{CH}_3)$ vibrational modes.

Therefore, all together these data suggest that, among all the possible equilibria of NEt₃ in the reaction mixture (as described in the previous paragraph), the only one that is actually photographed by UV–Vis–NIR and FT-IR spectroscopy is that involving the Al–activator, and this is likely the reason behind the great influence of NEt₃ on the ethylene polymerization catalysis. In Figure 2.14 a sketched hypothetical active chromium site is depicted as emerging from the spectroscopic analysis.

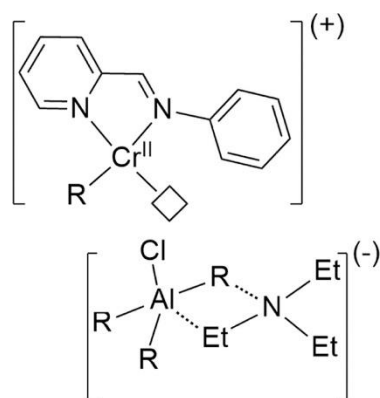


Figure 2.14. Active species resulting from the activation of **Cr1** by AlR_3 in the presence of NR_3 .

2.2.11 NEt_3 and its role behind the scenes

The spectroscopic data discussed so far suggest that the nature of the active chromium species does not change significantly in terms of the oxidation state and coordination environment whether it has been activated by TEAL or MAO (both alone, as reported in Ref 33, and in the presence of NEt_3 , as shown in Figure 2.7). Thus, the different catalytic behaviors of the two catalysts, namely **Cr1**/TEAL and **Cr1**/MAO (as discussed in the paragraph 2.2.3), can be ascribed to the different influences of the respective counterions on the olefin coordination/insertion path.³⁵⁻³⁷ Hence, MAO and TEAL behave in the same manner with respect to the presence or absence of NEt_3 , confirming the general relevance of the insights achieved on the **Cr1**/TEAL/ NEt_3 system.

Therefore, even if the structural complexity of MAO and its variable content of free- AlMe_3 prevent drawing of a univocal picture for the NEt_3 influence on the catalytic process (we cannot even incontrovertibly discriminate between NEt_3 interacting with either $[\text{AlOMe}]_n$, structural-TMA or free-TMA), contrarily to what has been obtained for the TEAL-activated **Cr1**+ NEt_3 catalyst, some hypotheses can be sketched and are presented hereafter.

The first possibility is that NEt_3 coordinates only with free- AlMe_3 : as reported above, aromatic amines can be used to trap it, analogously to what BHT does.^{49,53} This would explain the increase in the molecular weight of the resulting PE, since the chain-transfer to the Al-compound is one of the main chain-termination path (molecular weight decreased increasing the Al/Cr ratio).³³ An analogous increase in the molecular weight of PE by trapping the free-TMA with different molecules (namely, BHT and 9-BBN) is documented.^{21,22} Moreover, TMA can form heterodinuclear adducts with the metal complexes interposing in the ionic pair (as $\text{L}_n\text{Mt}(\text{Me})_2\text{Al}(\text{Me})_2^+ \cdots \text{ClMAO}^-$), a situation that is considered as dormant

species towards olefin polymerization and connected with several decomposition or chain-termination pathways.⁵⁴ In this regard, trapping the free-TMA would explain also the increase in overall catalytic activity.

The second possibility is that NEt_3 interacts with the other Al species of the cocatalyst, namely oligomeric MAO or the structural-TMA present, helping the stabilization of the negative charge by delocalization once the active species is formed. Whether NEt_3 interacts with structural-TMA or with MAO itself, the effect would be the same of increasing the steric hindrance of the anion and helping the charge dissipation in the ion pair. Both these modifications bring to the generation of weakly or less coordinating anions, which allow for an easier “approach” of the incoming monomer to the active site, facilitating its polymerization.^{36,37} The importance of having a large anion (and hence a looser ion pair) for **Cr1** to be active in the polymerization of ethylene has been already proved by the fact that all the other Al-alkyl, that generate a tighter ion pair, are ineffective and stop the catalysis (Table 2.1).

At this point is hard to state which one of the two hypotheses takes place, and it might also be that both situations are equally possible.

In any case, regardless of its precise mechanism of action, this simple and cheap additive, NEt_3 , allows the synthesis of a higher value-added product. UHMWPE is an engineering and smart polymer: it has high wear-resistance, toughness, durability, and biocompatibility that make it useful in many fields such as chemical, machinery, joint replacement, and other fields.

2.3 Cr(III) Complexes Bearing a β -Ketoimine Ligand for Cyclic Olefins Polymerization

2.3.1 Materials and Methods

Catalysts and polymers were synthesized and supplied by Dr. Giuseppe Leone (CNR-ISMAL Milan) within a collaborative project “Chromium catalysis: from fundamental understanding to functional aliphatic polymers (Cr4FUN)” (PRIN -MIUR DD 3402 del 21/12/2018). The details about synthesis of complexes and polymers are discussed in a Ref 55.

Molecular weight (M_w) and molecular weight distribution (M_w/M_n) were obtained by a high-temperature Waters GPCV2000 size exclusion chromatography (SEC) system using an online refractometer detector. The experimental conditions consisted of three PL Gel Olexis columns, o-dichlorobenzene as the mobile phase, 0.8 mL min^{-1} flow rate, and $145 \text{ }^\circ\text{C}$ temperature. The calibration of the SEC system was constructed using 18 narrow M_w/M_n PS standards with M_w

values ranging from 162 to $5.6 \times 10^6 \text{ g mol}^{-1}$. For SEC analysis, about 12 mg of the polymer was dissolved in 5 mL of *o*-dichlorobenzene. The calorimetric measurements were performed with a Mettler-DSC822 operating in N_2 atmosphere. The sample, typically 5 mg, was placed in a sealed aluminum pan, and the measurement was carried out from 0 to 350 °C using a heating and cooling rate of $20 \text{ }^\circ\text{C min}^{-1}$ for cyclic olefin polymers and from -70 to 160°C at $10 \text{ }^\circ\text{C/min}$ for polyethylene samples.

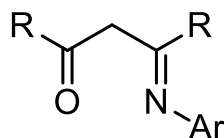
Thermogravimetric analysis (TGA) was carried using a Perkin-Elmer (Waltham, MA, USA) TA4000 instrument at a heating rate of $10 \text{ }^\circ\text{C min}^{-1}$ under a flowing N_2 atmosphere in the temperature range 30–900 °C.

The X-ray powder diffraction profiles of the as-prepared samples were obtained with Ni filtered $\text{Cu K}\alpha$ radiation (wavelength $\lambda=0.15418 \text{ nm}$) by using an Empyrean diffractometer by Panalytical operating in the reflection geometry.

2.3.2 General Introduction

As already described in the section 2.2.2, bidentate complexes bearing β -ketoimines, β -diketones and β -diketimines¹⁸ ligands have gained profound interest from a broad perspective of coordination chemistry by virtue of their tunable electronic and steric features. They have been extensively used in coordination chemistry as supporting ligands⁵⁶ and are especially prominent in catalysis for olefin polymerization.⁵⁷⁻⁶⁰

β -ketoimines (Figure 2.15) are formed by the condensation of primary amines with β -diketones or β -ketoaldehydes. They have been less investigated with respect to their isoelectronic analogues β -diketones and β -diketimines. Beyond being largely exploited for the preparation of organic light-emitting diodes (OLEDs),⁶¹ there are some examples of metal complexes with β -enaminoketonato chelate ligands employed as single component initiators for the ring-opening polymerization of cyclic esters,⁶² or as pre-catalysts for the polymerization of (cyclic) olefins.⁶³



β -ketoimine

R = H, alkyl or aryl group
Ar = variously substituted aryl

Figure 2.15. β -ketoimine ligand.

Some papers appeared in the recent literature reporting on the synthesis of chromium complexes with similar ligands,^{56,60,64,65} the interest in these bidentate chromium complexes developed since they can be considered homogeneous models of the heterogeneous Phillips catalyst, and hence they help to improve the understanding of the underlying organometallic chemistry. However, Cr-complexes bearing β -ketoimine ligands have never been reported before, in contrast to the huge amount of literature present for other related chromium complexes, as comprehensively reviewed by Sun et al.⁶⁶ and references therein.

In this regard, in this section will be show the synthesis and catalytic testing of two Cr(III) complexes with a β -ketoimine ligand, obtained from two different synthetic routes: coordination and covalent bonding of the ligand with the metal. The complexes were evaluated as catalysts for the polymerization of ethylene, and some cyclic olefins (namely, norbornene (NB), dicyclopentadiene (DCPD), 5-ethylidene-2-norbornene (ENB), 3,5-norbornadiene (NBD)).

2.3.3 Synthesis of the complexes

The ketoimine ligand **L** was synthesized in good yield by condensing the 2,4-pentanedione with the aniline, according to a published procedure.⁶⁷ Successively, the ligand **L** was reacted employing two different procedures with a chromium(III) salt in dry THF at room temperature to give the desired complexes **1** and **2** (Figure 2.16): for complex **1**, the ligand **L** was directly reacted with $\text{CrCl}_3(\text{THF})_3$, while in the case of complex **2**, the β -ketoimine **L** was previously deprotonated with an equimolar amount of $n\text{BuLi}$, giving the β -ketoiminato ligand $\text{L}^- \text{Li}^+$, and then reacted with $\text{CrCl}_3(\text{THF})_3$. In the latter case, the Cr-cation is expected to be covalently bonded to the deprotonated ligand L^- . The detailed synthesis procedure is reported in Ref 55.

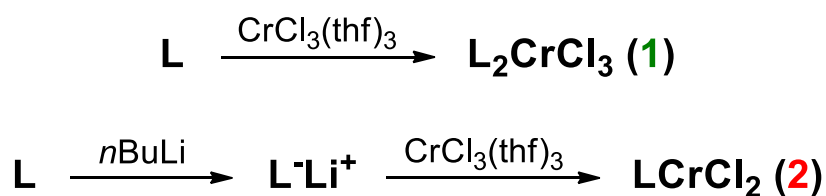


Figure 2.16. Schematic representation of the two synthetic routes.

As reported in detail in Ref 55, ATR-IR spectroscopy and elemental analysis measurements, performed by the research group of Dr. Giuseppe Leone (CNR-ISMAL Milan) and Prof. Elena Groppo (University of Turin) proved that the molecular structure of the two Cr-based

ketoiminato complexes is that shown in Figure 2.17 with the Cr(III) ion coordinatively bonded to L in **1** and covalently bonded to L in **2**.

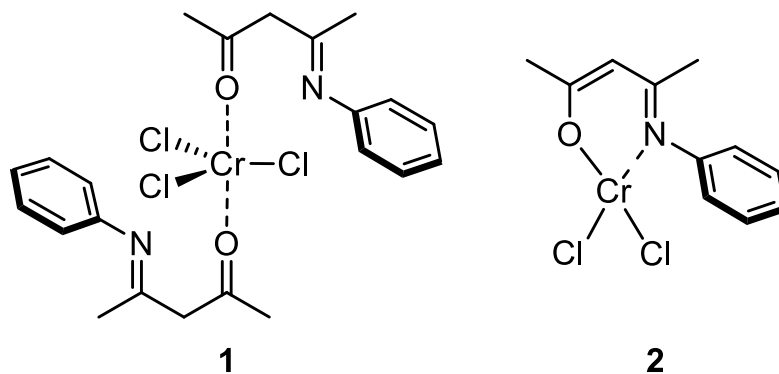


Figure 2.17. Schematic representation of the molecular structure of the two Cr-based ketoiminato complexes, as determined in Ref 55 by ATR-IR spectroscopy coupled with elemental analysis. Full lines indicate covalent bonds, while dashed and dotted bonds indicate ionic interactions of decreasing strength.

2.3.4 Polymerization Tests

-Ethylene

The catalytic utility of **1** and **2** was first investigated in the polymerization of ethylene. Both the complexes were used as precatalyst in combination with different aluminum alkyls (*i.e.*, Et_2AlCl , Et_3Al , MAO, and AlMe_3 -depleted MAO (dMAO)) as co-catalysts (Table 2.4). Both the chromium complexes were weakly active for ethylene polymerization. Only traces of solid polyethylene (PE) were recovered, despite wide variations in the polymerization conditions, *i.e.*, temperature, solvent, and amount of the Al-activator. Despite the low activities, the molecular weight of the PEs produced by precatalyst **1** in combination with Et_2AlCl and MAO are quite high, with relatively broad molecular weight distribution ($6.0 < M_w/M_n < 9.5$). The DSC curves of some PE samples reported in Table 2.4, recorded during first heating from -70°C to 180°C , successive cooling from the melt to -70°C , and second heating of the melt crystallized samples up to 180°C , all recorded at $10^\circ\text{C}/\text{min}$, are reported in Figure 2.18A-C. The melting and crystallization temperatures are in the range $132\text{--}137.5^\circ\text{C}$ and $113.3\text{--}116.7^\circ\text{C}$, respectively. The X-ray diffraction profiles of some as-prepared PE samples show two peaks at 2θ values of 21° and 24° , corresponding to the orthorhombic form of crystalline PE (Figure 2.19). All these data are in agreement with highly linear and high-molecular weight polymers.

Table 2.4. Polymerization of ethylene promoted by **1–2** precatalysts.^a

entry	complex	co-cat	Al/Cr	<i>T</i> (°C)	time (min)	Yield (mg)	act ^b	<i>T</i> _m ^{IIc} (°C)	<i>T</i> _c ^c (°C)	<i>M</i> _w ^d (g mol ⁻¹)	<i>M</i> _n ^d (g mol ⁻¹)	<i>M</i> _w / <i>M</i> _n ^d
9	1	MAO	250	20	24	42	11	134.9	113.3	519500	66000	7.9
10	1	Et ₃ Al	250	20	8	0	0					
11	1	Et ₂ AlCl	250	20	12	52	26	135.7	115.8	769900	126000	6.1
12	1	dMAO ^e	250	20	11	91	50	136.2	116.7			
13	1	Et ₂ AlCl	50	20	10	87	52	137.5	114.6			
14	1	dMAO ^e	50	20	11	0	0					
15 [#]	1	Et ₂ AlCl	50	20	10	32	19	132.2	115.7	1138600	120300	9.5
16	1	Et ₂ AlCl	50	50	7	8	7					
17	2	MAO	250		5	27	32					
18	2	Et ₂ AlCl	250		5	3	4					

^aPolymerization conditions: ethylene pressure, 1.01 bar; total volume, 25 mL (toluene); Cr complex, 10 μmol, complex solution in dry toluene; ^b activity in kg_{pol} mol_{Cr}⁻¹ h⁻¹; ^c determined by DSC; ^d determined by SEC; ^e dMAO was prepared removing toluene and free AlMe₃ from commercially available MAO. [#] reaction performed in dry dichloromethane.

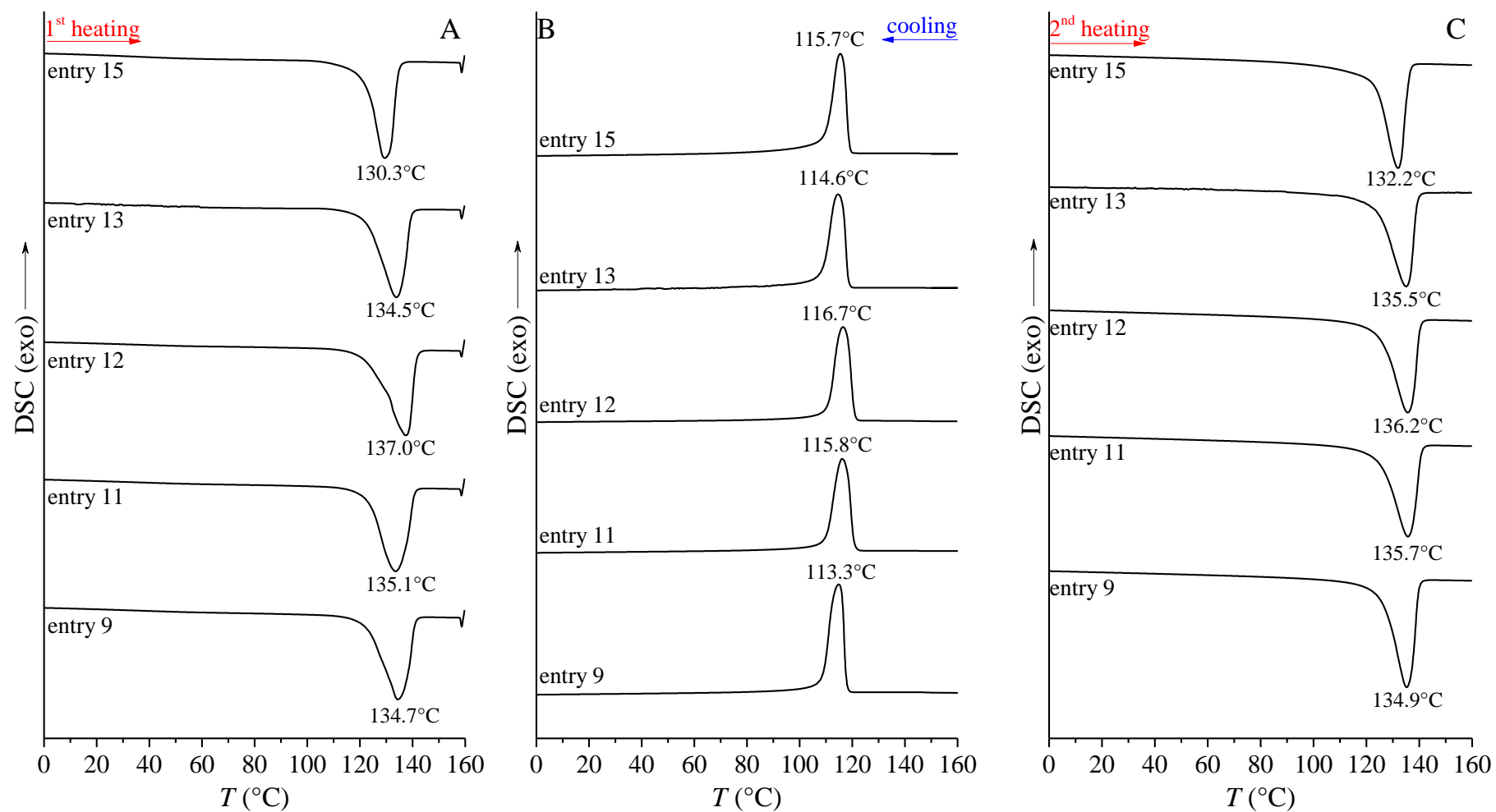


Figure 2.18. DSC thermograms of some PE samples reported in Table 2.4 recorded at 10 °C/min during heating of as-polymerized samples (A), cooling from the melt (B) and successive heating (C).

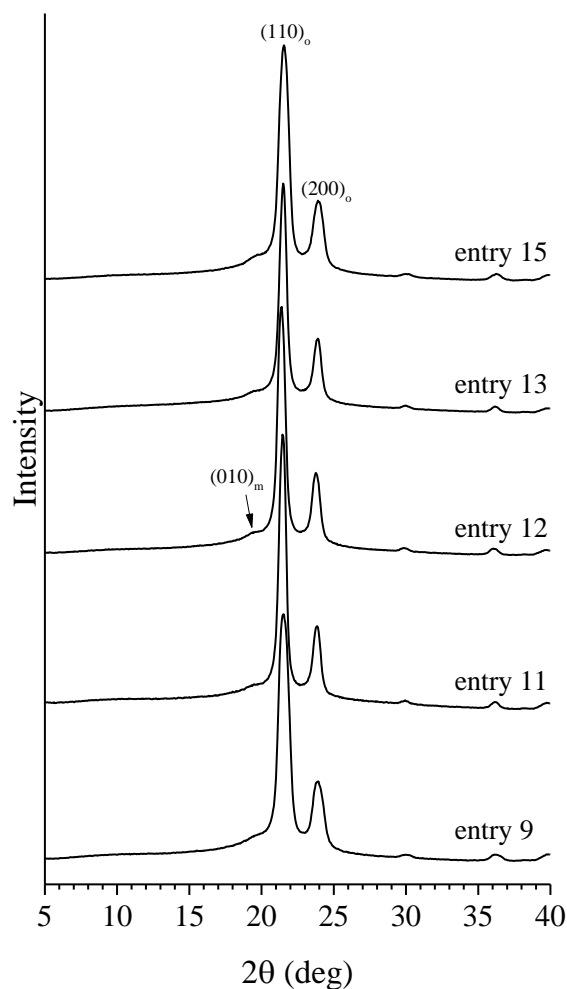


Figure 2.19. WAXS profiles of some as-polymerized PE samples reported in Table 2.4.

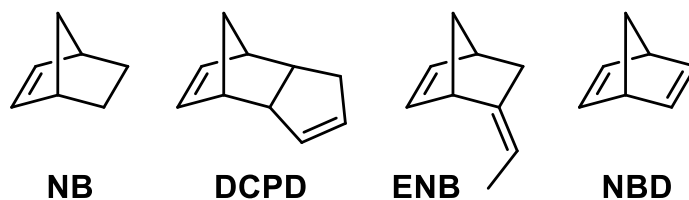
-Cyclic Olefins

The same complexes **1** and **2** were also tested as precatalysts in the polymerization of NB and other derivatives, namely, DCPD, ENB, and NBD (Figure 2.20). Cyclic olefin polymers have high thermal resistance and chemical stability, becoming attractive candidates for a wide variety of applications such as gas-separation and proton-conducting membranes, microelectronics, photoresists, dielectric materials, and pervaporation applications.^{68,69} Polymerization conditions and results are summarized in Table 2.5.

Table 2.5. Polymerization of NB, DCPD, ENB, NBD promoted by **1–2** precatalysts.^a

entry	monomer	complex	T (°C)	Yield (g)	Yield (%)	M_w^b (g mol ⁻¹)	M_n^b (g mol ⁻¹)	M_w/M_n^b
1	NB	1	20	1.05	78	1790	1055	1.7
2	NB	2	20	1.00	74	1740	1210	1.4
3	NB	1	0	1.20	89	1990	1080	1.8
4	NB	2	0	1.20	89	2330	1385	1.7
5	DCPD	1	20	0.32	13	1140	880	1.3
6	DCPD	2	20	0.30	13	1140	855	1.3
7	ENB	1	20	1.98	92	2320	1420	1.6
8	NBD	1	20	1.21	73		insoluble	

^aPolymerization conditions: [monomer] = 1 mol L⁻¹ (that is, NB, 1.35 g, DCPD, 2.36 g, ENB, 2.16 g, NBD, 1.66 g); total volume, 18 mL (toluene); t = 24 h; Cr, 10 μmol; MAO as cocatalyst, Al/Cr = 1000. ^b M_w , M_n , and M_w/M_n by SEC.

**Figure 2.20.** Cyclic olefins employed as monomers in this study.

When activated with MAO, both the complexes are active in the polymerization of NB, affording solid polymers (Table 2.5, entry 1 and 2). The conversion of NB was in the range 74–78% at room temperature, while reaching 89% for the same experiment at 0 °C (Table 2.5, entry 3 and 4). Surprisingly enough, the monomer conversion in the polymerizations performed with **1**/MAO and **2**/MAO are comparable. The molecular weights of the polymers obtained are all in the range from 1050 to 1400 g mol⁻¹ (M_n in Table 2.5), meaning that the resultant materials are oligomers constituted by a few repeating units (7–15 units), with narrow molecular weight distribution ($1.4 < M_w/M_n < 1.8$).

When DCPD, the bicyclic analogue of NB, was polymerized, a steep reduction in the monomer conversion, as low as 13% for both complexes, was recorded (Table 2.5, entry 5 and 6). The large steric hindrance of DCPD may account for the low insertion-coordination rate of DCPD, and hence for the low productivities. The molecular weight is rather low: the DCPD oligomers are made up of a few (less than 10) repeating units. Similar results were obtained in the polymerization of DCPD catalyzed by Cr-iminopyridine complexes.

Conversely, the polymerization of ENB brings an increase of monomer conversion up to 92% (Table 2.5, entry 7), even higher than that of NB. In this case, the presence of the second double

bond, *i.e.*, the ethylidene moiety on the C5 of NB ring, may have a beneficial effect, probably binding the active species and making it more reactive and prone toward polymerization. Finally, concerning the polymerization of the non-conjugated NBD, a different situation occurred: the reaction was extremely rapid and exothermic, and the viscosity of the reaction medium increased so rapidly that the polymerization was stopped within 10 min, with monomer diffusion issues limiting the conversion to 73% (Table 2.5, entry 8). Note that the resultant powder sample was insoluble, even at high temperatures, thus making it impossible to determine the molecular weight.

2.3.5 Cyclic Olefin Oligomers Characterization

The cyclic olefin oligomers obtained were characterized with the aid of different techniques to get information on their structure, that is monomer enchainment, and therefore on the possible different polymerization mechanisms involved. In fact, cyclic olefins can be polymerized by three different catalytic routes (Figure 2.21): (i) ring-opening metathesis polymerization (ROMP), which gives polymers containing double bonds within the main chain, (ii) vinyl addition polymerization, which gives completely saturated polymer, and (iii) cationic polymerization, which gives low-molecular weight products containing rearranged monomer units.⁶⁸

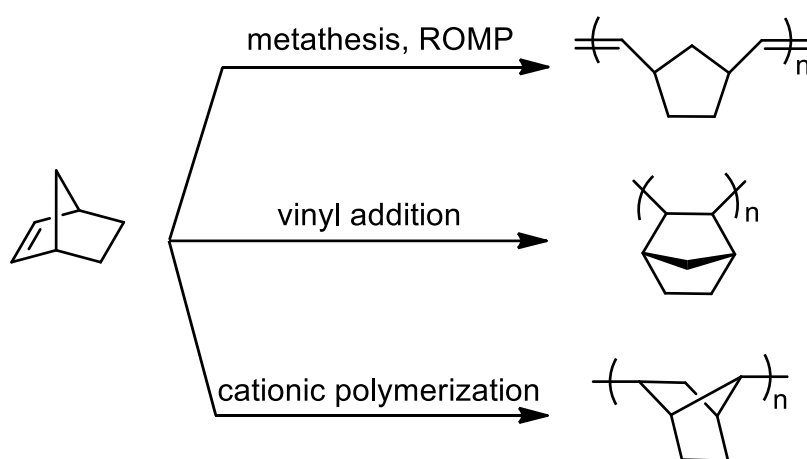


Figure 2.21. Schematic representation of the types of NB polymerization.

The IR characterization of the polymers showed that the polymerization of NB, DCPD, and ENB mediated by the catalytic system **1–2**/MAO occurs through a vinyl-type addition rather than via ROMP.

The IR spectra of the sample 4 reported in Table 2.5, show characteristic absorption bands at 2942, 2865, 1451, 1294, 1110, and 891 cm^{-1} (Figure 2.22). The selective occurrence of addition polymerization via opening of only the endocyclic double bond is well demonstrated by the absence of any band at 1680–1620 cm^{-1} , characteristic of the unsaturated NB ring.⁷⁰

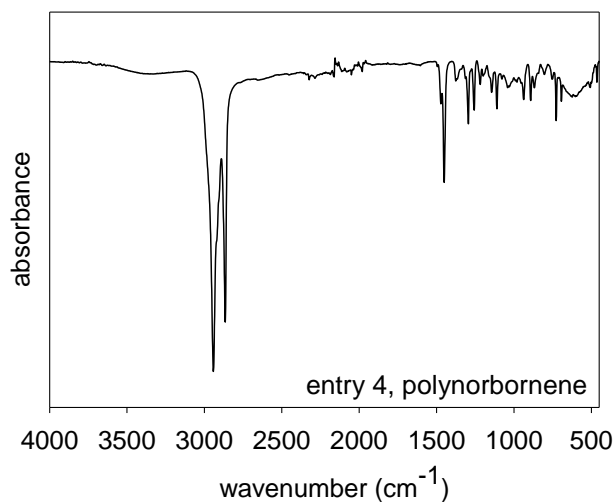


Figure 2.22. FTIR of polynorbornene (Table 2.5, entry 4).

The IR spectra of both the DCPD and ENB oligomers (Figure 2.23) show the typical signals of the norbornenic ring, as observed in Figure 2.22 for the NB oligomer sample (2940, 2910, 2865, 1450, 1268, 1100 cm^{-1}), and in addition the signals of the double bonds, that is the =C–H stretching at 3040 cm^{-1} and the C=C stretching at 1650–1680 cm^{-1} . The presence of bands at 3040 (=C–H stretching vibration) and 1613 cm^{-1} (C=C stretching vibration) and the absence of any band at about 1580 cm^{-1} indicate that all the bicycloheptene double bonds were consumed during the oligomerization.⁷¹ The remaining unsaturations are entirely due to the cyclopentene double bond or to the ethylidene moiety, which are not involved in the polymerization.³³

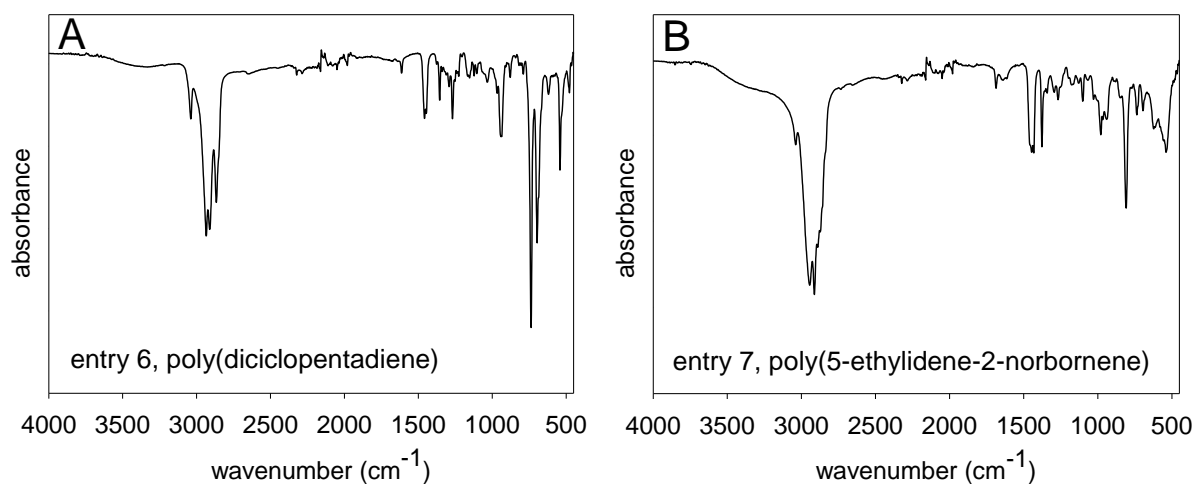


Figure 2.23. FTIR of poly(dicyclopentadiene) (A) and poly(5-ethylidene-2-norbornene) (B) (Table 2.5, entries 6 and 7, respectively).

The X-ray powder diffraction profiles of synthesized NB oligomer samples reported in Table 2.5 (entries 1-4) are shown in Figure 2.24A. The diffraction profiles of Figure 2.24A, indicate that these samples are semi-crystalline and highly stereoregular. All diffraction patterns are characterized by two broad reflections centered at $2\theta \approx 11.5$ and 18.5° , according with the results obtained for the 2,3-*exo*-diheterotactic polymer reported in a previous work by using different Cr(II) complexes, and a further diffraction peak at $2\theta \approx 10^\circ$, not observed in the case of 2,3-*exo*-diheterotactic structure.^{33,70} In order to verify the origin of the high intensity diffraction peak at $2\theta \approx 10^\circ$ observed in the diffraction profiles of Figure 2.24A, fractionation experiments with different solvents (acetone, diethyl ether, heptane at boiling point) were performed on sample 2 (profile b of Figure 2.24A) in order to isolate and characterize the resulting fractions presenting different molecular weight and/or tacticity. The X-ray powder diffraction profiles of all the isolated fractions are reported in Figure 2.24B. In particular, the fractions extracted with the lower boiling solvents (acetone, diethyl ether) are essentially amorphous, in fact the X-ray profiles (profiles a,b of Figure 2.24B) show two broad haloes centered at $2\theta \approx 11$ and 18.6° , whereas the heptane insoluble fraction shows considerable crystallinity (profile d of Figure 2.24B). In particular, the diffraction profile of this fraction is characterized by the presence of two new peaks at 2θ values of 11.2 e 11.9° and a broader reflection at $2\theta \approx 18.6^\circ$, already present in the unfractionated sample. A similar result is also obtained in the case of the heptane soluble fraction (profile c of Figure 2.24) but it is worth noting that both these two crystalline fractions do not present the diffraction peak observed at $2\theta \approx 10^\circ$ in the as-prepared sample that is probably due to traces of impurities and/or very low molecular weight molecules that are removed upon fractionation.

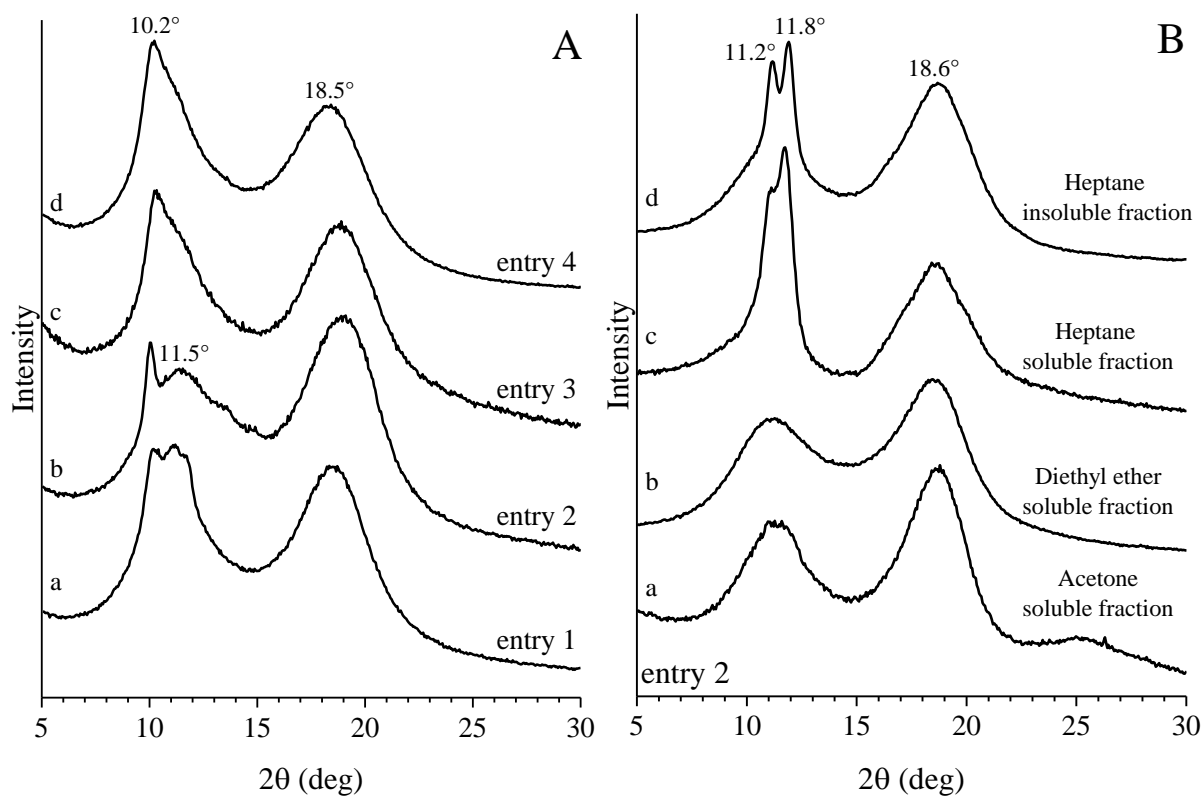


Figure 2.24. X-ray powder diffraction profiles of the as-prepared NB oligomer samples reported in Table 2.5 (A) and of different fractions of the sample 2 extracted with various boiling solvents (B).

Since poly(cyclicolefin)s generally show outstanding thermal resistance, the thermal stability of all NB oligomer samples was investigated with TGA experiments (Figure 2.25). The data of Figure 2.25 show that in addition to the main degradation phenomenon (observed at $T \approx 450^\circ\text{C}$), there is a further thermal phenomenon at lower temperatures (in the range $100\text{-}200^\circ\text{C}$), which is compatible with the removal of low molecular weight molecules.

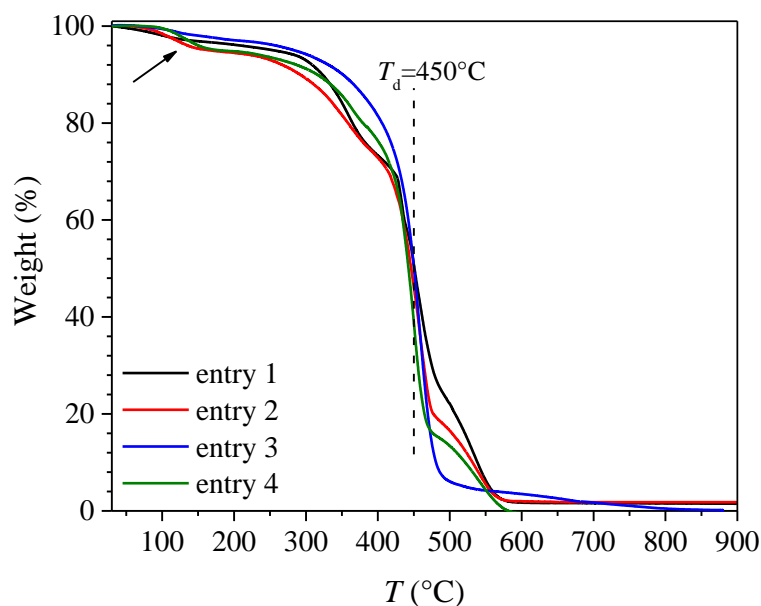


Figure 2.25. TGA curves of the as-prepared NB oligomer samples reported in Table 2.5 acquired under a flowing N₂ atmosphere by heating the sample at 10 °C min⁻¹.

Based on these observations, X-ray diffraction profiles were recorded on all NB oligomer samples treated at 200°C for 5 minutes and then cooled down to 25°C (Figure 2.26). The diffraction peak visible at $2\theta \approx 10^\circ$ in the as-prepared sample 2 and also on the other three samples, is not observed in the X-ray profiles of annealed samples reported in Figure 2.25 demonstrating that the crystalline phase associated with reflection at 10° of 2θ is lost during the thermal treatment. Moreover, the diffraction profile of the heat-treated sample 2 (profile b of Figure 2.25) and that of the high crystalline fractions (heptane soluble and heptane residue), are very similar and to the best of our knowledge they do not correspond to any diffraction patterns reported in literature for crystalline polynorbornenes.

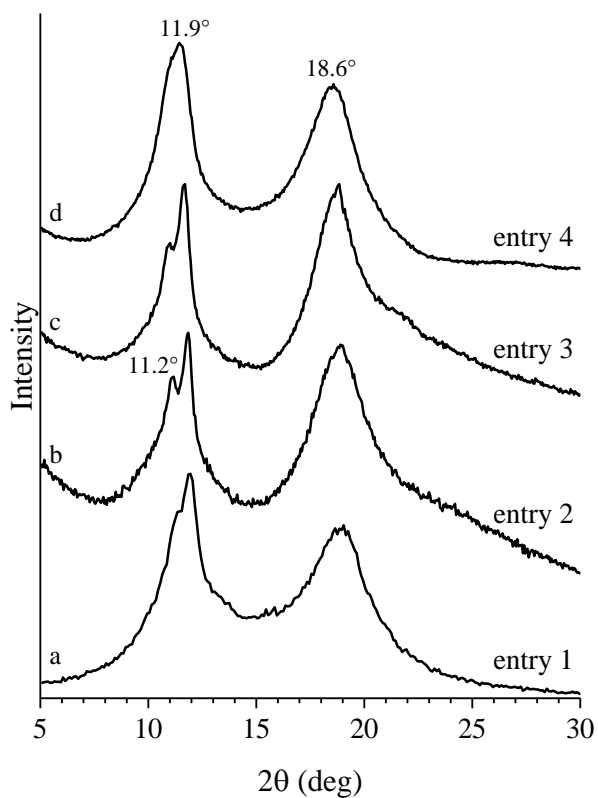


Figure 2.26. X-ray powder diffraction profiles of the NB oligomer samples reported in Table 2.5 annealed at 200°C for 5 minutes and then cooled down to 25°C .

The DSC curves recorded at scanning rates of $20^\circ\text{C min}^{-1}$ during heating of the as-prepared NB oligomer samples (entries 1-4 of Table 2.5) from 0°C up to 350°C are shown in Figure 2.27. From the heating curves of Figure 2.27, it is possible to appreciate an inflection point due probably to the glass transition in the range $220 - 250^\circ\text{C}$, followed in some cases by a broad endothermic signal at $\approx 300^\circ\text{C}$ due to the possible overlap of melting with the onset of degradation.

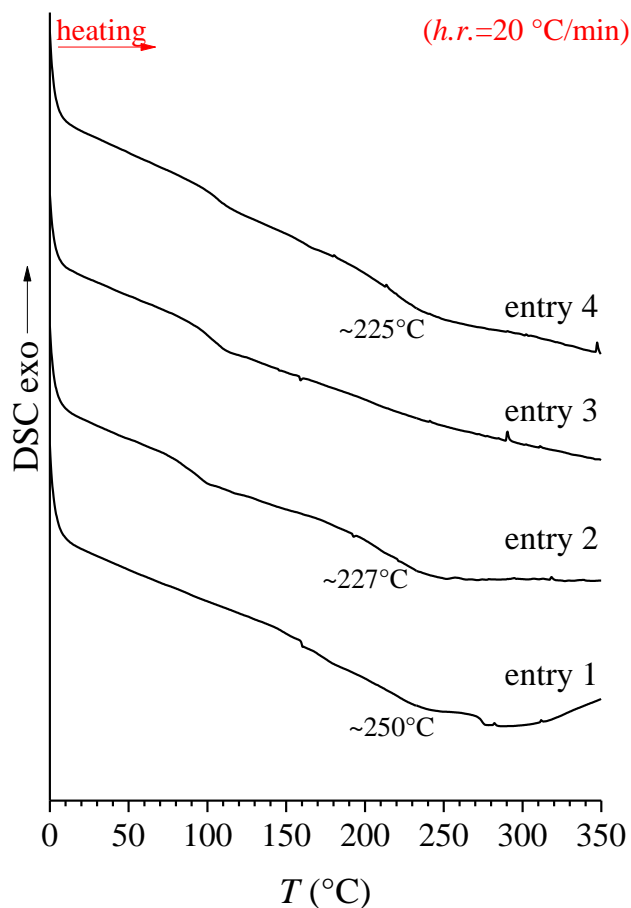


Figure 2.27. DSC heating curves recorded at 20 °C min^{-1} heating rates for the as-prepared NB oligomer samples reported in Table 2.5.

The X-ray powder diffraction profile of the as-prepared sample 6 (DCPD oligomer) is reported in Figure 2.28. The polymer is crystalline and, in particular, the diffraction profile is superimposable to that of the previously reported semicrystalline DCPD oligomers.⁷² With regard to the chain stereochemistry of the DCPD oligomers obtained, it was possible to speculate that they have the same 2,3-exo-diheterotactic stereoregularity found in the case of the polyDCPD and polyNB obtained with a chromium iminopyridine catalyst.³³

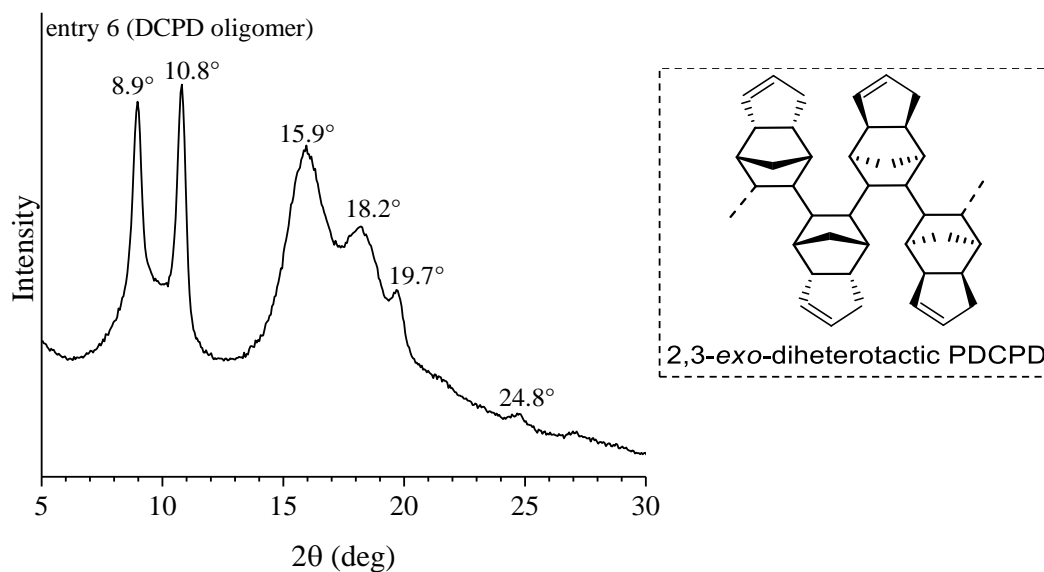


Figure 2.28. X-ray powder diffraction profile of entry 6 (DCPD oligomer) reported in Table 2.5.

By contrast, the situation is different for the poly(NBD) sample (Table 2.5, entry 8). The IR spectrum and X-ray diffraction profile recorded on the as-prepared sample 8 are shown in Figures 2.29A and 2.29B, respectively. The IR spectrum (Figure 2.29A) clearly shows the presence of a sharp and very strong band at 802 cm^{-1} , attributable to the C–H stretching of a cyclopropylic ring (*i.e.*, 2,6-disubstituted nortricyclene structure),⁷³ and the concomitant absence of a band at about 1580 cm^{-1} , characteristic of the double bond of the norbornenic ring. On the other side, the X-ray powder diffraction profile of the sample (Figure 2.29B) proves that it is crystalline, as indicated by the presence of Bragg diffraction peaks at 2θ values of 13.7, 16, and 20.4° .

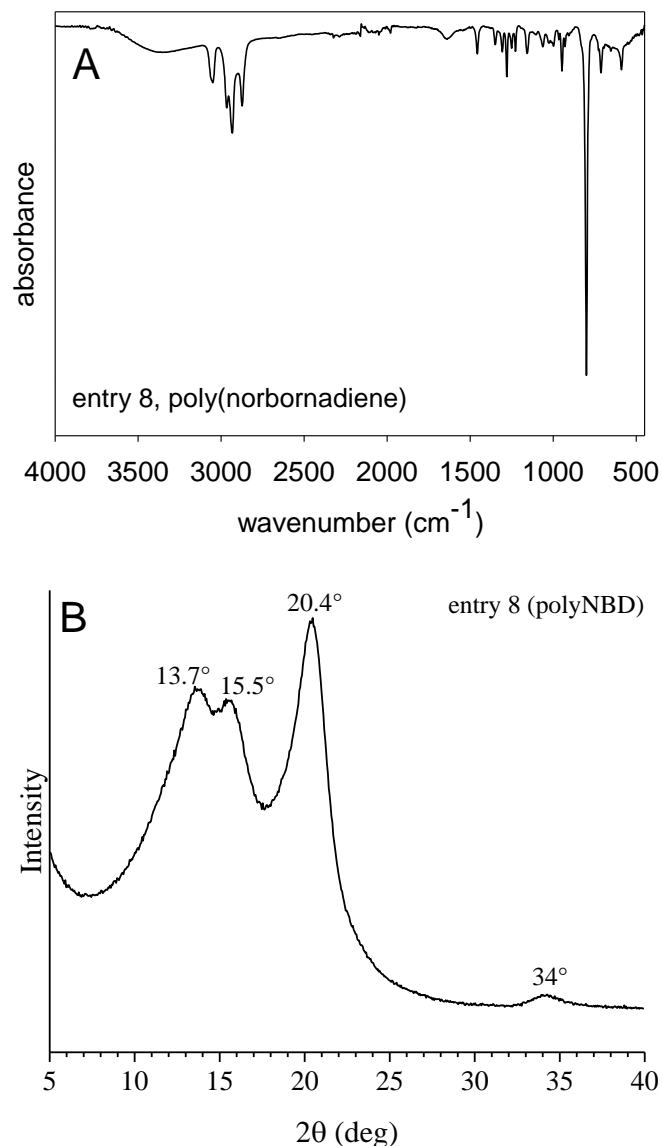


Figure 2.28. FTIR (A) and X-ray powder diffraction profile (B) of entry 8 (poly(NBD)) reported in Table 2.5.

Both analyses demonstrate that the polymer is characterized by an unusual structure with rigid nortricyclene repeating units and a unique 3,5-enchainment (Figure 2.29). In fact, these results are in clear analogy with those reported in the literature regarding the polymerisation of NBD catalysed by the $\text{TiCl}_4/\text{Et}_2\text{AlCl}$ system,⁷⁴ which leads to the formation of a PolyNBD characterised by the structure shown in Figure 2.29. Considering this result, it is likely that the polymer is obtained through a transannular cationic polymerization of NBD involving both double bonds (Figure 2.29), rather than through vinyl-type addition previously observed with NB and its other derivatives.

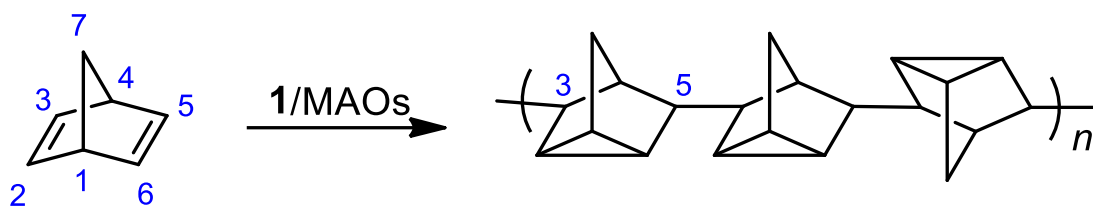


Figure 2.29. Probable structure of polyNBD sample 8 characterized by a rigid nortricyclene repeating units and a unique 3,5-enchainment.

TGA experiments were performed also for samples corresponding to entry 6 (DCPD oligomer) and 8 (polyNBD), indicating that these samples present a thermal stability ($T_{95\text{wt}\%}$) ranging from 330 to 350 °C (Figure 2.30).

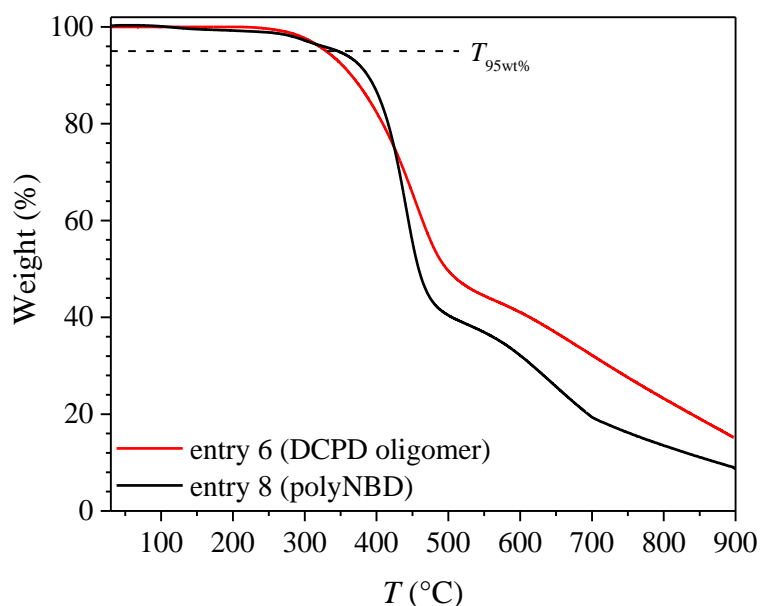


Figure 2.30. TGA curves of the as-prepared sample 6 (DCPD oligomer) and sample 8 (polyNBD) reported in Table 2.5 acquired under a flowing N_2 atmosphere by heating the sample at 10 °C min^{-1} .

In Figure 2.27 are shown the DSC heating curves recorded at scanning rates of 20 °C min^{-1} of the as-prepared samples 6 and 8. As with the polynorbornene samples previously shown (Figure 2.27), it is also possible to observe an inflection point due probably to the glass transition at around 240 °C and 175 °C for the DCPD oligomer and polyNBD samples, respectively.

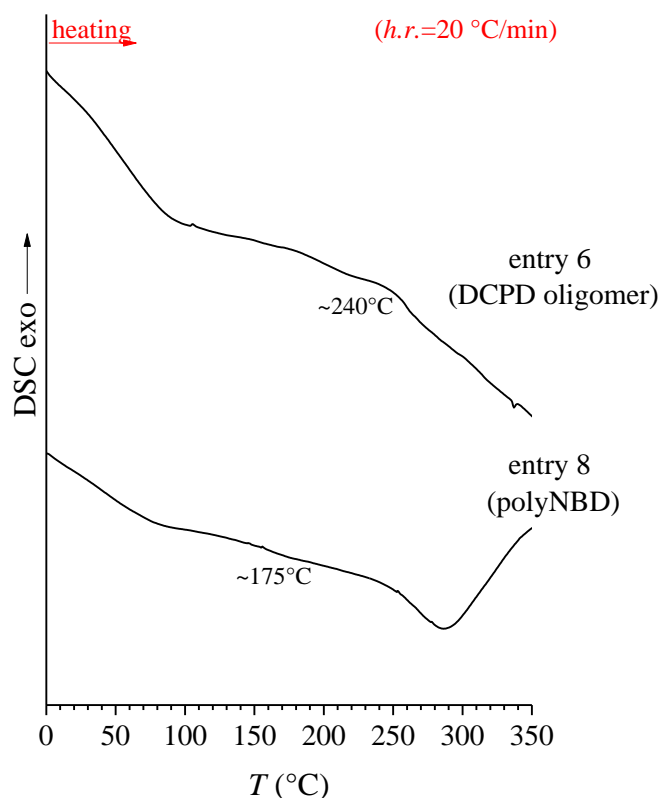


Figure 2.31. DSC heating curves recorded at 20 °C min^{-1} heating rates for the as-prepared sample 6 (DCPD oligomer) and sample 8 (polyNBD) reported in Table 2.5.

Summing up the results obtained for the polymerization of cyclic olefins, the catalytic system **1–2/MAO** is able to promote the vinyl-addition polymerization of NB and derivatives, bringing to considerable levels of monomer conversion, but being influenced by the steric hindrance of the monomer, as in the case of DCPD. The nature of the metal-ligand bond did not influence the results of the polymerization. In this series, NBD represents an exception, since the polymerization followed a different mechanistic pathway, resulting in the synthesis of a poly(NBD) having repeating 3,5-enchained nortricyclene units.

2.4 Copolymerization of cyclohexene oxide (CHO) and phthalic anhydride (PA)

2.4.1 Materials and Methods

Polyesters were synthesized and supplied by Dr. Giuseppe Leone (CNR-ISMAL Milan) within a collaborative project “Chromium catalysis: from fundamental understanding to functional aliphatic polymers (Cr4FUN)” (PRIN -MIUR DD 3402 del 21/12/2018).

Molecular weight (M_w) and molecular weight distribution (M_w/M_n) were obtained by a high-temperature Waters GPCV2000 size exclusion chromatography (SEC) system using an online

refractometer detector. The experimental conditions consisted of three PL Gel Olexis columns, o-dichlorobenzene as the mobile phase, 0.8 mL min⁻¹ flow rate, and 145 °C temperature. The calibration of the SEC system was constructed using 18 narrow M_w/M_n PS standards with M_w values ranging from 162 to 5.6×10^6 g mol⁻¹. For SEC analysis, about 12 mg of the polymer was dissolved in 5 mL of o-dichlorobenzene.

Thermogravimetric analysis (TGA) was carried using a Perkin-Elmer (Waltham, MA, USA) TA4000 instrument at a heating rate of 10 °C min⁻¹ under a flowing N₂ atmosphere in the temperature range 30–900 °C.

The calorimetric measurements were performed with a Mettler-DSC822 operating in N₂ atmosphere. The sample, typically 5 mg, was placed in a sealed aluminum pan, and the measurement was carried from -40 to 200°C at 10 °C/min.

The X-ray powder diffraction profiles of the as-prepared samples were obtained with Ni filtered Cu K α radiation (wavelength $\lambda=0.15418$ nm) by using an Empyrean diffractometer by Panalytical operating in the reflection geometry.

2.4.2 General Introduction

Because of their possible use in the synthesis of aliphatic polyesters and polycarbonates, chromium complexes have garnered increased interest in recent years.⁷⁵ Because of their many renewable sources, ease of hydrolytic decomposition into largely benign chemicals, and excellent biocompatibility, these groups of polymers have attracted attention as attractive, potentially sustainable alternatives to petroleum-based polymers.⁷⁶ In this regard, the growing environmental concern about the detrimental effects of non-degradable polyolefins is acting as a strong motivator to find biodegradable polymers with equivalent physical qualities, which is advancing research on these topics.

Ring-opening polymerization (ROP) of lactones and lactides is the most common controlled polymerization method for the synthesis of aliphatic polyesters (PEs) and generally yields polymers with relatively low glass transition temperatures.⁷⁷⁻⁸⁰ The alternating ring-opening copolymerization (ROCOP) of cyclic anhydrides and epoxides is emerging as a promising technique for the production of PEs.⁸¹⁻⁸³

With the respect to the ring-opening polymerization (ROP) of lactones, it represents an alternate chain-growth route to polyesters. It also presents a chance to increase the variety of materials generated and get around some of ROP's drawbacks. In particular, by varying the

epoxide or cyclic anhydride, the properties of the resulting materials, particularly the thermal properties (glass transition temperature (T_g)), can be controlled.⁸³

Numerous organometallic catalysts based on different metals such as Mg,⁸⁴ Al,⁸² Cr,^{80,83} Mn,⁸⁵ Fe,⁸² Zn,⁸³ and heterodinuclear polymerization complexes,⁸⁶ have been developed recently for the epoxide/anhydride copolymerization. Many of these catalysts showed noticeably higher activity when a nucleophilic co-catalyst was added.⁸⁷

In the present context, within this section is reported the synthesis and the characterization of poly(anhydride-*alt*-epoxide) samples obtained from ROCOP by using a novel chromium complex.

2.4.3 Polymerization

Cyclohexene oxide (CHO) and phthalic anhydride (PA) alternating copolymers have been synthesized using a novel chromium complex (**Cr-OH**) as reported in Figure 2.32. These two monomers were selected since they are the ones most commonly used as models for testing the catalytic activity of new complexes.⁸⁰

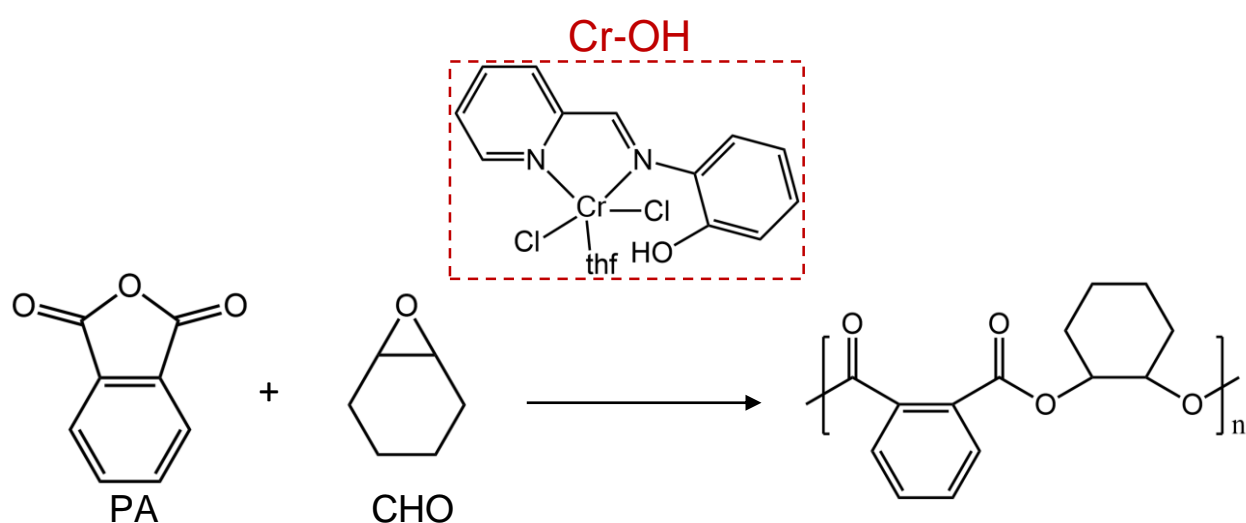


Figure 2.32. Copolymerization of cyclohexene oxide (CHO) with phthalic anhydride (PA) catalyzed by **Cr-OH**.

Details of polymerization conditions and all synthesized samples are summarized in Table 2.6. The copolymerization behavior of the used chromium complex was investigated for different polymerization conditions.

In particular, the copolymerization behavior of **Cr-OH** was studied by varying different reaction conditions:

- the used co-catalyst (entries 1 and 2). The two co-catalysts tested in combination with **Cr-OH** are shown in Figure 2.33. Both bis(triphenylphosphoranylidene)ammonium chloride (PPNCl) and 4-(dimethylamino)pyridine (DMAP);
- the ratio between epoxide and anhydride (CHO:PA) (entry 3);
- the ratio between catalyst and co-catalyst (Cr:PPNCl) (entries 4 and 5);
- the reaction time (entries 6, 7 and 8).

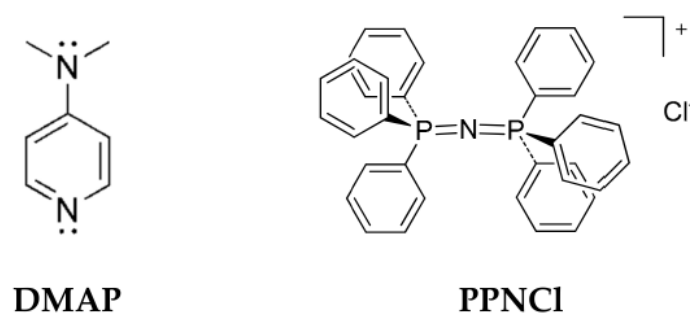


Figure 2.33. Structures of co-catalysts utilized in combination with **Cr-OH** for the copolymerization reactions.

Table 2.6. Polymerization of CHO and PA promoted by **Cr-OH** precatalysts.^a

entry	co-cat	cat:co-cat:CHO:PA	<i>T</i> (°C)	time (h)	Yield (g)	conversion (%)	<i>M_w</i> ^b (g mol ⁻¹)	<i>M_n</i> ^b (g mol ⁻¹)	<i>M_w</i> / <i>M_n</i> ^b
1	DMAP	1:1:250:250	100	5	0.853	84	12830	9520	1.3
2	PPNCl	1:1:250:250	100	5	0.504	80	16600	8880	1.9
3	PPNCl	1:1:500:250	100	5	0.540	64	9700	7750	1.2
4	PPNCl	1:5:250:250	100	5	0.363	86	8000	5600	1.4
5	PPNCl	1:10:250:250	100	5	0.273	84	4600	3510	1.3
6	PPNCl	1:1:250:250	100	1	0.123	25	5750	3800	1.5
7	PPNCl	1:1:250:250	100	3	0.300	68	10300	6550	1.6
8	PPNCl	1:1:250:250	100	24	0.510	89	11810	7590	1.6

^aPolymerization conditions: total volume, 1 mL (toluene); pre-contact step between catalyst and co-catalyst, 1 min. ^b*M_w*, *M_n*, and *M_w*/*M_n* by SEC.

From the data reported in Table 2.6 it is evident that the conversion obtained in the various cases is comparable, regardless of the reaction conditions used.

The measured average molecular weights *M_w* are similar to each other and range from 4600 to 16600 g/mol, in line with the data found in the literature regarding this type of copolymer.⁸⁰

2.4.4 Structural and Thermal Characterization

The X-ray powder diffraction profiles of the as-prepared samples of the eight polyesters samples are reported in Figure 2.34. All as-prepared samples are amorphous, in fact the X-ray diffraction profiles only show two broad haloes centered at $2\theta \approx 10.5$ and 18° .

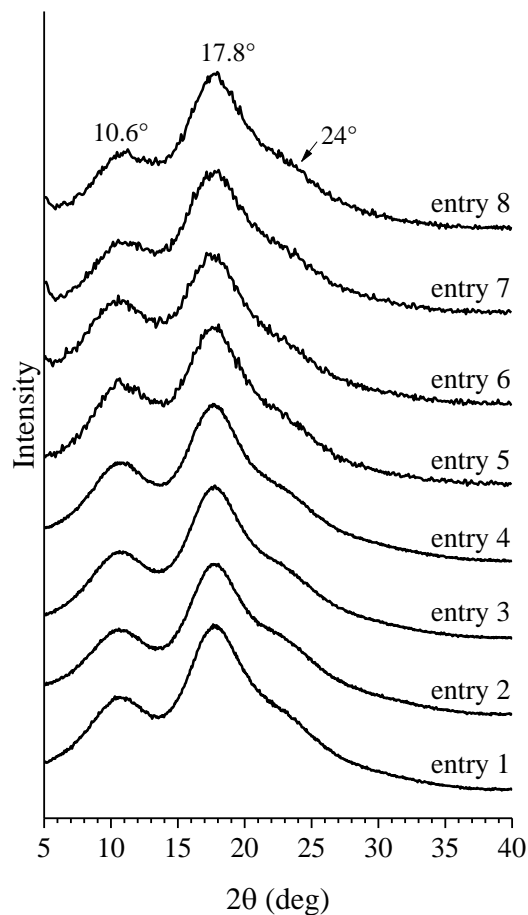


Figure 2.34. WAXS profiles of as-polymerized polyester samples reported in Table 2.6.

Thermogravimetric analysis of all polyester samples, performed under a N₂ atmosphere, is reported in Figure 2.35. All polymers show a 5% weight loss at comparable temperatures ($T_{95wt\%}$), in the range 290 – 310 °C. At approximately $T_d \approx 340$ °C, rapid thermal degradation proceeds, and at 900 °C, nearly 2-5% of the materials is left (Figure 2.35).

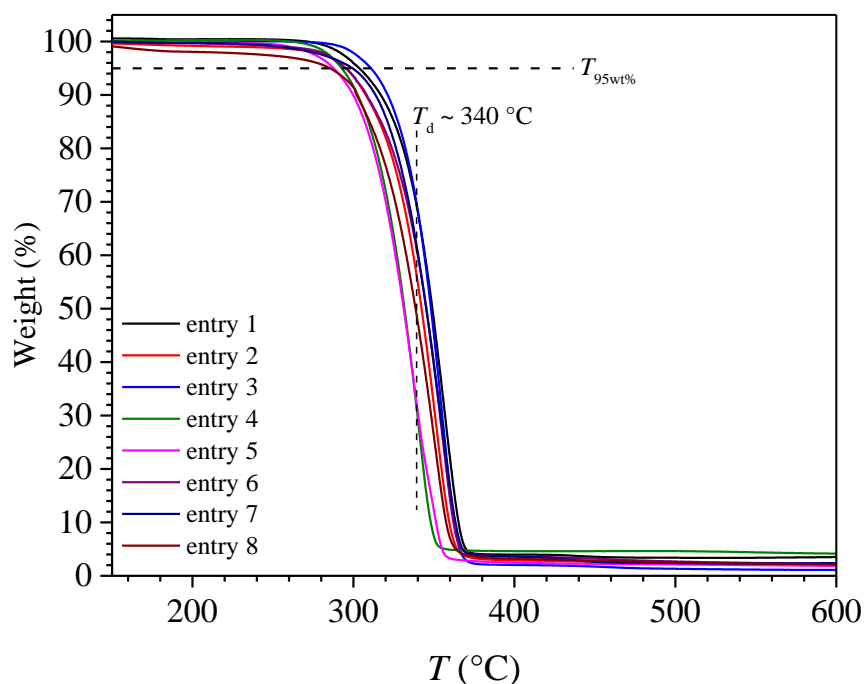


Figure 2.35. TGA curves of as-polymerized polyester samples reported in Table 2.6 acquired under a flowing N₂ atmosphere by heating the sample at 10 °C min⁻¹

The DSC curves of samples reported in Table 2.6, recorded during first heating from -40°C to 200°C, successive cooling from the melt to -40°C, and second heating of the melt crystallized samples up to 200°C, all recorded at 10 °C/min, are reported in Figure 2.36A-C. The data reported in Figure 2.6 clearly indicate that of polyesters show similar thermal properties despite they were polymerized using different reaction conditions. In particular, all DSC thermograms are characterized by the absence of endothermic and exothermic phenomena and by only the event corresponding to the glass transition (T_g) associated by an apparent hysteresis phenomenon in the first heating curves (Figure 2.36A). DSC results are in agreement with the amorphous nature of these materials already highlighted at WAXS (Figure 2.34). The values of glass transition temperatures evaluated from the second heating curves of Figure 2.36C are reported in Table 2.7 and in Figure 2.37 as a function of the average molecular weight (M_w). As expected, glass transition temperatures increase as molecular weight increases, reaching a plateau from M_w values of around 13000 g/mol. Anyway, all samples exhibit high T_g values, ranging from 120 to 135°C (Figures 2.36C and 2.37).

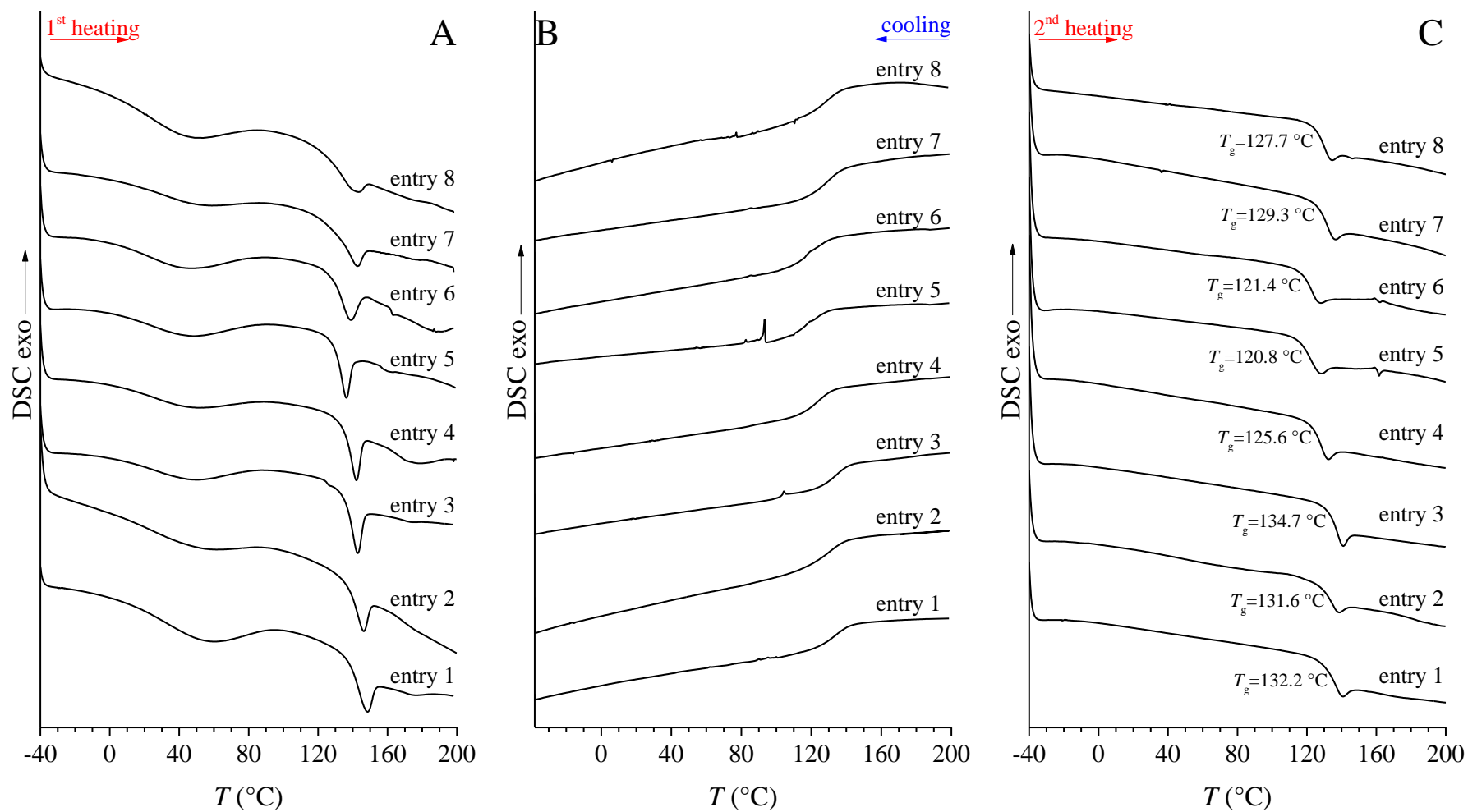


Figure 2.36. DSC curves recorded during heating of the as-prepared sample (A), cooling (B) and successive second heating (C) at scanning rate of 10 °C/min, of polyester samples reported in Table 2.6.

Table 2.7. Values of the glass transition temperature of samples of polyesters reported in Table 2.6.

entry	M_w (g/mol)	T_g (°C) ^a
1	12830	132.2
2	16600	131.6
3	9700	134.7
4	8000	125.6
5	4600	120.8
6	5750	121.4
7	10300	129.3
8	11810	127.7

^aevaluated from second heating curves of Figure 2.36C.

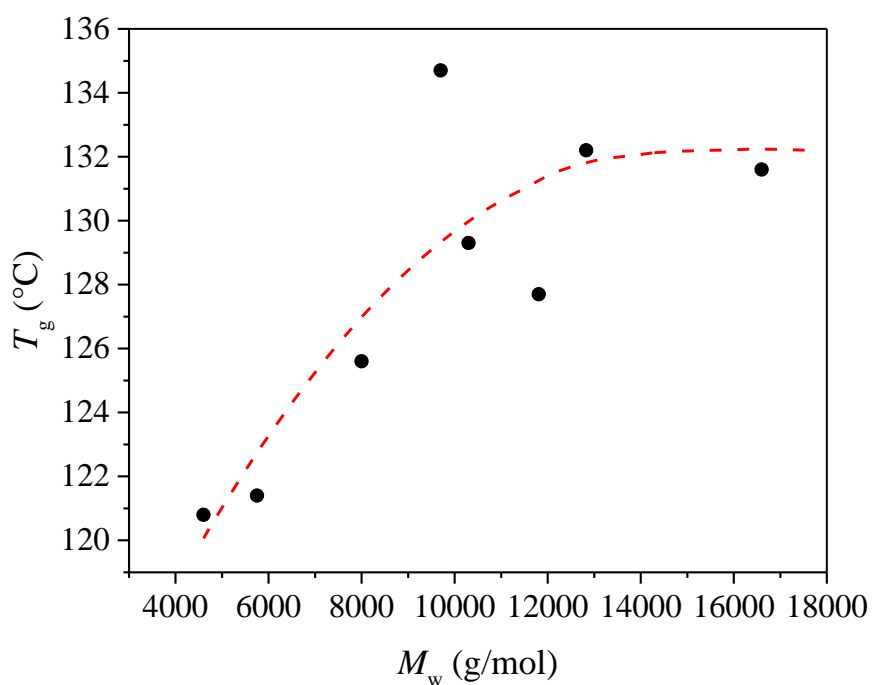


Figure 2.37. Glass transition temperatures values of samples reported in Table 2.6, evaluated from the DSC second heating curves of Figure 2.36C, as a function of the average molecular weights M_w .

2.4.5 Conclusions Chapter 2

In this chapter a study on a chromium-iminopyridine complex used as precatalyst, in combination with different aluminum cocatalysts and NEt_3 as additive, for the polymerization of ethylene have been accomplished. The study has shown that the Cr-complex is active in polymerization only in the presence of MAO as cocatalyst, and that adding NEt_3 in different amounts is possible to obtain polyethylene samples with tunable molecular weights ranging from high to ultrahigh and relatively narrow molecular weight distributions, even at high temperatures. This is quite rare for molecular Cr-complexes since they typically promote only ethylene oligomerization. A systematic FT-IR and UV-vis-NIR spectroscopy analysis was performed to determine the specific mechanism of action of the NEt_3 additive. Spectroscopic findings showed that the amine and the Al activator interact, leading to the creation of a looser ion pair that is advantageous for promoting the synthesis of UHMWPE.

In the same chapter is also reported an investigation on the polymerization of ethylene, and some cyclic olefins (norbornene (NB), dicyclopentadiene (DCPD), 5-ethylidene-2-norbornene (ENB) and 3,5-norbornadiene (NBD)) catalyzed by two β -ketoimine Cr(III) complexes. The results revealed that both complexes show low activity in ethylene polymerization. In contrast, with the exception of bulky DCPD, high productivities were achieved during the polymerization of the other cyclic olefins.

In particular, for NB and DCPD, vinyl-enriched, stereoregular, and semicrystalline oligomers were produced, whereas NBD polymerization produced a polymer with a characteristic repeating 3,5-enriched nortricyclene units.

Finally, the last part of the Chapter was focused on the synthesis and the characterization of cyclohexene oxide (CHO) - phthalic anhydride (PA) alternating copolymers obtained from ROCOP by using a novel chromium complex. Characterization of the resulting polymers showed that polyesters with molecular weights comparable to those obtained with similar catalytic systems reported in the literature were obtained. All synthesized polyesters are amorphous and are characterized by glass transition temperature values (T_g) that depend on molecular weight. In particular, T_g increases with increasing molecular weight from 120 to 135 °C for lower ($M_w \approx 4000$ g/mol) and higher ($M_w \approx 17000$ g/mol) molecular weight samples, respectively.

References

- 1) M.P. McDaniel *Adv. Catal.* **2010**, *53*, 123-606.
- 2) E. Groppo, C. Lamberti, S. Bordiga, G. Spoto, A. Zecchina *Chem. Rev.* **2005**, *105*, 115-183.
- 3) E. Groppo, K. Seenivasan, C. Barzan *Catal. Sci. Technol.* **2013**, *3*, 858-878.
- 4) J.P. Hogan, R.L. Banks U.S. Patent 2, 825, 721, **1958**.
- 5) C. Barzan, A. Piovano, L. Braglia, G.A. Martino, C. Lamberti, S. Bordiga, E. Groppo *J. Am. Chem. Soc.* **2017**, *139*, 17064–17073.
- 6) A. Fong, C. Vandervelden, S.L. Scott, B. Peters *ACS Catal.* **2018**, *8*, 1728-1733.
- 7) C. Brown, A. Lita, Y. Tao, N. Peek, M. Crosswhite, M. Mileham, J. Krzystek, R. Achey, R. Fu, J.K. Bindra, M. Polinski, Y. Wang, L.J. Van De Burgt, D. Jeffcoat, S. Profeta, A.E. Stiegman, S.L. Scott *ACS Catal.* **2017**, *7*, 7442-7455.
- 8) A. Fong, B. Peters, S.L. Scott, *ACS Catal.* **2016**, *6*, 6073-6085.
- 9) A. Fong, Y. Yuan, S.L. Ivry, S.L. Scott, B. Peters, *ACS Catal.* **2015**, *5*, 3360-3374
- 10) A. K. Tomov, J. D. Nobbs, J. J. Chirinos, P. K. Saini, R. Malinowski, S. K. Y. Ho, C. T. Young, D. S. McGuinness, A. J. P. White, M. R. J. Elsegood, G. J. P. Britovsek *Organometallics* **2017**, *36*, 510–522.
- 11) N. Peulecke, B. H. Müller, A. Spannenberg, M. Höhne, U. Rosenthal, A. Wöhl, W. Müller, A. Alqahtani, M. Al Hazmi *Dalton Trans.* **2016**, *45*, 8869–8874.
- 12) O. L. Sydora, T. C. Jones, B. L. Small, A. J. Nett, A. Fischer, M. J. S. Carney *ACS Catal.* **2012**, *2*, 2452–2455.
- 13) D. S. McGuinness *Chem. Rev.* **2011**, *111*, 2321–2341.
- 14) T. Agapie, J.A. Labinger, J. Bercaw *J. Am. Chem. Soc.* **2007**, *129*, 14281-14295.
- 15) V.C. Gibson, S.K. Spitzmesser *Chem. Rev.* **2003**, *103*, 283-315.
- 16) G. Zanchin, A. Piovano, A. Amodio, F. De Stefano, R. Di Girolamo, E. Groppo, G. Leone *Macromolecules* **2021**, *54*, 1243-1253.
- 17) T. Agapie *Coord. Chem. Rev.* **2011**, *255*, 861–880.
- 18) Y. -B. Huang, G.-X Jin *Dalton Trans.* **2009**, *5*, 767–769.
- 19) T. Xu, Y. Mu, W. Gao, J. Ni, L. Ye, Y. Tao *J. Am. Chem. Soc.* **2007**, *129*, 2236–2237.
- 20) V. C. Gibson, S. Mastroianni, C. Newton, C. Redshaw, G. A. Solan, A. J. P. White, D. J. Williams *Dalton Trans.* **2000**, *3*, 1969–1971.
- 21) D. Romano, S. Ronca, S. Rastogi *Macromol. Rapid Commun.* **2015**, *36*, 327–331.
- 22) S. Mark, A. Kurek, R. Mülhaupt, R. Xu, G. Klatt, H. Köppel, M. Enders *Angew. Chem., Int. Ed.* **2010**, *49*, 8751–8754.

- 23) E. Despagnet-Ayoub, M. K. Takase, L. M. Henling, J. A. Labinger, J. E. Bercaw, *Organometallics* **2015**, *34*, 4707–4716.
- 24) P. G. Belelli, M. L. Ferreira, D. E. Damiani *Macromol. Chem. Phys.* **2000**, *201*, 1466–1475.
- 25) P. G. Belelli, M. L. Ferreira, D. E. Damiani *Macromol. Chem. Phys.* **2000**, *201*, 1466–1475.
- 26) H. Liu, F. Wang, L. Liu, B. Dong, H. X. Zhang, C. X. Bai, Y. M. Hu, X. Q. Zhang *Inorganica Chim. Acta* **2014**, *421*, 284–291.
- 27) R. Cariou, J. J. Chirinos, V. C. Gibson, G. Jacobsen, A. K. Tomov, G. J. P. Britovsek, A. J. P. White *Dalton Trans.* **2010**, *39*, 9039–9045.
- 28) J. R. V. Lang, C. E. Denner, H. G. Alt *J. Mol. Catal. A Chem.* **2010**, *322*, 45–49.
- 29) A. M. Messinis, W. R. H. Wright, M. J. Hanton, P. W. Dyer *Chem. Commun.* **2020**, *56*, 6886–6889.
- 30) G. Wang, M. Li, W. Pang, M. Chen, C. Tan *New J. Chem.* **2019**, *43*, 13630–13634.
- 31) S. V. Zubkevich, V. A. Tuskaev, S. C. Gagieva, A. A. Pavlov, V. N. Khrustalev, O. V. Polyakova, D. N. Zarubin, D. A. Kurmaev, N. A. Kolosov, B. M. Bulychev *New J. Chem.* **2020**, *44*, 981–993.
- 32) C. Tan, M. Qasim, W. Pang, C. Chen *Polym. Chem.* **2020**, *11*, 411–416.
- 33) G. Leone, E. Groppo, G. Zanchin, G. A. Martino, A. Piovano, F. Bertini, J. Martí-Rujas, E. Parisini, G. Ricci *Organometallics* **2018**, *37*, 4827–4840.
- 34) D. S. McGuinness *Chem. Rev.* **2011**, *111*, 2321–2341.
- 35) F. Zaccaria, L. Sian, C. Zuccaccia, A. Macchioni *Advances in Organometallic Chemistry* **2020**, *73*, 1-78.
- 36) J. L. Eilertsen, J. A. Støvneng, M. Ystenes, E. Rytter *Inorg. Chem.* **2005**, *44*, 4843–4851.
- 37) E. Y. X. Chen, T. J. Marks *Chem. Rev.* **2000**, *100*, 1391–1434.
- 38) K. Nomura, S. Zhang *Chem. Rev.* **2011**, *111*, 2342–2362.
- 39) H. Makio, A. V. Prasad, H. Terao, J. Saito, T. Fujita *Dalton Trans.* **2013**, *42*, 9112–9119.
- 40) S. Matsui, M. Mitani, J. Saito, Y. Tohi, H. Makio, N. Matsukawa, Y. Takagi, K. Tsuru, M. Nitabaru, T. Nakano, H. Tanaka, N. Kashiwa, T. Fujita *J. Am. Chem. Soc.* **2001**, *123*, 6847–6856.
- 41) I. Tritto, M. C. Sacchi, P. Locatelli, S. X. Li *Macromol. Symp.* **1995**, *89*, 289–298.
- 42) I. Tritto, M. C. Sacchi, S. X. Li *Macromol. Rapid Commun.* **1994**, *15*, 217–223.
- 43) W. Zhang, W.-H. Sun, S. Zhang, J. Hou, K. Wedeking, S. Schultz, R. Fröhlich, H. Song *Organometallics* **2006**, *25*, 1961–1969.
- 44) E. Groppo, C. Lamberti, S. Bordiga, G. Spoto, A. Zecchina *Chem. Rev.* **2005**, *105*, 115–183.

- 45) E. Groppo, K. Seenivasan, C. Barzan *Catal. Sci. Technol.* **2013**, *3*, 858.
- 46) E. Groppo, G. A. Martino, A. Piovano, C. Barzan *ACS Catal.* **2018**, *8*, 10846–10863.
- 47) J. C. W. Chien, D. He *J. Polym. Sci., Part A: Polym. Chem.* **1991**, *29*, 1595–1601.
- 48) S. Kvisle, E. Rytter *Spectrochim. Acta, Part A* **1984**, *40*, 939–951.
- 49) H. S. Zijlstra, A. Joshi, M. Linnolahti, S. Collins, J. S. McIndoe *Eur. J. Inorg. Chem.* **2019**, 2346–2355.
- 50) J. C. W. Chien, D. He *J. Polym. Sci., Part A: Polym. Chem.* **1991**, *29*, 1595–1601.
- 51) A. R. Barron *J. Chem. Soc. Dalton Trans.* **1988**, *12*, 3047–3050.
- 52) D. W. Imhoff, L. S. Simeral, S. A. Sangokoya, J. H. Peel *Organometallics* **1998**, *17*, 1941–1945.
- 53) V. Busico, R. Cipullo, F. Cutillo, N. Friederichs, S. Ronca *J. Am. Chem. Soc.* **2003**, *125*, 12402–12403.
- 54) C. Ehm, R. Cipullo, P. H. M. Budzelaar, V. Busico *Dalton Trans.* **2016**, *45*, 6847.
- 55) A. Amodio, G. Zanchin, F. De Stefano, A. Piovano, B. Palucci, V. Guiotto, R. Di Girolamo, G. Leone, E. Groppo *Catalysts* **2022**, *12*, 119.
- 56) L. Bourget-Merle, M. F. Lappert, J. R. Severn *Chem. Rev.* **2002**, *102*, 3031–3065.
- 57) B. M. Chamberlain, M. Cheng, D. R. Moore, T. M. Ovitt, E. B. Lobkovsky, G. W. Coates *J. Am. Chem. Soc.* **2001**, *123*, 3229–3238.
- 58) P. G. Hayes, W. E. Piers, R. McDonald *J. Am. Chem. Soc.* **2002**, *124*, 2132–2133.
- 59) W. K. Kim, M. J. Fevola, L. M. Liable-Sands, A. L. Rheingold, K. H. Theopold *Organometallics* **1998**, *17*, 4541–4543.
- 60) L. A. MacAdams, W. K. Kim, L. M. Liable-Sands, I. A. Guzei, A. L. Rheingold, K. H. Theopold *Organometallics* **2002**, *21*, 952–960.
- 61) S. Yoon, T. S. Teets *Chem. Commun.* **2021**, *57*, 1975–1988.
- 62) C. T. Altaf, H. Wang, M. Keram, Y. Yang, H. Ma *Polyhedron* **2014**, *81*, 11–20.
- 63) X. F. Li, K. Dai, W. P. Ye, L. Pan, Y. S. Li *Organometallics* **2004**, *23*, 1223–1230.
- 64) S. Latreche, F. Schaper *Organometallics* **2010**, *29*, 2180–2185.
- 65) V. C. Gibson, C. Newton, C. Redshaw, G. A. Solan, A. J. P. White, D. J. Williams *Eur. J. Inorg. Chem.* **2001**, *7*, 1895–1903.
- 66) C. Bariashir, C. Huang, G. A. Solan, W. H. Sun *Coord. Chem. Rev.* **2019**, *385*, 208–229.
- 67) F. A. Cotton, W. H. Ilsley, W. Kaim *Inorg. Chim. Acta* **1979**, *37*, 267–272.
- 68) M. V. Bermeshev, P. P. Chapala *Prog. Polym. Sci.* **2018**, *84*, 1–46.
- 69) G. Zanchin, G. Leone *Prog. Polym. Sci.* **2021**, *113*, 101342.

- 70) G. Ricci, A. Boglia, A. C. Boccia, L. Zetta, A. Famulari, S. V. Meille *Macromolecules* **2008**, *41*, 3109–3113.
- 71) G. Zanchin, G. Leone, I. Pierro, A. Rapallo, W. Porzio, F. Bertini, G. Ricci, G. *Macromol. Chem. Phys.* **2017**, *218*, 1600602.
- 72) A. Rapallo, W. Porzio, G. Zanchin, G. Ricci, G. Leone *Chem. Mater.* **2019**, *31*, 6650.
- 73) M. B. Roller, J. K. Gillham, J. P. Kennedy *J. Appl. Polym. Sci.* **1973**, *17*, 2223.
- 74) C. De Rosa, A. Malafrente, F. Auriemma, M. Scoti, R. Di Girolamo, M. C. D'Alterio, G. Ricci, G. Zanchin, G. Leone *Polym. Chem.* **2019**, *10*, 4593.
- 75) X. Zhang, M. Fevre, G.O. Jones, R.M. Waymouth *Chem. Rev.* **2018**, *118*, 839; (b) Y.W. Wang, D.J. Darensbourg *Coord. Chem. Rev.* **2018**, *372*, 85.
- 76) Y. Zhu, C. Romain, C.K. Williams *Nature* **2016**, *540*, 354.
- 77) N. Ajellal, J. F. Carpentier, C. Guillaume, S. M. Guillaume, M. Helou, V. Poirier, Y. Sarazin, A. Trifonov *Dalton Trans.* **2010**, *39*, 8363.
- 78) D. Mecerreyes, R. Jerome, P. Dubois *Advances in Polymer Science*; Springer: Berlin/Heidelberg, Germany, 1999; *147*, 1.
- 79) P. J. Dijkstra, H. Du, J. Feijen *Polym. Chem.* **2011**, *2*, 520.
- 80) a) M. Proverbio, N. Galotto Galotto, S. Losio, I. tritto, L. Boggioni *Polymers* **2019**, *11*, 1222. b) W. Bukowski, A. Bukowska, A. Sobota, M. Pytel, K. Bester **2021**, *13*, 1785.
- 81) J. M. Longo, M. J. Sanford, G. W. Coates *Chem. Rev.* **2016**, *116*, 15167.
- 82) M. J. Sanford, L. P. Carrodegua, N. J. Van Zee, A. W. Kleij, G. W. Coates *Macromolecules* **2016**, *49*, 6394–6400.
- 83) A. M. DiCiccio, G. W. Coates *J. Am. Chem. Soc.* **2011**, *133*, 10724.
- 84) P. K. Saini, C. Romain, Y. Zhu, C. K. Williams *Polym. Chem.* **2014**, *5*, 6068.
- 85) A. Paoniasari, R. Duchateau, E. H. Nejad, C. E. Koning *Polym. Chem.* **2012**, *3*, 1308.
- 86) J. A. Garden, P. K. Saini, C. K. Williams *J. Am. Chem. Soc.* **2015**, *137*, 15078.
- 87) B. Han, L. Zhang, B. Liu, X. Dong, I. Kim, Z. P. Duan, P. Theato *Macromolecules* **2015**, *48*, 3431.

Chapter 3

pag. 144 – pag. 320

under embargo

Chapter 4

Cobalt, Iron, Copper, Neodymium



One of the topics addressed in this PhD project concerned the study of stereoregular polydienes obtained by polymerizing the corresponding conjugated dienes (*i.e.*, isoprene and myrcene) with catalysts based on different transition metals such as Cobalt, Iron, Copper and Neodymium. The first catalysts for the stereospecific polymerization of conjugated dienes, *i.e.* the same catalytic system previously used for the polymerization of ethylene and propylene, were developed in 1954 by mixing TiCl_4 or TiCl_3 with aluminum-alkyls.¹⁻³ Since then, using a combination of transition metal or lanthanide compounds with the proper alkylating agents, many other catalysts have been synthesised and tested in polymerization.

From the 1980s, the discovery of the alkylating agent methylaluminoxane (MAO)^{4,5} led to the introduction of new catalytic systems, some of which were significantly more active and stereospecific than those based on common aluminum-alkyls.⁶⁻¹² For example, MAO allowed the use of transition metal cyclopentadienyl derivatives (*i.e.*, CpTiCl_3 , Cp_2TiCl_2 , and CpVCl_2) as catalytic precursors,¹³⁻¹⁸ which were practically inactive in combination with the normal aluminum alkyls. The use of these complexes, in combination with MAO, allowed the synthesis of new polymers¹⁹⁻²² from monomers whose polymerisation was not possible with classical Ziegler-Natta catalytic systems. More recently, new generations of catalysts based on complexes of transition metals and lanthanides with a precise structure have been developed, enabling the synthesis of stereoregular polydienes from various monomers of both fossil (*e.g.* isoprene, 1,3-pentadiene, 1,3-hexadiene, 3-methyl-1,3-pentadiene and others) and natural (*e.g.* myrcene, farnesene, ocimene) sources.²³⁻³¹

In the present Chapter is reported the synthesis and the study of the structure and of the thermal and mechanical properties of some stereoregular polydienes obtained by using different novel catalysts. The relationships between the properties and the molecular structures determined by the different used catalysts will be discussed.

The state of the art of complexes based on the same transition metals and lanthanides used to obtain the materials that will be presented in this Chapter is briefly described below.

4.1 Catalytic systems for the stereospecific polymerization of 1,3-dienes

4.1.1 Cobalt Catalysts

Cobalt based catalysts are likely the most versatile among the many transition metal-based catalytic systems for the polymerization of 1,3-dienes.^{1,32-42} By combining MAO with CoCl_2 complexes with phosphine ligands, novel catalytic systems have recently been obtained.⁴³⁻⁵¹ These new systems are very peculiar as they are able to produce poly(diene)s with a controlled microstructure (*cis*-1,4; 1,2; mixed *cis*-1,4/1,2 structure) by simply changing the type of ligand coordinated to the cobalt atom. For instance, the system $\text{CoCl}_2(\text{P}^t\text{Bu}_2\text{Me})_2$ -MAO produced highly syndiotactic *cis*-1,4 polymers from a variety of terminally substituted 1,3-dienes, including (*E*)-1,3-pentadiene, (*E*)-1,3-hexadiene, (*E*)-3-methyl-1,3-pentadiene, (*E*)-1,3-heptadiene, and (*E*)-1,3-octadiene (Figure 4.1). On the other hand, highly 1,2 iso- or syndiotactic polymers, depending on the monomer structure, were obtained with the system $\text{CoCl}_2(\text{P}^i\text{PrPh}_2)_2$ -MAO from the same monomers (Figure 4.2). The same catalytic system allowed the synthesis of a polyisoprene with a perfectly alternating *cis*-1,4-*alt*-3,4 structure, unusual in the field of stereospecific polymerization (Figure 4.2).

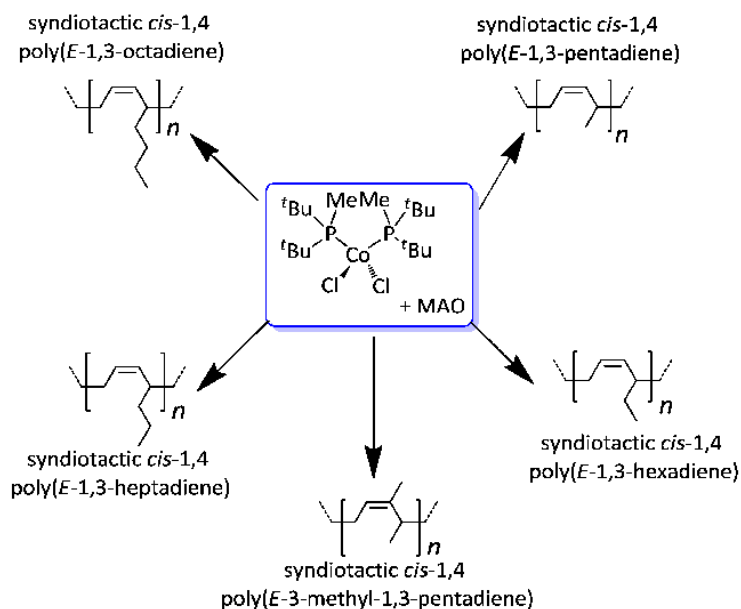


Figure 4.1. Example of syndiotactic *cis*-1,4 polymers obtained by system $\text{CoCl}_2(\text{P}^t\text{Bu}_2\text{Me})_2$ -MAO.

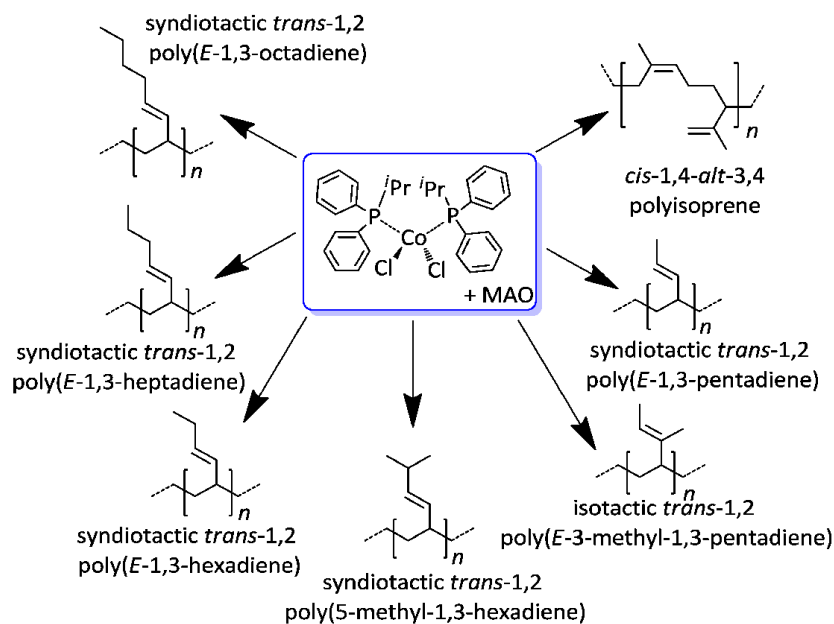


Figure 4.2. Example of 1,2 polymers, iso- or syndiotactic, obtained by system $\text{CoCl}_2(\text{P}^i\text{PrPh}_2)_2\text{-MAO}$.

4.1.2 Iron Catalysts

In recent years, interest in iron-based complexes has increased significantly due to the abundance, low toxicity and low environmental impact of this metal. In the field of stereoregular polydienes, a class of very active catalysts have been obtained by combining iron complexes with aromatic bidentate amines with aluminum-alkyls or MAO.⁴³⁻⁵⁵ By using these catalytic systems is possible to obtain highly stereoregular polymers, in some cases never described before (*e.g.*, syndiotactic 3,4-poly(isoprene), and syndiotactic (*E*)-1,2 poly(3-methyl-1,3-pentadiene))⁵⁶⁻⁵⁸ (Figure 4.3).

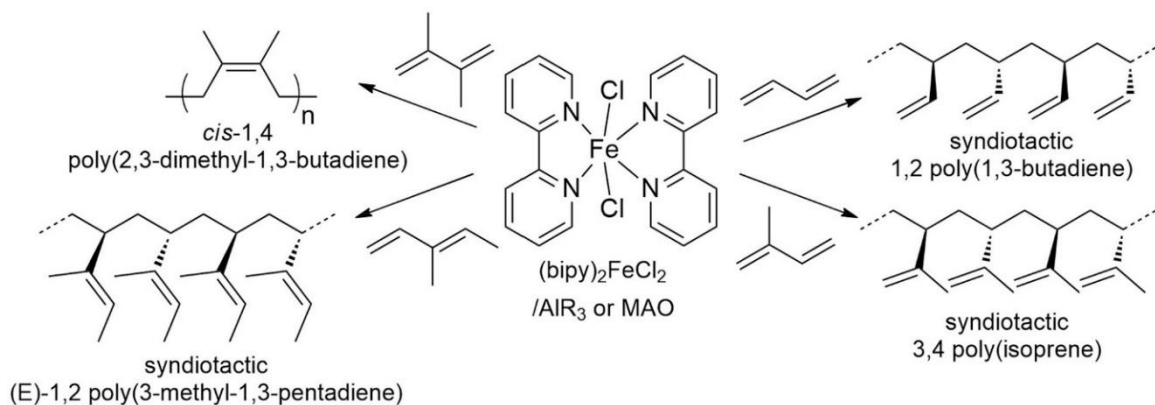


Figure 4.3. Highly Stereoregular Poly(1,3-diene)s from $(\text{bipy})_2\text{FeCl}_2$ (Bipy = Bipyridine).

Ritter et al.⁵⁹ introduced a new class of iron-based catalysts characterized by iminopyridine complexes. Using two different types of iminopyridine iron(II) complexes, in combination with the trialkylaluminum alkylating reagent and $[\text{Ph}_3\text{C}][\text{B}(\text{C}_6\text{F}_5)_4]$, for the polymerization of isoprene, the authors found that the imine moiety of the iminopyridine skeleton was able to tune the selectivity of the monomer insertion, providing *cis*-1,4 or *trans*-1,4 poly(isoprene)s (Figure 4.4).

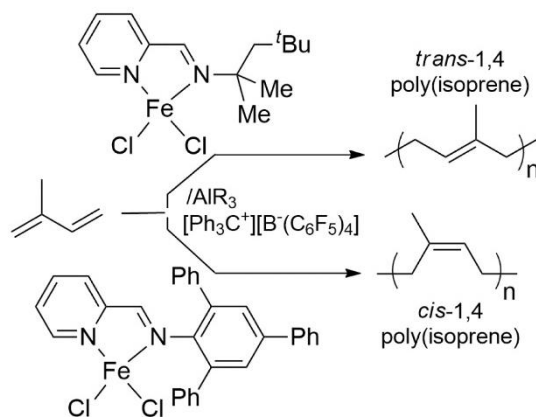


Figure 4.4. (Iminopyridine)FeCl₂-Based Catalysts for the Polymerization of Isoprene.

Further works on the polymerization of isoprene with catalysts based on substituted iminopyridine Fe(II) complexes were carried out by Chen and co-workers⁶⁰ and Visseaux and co-workers.^{61,62} Specifically, by using di- and trisubstituted aryliminopyridine Fe(II) complexes (Figure 4.5a), Chen et al. obtained high molecular weight poly(isoprene)s with a predominantly *cis*-1,4 structure (3,4 content up to 34%); by using disubstituted aryl iminopyridine iron(II) complexes (Figure 4.5b), Visseaux et al. obtained essentially 1,4 poly(isoprene)s (80–90%) having a predominantly *cis* or *trans* structure depending on the ligand nature, while mixed *cis*-1,4/3,4 poly(isoprene)s were obtained by using catalysts based on iminopyridine iron(II) complexes having fluorinated N-aryl substituents.

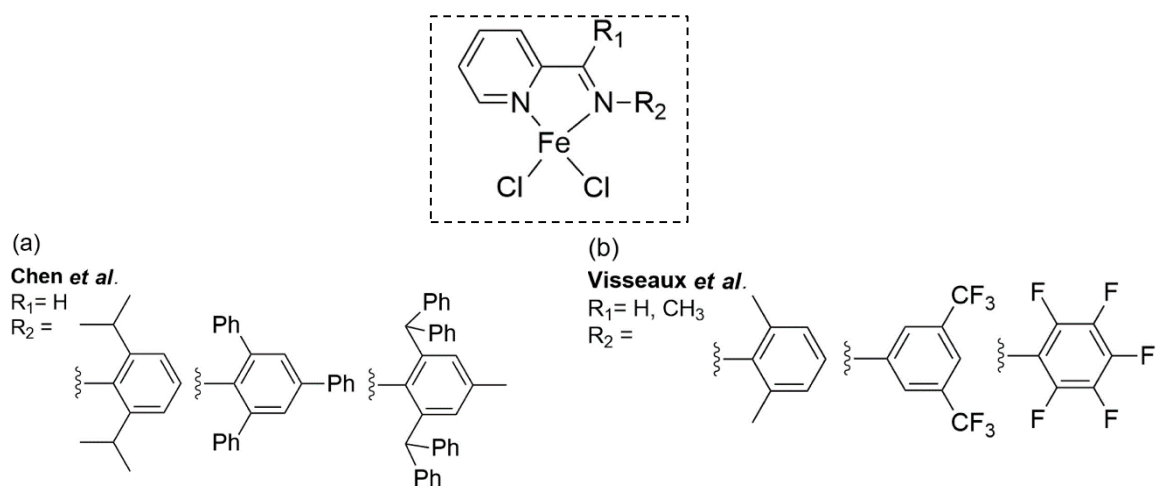


Figure 4.5. Structural evolution of iminopyridine iron complexes by (a) Chen et al.⁶⁰ and (b) Visseaux et al.^{61,62}

4.1.3 Copper Catalysts

Examples of copper-based catalysts for the synthesis of stereoregular polydienes are quite rare. As with iron, interest in copper has emerged in recent years from the need to find and test new catalytic systems with a lower environmental impact and consequently more sustainable, capable of replacing, by exhibiting comparable catalytic activities and selectivities, the catalytic systems currently used today, based on metals characterized by high toxicity such as chromium and nickel. Only recently⁶³ has it been shown that the combination of iminopyridyl copper complexes and MAO can produce essentially syndiotactic 1,2 polymers from butadiene (Figure 4.6) and predominantly alternating *cis*-1,4/3,4 polymers from isoprene and myrcene.

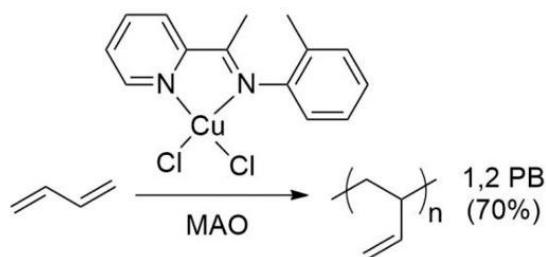


Figure 4.6. Polymerization of 1,3-butadiene with copper-based catalysts.

4.1.4 Neodymium Catalysts

It is well known that lanthanide-based catalysts are extremely *cis*-specific in the polymerization of several different substituted butadienes in addition to butadiene.^{1,64-66} In particular, lanthanide-based catalysts produce a *cis*-polybutadiene that is better appropriate for the manufacture of tires—by far the most significant practical use of *cis*-polybutadiene—since it has a more linear structure than those from Co, Ni, and Ti. Among the various Lanthanide-

based systems, Neodymium-based systems currently have the greatest relevance with regard to the synthesis of polydienes. In fact, the catalytic system obtained by reacting a Nd compound (*e.g.*, Nd(acac)₃, Nd(OCOC₇H₁₅)₃) with a chlorine donor (*e.g.*, AlEt₂Cl, Al₂Et₃Cl₃, and *tert*-butyl chloride) and an aluminum alkyl (*e.g.*, Al^{*i*}Bu₃, Al^{*i*}Bu₂H) is currently used for the industrial production of polybutadiene with a very high *cis*-1,4 content (~98%).⁶⁶⁻⁷⁰ Furthermore, the same catalytic system is able to polymerize different types of terminally substituted 1,3-butadienes allowing the production of polymers with a high isotactic *cis*-1,4 structure. Finally, Nd complexes with bis-imine, bis-imino-pyridine, and keto-imine ligands, in combination with tetraisobutylaluminumoxane (TIBAO), have made it possible to obtain polybutadienes and polyisoprenes with very high *cis*-1,4 content, 99.9% and 98%, respectively (Figure 61), and a good activity (up to 182 kg polymer (mol Nd)⁻¹ h⁻¹)⁵⁹

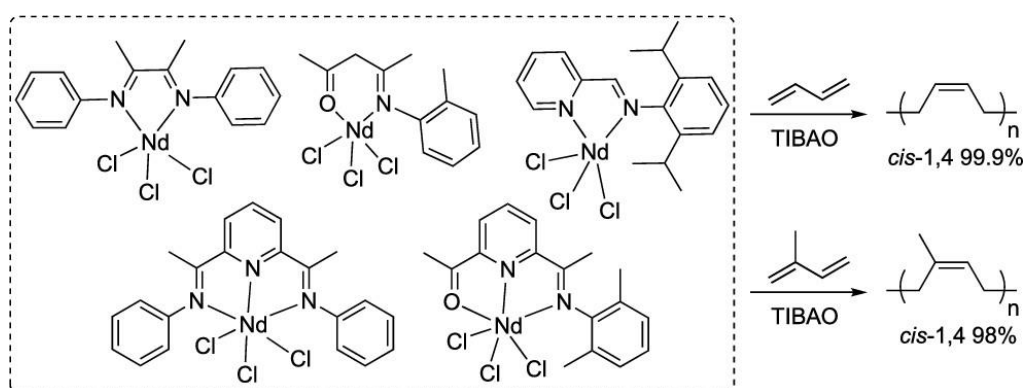


Figure 4.7. Polymerization of butadiene and isoprene with neodymium complex-based catalysts.

4.2 Synthesis and characterization of Poly(isoprene)s of different molecular structure prepared with different catalysts based on complexes of Co, Fe, Cu and Nd

4.2.1 Materials and Methods

Poly(isoprene) samples (characterized with ^1H , ^{13}C analysis and SEC) were synthesized and supplied by Drs. Giovanni Ricci and Giuseppe Leone (CNR-ISMAL Milano) within a collaborative project.

DSC scans were carried out on a Mettler-DSC822 calorimeter equipped with a liquid nitrogen subambient device. The sample, ca. 4 mg, was placed in a sealed aluminum pan, and the measurements were carried out using heating and cooling rates of $10^\circ\text{C}/\text{min}$.

X-ray powder diffraction profiles were recorded with Ni filtered Cu $K\alpha$ radiation by using an Empyrean diffractometer by Malvern Panalytical operating in the reflection geometry with continuous scans of the 2θ angle and scanning rate of 0.02 degree/s. The degrees of crystallinity (x_c) were determined from the powder diffraction profiles by the ratio between the crystalline diffraction area (A_c) and the area of the whole diffraction profiles (A_t), $x_c = (A_c/A_t) \times 100$. The area of the crystalline diffraction A_c was evaluated by subtracting the area of the amorphous halo from the area of the whole diffraction profiles A_t .

Compression molded films were prepared by heating the as-polymerized samples at temperatures 20 - 30 $^\circ\text{C}$ higher than the melting temperatures under a press at low pressure to avoid preferred orientations in the sample, and by slow cooling to room temperature. Oriented fibers of the samples were obtained by stretching at room temperature compression molded samples at different degrees of deformation $\varepsilon = 100 \times (L_f - L_0)/L_0$, where L_0 and L_f are the initial and final lengths of the specimen, respectively.

The X-ray fiber diffraction patterns were obtained with Ni filtered Cu $K\alpha$ radiation and recorded on a BAS-MS imaging plate (FUJIFILM) using a cylindrical camera and processed with a digital imaging reader Perkin Elmer Cyclone Plus (storage phosphor system).

The mechanical properties were evaluated performing mechanical tests at room temperature on compression-molded films with a mechanical tester apparatus (Zwick by Zwick Roell) following the standard test method for tensile properties of thin plastic sheeting ASTM D882-83. Rectangular specimens 3 mm long, 2 mm wide and 0.3 mm thick have been stretched up to the break or up to a given deformation $\varepsilon = 100 \times (L_f - L_0)/L_0$, where L_0 and L_f are the initial and final lengths of the specimen, respectively. Two benchmarks have been placed on the test specimens and used to measure elongation. Values of tension set and elastic recovery have been measured after breaking. Ten minutes after breaking, the two pieces of the sample have

been fit carefully together so that they are in contact over the full area of the break and the final length L_r of the specimen has been obtained by measuring the distance between the two benchmarks. The residual deformation (tension set) after breaking has been calculated as $t_b = 100 \times (L_r - L_0) / L_0$, whereas the elastic recovery has been calculated as $r_b = 100 \times (L_f - L_r) / L_r$ and the percentage of the total strain achieved at breaking $\varepsilon_b = 100 \times (L_f - L_0) / L_0$ that is recovered after breaking is calculated as $R_b = 100 \times (L_f - L_r) / (L_f - L_0) = 100 \times (\varepsilon_b - t_b) / \varepsilon_b$.

In the mechanical tests, the ratio between the drawing rate and the initial length was fixed equal to 0.1 mm/(mm×min) for the measurement of Young's modulus and 10 mm/(mm×min) for the measurement of stress–strain curves and the determination of the other mechanical properties (stress and strain at break and tension set). The reported values of the mechanical parameters are averaged over at least five-eight independent experiments.

Stress-relaxed oriented films have been prepared by stretching compression-molded films of initial length L_0 up to a maximum deformation $\varepsilon_{\max} = 220\%$, that is up to a final length $L_f = 3.2L_0$, and then removing the tension allowing the complete relaxation of the films up to the relaxed length L_r . The final length of the relaxed specimens L_r (lower than L_f) was measured after 10 min the removal of the tension. The values of tension set and elastic recovery were calculated after the relaxation as $t_s(\varepsilon_{\max}) = 100 \times (L_r - L_0) / L_0$ and $r(\varepsilon_{\max}) = 100 \times (L_f - L_r) / L_r$, respectively, and the percentage of the maximum strain achieved $\varepsilon_{\max} = 100 \times (L_f - L_0) / L_0$ that is recovered after breaking is calculated as $R(\varepsilon_{\max}) = 100 \times (L_f - L_r) / (L_f - L_0) = 100 \times (\varepsilon_{\max} - t_s(\varepsilon_{\max})) / \varepsilon_{\max}$.

Mechanical cycles of stretching and relaxation (hysteresis stress-strain cycles) were performed at room temperature on the stress-relaxed oriented films recording the corresponding hysteresis following the standard test method ASTM D412 87. In these cycles stress-relaxed films of initial length L_r were stretched up to the final length $L_f = 3.2L_0$ that is, up to the maximum length achieved during the stretching of the starting unoriented film used for the preparation of the oriented films, so that the maximum deformation achieved during the first cycle ($\varepsilon = 100 \times (L_f - L_r) / L_r$) for each sample is numerically equal to the elastic recovery $r(\varepsilon_{\max})$ of the unoriented film. For each oriented film at least three consecutive hysteresis cycles have been recorded, each cycle has been performed 10 min after the end of the previous cycle. The values of tension set $t(\varepsilon)$ and elastic recovery $r(\varepsilon)$ after each cycle were evaluated as $t(\varepsilon) = 100 \times (L_r' - L_r) / L_r$ and $r(\varepsilon) = 100 \times (L_f - L_r') / L_r'$ where L_r' is the length of the specimen after relaxation at the end of each cycle.

4.2.2 General Introduction

Polyisoprene elastomers are produced via solution polymerization of isoprene using stereospecific catalysts. This polymerization yields various isomeric polymers having different structures depending on the nature of the catalyst used for their synthesis. Eight possible isomeric poly(isoprene)s are possible, as shown in Figure 4.8: *cis*-1,4; *trans*-1,4; 1,2-isotactic, 1,2-syndiotactic and 1,2-atactic; 3,4-isotactic, 3,4-syndiotactic and 3,4-atactic. Of these, 1,4-polymers and atactic 3,4-polymers have been known for a long time, since the beginning of the stereospecific polymerization of conjugated dienes,¹ while 3,4-isotactic and syndiotactic polymers have only recently been obtained⁵²⁻⁵⁴, thanks to the introduction of new catalytic systems based on transition metal and lanthanide complexes with organic ligands of various nature, having a well-defined structure. The chemical structure and properties of synthetic *cis*-1,4 isoprene rubber (*cis*-IR) are almost identical to those of common natural rubber (from *Hevea brasiliensis* lattice). Chemically, natural rubber is pure *cis*-1,4 polyisoprene, while commercial grades of synthetic *cis*-IR have content of *cis*-1,4 isoprene units greater than 95%. There are three main types of catalyst systems employed to produce synthetic *cis*-1,4 polyisoprene worldwide: Ziegler-Natta catalyst based on TiCl₄ and alkylaluminum, with *cis* content up to 98%¹; lithium organic catalysts with *cis* content up to 93%⁷¹; neodymium catalyst with *cis* content up to 99%⁶³. Polyisoprene elastomers are currently being used in a variety of end-use applications requiring good resilience, low water swell, high gum tensile strength, good track, and high hot tensile strength. The largest end use for polyisoprene by far is in tires. Black-loaded polyisoprene finds uses in tires, motor mounts, pipe gaskets, shock absorber bushings, and many other molded and mechanical goods. Gum polyisoprene compounds are used in rubber bands, cut thread, baby bottle nipples, and extruded hoses, along with other items. Polyisoprene that is mineral filled, finds application in footwear, sponges, and sporting goods. Other important uses include medical applications and sealants and adhesives. Of all the applications, medical applications have witnessed the fastest growth. Compared with natural rubber, synthetic *cis*-1,4 polyisoprene is cleaner, contains no water-sensitive residues, is 100% hydrocarbon, processes more easily due to controlled Mooney viscosity, and has less cure variations and little or no contamination. Moreover, synthetic polyisoprene is sometimes blended with natural rubber and other synthetic rubbers to impart beneficial characteristics to the final product. *trans*-1,4 isoprene rubber (*trans*-IR) and 3,4 polyisoprene are also produced synthetically, but are of minor commercial importance.

The chemical structure and properties of *trans*-IR are very similar to those of balata and gutta-percha rubbers, which in purified form are almost 100% *trans*-1,4 polyisoprene. The properties

of trans-IR are quite different from those of cis-IR. Trans-IR is a crystalline thermoplastic polymer with a melting point of 54-60°C, produced by polymerizing isoprene with a vanadium trichloride/triethylaluminum catalyst system⁷². At room temperature, it has high tensile strength and a high resistance to cutting, abrasion, and scuffing. Trans-IR's high selling price restricts its use to high-value applications that can pass along its cost, including golf ball covers, hot-melt adhesives, and medical/dental applications such as orthopedic devices, splints, crown implant fillers, cable and wire coverings, and transmission belts, as well as other applications. The total global market for trans-IR is very small and fragmented.

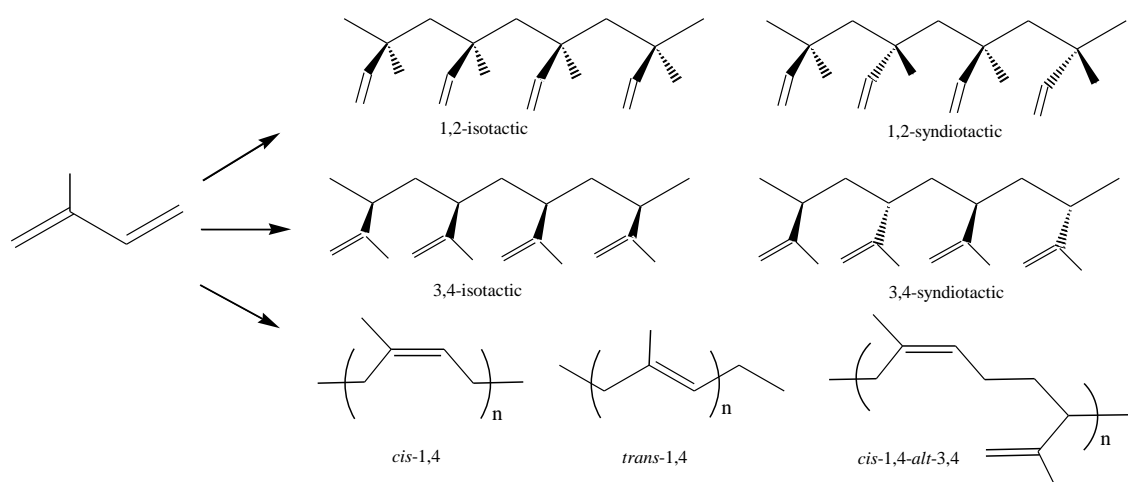


Figure 4.8. Possible isoprene isomeric polymers.

4.2.3 Polymerization

Samples of different poly(isoprene)s characterized by different molecular structures have been prepared with the different catalysts reported in the Figure 4.9 based on complexes of Nd, Co, Fe and Cu. Poly(isoprene) samples with prevalent *cis*-1,4 structure has been prepared with Nd based catalyst, samples with regular alternating *cis*-1,4-*alt*-3,4 structure have been prepared with Co based catalyst, samples random *cis*-1,4/3,4 structure with prevalent 3,4 syndiotactic and concentration of 3,4 unit of nearly 75% have been prepared with CuCl₂(bipy) and samples with almost regular 3,4 syndiotactic structure with 90-100% of 3,4 units and low amount of *cis*-1,4 units have been obtained with FeCl₂(bipy). Finally, poly(isoprene)s with rather unusual predominantly alternating *cis*-1,4-*alt*-3,4 structure but containing along the polymer chain *cis*-1,4 unit sequences of different length (3 or 5 units) have been obtained with iron dichloride and copper dichloride pyridylimino complexes. All samples are reported in Table 4.1, where the

conditions of polymerization, the catalysts and the molecular structures of the samples induced by the used catalysts are shown. The samples are identified with the code PI $cisAx$ or PI $altAx$ or PI $s3,4Ax$, where the symbols *cis*, *alt* and *s3,4* indicate a *cis*-1,4 structure, a mainly alternating *cis*-1,4-*alt*-3,4 structure and a syndiotactic 3,4 structure, respectively, whereas the symbol A indicates the catalyst (Nd, Fe, Cu or Co) and x the number of the sample. In the following sections, the properties of all these materials will be discussed separately according to their structure for clarity's sake.

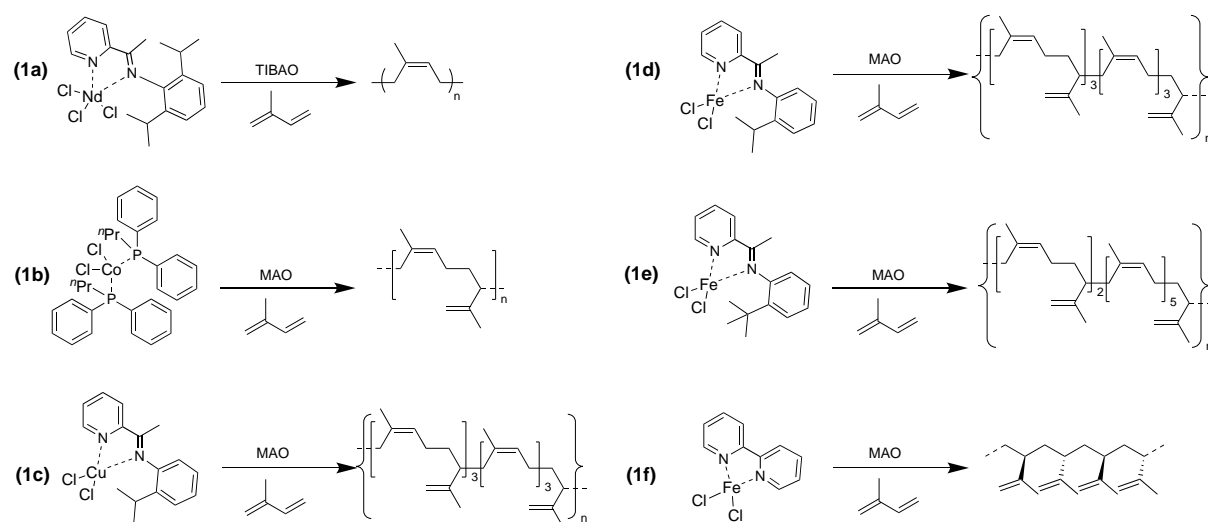


Figure 4.9. Complexes of Nd (1a), Co (1b), Cu (1c) and Fe (1d, 1e, 1f) used as catalysts for the synthesis of polyisoprenes having different molecular structures, 1,4-*cis* (1a), 1,4-*cis-alt-3,4* (1b-1e) and 3,4-syndiotactic (1f).

Table 4.1. Conditions of polymerization of isoprene with catalysts based on complexes of Nd, Fe, Co and Cu of Figure 4.9, molecular structure (*cis*-1,4, 3,4-syndiotactic, alternating *cis*-1,4-*alt*-3,4 and random *cis*-1,4/3,4) of the obtained samples of poly(isoprene)s, concentrations of *cis*-1,4 and 3,4 syndiotactic units, concentration of *rr* diads of the sequences of 3,4 syndiotactic units and molecular mass of the poly(isoprene) samples.

entry	cat	$M_w \times 10^{3**}$	M_w/M_n^{**}	structure	composition ^{***}	<i>rr</i> (%) ^{***}	consecutive <i>cis</i> -1,4 units ^{***}
PIcisNd	1a			<i>cis</i> 1,4	97% <i>cis</i> -1,4		/
PIaltFe1	1e	130	2.0	<i>cis</i> -1,4- <i>alt</i> -3,4	<i>cis</i> -1,4 /3,4 = 71/29		5
PIaltFe2	1e	148	2.0	<i>cis</i> -1,4- <i>alt</i> -3,4	<i>cis</i> -1,4 /3,4 = 69/31		5
PIaltFe3	1d	730	3.6	<i>cis</i> -1,4- <i>alt</i> -3,4	<i>cis</i> -1,4 /3,4 = 61.5/38.5		3
PIaltFe4	1d	183	1.9	<i>cis</i> -1,4- <i>alt</i> -3,4	<i>cis</i> -1,4 /3,4 = 58/42		3
PIaltFe5	1d	4.095	2.8	<i>cis</i> -1,4- <i>alt</i> -3,4	<i>cis</i> -1,4 /3,4 = 58/42		3
PIaltFe6	1d	1.067	3.8	<i>cis</i> -1,4- <i>alt</i> -3,4	<i>cis</i> -1,4 /3,4 = 58/42		3
PIaltCu1	1c	1.800	2.0	<i>cis</i> -1,4- <i>alt</i> -3,4	<i>cis</i> -1,4 /3,4 = 56.5/43.5		< 3
PIaltCu2	1c	311	1.6	<i>cis</i> -1,4- <i>alt</i> -3,4	<i>cis</i> -1,4 /3,4 = 55.1/44.9		< 3
PIaltCu3	1c	839	1.8	<i>cis</i> -1,4- <i>alt</i> -3,4	<i>cis</i> -1,4 /3,4 = 48.1/51.9		< 3
PIaltCo	1b	171	-	<i>cis</i> -1,4- <i>alt</i> -3,4	<i>cis</i> -1,4 /3,4 = 50/50		/
PI3,4sCu	*	310	1.6	<i>cis</i> -1,4/3,4s	<i>cis</i> -1,4/3,4s = 24.1/75.9	49.5	/
1							
PI3,4sCu	*	1.327	2.8	<i>cis</i> -1,4/3,4s	<i>cis</i> -1,4/3,4s = 26.5/73.5	57.2	-
2							
PI3,4sCu	*	1.669	2	<i>cis</i> -1,4/3,4s	<i>cis</i> -1,4/3,4s = 25.7/74.3	56.9	-
3							
PI3,4sCu	*	458	3.7	<i>cis</i> -1,4/3,4s	<i>cis</i> -1,4/3,4s = 31.8/68.2	40.5	-
4							
PI3,4sCu	*	2473	1.4	<i>cis</i> -1,4/3,4s	<i>cis</i> -1,4/3,4s = 24.4/75.6	57.6	-
5							
PI3,4sCu	*	2943	1.6	<i>cis</i> -1,4/3,4s	<i>cis</i> -1,4/3,4s = 25.1/74.9	54.4	-
6							
PI3,4sFe1	1f			3,4 syndiotactic	<i>cis</i> -1,4/3,4s = 10/90		-
PI3,4sFe2	1f			3,4 syndiotactic	<i>cis</i> -1,4/3,4s = 10/90		-
PI3,4sFe3	1f			3,4 syndiotactic	<i>cis</i> -1,4/3,4s = 10/90		-

3,4s = 3,4 syndiotactic

cis-1,4/3,4s = random *cis*-1,4/3,4 syndiotactic structure

cis-1,4-*alt*-/3,4 = alternating *cis*-1,4/3,4 structure

*the catalyst used for the synthesis of these poly(isoprene)s is not showed in Figure 9.

**determined by SEC.

**determined by ¹H and ¹³C NMR.

4.2.4 *cis*-1,4 poly(isoprene) from Neodymium catalyst

The sample PIcisNd (Table 4.1) synthesized with the catalyst **1a** of Figure 4.9, based on neodymium pyridylimino complex in combination with tetraisobutylaluminumoxane (TIBAO), is characterized by an almost regular *cis*-1,4 structure with a concentration of *cis*-1,4 isoprene units of 97%. The sample shows, therefore, a structure similar to that of natural rubber.

The X-ray powder diffraction profiles of the as-prepared and compression-molded samples of the sample PIcisNd are reported in Figure 4.10A. The DSC thermograms recorded during heating of the as-prepared sample, cooling from 150 °C down to -90 °C and successive second heating are shown in Figure 4.10B. The as-prepared and compression-molded samples are

amorphous (Figure 4.10A) and crystallization is not observed even by cooling at low temperatures (Figure 4.10B). The DSC thermograms present, indeed, only a glass transition at temperature of $-64\text{ }^{\circ}\text{C}$ during both heating and cooling scans (Figure 4.10B), similar to the glass transition temperature of natural rubber⁷³ and synthetic *cis*-1,4 poly(isoprene)s.⁷³

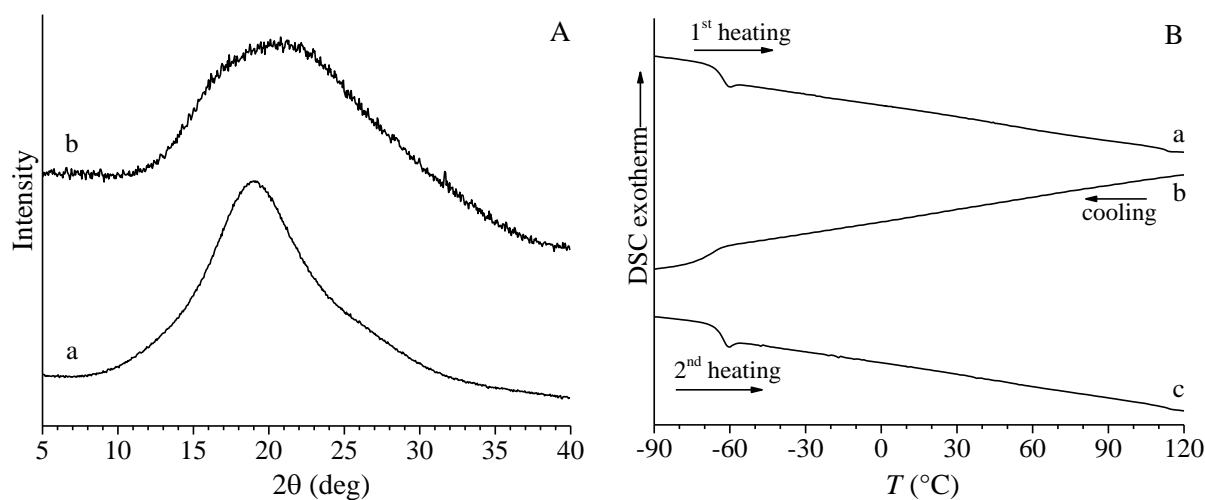


Figure 4.10. X-ray powder diffraction profiles (A) of the as-prepared sample (a) and of the compression-molded sample (b) and DSC curves (B) recorded during heating of the as-prepared sample (a), cooling (b) and successive second heating (b) at scanning rate of $10\text{ }^{\circ}\text{C}/\text{min}$, of the sample PIcisNd with an almost regular *cis*-1,4 structure synthesized with the Nd based catalyst 1a of Figure 4.9.

The stress-strain curve of the compression molded films of the sample PIcisNd is shown in Figure 4.11. The sample shows low values of the modulus and of stresses at any strain and experiences viscous flow at low values of strain, according to the fact that the sample is amorphous and probably with a molecular mass not high enough to guarantee a degree of entanglements high enough to prevent viscous flow under strain.

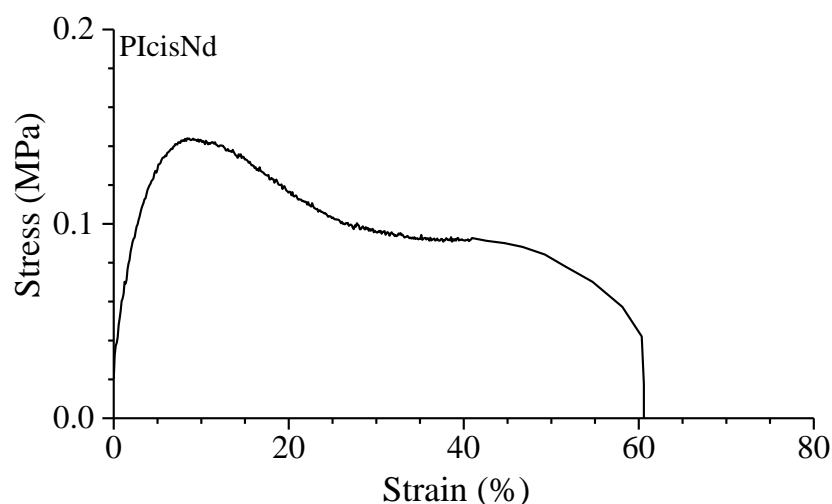


Figure 4.11. Stress-strain curve of the amorphous compression molded films of the sample PIcisNd with an almost regular *cis*-1,4 structure.

4.2.5 *cis*-1,4-*alt*-3,4 alternating poly(isoprene)s from Fe and Cu based catalysts

Samples of PIs prepared with catalysts based on iron dichloride and copper dichloride pyridylimino complexes (catalysts **1c-e** of Figure 4.9) are characterized by rather unusual structures with a predominantly alternating *cis*-1,4-*alt*-3,4 structure but containing along the polymer chain sequences of *cis* unit of different length (3 or 5 units) depending on the nature of the pyridylimine ligand coordinated to the metal atom (six samples PIaltFe1-PIaltFe6 and three samples PIaltCu1-PIaltCu3 of Table 4.1).

The X-ray powder diffraction profiles of the as-prepared and compression-molded samples of the six samples PIaltFe1-PIaltFe6 and of the three samples PIaltCu1-PIaltCu3 are reported in Figure 4.11. All as-prepared and compression-molded samples are amorphous as expected due to the not regular alternating *cis*-1,4-*alt*-3,4 structure.

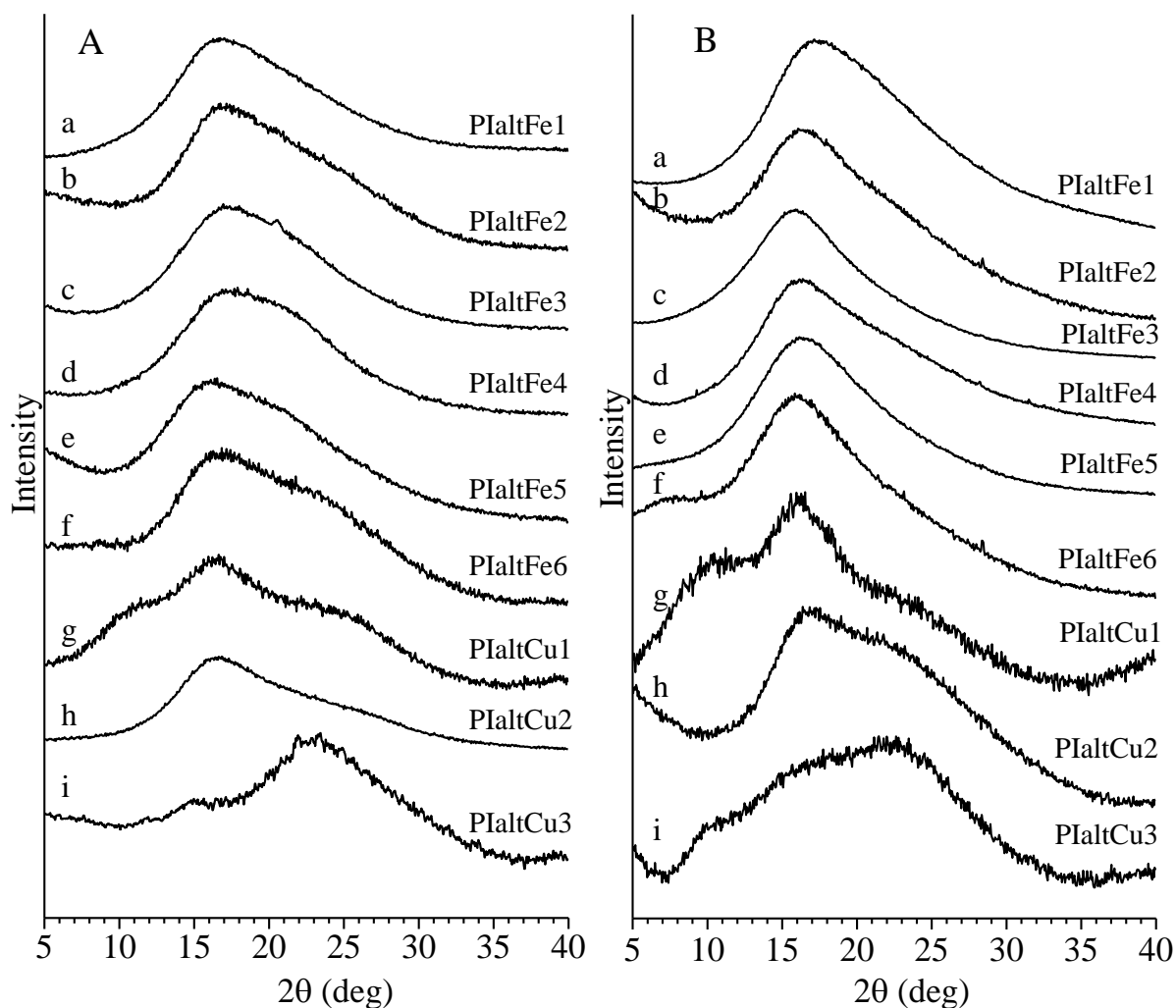


Figure 4.11. X-ray powder diffraction profiles of the as-prepared samples (A) and of the compression-molded samples (B) of poly(isoprene)s samples with a predominantly alternating *cis*-1,4-*alt*-3,4 structure prepared with Fe and Cu based catalysts 1c-e of Figure 4.9 (samples PIaltFe1-PIaltFe6 and PIaltCu1-PIaltCu3 of Table 4.1).

The DSC curves of all samples are displayed in Figure 4.12. The samples have been first heated up to 140 °C to eliminate previous thermal history of the as-prepared samples allowing eventual evaporation of residual solvent, then the DSC thermograms have been recorded during cooling from 140 °C down to -80 °C (Figure 4.12A) and during successive heating from -80 °C up to 140 °C (Figure 4.12B) at scanning rate of 10 °C/min.

According to the X-ray diffraction profiles of Figure 4.11, the DSC curves do not show neither crystallization phenomena during cooling nor endothermic melting phenomena during heating, indicating that all samples are amorphous and do not crystallize even upon cooling at very low temperature.

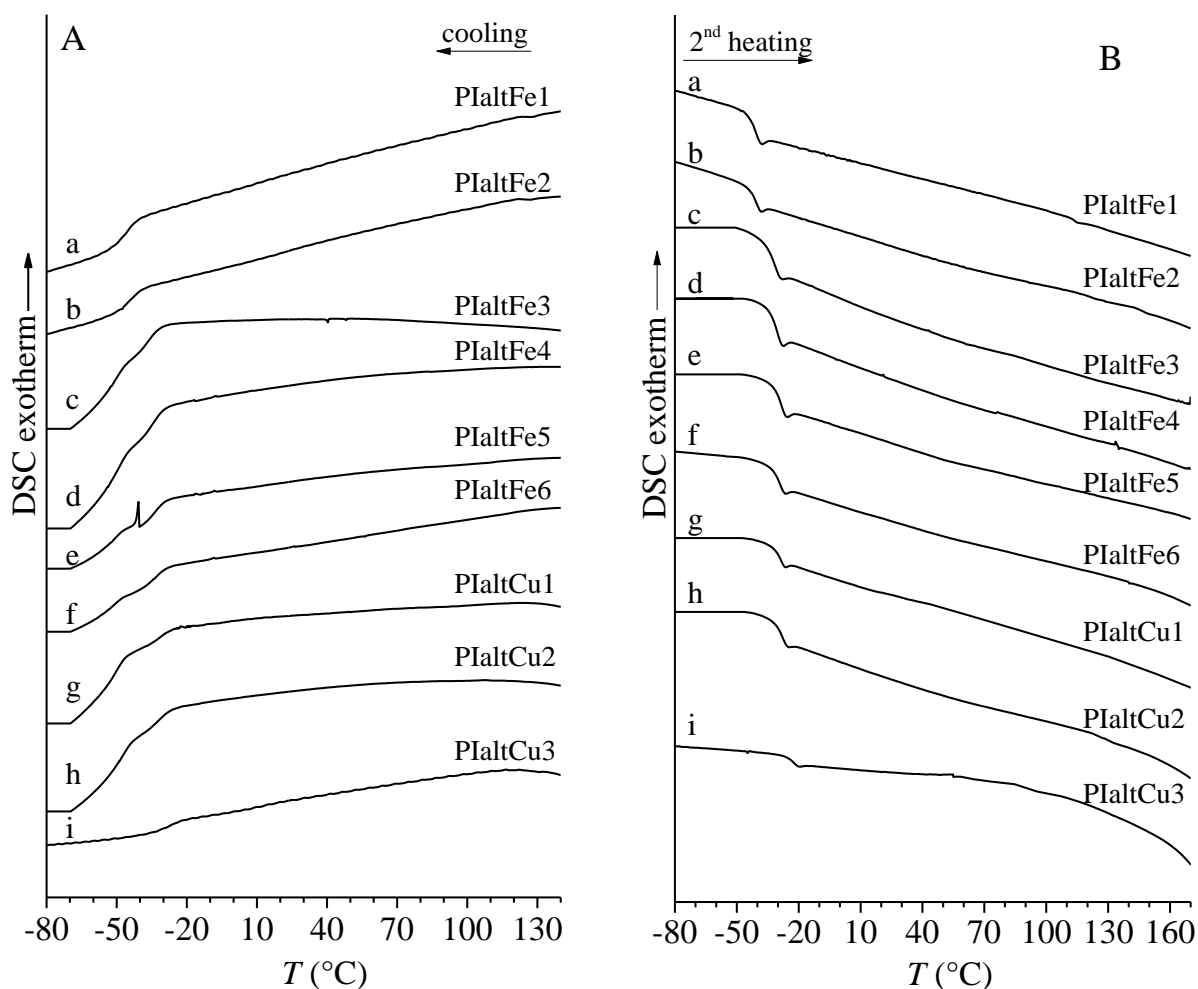


Figure 4.12. DSC curves recorded during cooling (A) and successive heating (B) at scanning rate of 10 °C/min of samples PIaltFe1-PIaltFe6 and samples PIaltCu1-PIaltCu3 having a predominantly alternating *cis*-1,4-*alt*-3,4 structure prepared with Fe and Cu based catalysts 1c-e of Figure 4.9.

All the DSC curves present only the glass transition at different temperatures depending on the composition and concentration of *cis*-1,4 units. The values of the glass transition temperature evaluated from the heating scans are reported in Table 4.2 and in Figure 4.13 as a function of the concentration of *cis*-1,4 units. The values of the glass transition temperature of the sample PIcisNd with 97% of *cis*-1,4 units (-64 °C) and of samples with random *cis*-1,4/3,4 syndiotactic structure, which will be discussed in the following paragraphs, are also included in the plot of Figure 4.13 and in Table 4.2. It is apparent that the glass transition temperature decreases almost linearly with increasing concentration of *cis*-1,4 unit, from nearly -20 ÷ -40 °C of the samples with alternating *cis*-1,4-*alt*-3,4 structure and concentration of *cis*-1,4 units in the range 50-80 mol%, to -64 °C of the samples with almost regular *cis*-1,4 structure (97% of *cis*-1,4units).

Table 4.2. Values of the glass transition temperature of samples of poly(isoprene)s having a different molecular structures and different concentration of *cis*-1,4 units. The sample PI_{cis}Nd has a regular *cis*-1,4 structure, the samples PI_{alt}Fe1 – PI_{alt}Fe6 and PI_{alt}Cu1-PI_{alt}Cu3 have alternating *cis*-1,4-*alt*-3,4 structure, the sample PI_{alt}Co has regular alternating *cis*-1,4-*alt*-3,4 structure, the samples PI_{3,4s}Cu1 - PI_{3,4s}Cu6 have a random *cis*-1,4/3,4-syndiotactic structure with prevailing 3,4 syndiotactic units from CuCl₂(bipy)/MAO the samples PI_{3,4s}Fe1 - PI_{3,4s}Fe3 have a regular 3,4-syndiotactic structure from FeCl₂(bipy)/MAO.

entry	[<i>cis</i> 1,4] (mol%)*	<i>T_g</i> (°C)**
PI _{cis} Nd	97	64
PI _{alt} Fe1	71	-42.3
PI _{alt} Fe2	69	-42
PI _{alt} Fe3	61.5	-33.5
PI _{alt} Fe4	58	-31
PI _{alt} Fe5	58	-29.3
PI _{alt} Fe6	58	-31
PI _{alt} Cu1	56.5	-30.1
PI _{alt} Cu2	55.1	-29.1
PI _{alt} Cu3	48.1	-24
PI _{alt} Co	50	-18.1
PI _{3,4s} Cu1	24.1	5.4
PI _{3,4s} Cu2	26.5	8.4
PI _{3,4s} Cu3	25.7	9.4
PI _{3,4s} Cu4	31.8	1.2
PI _{3,4s} Cu5	24.4	8.1
PI _{3,4s} Cu6	25.1	9.6
PI _{3,4s} Fe1	10	16.3
PI _{3,4s} Fe2	10	15.6
PI _{3,4s} Fe3	10	15.6

*determined by ¹H and ¹³C NMR.

**evaluated from the second DSC heating curves of Figures 4.10B, 4.12B, 4.15B, 4.18B, 4.21B.

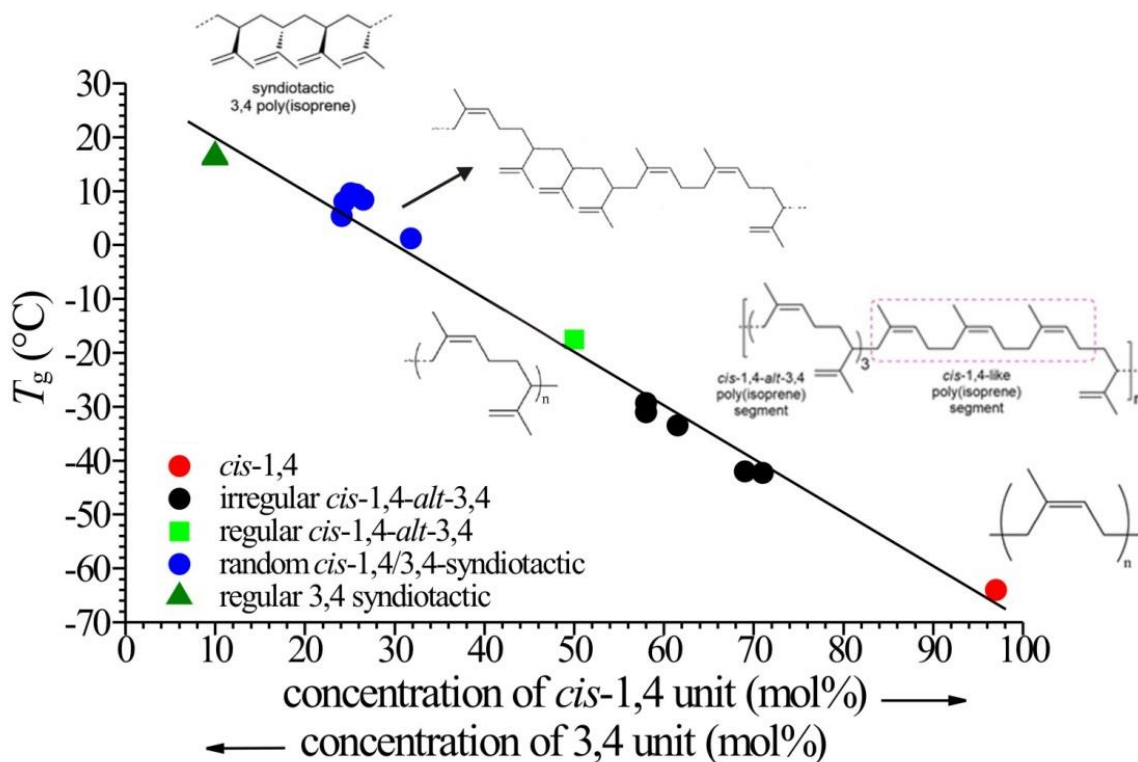


Figure 4.13. Values of the glass transition temperature (T_g) of samples of poly(isoprenes) having different molecular structures as a function of the concentration of *cis*-1,4 units. In A samples with almost regular *cis*-1,4 structure (●), alternating *cis*-1,4-*alt*-3,4 structure (●), regular alternating *cis*-1,4-*alt*-3,4 structure (■), random *cis*-1,4/3,4-syndiotactic structure (●) and regular 3,4 syndiotactic structure (▲) are reported with different symbols.

The stress-strain curves of the compression-molded films of prevalingly alternating *cis*-1,4-*alt*-3,4 samples PIaltFe1-PIaltFe6 and PIaltCu1-PIaltCu3 of Figures 4.11 and 4.12 are reported in Figure 4.14. All samples show low values of the modulus and of stresses at any strain and experiences viscous flow during deformation. Some samples show viscous flow and breaking at low deformation (Figure 4.14A), whereas other samples show viscous flow at higher deformation and breaking only at values of strain higher than 1000% (Figure 4.14B).

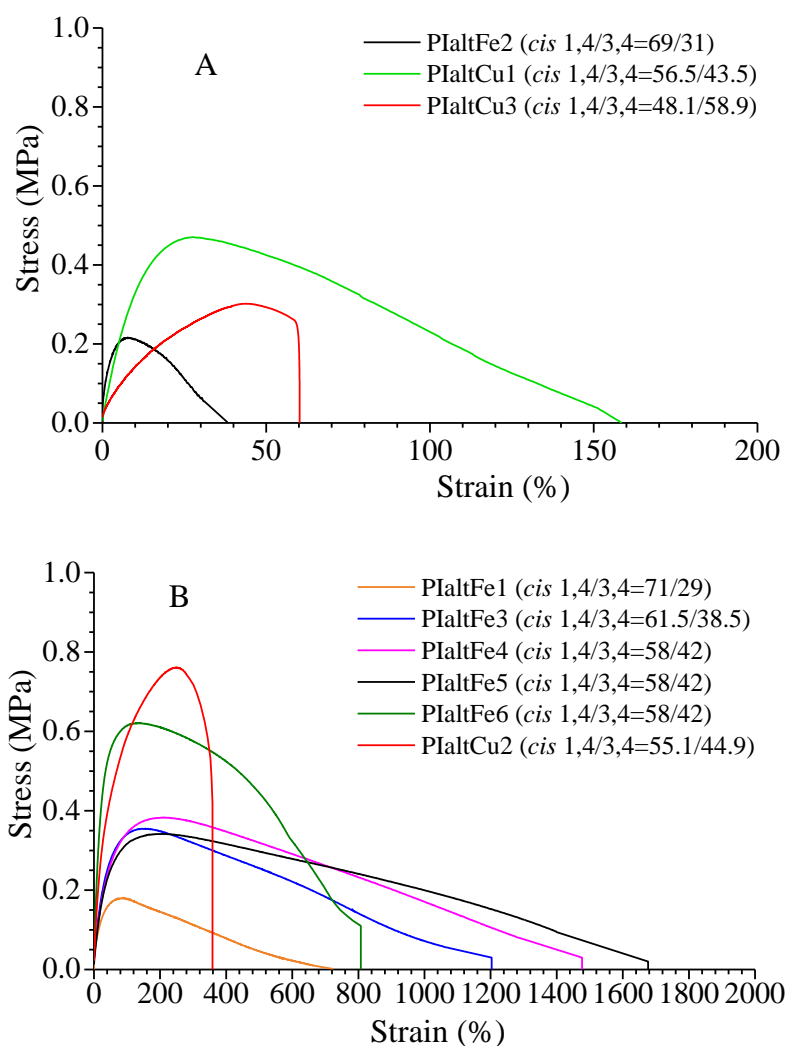


Figure 4.14. The stress-strain curves of the compression-molded films of samples PIaltFe1-PIaltFe6 and samples PIaltCu1-PIaltCu3 of Figures 4.11 and 4.12 having a predominantly alternating *cis*-1,4-*alt*-3,4 structure prepared with Fe and Cu based catalysts 1c-e of Figure 4.9.

The values of the mechanical parameters (Young's modulus, stress and strain at yielding and stress and strain at breaking) of samples PIaltFe1-PIaltFe6 and samples PIaltCu1-PIaltCu3 evaluated for the stress-strain curves of Figure 4.14, along with those of the samples PICisNd (from Figure 4.11) and PIaltCo (from Figure 4.16), with regular *cis*-1,4 structure and regular alternating *cis*-1,4-*alt*-3,4 structure, respectively, are reported in Table 4.3. Since all samples are very soft and show very low mechanical strength, in addition to Young's modulus, the stress values at a certain strain (30%) were also evaluated in order to compare the different poly(isoprene)s reported in Figure 4.14. The obtained values are also shown in Table 4.3.

Table 4.3. Average values of Young modulus (E), stress at 30% of strain ($\sigma_{30\%}$), strain (ϵ_b) and stress at break (σ_b), of samples of poly(isoprene)s of Table 4.1 of different molecular structure and different concentration of *cis*-1,4 units. The sample PIcisNd has a regular *cis*-1,4 structure, the samples PIaltFe1 – PIaltFe6 and PIaltCu1-PIaltCu3 have alternating *cis*-1,4-*alt*-3,4 structure and the sample PIaltCo has regular alternating *cis*-1,4-*alt*-3,4 structure.

entry	E (MPa)	$\sigma_{30\%}$ (MPa)	ϵ_b (%)	σ_b (MPa)
PIcisNd	0.2 ± 0.1	0.10 ± 0.02	$(6 \pm 4) \times 10$	
PIaltFe1	0.8 ± 0.4	0.14 ± 0.02	$(72 \pm 8) \times 10$	$(2 \pm 0.5) \times 10^{-3}$
PIaltFe2	0.8 ± 0.3	0.02 ± 0.01	38 ± 6	-
PIaltFe3	0.4 ± 0.2	0.22 ± 0.02	$(12 \pm 1) \times 10^2$	-
PIaltFe4	0.5 ± 0.07	0.20 ± 0.04	$(15 \pm 1) \times 10^2$	-
PIaltFe5	0.3 ± 0.1	0.19 ± 0.03	$(17 \pm 2) \times 10^2$	-
PIaltFe6	1.7 ± 0.3	0.48 ± 0.06	$(8 \pm 2) \times 10^2$	-
PIaltCu1	4.4 ± 1.8	0.26 ± 0.04	$(16 \pm 6) \times 10$	-
PIaltCu2	1.9 ± 0.7	0.19 ± 0.03	$(36 \pm 4) \times 10$	-
PIaltCu3	2 ± 0.7	0.47 ± 0.06	60.2 ± 0.5	0.3 ± 0.1
PIaltCo	0.6 ± 0.2	0.16 ± 0.03	$(31 \pm 6) \times 10$	$(1 \pm 0.3) \times 10^{-3}$

4.2.6 Regular *cis*-1,4-*alt*-3,4 alternating poly(isoprene) from Co based catalyst

The sample PIaltCo prepared with catalytic system based on cobalt diphenylalkylphosphine complex ($\text{CoCl}_2(\text{PRPh}_2)_2$) (complex **1b** of Figure 4.9) is characterized by a regular alternating *cis*-1,4-*alt*-3,4 structure. The X-ray powder diffraction profiles of the as-prepared and compression-molded samples of the sample PIaltCo are reported in Figure 4.15. The DSC curves recorded during heating of the as-prepared sample, cooling from 150 °C down to -60 °C and successive second heating are shown in Figure 4.15. The as-prepared and compression-molded samples are amorphous (Figure 4.15A) and the DSC curves present only a glass transition at temperature of -17 °C during both heating and cooling scans (Figure 4.15B). The value of T_g of the sample PIaltCo with 50% concentration of *cis*-1,4 units fits on the linear plot of Figure 4.13. Therefore, also the regular alternating *cis*-1,4-*alt*-3,4 structure does not allow crystallization.

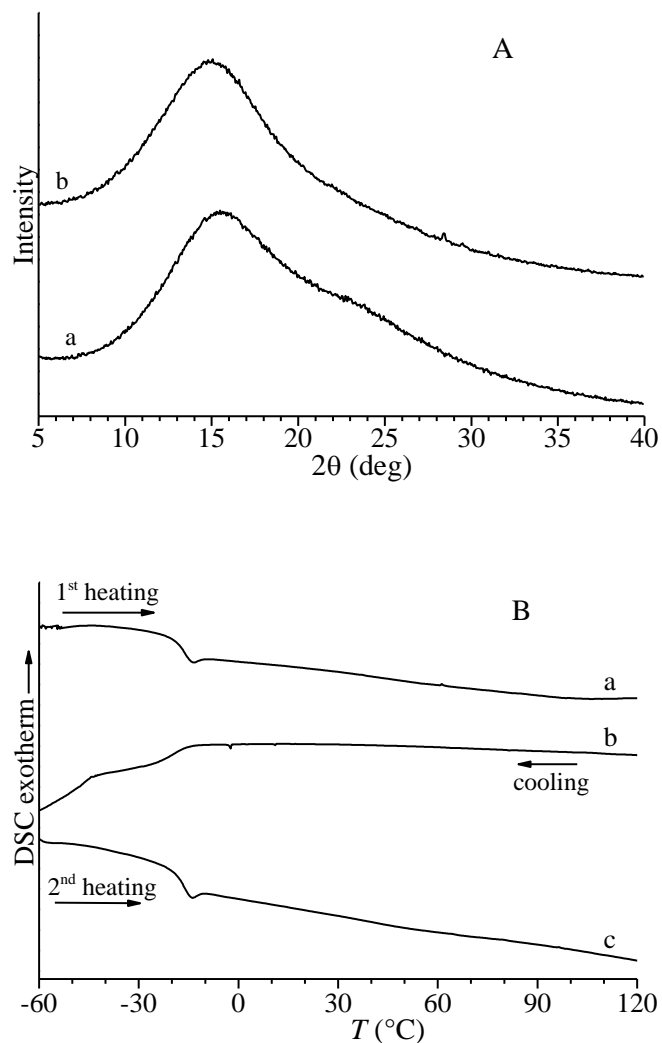


Figure 4.15. X-ray powder diffraction profiles (A) of the as-prepared sample (a) and of the compression-molded sample (b) and DSC curves (B) recorded during heating of the as-prepared sample (a), cooling (b) and successive second heating (c) at scanning rate of 10 °C/min, of the sample PIaltCo with regular alternating *cis*-1,4-*alt*-3,4 structure synthesized with the Co based catalyst 1b of Figure 4.9.

The stress-strain curve of the compression molded films of the sample PIaltCo is shown in Figure 4.16. Also for this sample low modulus and stresses are observed with viscous flow at rather high values strain and breaking at 600% deformation.

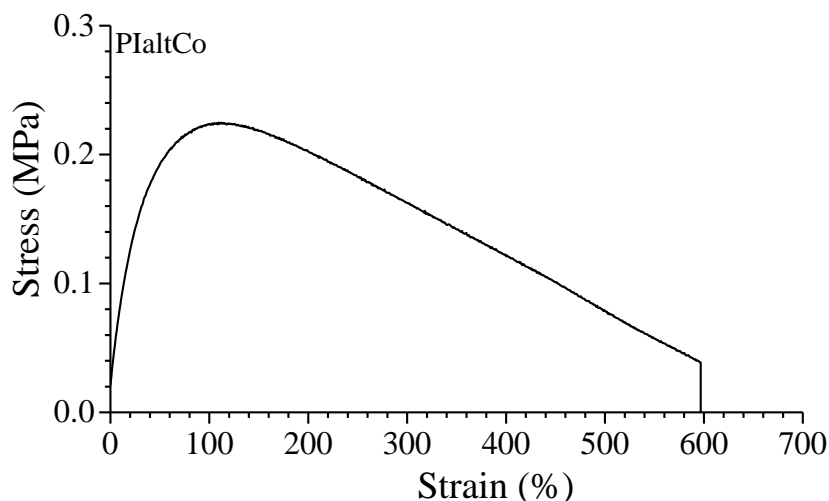


Figure 4.16. Stress-strain curve of compression-molded films of the sample PIaltCo with regular alternating *cis*-1,4-*alt*-3,4 structure synthesized with the Co based catalyst 1b of Figure 4.9.

4.2.7 Random *cis*-1,4/3,4 poly(isoprene)s with prevailing 3,4 syndiotactic structure from Cu based catalysts

The polymerization of isoprene with the catalysts based on CuCl₂(bipy)/MAO system gives poly(isoprene)s of high molecular mass having an essentially 3,4 syndiotactic structure, with about 75 mol% of 3,4 syndiotactic units (3,4s) and 25 mol% of randomly distributed *cis*-1,4 units (six samples PI_{3,4s}Cu1 - PI_{3,4s}Cu6 of Table 4.1). Furthermore, the concentration of *rr* diads in the sequences of 3,4 syndiotactic units are in the range 40-57% (Table 4.1).

The X-ray powder diffraction profiles of the as-prepared specimens of the six samples PI_{3,4s}Cu1 - PI_{3,4s}Cu6 are reported in Figure 4.17. All samples are crystalline with different degrees of crystallinity depending on the composition from 20 to 32% that increase with increasing concentration of the 3,4 units. Only the sample PI_{3,4s}Cu4 with lower concentration of 3,4 syndiotactic units (68.2 mol%) and lower stereoregularity (40.5 mol% of *rr* diads) is almost amorphous with very low crystallinity (3%). The presence in all the diffraction profiles of Figure 4.17 of the reflections at $2\theta = 13.9^\circ$, 15° and 22° indicates that the sample crystallize in the stable crystalline form of 3,4-syndiotactic poly(isoprene).^{54,58} The reflections at $2\theta = 13.9^\circ$, 15° and 22° , indeed, correspond to the 020, 110 and 021 reflections of the stable form of 3,4 syndiotactic poly(isoprene) characterized by the orthorhombic unit cell with axes $a = 6.6 \text{ \AA}$, $b = 13.2 \text{ \AA}$ and $c = 5.27 \text{ \AA}$ (space group *Pbcm*) and chains in the ordered trans-planar conformation.⁵⁸

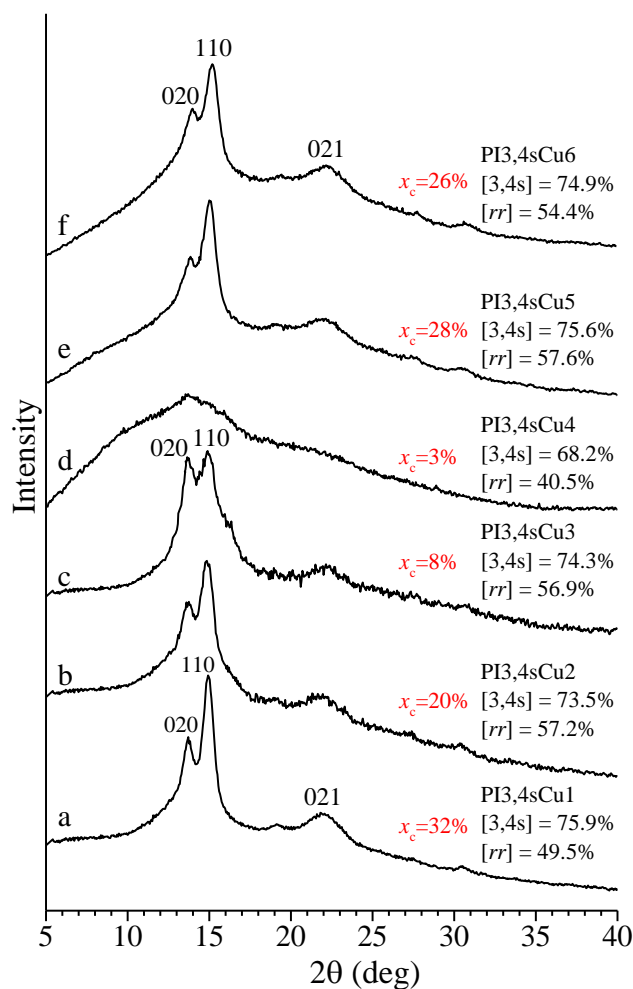


Figure 4.17. X-ray powder diffraction profiles of PI samples having a prevailing 3,4 syndiotactic structure with concentration of 3,4 syndiotactic units in the range 68 – 75% and concentration of *rr* diads in the range 40-57% prepared with the catalyst $\text{CuCl}_2(\text{bipy})/\text{MAO}$ (samples PI3,4sCu1 - PI3,4sCu6 of Table 4.1). The crystallinity and the 020, 110 and 021 reflections at $2\theta = 13.9$, 15 and 22° , respectively, of the crystalline form of 3,4 syndiotactic poly(isoprene)^{54,58} are indicated.

Therefore, in the samples PI3,4sCu1 - PI3,4sCu6 the presence of not negligible amount of *cis*-1,4 units does not prevent crystallization and the amount 3,4 syndiotactic units and their stereoregularity are enough to produce sequences of 3,4 syndiotactic units long enough to allow their crystallization.

The DSC thermograms of the samples PI3,4sCu1 - PI3,4sCu6 of Figure 4.17 are reported in Figure 4.18. As for the other samples of Table 4.1 discussed above, the samples have been first heated up to 170°C to eliminate previous thermal history of the as-prepared samples allowing eventual evaporation of residual solvent, then the DSC thermograms have been recorded during cooling from 170°C down to -80°C (Figure 4.18A) and during successive heating from -80°C up to 140°C (Figure 4.18B) at scanning rate of $10^\circ\text{C}/\text{min}$. According to the X-ray diffraction profiles, all samples crystallize by cooling from the melt at temperatures between

65 and 78 °C (Figure 4.18A) and melt in the successive heating scan at temperatures between 105 and 115 °C. Only the almost amorphous sample PI3,4sCu4 that shows a broad halo in the diffraction profile (curve d of Figure 4.17), does not present exothermic or endothermic peaks in the DSC cooling and heating scans (curves d of Figure 4.18). Moreover, in the thermograms of all samples a glass transition temperature between 0 °C and 10 °C is observed in both cooling and heating scans (Figure 4.18).

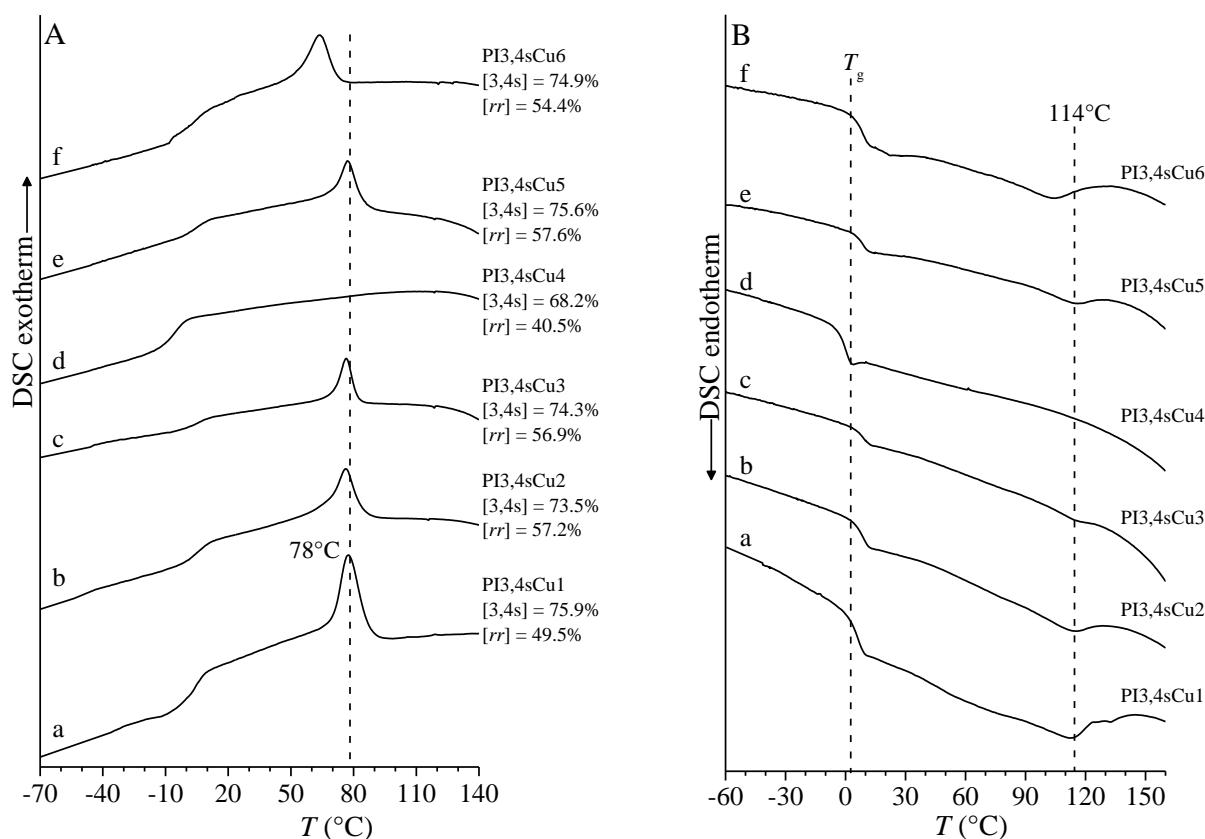


Figure 4.18. DSC curves recorded during cooling (A) and successive heating (B) at scanning rate of 10 °C/min of PI samples having a prevailing 3,4 syndiotactic structure with concentration of 3,4 syndiotactic units in the range 68 – 75% and concentration of *rr* diads in the range 40-57% prepared with the catalyst CuCl₂(bipy)/MAO (samples PI3,4sCu1 - PI3,4sCu6 of Table 4.1).

The values of the glass transition temperature are reported in Table 4.2 and in Figure 4.13 as a function of the concentration of *cis*-1,4 unit. The values of crystallization and melting temperatures of samples PI3,4sCu1- PI3,4sCu6 along with those of the samples PI3,4sFe1 – PI3,4sFe3, which will be discussed in the next section (4.2.8), are reported in Table 4.4 and in Figure 4.19 as a function of the concentration of 3,4 syndiotactic units. It is evident from the data of Figure 4.19 that both the crystallization and the melting temperatures decrease with decreasing concentration of 3,4 syndiotactic units.

Table 4.4. Values of the crystallization and melting temperatures of samples PI3,4sCu1 - PI3,4sCu6 with a random *cis*-1,4/3,4-syndiotactic structure with prevailing 3,4 syndiotactic units from CuCl₂(bipy)/MAO and of samples PI3,4sFe1 - PI3,4sFe3 with a regular 3,4-syndiotactic structure from FeCl₂(bipy)/MAO.

entry	[<i>cis</i> 1,4] (mol%)	T_c (°C) ^a	T_m (°C) ^b
PI3,4sCu1	24.1	78	113.0
PI3,4sCu2	26.5	76.2	114.2
PI3,4sCu3	25.7	76.5	114.7
PI3,4sCu4	31.8	-	-
PI3,4sCu5	24.4	77	115.4
PI3,4sCu6	25.1	68.9	105.5
PI3,4sFe1	10	116.6	151.8
PI3,4sFe2	10	124.8	158.4
PI3,4sFe3	10	121.6	152.6

^a) crystallization temperature evaluated from the DSC cooling curves from 170-200°C down to -70 °C at cooling rate of 10 °C/min.

^b) melting temperature evaluated from the second DSC heating curves after cooling from 170-200°C down to -70 °C at cooling and heating rates of 10°C/min

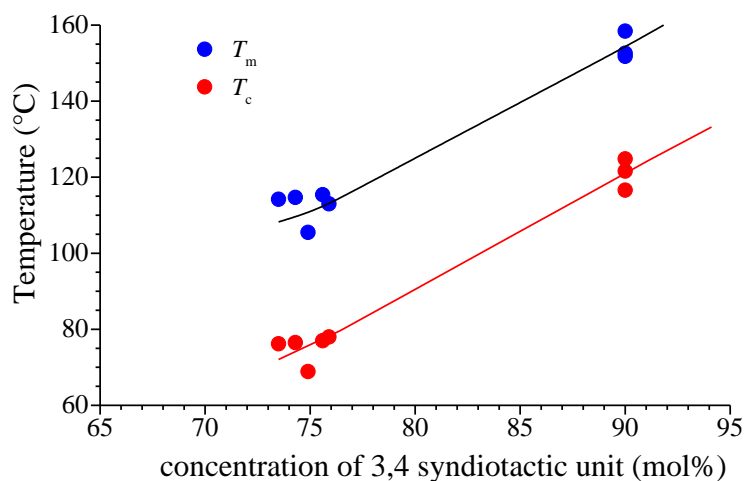


Figure 4.19. Values of the melting T_m (●) and crystallization T_c (●) temperatures of samples PI3,4sCu1-PI3,4sCu6 having a random *cis*-1,4/3,4-syndiotactic structure and samples PI3,4sFe1- PI3,4sFe3 having a regular 3,4 syndiotactic structure as a function of the concentration of 3,4-syndiotactic units.

4.2.8 Regular 3,4 syndiotactic poly(isoprene)s from Fe based catalyst

The polymerization of isoprene with the catalysts based on $\text{FeCl}_2(\text{bipy})/\text{MAO}$ system also gives poly(isoprene)s having a prevalent 3,4 syndiotactic structure, with concentration of 3,4 unit of 90% (samples PI3,4sFe1 - PI3,4sFe3 of Table 1). Moreover, these samples are highly stereoregular, with a higher concentration of *rr* diad than samples with the predominantly 3,4-syndiotactic structure synthesized with the copper-based complex (paragraph 4.2.7). The X-ray powder diffraction profiles of the as-prepared and melt-crystallized compression-molded samples of the three samples PI3,4sFe1 - PI3,4sFe3 are reported in Figure 4.20.

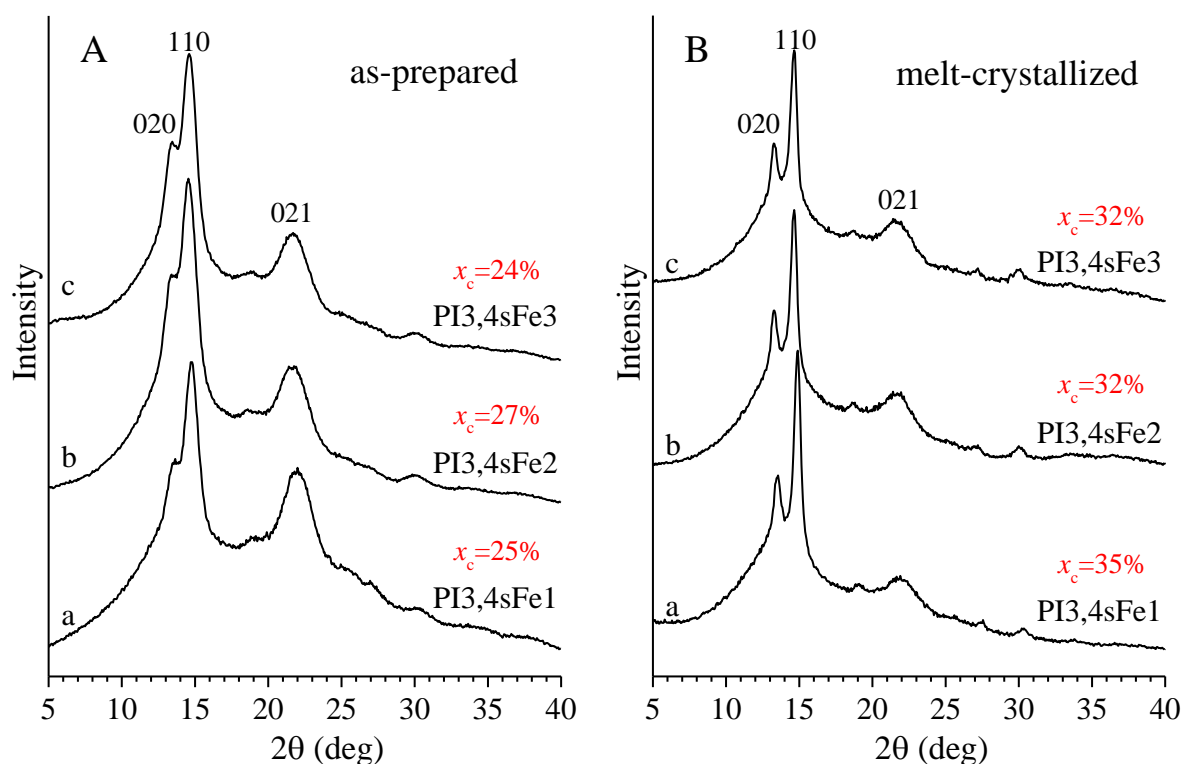


Figure 4.20. X-ray powder diffraction profiles of the as-prepared (A) and melt-crystallized compression-molded samples (B) of PIs having a prevailing 3,4 syndiotactic structure with concentration of 3,4 unit of 90% prepared with the catalyst $\text{FeCl}_2(\text{bipy})/\text{MAO}$. The crystallinity and the 020, 110 and 021 reflections at $2\theta = 13.9$, 15 and 22° , respectively, of the crystalline form of 3,4 syndiotactic poly(isoprene)^{54,58} are indicated.

All three samples are crystalline with degrees of crystallinity of nearly 25% in the as-prepared samples (Figure 4.20A) that increases to 30-35% in the melt-crystallized samples (Figure 4.20B). As in the case of the samples of Figure 4.17 prepared with the catalyst $\text{CuCl}_2(\text{bipy})/\text{MAO}$, the diffraction profiles of Figure 4.20 present the 020, 110 and 021 reflections at $2\theta = 13.9^\circ$, 15° and 22° of the crystalline form of 3,4 syndiotactic poly(isoprene). This confirms that all three samples PI3,4sFe1 - PI3,4sFe3 have a predominant 3,4 syndiotactic structure and crystallize in the stable form of 3,4 syndiotactic poly(isoprene)⁵⁸.

The DSC thermograms of the samples PI3,4sFe1 - PI3,4sFe3 recorded during heating of the as-prepared samples up to 200 °C, cooling from the melt down to -70 °C and successive heating of the melt-crystallized samples at scanning rate of 10 °C/min are reported in Figure 4.21. The DSC curves show that the three samples melt at temperatures of 153-158 °C and crystallize at temperatures of 118-125 °C, that is at temperatures much higher than the melting and crystallization temperatures of the samples PI3,4sCu1 - PI3,4sCu8 of Figure 4.18 ($T_m = 103 - 115$ °C and $T_c = 65$ and 78 °C). This is in agreement with the regular 3,4 syndiotactic structure of the samples PI3,4sFe1 - PI3,4sFe3 (with concentration of 3,4 unit of 90%), and lower concentration of 3,4 units of the samples PI3,4sCu1 - PI3,4sCu8 (about 75%). The DSC curves also show a glass transition temperature of the three samples PI3,4sFe1 - PI3,4sFe3 of about 16 °C (Figure 4.21B,C), higher than that of the samples PI3,4sCu1 - PI3,4sCu8, according with the regular 3,4 syndiotactic structure of the samples PI3,4sFe1 - PI3,4sFe3 and very low concentration of *cis*-1,4 unit. The values of the glass transition temperature are reported in Table 4.2 and in Figure 4.13 as a function of the concentration of *cis*-1,4 units. The values of crystallization and melting temperature are reported in Table 4.4 and in Figure 4.19 as a function of the concentration of 3,4 syndiotactic units. It is still confirmed from the data of Figures 4.13 and 4.19 that the glass transition temperature decreases linearly with increasing concentration of *cis*-1,4 units and the melting and crystallization temperatures increase with increasing concentration of 3,4 units.

The stress-strain curves of compression-molded films of the three samples PI3,4sFe1 - PI3,4sFe3 are reported in Figure 4.22. It is apparent that the presence of non-negligible crystallinity (Figure 4.20) prevents viscous flow and the samples show better mechanical properties of deformability and flexibility with plastic deformation via evident yielding and breaking at relatively high strain around 300-400%, with relatively high values of tensile strength and modulus between 50 and 85 MPa (Figure 4.22). The values of the mechanical parameters are reported in Table 4.5. All three samples show elastic properties with low values of tension set and almost complete elastic recovery after breaking, the values of the percentage of deformation recovered after breaking (R_b in Table 4.5) being close to 80% (Figure 4.22 and Table 4.5).

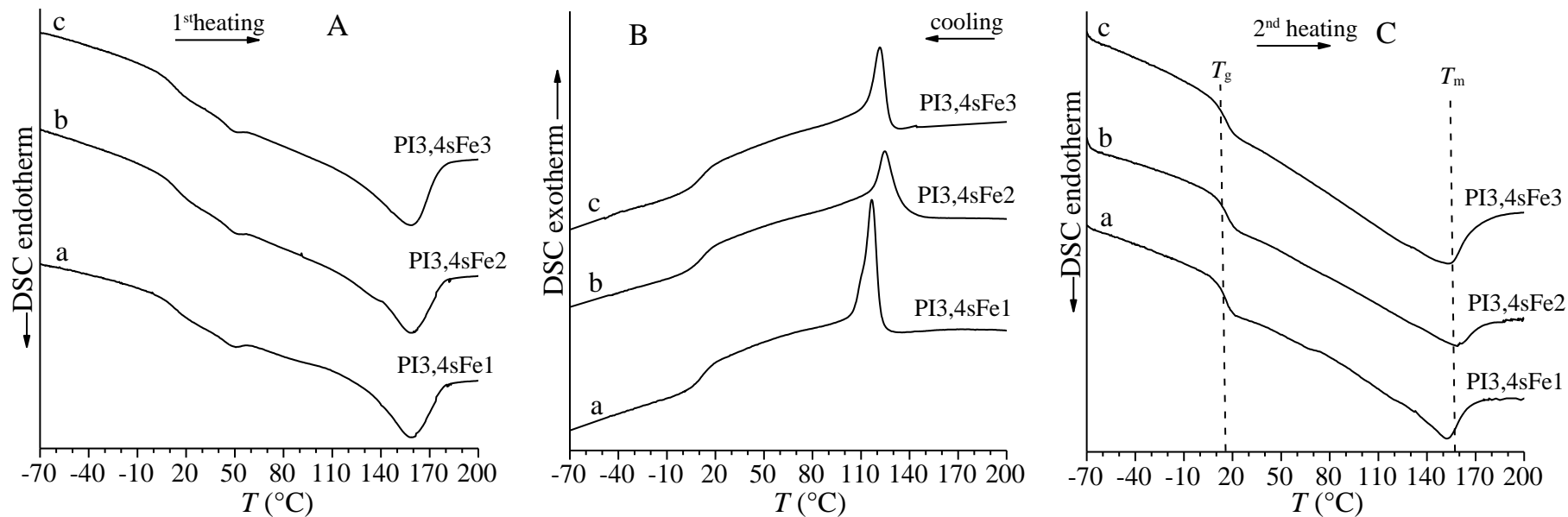


Figure 4.21. DSC curves recorded during heating of the as-prepared samples (A) cooling from the melt (B) and successive heating (C) at scanning rate of 10 $^{\circ}\text{C}/\text{min}$ of PI samples having a regular 3,4 syndiotactic structure with concentration of 3,4 syndiotactic units of 90% prepared with the catalyst $\text{FeCl}_2(\text{bipy})/\text{MAO}$.

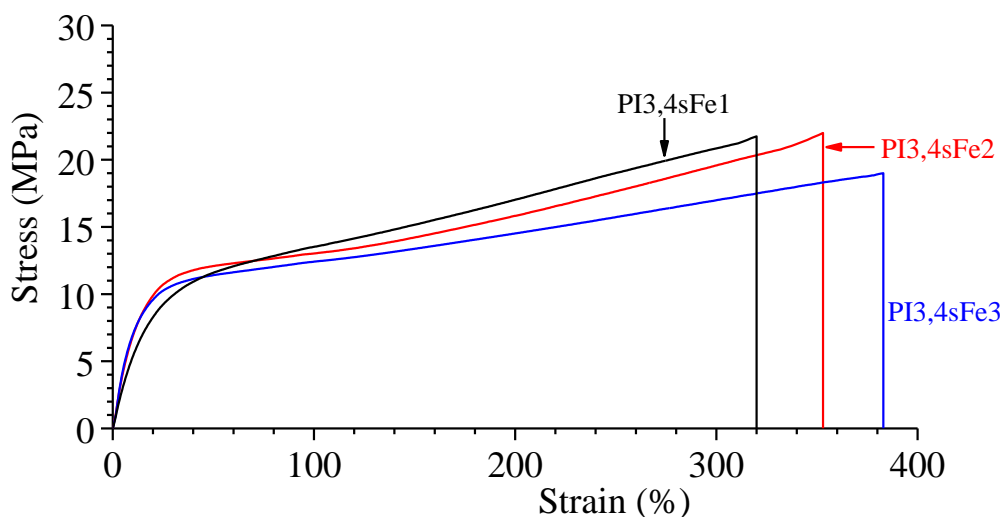


Figure 4.22. Stress-strain curves of PI samples having a regular 3,4 syndiotactic structure with concentration of 3,4 syndiotactic units of 90% prepared with the catalyst $\text{FeCl}_2(\text{bipy})/\text{MAO}$.

Table 4.5. Average values of Young modulus (E), strain (ϵ_y) and stress (σ_y) at yielding, strain (ϵ_b) and stress at break (σ_b), tension set (t_b) and percentage of deformation recovered after breaking (R_b), and crystallinity (x_c) of samples of poly(isoprene)s having a regular 3,4 syndiotactic structure with concentration of 3,4 syndiotactic units of 90% prepared with the catalyst $\text{FeCl}_2(\text{bipy})/\text{MAO}$.

entry	E (MPa)	ϵ_y (%)	σ_y (MPa)	ϵ_b (%)	σ_b (MPa)	t_b (%)	R_b (%)
PI3,4sFe1	37 ± 3	39	10.6	320 ± 64	22 ± 3	60 ± 2	81
PI3,4sFe2	84 ± 4	30	11	353 ± 34	22 ± 2	95 ± 6	73
PI3,4sFe3	76 ± 3	28	10.5	383 ± 14	19 ± 1	90 ± 16	77

The elastic properties of the samples PI3,4sFe1 - PI3,4sFe3 have been analyzed performing successive mechanical cycles of stretching and compression on stress-relaxed films previously stretched at a defined deformation and then relaxed. The stress-relaxed films have been prepared by stretching compression-molded films up to maximum deformation of 200% (ϵ_{\max}) and then removing the tension allowing relaxation. For all three samples, after removing the tension from 220% deformation elastic recovery $R(\epsilon_{\max})$ of nearly 80-85% has been observed (Table 5). The stress-strain hysteresis cycles performed on the stress-relaxed films of the three samples PI3,4sFe1, PI3,4sFe2, and PI3,4sFe3 are reported in Figure 4.23. The cycles clearly indicate that all samples show elastic recovery with residual deformation (tension set) of 10-20% after the first cycle, which decreases to nearly zero after successive cycles, the second and third cycles being nearly coincident. The hysteresis also decreases in cycles successive to the first one (Figure 4.23). The values of tension set $t_s(\epsilon_{\max})$ and percentage of recovered strain

$R(\epsilon_{\max})$ observed after preparation of the stress-relaxed films and the values of tension set and of the percentage of dissipated energy (hysteresis) observed at the end of each cycle of Figure 4.23 are reported in Table 4.6.

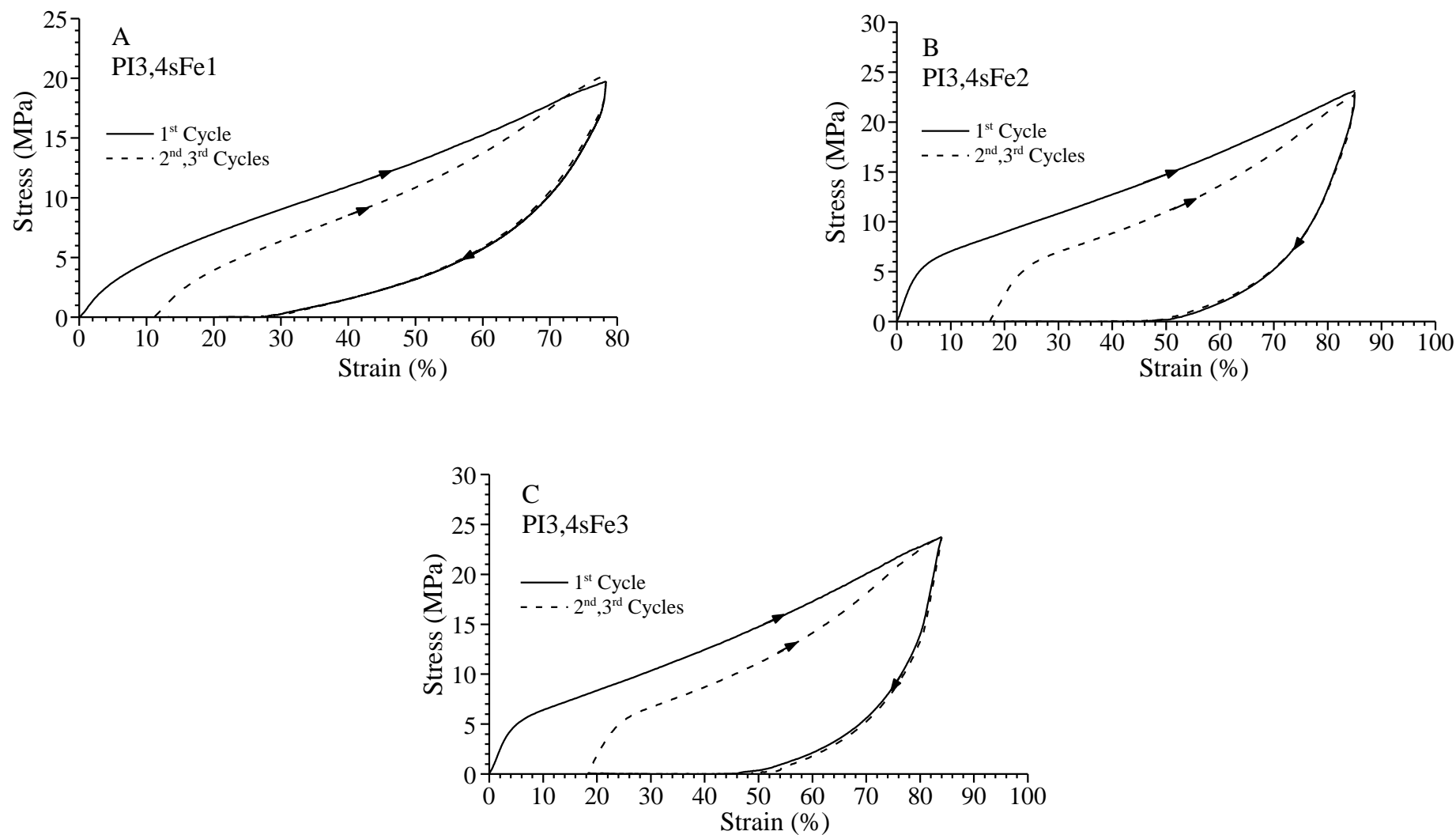


Figure 4.23. Stress-strain hysteresis cycles of stress-relaxed films of the PI samples PI3,4sFe1 (A), PI3,4sFe2 (B) and PI3,4sFe3 (C) having a regular 3,4 syndiotactic structure with concentration of 3,4 syndiotactic units of 90% prepared with the catalyst $\text{FeCl}_2(\text{bipy})/\text{MAO}$.

Table 4.6. Values of maximum deformation ϵ_{\max} achieved in the preparation of stress-relaxed films, tension set $t_s(\epsilon_{\max})$ and percentage of strain recovered $R(\epsilon_{\max})$ observed after removing the tension from the maximum deformation and the values of tension set and of the percentage of dissipated energy (W) observed at the end of each mechanical cycle of Figure 4.23 of the PI samples PI3,4sFe1, PI3,4sFe2 and PI3,4sFe3 having a regular 3,4 syndiotactic structure with concentration of 3,4 syndiotactic units of 90%.

entry	ϵ_{\max} (%)	$t_s(\epsilon_{\max})$ (%)	$R(\epsilon_{\max})$ (%)	t_s (%)	t_s (%)	W_1 (%)	W_{2-3} (%)
				1 st cycle	2 nd -3 rd cycles	1 st cycle	2 nd -3 rd cycles
PI3,4sFe1	220	48 ± 3	78 ± 3	11 ± 1	2 ± 1	95	50
PI3,4sFe2	220	33 ± 5	85 ± 5	17 ± 1	4 ± 2	94	60
PI3,4sFe3	220	35 ± 3	84 ± 3	18 ± 4	4 ± 1	70	45

The deformation behavior the elastic properties of the samples PI3,4sFe1, PI3,4sFe2 and PI3,4sFe3 have been further investigated by analysis of the possible occurrence of phase transformations and crystallization during deformation and relaxation. X-ray diffraction patterns of the samples PI3,4sFe1, PI3,4sFe2 and PI3,4sFe3 recorded during stretching of the compression-molded film at different degrees of deformations are reported in Figures 4.24-4.26. The corresponding profiles read along the equatorial layer line are also reported in Figures 4.24-4.26. The diffraction pattern of the undeformed compression-molded sample PI3,4sFe1 ($\epsilon = 0$) of Figure 4.24A,A' corresponds to the powder diffraction profile a of Figure 4.20B and shows un-oriented 020, 110 and 021 reflections at $2\theta = 13.9^\circ$, 15° and 22° of 3,4 syndiotactic poly(isoprene). Stretching produces polarization of the 020 and 110 reflections on the equator and of the 021 reflection on the first layer line (Figure 4.24B). However, the diffraction pattern of the fiber stretched at the maximum deformation of 300% presents only a broad equatorial reflection at $2\theta = 14^\circ$ (Figure 4.24C). Therefore, stretching at high deformation produces transformation of the two sharp 020 and 110 reflections into a unique broad reflection. This indicates formation of fibrils with small crystallites from fragmentation of lamellar stacks of the unoriented sample and/or transformation of the crystalline form of 3,4 syndiotactic poly(isoprene) (the orthorhombic form with axes $a = 6.6 \text{ \AA}$, $b = 13.2 \text{ \AA}$ and $c = 5.27 \text{ \AA}$ and space group $Pbcm$) into a mesomorphic form characterized by disorder in the lateral packing of chains having ordered trans-planar conformation. Similar considerations can also be made for samples PI3,4sFe2 and PI3,4sFe3 (Figures 4.25, 4.26). The diffraction patterns of the fibers relaxed upon removing the tension from the maximum deformation are shown in Figures 4.24D, 4.25C and 4.26C. As shown in Figure 4.23, the samples PI3,4sFe1 - PI3,4sFe3 present elastic recovery upon releasing the tension. The diffraction patterns of Figures 4.24D, 4.25C and 4.26C show the re-appearance of the 020 and 110 reflections at $2\theta = 13.9$ and 15° ,

indicating that the relaxation of the samples during elastic recovery produces recrystallization and transformation of the disordered mesomorphic form formed by stretching at high deformation into the crystalline orthorhombic form of 3,4 syndiotactic poly(isoprene). This transformation is reversible upon successive stretching and relaxation (Figures 4.24C,D, 4.25B,C and 4.26B,C).

Therefore, it is likely that the plastic deformation and the elastic behavior that characterizes these poly(isoprene) samples are associated with this reversible transformation.

PI_{3,4s}Fe₁

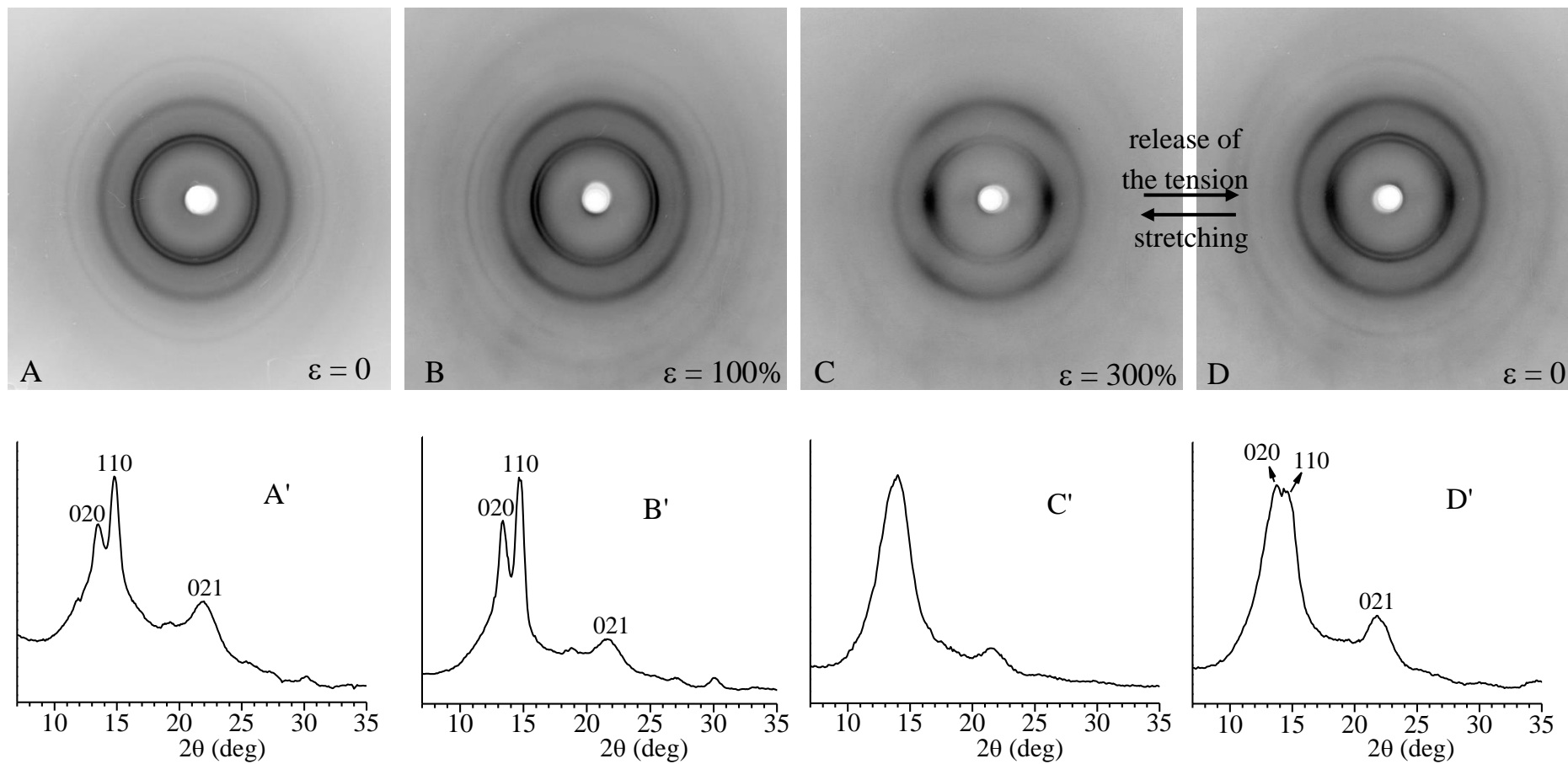


Figure 4.24. X-ray diffraction patterns of the compression-molded sample of the sample PI_{3,4s}Fe₁ stretched at the indicated different degrees of deformations ϵ (A-C) and after releasing the tension from the maximum strain (D), and corresponding profiles recorded along the equatorial layer line (A'-D'). The 020, 110 and 021 reflections at $2\theta = 13.9^\circ$, 15° and 22° are indicated.

PI_{3,4}sFe₂

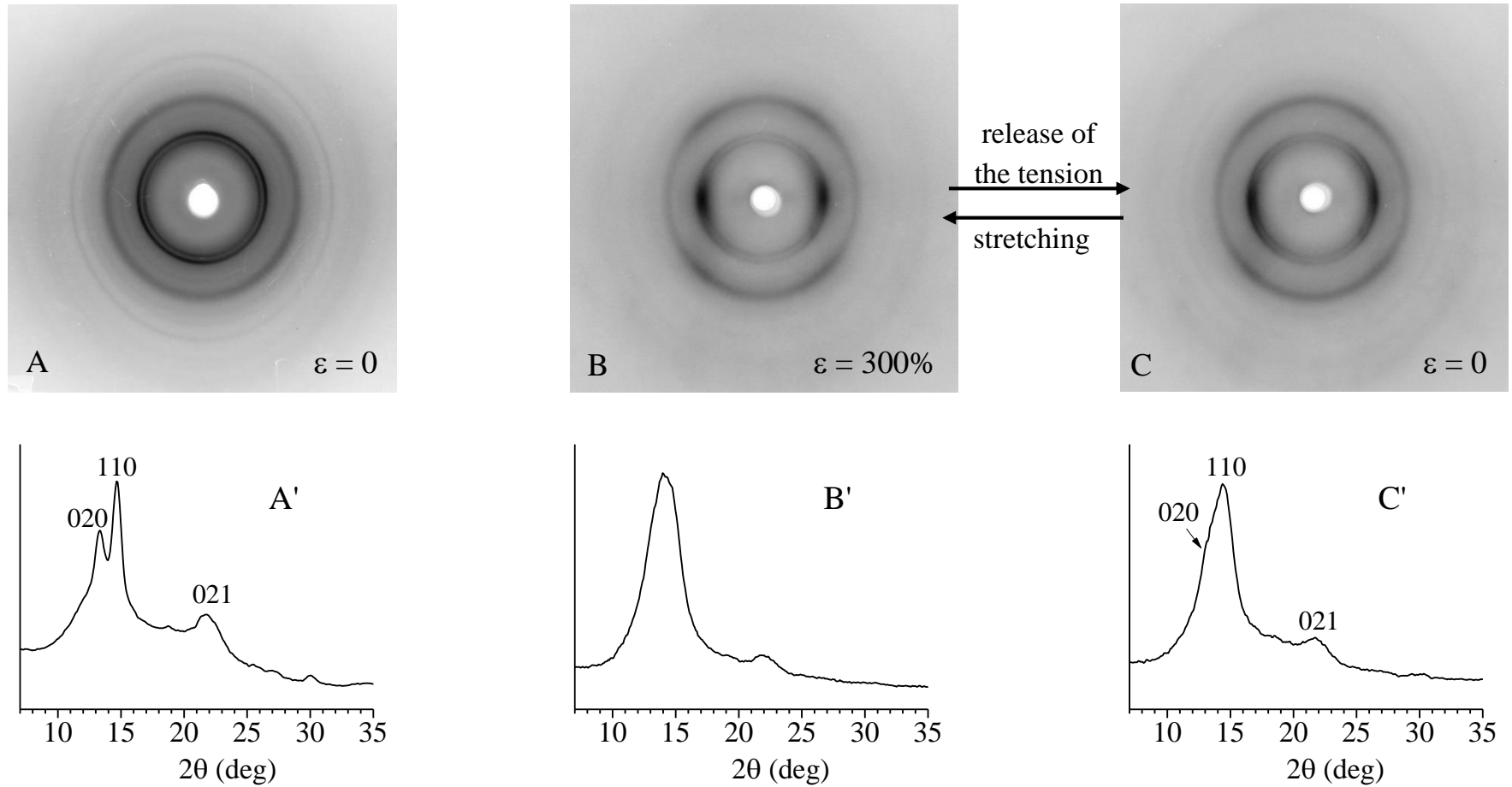


Figure 4.25. X-ray diffraction patterns of the compression-molded sample of the sample PI_{3,4}sFe₂ stretched at the indicated different degrees of deformations ϵ (A,B) and after releasing the tension from the maximum strain (C), and corresponding profiles recorded along the equatorial layer line (A'-C'). The 020, 110 and 021 reflections at $2\theta = 13.9^\circ$, 15° and 22° are indicated.

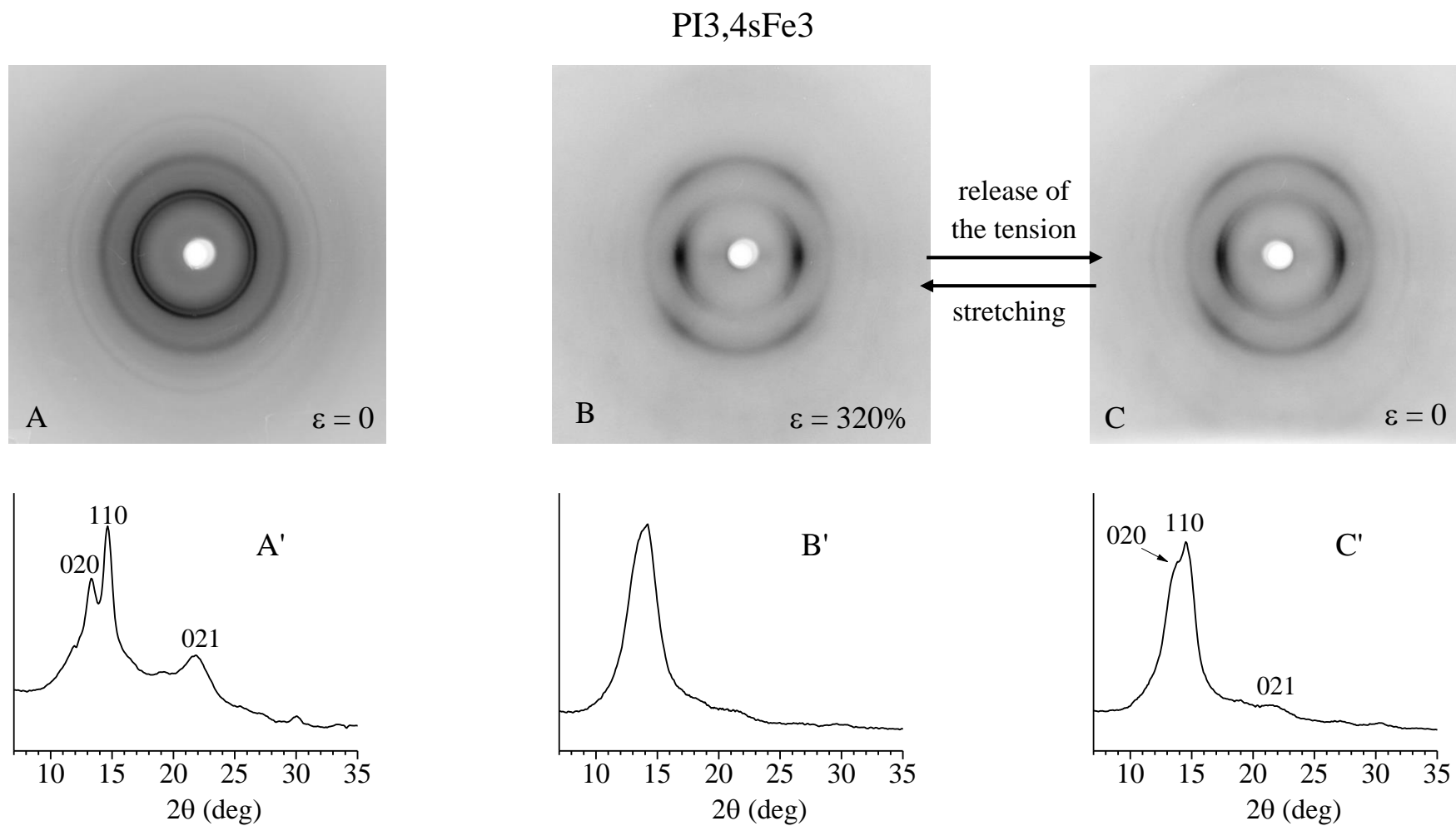


Figure 4.26. X-ray diffraction patterns of the compression-molded sample of the sample PI_{3,4}sFe₃ stretched at the indicated different degrees of deformations ϵ (A,B) and after releasing the tension from the maximum strain (C), and corresponding profiles recorded along the equatorial layer line (A'-C'). The 020, 110 and 021 reflections at $2\theta = 13.9^\circ$, 15° and 22° are indicated.

4.3 Synthesis and characterization of Stereoregular Poly(myrcene)s by Iron and Neodymium-based Catalysts

4.3.1 Materials and Methods

Poly(myrcene) samples (characterized with ^1H , ^{13}C analysis and SEC) were synthesized and supplied by Drs. Giovanni Ricci and Giuseppe Leone (CNR-ISMAL Milano) within a collaborative project.

X-ray powder diffraction profiles were recorded with Ni filtered Cu $K\alpha$ radiation by using an Empyrean diffractometer by Malvern Panalytical operating in the reflection geometry with continuous scans of the 2θ angle and scanning rate of 0.02 degree/s.

DSC scans were carried out on a Mettler 822 calorimeter equipped with a liquid nitrogen subambient device. The sample, ca. 4 mg, was placed in a sealed aluminum pan, and the measurements were carried out using heating and cooling rates of 10°C/min.

Compression molded films were prepared by heating the as-polymerized samples at temperatures of 120 °C under a press at low pressure and by slow cooling to room temperature. The mechanical properties were evaluated performing mechanical tests at room temperature on compression-molded films with a mechanical tester apparatus (Zwick by Zwick Roell) following the standard test method for tensile properties of thin plastic sheeting ASTM D882-83. Rectangular specimens 3 mm long, 2 mm wide and 0.3 mm thick have been stretched up to the break or up to a given deformation $\varepsilon = [(L_f - L_0)/L_0] \times 100$, where L_0 and L_f are the initial and final lengths of the specimen, respectively. Two benchmarks have been placed on the test specimens and used to measure elongation. In the mechanical tests, the ratio between the drawing rate and the initial length was fixed equal to 0.1 mm/(mm×min) for the measurement of Young's modulus and 10 mm/(mm×min) for the measurement of stress–strain curves and the determination of the other mechanical properties (stress and strain at break and tension set). The reported values of the mechanical parameters are averaged over at least five-eight independent experiments.

4.3.2 General Introduction

In recent years, interest in renewable resource polymers has grown enormously within both the scientific and industrial communities, and this is essentially attributable to the fact that i) fossil resources have finite availability and within the next century they will be nearly depleted; ii) the main oil producing countries are generally characterized by political instability which also determines a considerable fluctuation in prices with an overall tendency to rise and iii) the industrial activities associated with their transformation into commodity chemicals and polymers often cause significant environmental problems (e.g., accumulation of CO₂ in the atmosphere, global warming and dangerous climate change). In this context, all these issues have increased the necessity of finding sustainable alternatives to replace the petroleum-based diene monomers isoprene and butadiene that are currently used for the synthesis of synthetic rubber thermoplastic elastomers.⁷⁴ As a result, there is a growing interest in bio-based polymer materials made from renewable sources. One significant group of biomass chemicals is terpenes.⁷⁵⁻⁷⁹ They come from plants that are naturally abundant and employed, for example, in pharmaceutical products. Natural rubber, or *cis*-1,4-polyisoprene (PI), is the most well-known example of a polyterpene and accounts for around 40% of all rubber usage worldwide. β -myrcene is a member of the large family of terpenes which, due to the structural similarity to isoprene and butadiene and its large availability, has recently aroused a growing attention as building block for the synthesis of a vast range of polymers, including the elastomer synthesis. Myrcene can be polymerized using a variety of processes, including emulsion polymerization, controlled and free radical polymerization, and live anionic polymerization.⁷⁷⁻⁷⁹ In terms of molecular structure, poly(myrcene)s having *cis*-1,4, *trans*-1,4 and 3,4 structures were already obtained and characterized in literature (Figure 27).^{59,80-91} In this section, will be examined the polymerization of β -myrcene with different catalysts based on iron and neodymium complexes and the properties of the obtained poly(myrcene) samples will be discussed.

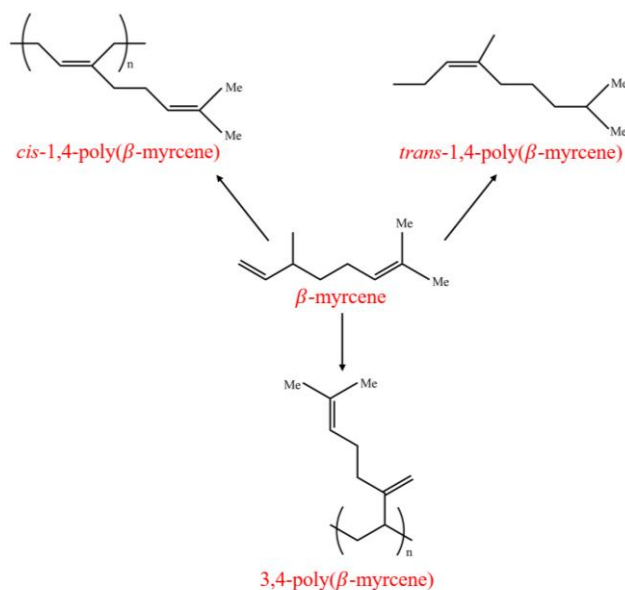


Figure 4.27. Stereoregular poly(β -myrcene)s.

4.3.3 Polymerization

Various poly(myrcene) samples have been prepared starting from β -Myrcene and using different iron and neodymium complexes (Figure 4.28) characterized by different ligands such as bipyridyl (complexes 4 of Figure 4.28) or iminopyridyl and monoalkyl-*N*-aryl substituted iminopyridine ligands (complex 1, 2, 3, 5, 7, 6 of Figure 4.28). All samples are reported in Table 4.6, where the catalysts and the molecular structures of the samples induced by the used catalysts and the molecular masses are shown. The samples are identified with the code PMcisAx or PMaltAx, where the symbols *cis* and *alt* indicate a *cis*-1,4 structure and a mainly alternating *cis*-1,4-*alt*-3,4 structure, respectively, whereas the symbol A indicates the catalyst (Nd, Fe) and x the number of the sample.

Neodymium based catalysts gave poly(myrcenes) with a rather high molecular weight, narrow polydispersion and an extremely high *cis*-1,4 content (around 97%) (samples PMcisNd1-PMcisNd3).

Catalysts based on iron complexes gave instead poly(myrcenes) with a mixed *cis*-1,4/3,4 structure. The polymer molecular weight was rather high (in the range 100-150000 $\text{g}\times\text{mol}^{-1}$) with a polydispersion around 2.

The amount and distribution mode of the *cis*-1,4 and 3,4 units along the polymeric chain was found to be different according to the nature of the used catalytic system. The poly(myrcene) obtained with the system $\text{Fe}(\text{bipy})_2\text{Cl}_2/\text{MAO}$ (complex 4 of Figure 4.28) exhibited a predominantly 3,4 structure (around 60%) (sample PMaltFe1), while the poly(myrcene)s

obtained with catalysts based on iminopyridyl iron complexes (3, 5, 6, 7 of Figure 4.28) exhibited a predominantly *cis*-1,4 structure (around 70%) (samples PMaltFe2- PMaltFe9).

The poly(myrcene) obtained with the catalyst 6 of Figure 4.28, in particular, exhibited a highly stereoregular and constitutionally regular structure, that is, an alternating *cis*-1,4-*alt*-3,4 structure in which, however, long *cis*-1,4 sequences (5 units) are present within the polymer chain (sample PMaltFe9).

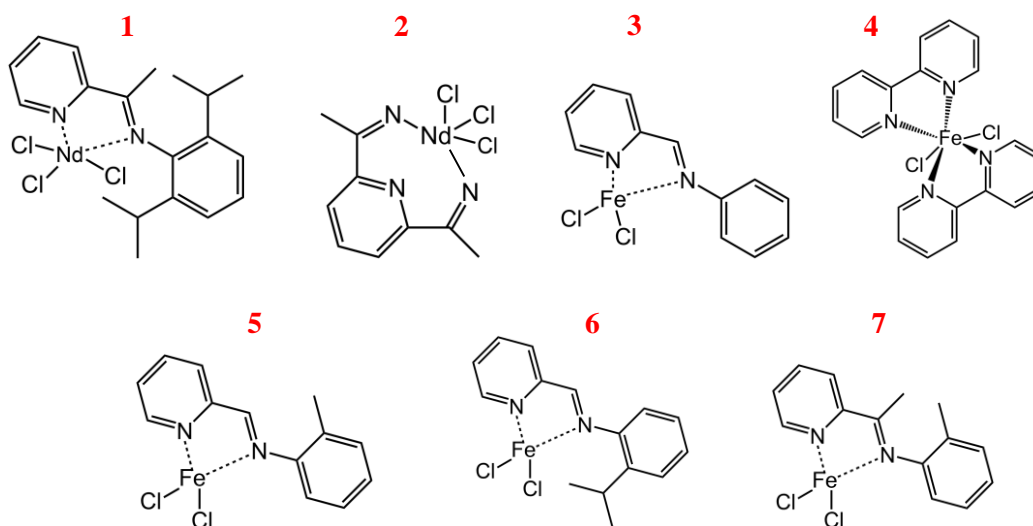


Figure 4.28. Iron and Neodymium complexes used for the synthesis of poly(myrcene) samples reported in Table 4.6.

Table 4.6. Conditions of polymerization of myrcene with catalysts based on complexes of Nd and Fe of Figure 4.28, concentrations of *cis*-1,4 and 3,4 units and molecular mass of the poly(myrcene) samples.

entry	cat	$M_w \times 10^{3*}$	M_w/M_n^*	<i>cis</i> -1,4 (mol%)**	3,4 (mol%)**
PMcisNd1	2			97	3
PMcisNd2	1	319	2.4	97	3
PMcisNd3	1			97	3
PMaltFe1	4			41.7	58.3
PMaltFe2	3	785	3.6	63.9	36.1
PMaltFe3	3	187	4.5	64.1	35.9
PMaltFe4	5	160	2.3	70.9	29.1
PMaltFe5	5	39	1.9	70.3	29.7
PMaltFe6	7	41	1.9	68.8	31.2
PMaltFe7	7	65	2.0	67.3	32.7
PMaltFe8	7	31	2.0	68.3	31.7
PMaltFe9	6	110	2.0	66.1	33.9

**determined by SEC.

**determined by ^1H and ^{13}C NMR.

4.3.4 Structural and thermal characterization

The X-ray powder diffraction profiles of the as-prepared and compression-molded samples of all samples of poly(myrcenes) of Table 4.6 are reported in Figure 4.29. All samples show diffuse scattering with two broad maxima at $2\theta = 7^\circ$ and 18° , indicating that all samples are amorphous according with the molecular structure, which although it is stereoregular, as described in the paragraph 4.3.3, contains a significant amount of constitutional defects with the presence of both *cis*-1,4 and 3,4 structural units, whose relative concentration depends on the catalyst (Table 4.6). Even in the case of samples PMcisNd1-PMcisNd3 prepared with Neodymium based catalysts characterized by high content of *cis*-1,4 units (about 97%), the presence of small concentration of 3,4 units prevent crystallization. Analogously, the sample PMaltFe1 prepared with the catalyst $\text{Fe}(\text{bipy})_2\text{Cl}_2$ (complex 4 of Figure 4.28) show a predominant 3,4 structure (around 60-70%) but with still high content of *cis*-1,4 units that prevents crystallization. Other samples prepared with iron based catalysts are characterized by alternating *cis*-1,4-*alt*-3,4 sequences but, again, with high concentration of *cis*-1,4 units that produce even rather long *cis*-1,4 sequences, giving a structure not sufficiently regular to crystallize.

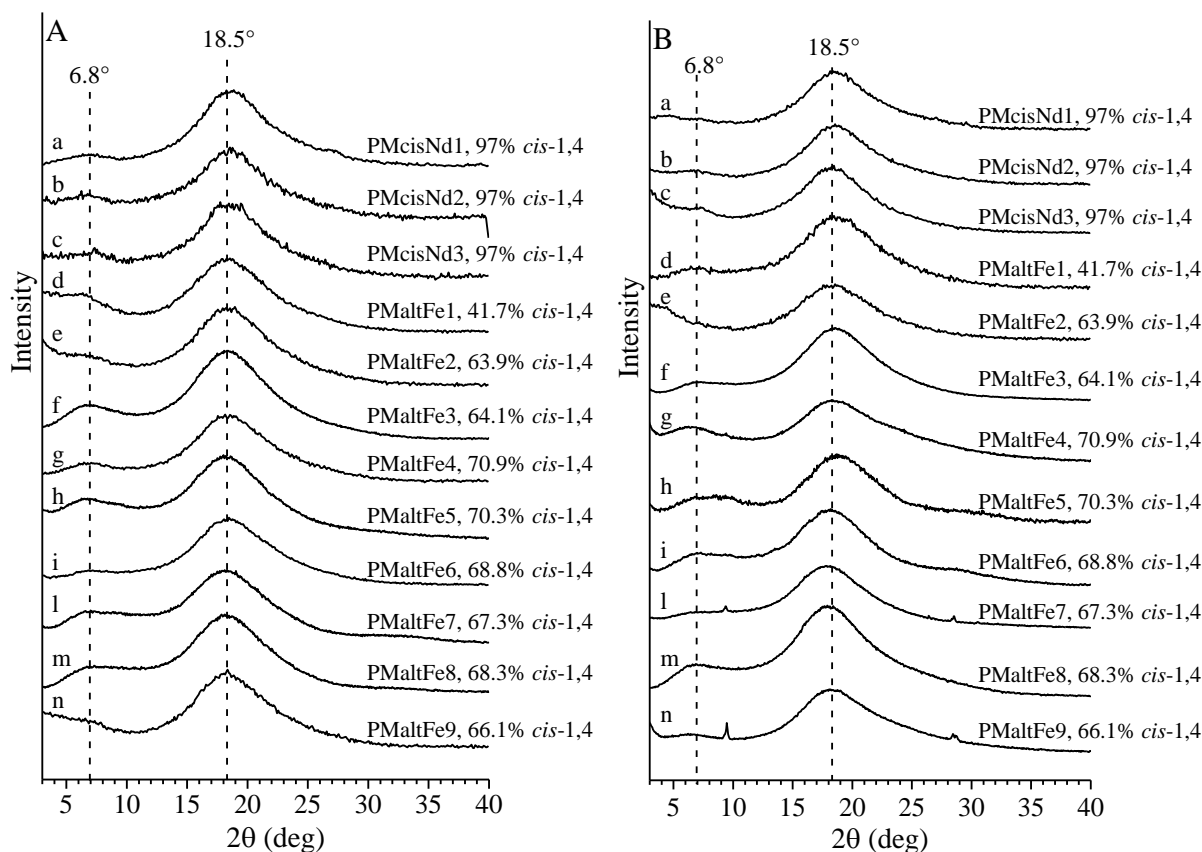


Figure 4.29. X-ray powder diffraction profiles of the as-prepared samples (A) and of the compression-molded samples (B) of poly(myrcene) samples PMcisNd1-PMcisNd3 having an almost regular *cis*-1,4 structure prepared with Nd based catalysts 1 and 2 of Figure 4.28 and samples PMaltFe1-PMaltFe9 having a predominantly alternating *cis*-1,4-*alt*-3,4 structure prepared with Fe based catalysts 3-7 of Figure 4.28.

The DSC curves of all the amorphous as-prepared samples of poly(myrcene) of Figure 4.29 recorded during heating show only a glass transition temperature around -60°C and absence of any endothermic or exothermic signals. The values of glass transition temperatures have been evaluated in the DSC cooling and successive heating curves recorded at the same scanning rates ($10^\circ\text{C}/\text{min}$) to avoid hysteresis phenomena. The DSC curves recorded during heating of the as-prepared samples up to 110°C , cooling from 110°C down to -80°C and successive heating are reported in Figure 4.30. Also these scans show absence of crystallization and melting phenomena.

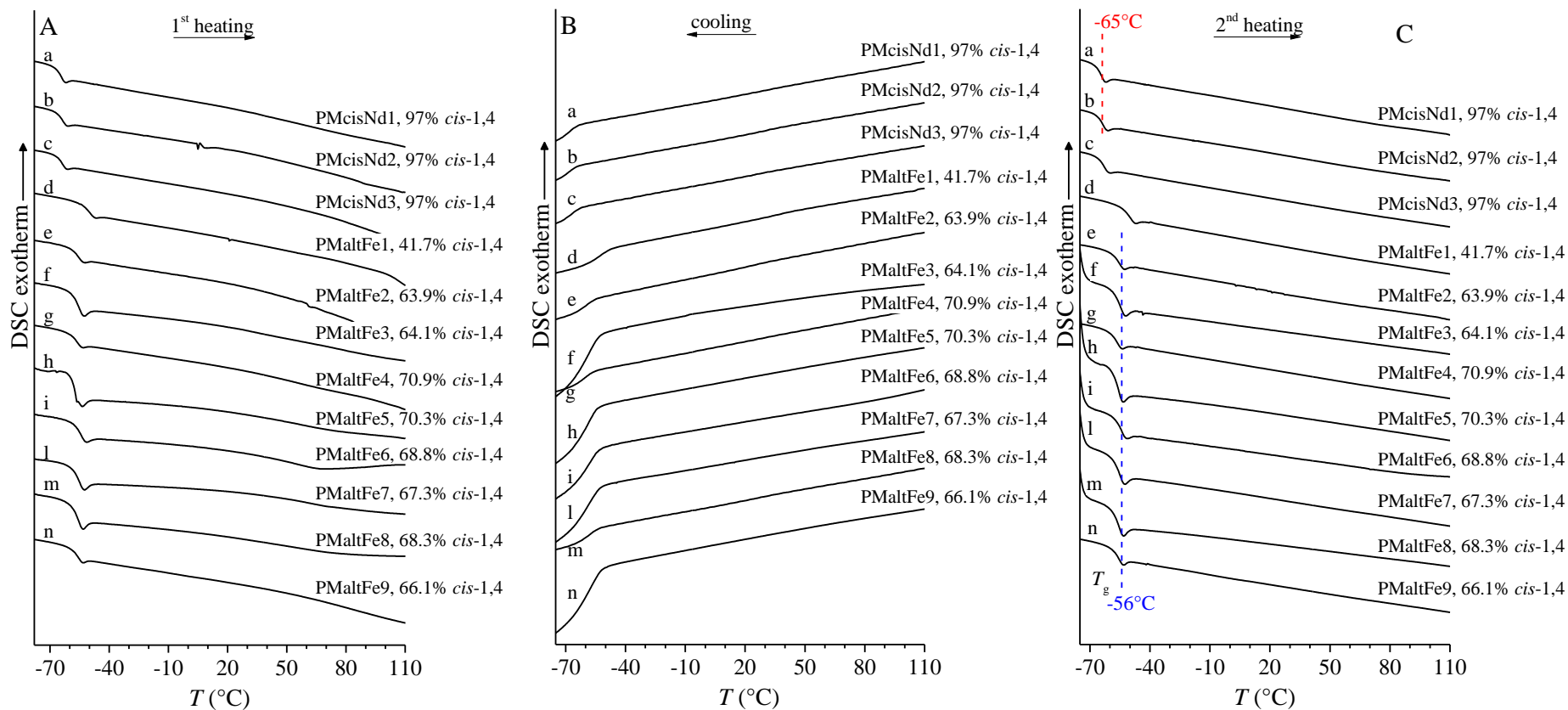


Figure 4.30. DSC curves recorded during heating of the as-prepared samples (A) cooling from the melt (B) and successive heating (C) at scanning rate of 10 °C/min of poly(myrcene) samples PMcisNd1-PMcisNd3 having an almost regular *cis*-1,4 structure prepared with Nd based catalysts 1 and 2 of Figure 4.28 and samples PMaltFe1-PMaltFe9 having a predominantly alternating *cis*-1,4-*alt*-3,4 structure prepared with Fe based catalysts 3-7 of Figure 4.28.

The values of the glass transition temperature evaluated from the DSC second heating curves of Figure 4.30C are reported in Table 4.7 and in Figure 4.31 as a function of the concentration of *cis*-1,4 units. It is apparent that the glass transition temperature decreases with increasing concentration of *cis*-1,4 units. In particular, the sample PMaltFe1 prepared with the catalyst Fe(bipy)₂Cl₂ with a predominant 3,4 structure and low amount of *cis*-1,4 units (41.7 mol%) shows the highest value of the glass transition temperature of -51 °C. Samples with 60-70 mol% of *cis*-1,4 units prepared with iron based catalysts or the sample PMaltFe9 with prevalent alternating *cis*-1,4-*alt*-3,4 structure, prepared with the system 6, show intermediate glass transition temperatures of -55 ÷ -57 °C. Finally, samples PMcisNd1, PMcisNd2 and PMcisNd3 prepared with Neodymium based catalysts characterized by high content of *cis*-1,4 units (about 97%) show the lowest glass transition temperature of about -65 °C.

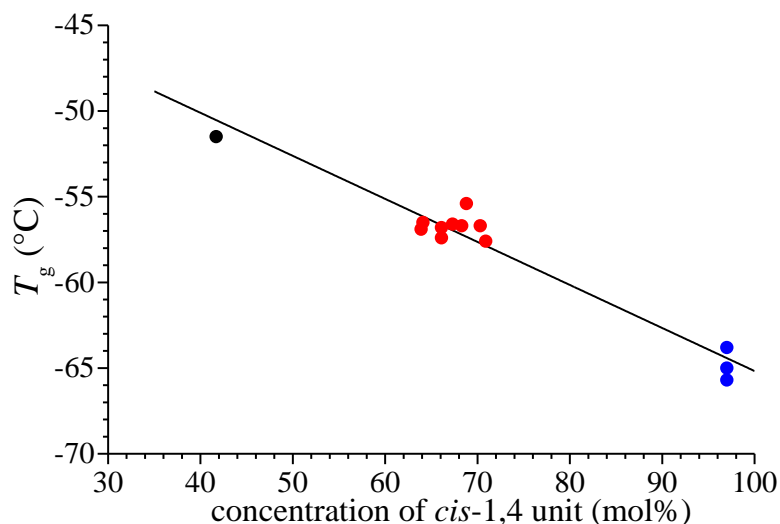


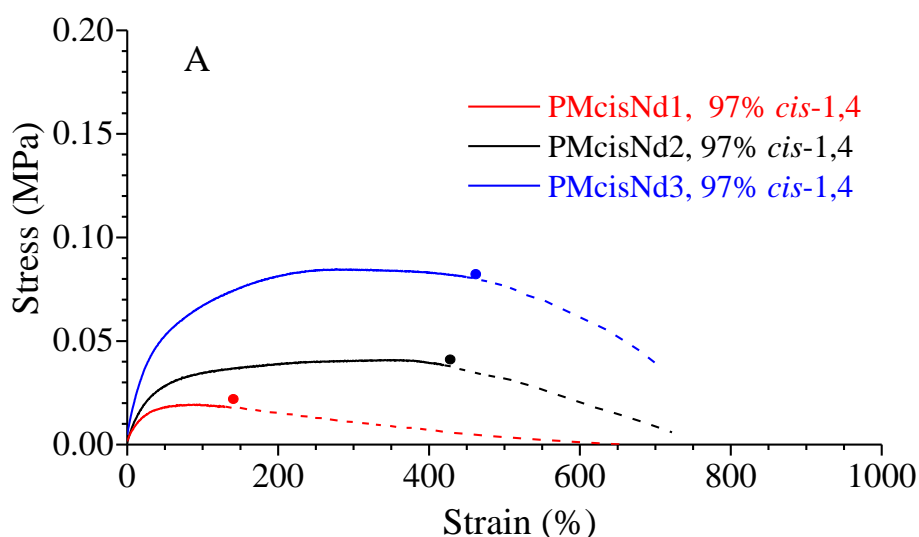
Figure 4.31. Values of glass transition temperature (T_g) of samples of poly(myrcene) having different molecular structures as a function of the concentration of *cis*-1,4 units, evaluated from the DSC heating curves of Figure 4.30C. Samples with almost regular *cis*-1,4 structure (●), alternating *cis*-1,4-*alt*-3,4 structure (●) and predominant 3,4 structure (●) are reported with different symbols.

4.3.5 Mechanical properties

Compression molded films of samples of poly(myrcene) of Table 4.6 have been prepared by heating the as-prepared powder samples up to 120 °C under a press at low pressure and slowly cooling down to room temperature. The stress-strain curves of compression-molded films of poly(myrcene) are reported in Figure 4.32. All samples show mechanical behavior typical of amorphous polymers with low values of modulus and stress at any strain. Moreover, the samples show uniform deformation without evident yielding up to achieve maximum values of stress at deformations in the range 300 - 600%. At higher deformations all samples

experience viscous flow without breaking up to 800-1000% strain (Figure 4.32). In particular, the three samples PMcisNd1, PMcisNd2 and PMcisNd3 with almost regular *cis*-1,4 structure (97% of *cis*-1,4 units) and lowest glass transition temperature, prepared with the neodymium catalysts Nd1 and Nd2, show lower values of modulus and stress and tensile stress.

The values of the mechanical parameters are reported in Table 4.7 and in Figure 4.33 as a function of the concentration of *cis*-1,4 units. As already shown for the polyisoprene samples (section 4.2.5), an additional mechanical parameter besides Young's modulus was also evaluated and reported in Table 4.7, namely the stress reached at a certain fixed strain value (100%). The values of Young modulus (Figure 4.33A) and stress at breaking (Figure 4.33C) decrease and deformation at break (Figure 4.33B) increases with increasing content of *cis*-1,4 units. The highest values of Young modulus and stress during deformation are observed for the samples PMaltFe9 with 66.1 mol% of *cis*-1,4 units characterized by an alternating *cis*-1,4-*alt*-3,4 structure in which are present long *cis*-1,4 sequences (5 units) (Figure 4.33A,C). Remarkable ductility with deformation at break around 800-1000% are observed for the samples PMcisNd1, PMcisNd2 and PMcisNd3 with almost regular *cis*-1,4 structure (97% of *cis*-1,4 units) and the samples with about 70 mol% of *cis*-1,4 units, as the samples PMaltFe4 and PMaltFe6 and PMaltFe7 prepared with the catalysts 5 and 7 of Figure 4.28 (Figure 4.32A, B).



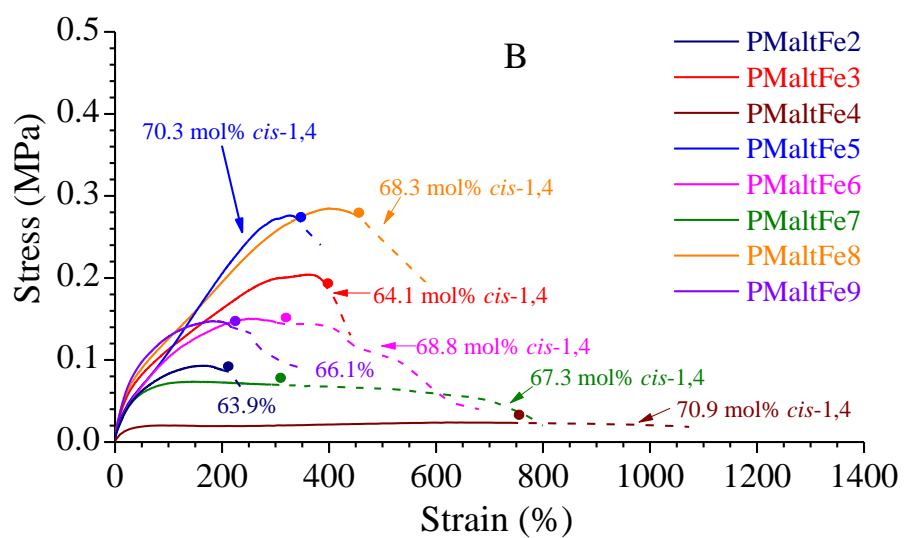


Figure 4.32. Stress-strain curves of compression molded films of samples of poly(myrcene) of Table 4.6 prepared with the Nd based catalysts 1 and 2 of Figure 4.28 (A) and with the Fe based catalysts 3-7 of Figure 4.28 (B).

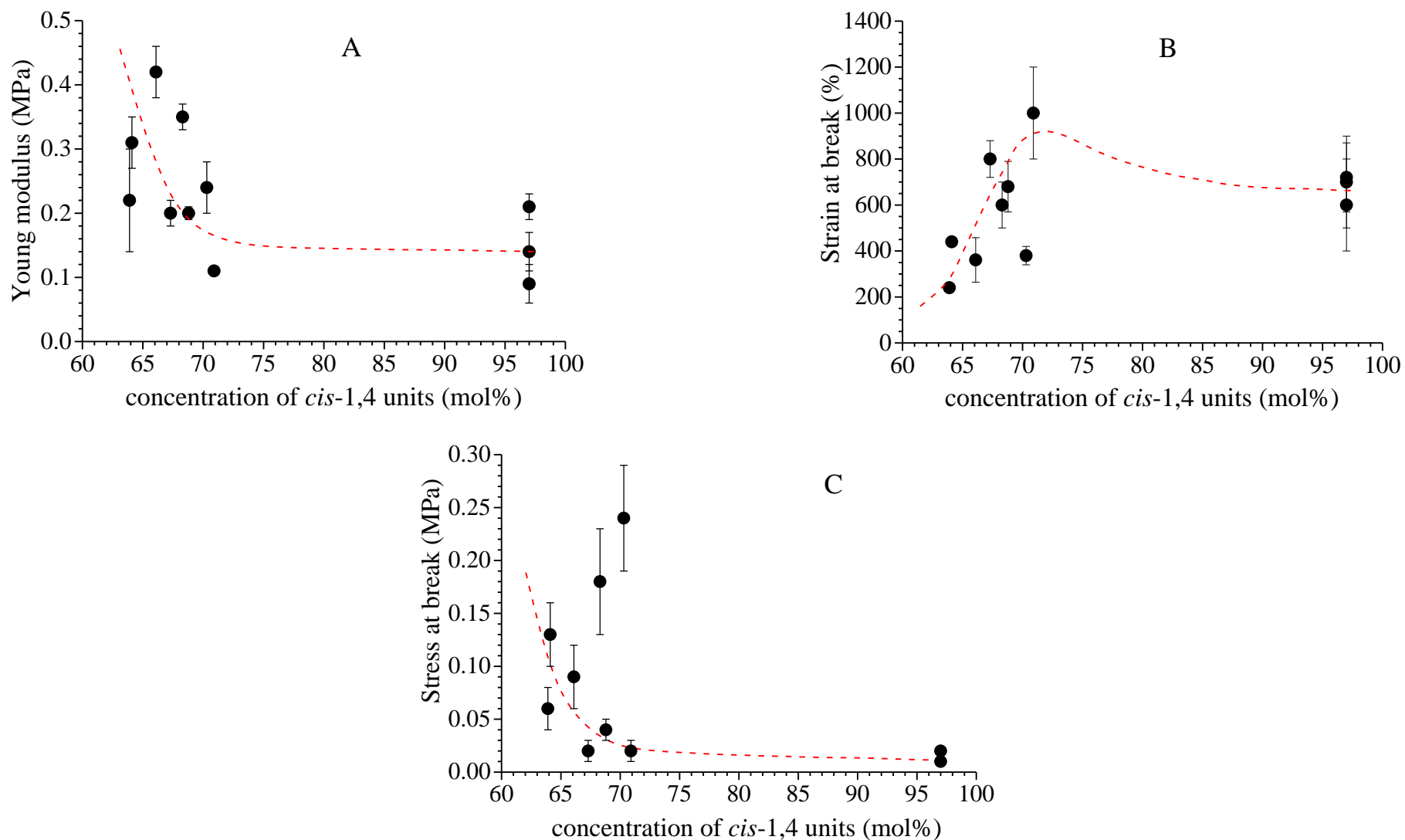


Figure 4.33. Average values of the Young modulus (A), deformation at break (B), stress at break (C) evaluated from the stress strain curves of Figure 4.32 of poly(myrcene)s obtained with neodymium and iron complexes based catalysts.

Table 4.7. Composition, molecular mass (M_w), polydispersion (M_w/M_n), glass transition temperature (T_g), average values of the Young modulus (E), stress at 100% of strain ($\sigma_{100\%}$) deformation at break (ε_b), stress at break (σ_b) and maximum stress before viscous flow ($\sigma_{b(max)}$) evaluated from the stress strain curves of Figure 4.32 of poly(myrcene)s obtained with neodymium and iron complexes based catalysts.

entry	Catalyst	<i>cis</i> -1,4 unit (%)	3,4 unit (%)	$M_w \times 10^3$	M_w/M_n	T_g^a (°C)	E (MPa)	$\sigma_{100\%}$ (MPa)	ε_b (MPa)	σ_b (MPa)	$\sigma_{b(max)}$ (MPa)
PMcisNd1	2	97	3			-65.0	0.14±0.03	0.02±0.01	720±100	0.01	0.02
PMcisNd2	1	97	3	319	2.4	-65.7	0.10±0.03	0.03±0.01	600±150	0.01	0.04
PMcisNd3	1	97	3			-63.8	0.21±0.02	0.07±0.01	700±150	0.02	0.08
PMaltFe1	4	41.7	58.3			-51.5	-	-	-	-	-
PMaltFe2	3	63.9	36.1	785	3.6	-56.9	0.22±0.08	0.08±0.02	240±20	0.06±0.02	0.09±0.02
PMaltFe3		64.1	35.9	187	4.5	-56.5	0.31±0.04	0.12±0.01	440±20	0.13±0.03	0.20±0.03
PMaltFe4	5	70.9	29.1	160	2.3	-57.6	0.11±0.01	0.02±0.01	1000±200	0.02±0.01	0.02±0.01
PMaltFe5		70.3	29.7	39	1.9	-56.7	0.24±0.04	0.12±0.03	380±40	0.24±0.05	0.28±0.04
PMaltFe6	7	68.8	31.2	41	1.9	-55.4	0.20±0.01	0.10±0.02	680±100	0.04±0.01	0.15±0.02
PMaltFe7		67.3	32.7	65	2.0	-56.6	0.20±0.02	0.07±0.02	800±80	0.02±0.01	0.07±0.01
PMaltFe8		68.3	31.7	31	2.0	-56.7	0.35±0.02	0.13±0.01	600±100	0.18±0.05	0.28±0.04
PMaltFe9	6	66.1	33.9	110	2.0	-57.4	0.42±0.04	0.13±0.03	361±97	0.09±0.03	0.15±0.02

^{a)} Glass transition temperature evaluated from the DSC heating curves of Figure 4.30C recorded at heating rate of 10 °C/min.

4.3.6 Conclusions Chapter 4

In this chapter the synthesis and the characterization of poly(isoprene)s and poly(myrcene)s having different molecular structure, obtained with different catalysts based on complexes of different metals (Nd, Co, Cu and Fe), was investigated. Concerning Poly(isoprene)s, samples with prevalent *cis*-1,4 structure has been prepared with Nd based catalyst, samples with regular alternating *cis*-1,4-*alt*-3,4 structure have been prepared with Co based catalyst, samples random *cis*-1,4/3,4 structure with prevalent 3,4 syndiotactic and concentration of 3,4 unit of nearly 75% have been prepared with CuCl₂(bipy) and samples with almost regular 3,4 syndiotactic structure with 90-100% of 3,4 units and low amount of *cis*-1,4 units have been obtained with FeCl₂(bipy). Finally, poly(isoprene)s with rather unusual predominantly alternating *cis*-1,4-*alt*-3,4 structure but containing along the polymer chain *cis*-1,4 unit sequences of different length (3 or 5 units) have been obtained with iron dichloride and copper dichloride pyridylimino complexes. The length of the *cis*-1,4 unit sequences is depending on the nature of the pyridylimine ligand coordinated to the metal atom.

The structure and the thermal and mechanical properties of all these novel poly(isoprene)s have been characterized and the relationships of the properties with the molecular structures determined by the different used catalysts have been highlighted.

Poly(isoprene)s with almost regular *cis*-1,4 structure and samples with regular or almost regular alternating *cis*-1,4-*alt*-3,4 structure are amorphous and shown mechanical properties typical of amorphous materials with viscous flow at values of high or low deformation depending on the molecular mass. The glass transition temperature of the different poly(isoprene)s depends on the molecular structure and on the concentration of the *cis*-1,4 units. In particular, we have observed a linear decrease of the glass transition temperature with increasing concentration of *cis*-1,4 units, from 15-16 °C of samples with 90% of 3,4 units (10% of *cis*-1,4 units) to -64 °C of samples with 97% of *cis*-1,4 units. The linear relationship between the glass transition temperature and the composition can be used as calibration curve to obtain information about the molecular structure and concentration of *cis*-1,4 units from the values of the glass transition temperature.

Poly(isoprene)s with prevalent 3,4 syndiotactic structure (75% of 3,4 units) and almost regular 3,4 syndiotactic structure (about 90% of 3,4 units) crystallize in the stable orthorhombic form of 3,4 syndiotactic poly(isoprene), characterized by the orthorhombic unit cell with axes $a = 6.6 \text{ \AA}$, $b = 13.2 \text{ \AA}$ and $c = 5.27 \text{ \AA}$ with chains in trans-planar conformation. The melting and crystallization temperatures of these samples depend on the concentration of 3,4 units. The melting temperature increases from 105-115 °C of the samples with 75% of 3,4 units to about

158 °C of the samples with 90% of 3,4 units. Similarly, the crystallization temperature increases from 76-78 °C of the samples with 75% of 3,4 units to about 125 °C of the samples with 90% of 3,4 units.

The presence of crystallinity greatly improves the mechanical properties and samples with prevalent 3,4 syndiotactic structure show better deformability and flexibility with plastic deformation via evident yielding and breaking at relatively high strain around 300-400%, with relatively high values of tensile strength and modulus between 50 and 85 MPa. Moreover, these samples shown remarkable elastic properties in a wide deformation range. The plastic deformation and the elastic behavior are associated to a reversible transformation during tensile deformation of the orthorhombic crystalline form into a disordered mesomorphic form, which recrystallizes into the orthorhombic crystalline form upon relaxation during elastic recovery.

Regarding Poly(myrcene)s, highly stereoregular polymers were obtained from myrcene using neodymium and iron organometallic complexes, having a well-defined structure, in combination with methylaluminumoxane.

In particular, highly *cis*-1,4 polymers have been obtained with neodymium-based systems, while polymers having a rather unusual structure as regards the stereospecific polymerization of conjugated dienes, that is a mainly alternating *cis*-1,4-*alt*-3,4 structure, but with regular *cis*-1,4 sequences (5 units) along the polymer chain, were obtained by means of iron catalysts. The polymers have generally quite high molecular weights, glass transition temperature values in the range -50 ÷ -65°C, similar to those of natural rubber, which makes them of potential interest for possible uses as elastomers.

All samples are amorphous even in the case of samples prepared with Neodymium based catalysts characterized by high content of *cis*-1,4 units (about 97%) or samples characterized by alternating *cis*-1,4-*alt*-3,4 sequences. In fact, constitutional defects, as 3,4 units in a prevailing *cis*-1,4 structure, or *cis*-1,4 sequences in prevailing alternating *cis*-1,4-*alt*-3,4 sequences, are present and prevent crystallization. As a consequence, all samples show mechanical behavior of soft materials with uniform deformation without evident yielding up to achieve maximum values of stress at deformations in the range 300 - 600%. At higher deformations, all samples experience viscous flow without breaking up to 800-1000% strain.

References

- 1) Porri, L.; Giarrusso, A. Part II: Conjugated Diene Polymerization. In *Comprehensive Polymer Science*. Pergamon, Oxford, UK, **1989**, *4*, 53–108.
- 2) S.K.H. Thiele, D. R. Wilson *J. Macromol. Sci, Polym. Rev. C* **2003**, *43*, 581-628.
- 3) L. Friebe, O. Nuyken, W. Obrecht *Adv. Polym. Sci.* **2006**, *204*, 1-154.
- 4) H. Sinn, J. Bliemeister, D. Clausnitzer, L. Winter, O. Zarncke, In: W. Kaminsky, H. Sinn (eds) *Transition metals and organometallics as catalysts for olefin polymerization*. Springer-Verlag, Berlin Heidelberg, New York, **1998**, 257-268.
- 5) J. Bliemeister, W. Hagendorf, A. Harder, B. Heitmann, I. Schimmel, E. Schmedt, W. Schnuchel, H. Sinn, L. Tikwe, N. von Thiene, K. Urllass, H. Winter, O. Zarncke In: G. Fink, R. Mülhaupt, Brintzinger HH (eds) *Ziegler catalysts*. Springer-Verlag, Berlin Heidelberg, New York, **1995**, 57-82.
- 6) G. Ricci, S. Italia, C. Comitani, L. Porri *Polym. Commun.* **1991**, *32*, 514-517.
- 7) G. Ricci, S. Italia, L. Porri *Macromol. Chem. Phys.* **1994**, *195*, 1389-1397.
- 8) G. Ricci, L. Porri *Polymer*, **1997**, *38*, 4499-4503.
- 9) G. Ricci, L. Zetta, E. Alberti, T. Motta, M. Canetti, F. Bertini *J. Polym. Sci. Part A: Polym. Chem.* **2007**, *45*, 4635-4646.
- 10) A. Zambelli, P. Ammendola, A. Proto *Macromolecules*, **1989**, *22*, 2126-2128.
- 11) L. Oliva, P. Longo, A. Grassi, P. Ammendola, C. Pellicchia, *Die Makromol. Chem. Rapid Commun.* **1990**, *11*, 519-524.
- 12) V. Venditto, C. De Rosa, G. Guerra, R. Napolitano *Polymer* **1992**, *33*, 3547-3551.
- 13) G. Ricci, S. Italia, A. Giarrusso, L. Porri *J. Organomet. Chem.* **1993**, *451*, 67-72.
- 14) G. Ricci, A. Panagia, L. Porri *Polymer* **1996**, *37*, 363-365.
- 15) G. Ricci, C. Bosisio, L. Porri *Macromol. Chem. Rapid Commun.* **1996**, *17*, 781-785.
- 16) L. Porri, G. Ricci, A. Giarrusso In: W. Kaminsky (ed) *Metal organic catalysts for synthesis and polymerization*. Springer-Verlag, Berlin, Heidelberg, **1999**, 519-530.
- 17) L. Porri, A. Giarrusso, G. Ricci In: J. Scheirs, W. Kaminsky (eds) *Metallocene based polyolefins*. John Wiley, New York, **2000**, 115-141.
- 18) P. Longo, P. Oliva, A. Proto, A. Zambelli *Gazzetta Chimica italiana*, **1996**, *126*, 377-382.
- 19) G. Ricci, S. Italia, L. Porri *Macromolecules*, **1994**, *27*, 868-869.
- 20) G. Ricci, E. Alberti, L. Zetta, T. Motta, F. Bertini, R. Mendichi, P. Arosio, A. Famulari, S. V. Meille *Macromolecules*, **2005**, *38*, 8353-8361.

- 21) P. Longo, G. Guerra, F. Grisi, S. Pizzuti, A. Zambelli *Macromol. Chem. Phys.* **1998**, *199*, 149-154.
- 22) G. Ricci, L. Porri *Macromol. Chem. Phys.* **1997**, *198*, 3647-3650.
- 23) G. Ricci, A. Sommazzi, F. Masi, M. Ricci, A. Boglia, G. Leone *Coord. Chem. Rev.* **2010**, *254*, 661-676.
- 24) G. Ricci, G. Leone *Polyolefins J.* **2014**, *1*, 43-60.
- 25) G. Ricci, G. Leone Polymerization of 1,3-butadiene with organometallic complexes-based catalysts. In *Applied Homogeneous Catalysis with Organometallic Compounds: A Comprehensive Handbook*, 3rd ed, B. Cornils, W. A. Hermann, M. Beller, R. Paciello Eds. Wiley-VCH Verlag GmbH: Weinheim, **2017**, *1*, 251-273.
- 26) J. Huang, Z. Liu, D. Cui, X. Liu *ChemCatChem* **2018**, *10*, 42-61.
- 27) V. K. Srivastava, M. Maiti, G. C. Basak, R. V. Jasras *J. Chem. Sci.* **2014**, *126*, 415-427.
- 28) D. Takeuchi Stereoselective polymerization of conjugated dienes. In *Encyclopedia of Science and Technology*, John Wiley & Sons, **2013**.
- 29) Z. Zhang, D. Cui, B. Wang, B. Liu, Y. Yang Polymerization of 1,3-Conjugated Dienes with Rare-Earth Metal Precursors. *Struct. Bonding* (Berlin, Ger.) **2010**, *137*, 49-108.
- 30) A. Fischbach, R. Anwender *Organometallics. Adv. Polym. Sci.* **2006**, *204*, 155-281.
- 31) J. Jothieswaran, S. Fadlallah, F. Bonnet, M. Visseaux *Catalysts* **2017**, *7*, 378.
- 32) P. Racanelli, L. Porri *Eur. Polym. J.* **1970**, *6*, 751-761.
- 33) J. Furukawa, K. Haga, E. Kobayashi, Y. Iseda, T. Yoshimoto, K. Sakamoto *Polym. J.* **1971**, *2*, 371-378.
- 34) H. Ashitaka, H. Ishikawa, H. Ueno, A. Nagasaka *J. Polym. Sci. Polym. Chem.* **1983**, *21*, 1853-1860.
- 35) H. Ashitaka, K. Jinda, H. Ueno *J. Polym. Sci. Polym. Chem.* **1983**, *21*, 1951-1972.
- 36) H. Ashitaka, K. Inaishi, H. Ueno *J. Polym. Sci. Polym. Chem.* **1983**, *21*, 1973-1988.
- 37) H. Ashitaka, K. Jinda, H. Ueno *J. Polym. Sci. Polym. Chem.* **1983**, *21*, 1989-1995.
- 39) G. Natta, U. Giannini, P. Pino, A. Cassata Su *Un Nuovo complesso di cobalto con di-olefine coniugate che catalizza la dimerizzazione del butadiene a 3-metil-1,4,6-eptatriene*. *Chim. Ind., Milan* **1965**, *47*, 524.
- 40) G. Ricci, S. Italia, L. Porri *Polym. Commun.* **1988**, *29*, 305.
- 41) W. Cooper, D. E. Eaves, G. Vaughan *Adv. Chem. Ser.* **1966**, *52*, 46-66.
- 42) G. Ricci, G. Leone, A. Boglia, F. Masi, A. Sommazzi In *Cobalt: Characteristics, Compounds, and Applications*. Vidmar, L. J., Ed.; Nova Science Publisher, Inc. **2011**; Chapter 2, 39-81.

- 43) M. Takeuchi, T. Shiono, K. Soga *Polym. Int.* **1992**, 29, 209–212.
- 44) M. Takeuchi, T. Shiono, K. Soga. *Polym. Int.* **1995**, 36, 41–45.
- 45) M. Takeuchi, T. Shiono, K. Soga *Macromol. Chem. Phys.* **1996**, 197, 729–743.
- 46) G. Ricci, A. Boglia, R. Santi, A. Sommazzi, F. Masi Procedimento per la preparazione di polibutadiene a contenuto variabile cis-1,4/1,2. Patent number: ITMI20031807 A1: 2005-03-4 to Polimeri Europa (priority number: IT2003MI01807 20030923).
- 47) G. Ricci, A. Boglia, A. Forni, R. Santi, A. Sommazzi, F. Masi Complessi fosfinici di cobalto e procedimento per la loro preparazione. Patent number: ITMI20031808 A1: 2005-03-24 to Polimeri Europa (priority number: IT2003MI01808 20030923).
- 48) G. Ricci, A. Boglia, R. Santi, A. Sommazzi, F. Masi, Procedimento per polimerizzare butadiene a dare polibutadiene ad alto tenore di unità 1,2. Patent number: ITMI20031809 A1: 2005-03-24 to Polimeri Europa (priority number: IT2003MI0180920030923).
- 49) G. Ricci, A. Forni, A. Boglia, T. Motta *J. Mol. Catal. A: Chem.* **2005**, 226, 235–241.
- 50) G. Ricci, A. Forni, A. Boglia, T. Motta, G. Zannoni, M. Canetti, F. Bertini *Macromolecules* **2005**, 38, 1064–1070.
- 51) G. Ricci, A. Forni, A. Boglia, A. Sommazzi, F. Masi *J. Organomet. Chem.* **2005**, 690, 1845–1854.
- 52) C. Bazzini, A. Giarrusso, L. Porri *Macromol. Rapid Commun.* **2002**, 23, 922–927.
- 53) G. Ricci, D. Morganti, A. Sommazzi, R. Santi, F. Masi *J. Mol. Catal. A: Chem.* **2003**, 204, 287–293.
- 54) C. Bazzini, A. Giarrusso, L. Porri, B. Pirozzi, R. Napolitano *Polymer* **2004**, 45, 2871–2875.
- 55) F. Masi, A. Sommazzi, R. Santi, G. Ricci, G. Pampaloni, S. Bonsignore, S. Valenti, C. Bianchini . Process for the (co)-polymerization of conjugated dienes. Patent WO02102861 A2 2002-12-27 to Polimeri Europa (priority number: IT2001MI0125920010615).
- 56) G. Ricci, F. Bertini, A. Boccia, L. Zetta, E. Alberti, B. Pirozzi, A. Giarrusso, L. Porri *Macromolecules* **2007**, 40, 7238–7243.
- 57) B. Pirozzi, R. Napolitano, G. Giusto, S. Esposito, G. Ricci *Macromolecules* **2007**, 40, 8962–8968.
- 58) B. Pirozzi, R. Napolitano, V. Petraccone, S. Esposito *Macromol. Chem. Phys.* **2004**, 205, 1343–1350.
- 59) J. Raynaud, J. Y. Wu, T. Ritter *Angew. Chem., Int. Ed.* **2012**, 51, 11805–11808.
- 60) L. Guo, X. Jing, S. Xiong, W. Liu, Y. Liu, Z. Liu, C. Chen *Polymers* **2016**, 8, 389.
- 61) O. H. Hashmi, Y. Champouret, M. Visseaux *Molecules* **2019**, 24, 3024.
- 62) Y. Champouret, O. H. Hashmi, M. Visseaux *Coord. Chem. Rev.* **2019**, 390, 127–170.

- 63) G. Ricci, G. Pampaloni, A. Sommazzi, F. Masi *Macromolecules* **2021**, *54*, 5879-5914.
- 64) S. K. H. Thiele, D. R. Wilson. *J. Macromol. Sci., Polym. Rev.* **2003**, *43*, 581–628.
- 65) K. Osakada, D. Takeuchi *Adv. Polym. Sci.* **2004**, *171*, 137–181.
- 66) L. Friebe, O. Nuyken, W. Obrecht *Adv. Polym. Sci.* **2006**, *204*, 1–154.
- 67) G. Ricci, G Boffa, L. Porri *Makromol. Chem., Rapid Commun.* **1986**, *7*, 355–359.
- 68) F. Cabassi, S. Italia, G. Ricci, L. Porri L. In *Transition Metal Catalyzed Polymerizations; Quirk, R. P., Ed.; Cambridge University Press, Cambridge, MA, 1988*, 655.
- 69) G. Ricci, S. Italia, F. Cabassi, L. Porri *Polym. Commun.* **1987**, *28*, 223–226.
- 70) D. J. Wilson, D. K. Jenkins *Polym. Bull.* **1992**, *27*, 407–411.
- 71) A. C. Angood, S. A. Hurley, P. J. T. Tait *J. Polym. Sci. Polym. Chem.* **1973**, *11*, 2777-2791.
- 72) M. Zhao, Q. Mahmood, C. Jing, L. Wang, G. Zhu, X. Zhang, Q. Wang *Polymers* **2019**, *11*, 1122.
- 73) D. R. Burfield, K. L. Lim *Macromolecules* **1983**, *16*, 1175-1179.
- 74) R. Mülhaupt *Macromol. Chem. Phys.* **2013**, *214*, 159–174.
- 75) E. Breitmaier, *Terpenes: Flavors, Fragrances, Pharmaca, Pheromones*; Wiley-VCH: Weinheim, **2006**.
- 76) C. Tang, C. Y. Ryu *Sustainable Polymers from Biomass*; 1st ed.; Wiley-VCH: Weinheim, **2017**.
- 77) C. Wahlen, H. Frey *Macromolecules* **2021**, *54*, 7323–7336.
- 78) C. Wahlen, J. Blankenburg, P. von Tiedemann, J. Ewald, P. Sajkiewicz, A. H. Müller, G. Floudas, H. Frey *Macromolecules* **2020**, *53*, 10397–10408.
- 79) E. Grune, J. Bareuther, J. Blankenburg, M. Appold, L. Shaw, A. H. E. Müller, G. Floudas, L. R. Hutchings, M. Gallei, H. Frey *Polym. Chem.* **2019**, *10*, 1213–1220.
- 80) A. Behr, L. Johnen *ChemSusChem* **2009**, *2*, 1072– 1095.
- 81) A. Gandini *Green Chem.* **2011**, *13*, 1061–1083.
- 82) S. Loughmari, A. Hafid, A. Bouazza, A. El Bouadili, P. Zinck, M. Visseaux *J. Polym. Sci., Part A: Polym. Chem.* **2012**, *50*, 2898–2905.
- 83) P. A. Wilbon, F. Chu, C. Tang *Macromol. Rapid Commun.* **2013**, *34*, 8–37.
- 84) S. Georges, M. Bria, P. Zinck, M. Visseaux *Polymer* **2014**, *55*, 3869–3878.
- 85) A. Gandini, T. M. Lacerda *Prog. Polym. Sci.* **2015**, *48*, 1–39.
- 86) B. Liu, L. Li, G. Sun, D. Liu, S. Li, D. Cui *Chem. Commun.* **2015**, *51*, 1039–1041.
- 87) R. E. Diaz de Leon Gómez, F. J. Enriquez-Medrano, H. Maldonado Textle, R. Mendoza Carrizales, K. Reyes Acosta, H. R. Lopez Gonzalez, J. L. Olivares Romero, L. E. Lugo Uribe *Can. J. Chem. Eng.* **2016**, *94*, 823–832.

- 88) M. Naddeo, A. Buonerba, E. Luciano, A. Grassi, A. Proto, C. Capacchione *Polymer* **2017**, *131*, 151–159.
- 89) W. Li, J. Zhao, X. Zhang, D. Gong. *Ind. Eng. Chem. Res.* **2019**, *58*, 2792–2800.
- 90) X. Jia, W. Li, J. Zhao, F. Yi, Y. Luo, D. Gong *Organometallics* **2019**, *38*, 278– 288.
- 91) Q. Gan, Y. Xu, E. W. Huang, W. Luo, Z. Hu, F. Tang, X. Jia, D. Gong *Polym. Int.* **2020**, *69*, 763–770.

Chapter 5

Nickel, Palladium



5.1 Catalytic systems for copolymerization of olefins with polar monomer

Each year, about 150 million tons of polyolefins are produced.¹ They constitute the most widely used plastics and play a crucial part in contemporary civilization. The huge success of polyolefins is attributable to their exceptional properties, including corrosion resistance, chemical stability and low cost. These characteristics make polyolefins ideal materials for numerous applications, from packaging to electronics.² However, the nonpolar character of polyolefins severely restricts their use in a variety of industrial sectors. The incorporation of polar functional groups can effectively enhance a variety of properties, including adhesion, toughness, surface characteristics, compatibility, dyeability, barrier characteristics, and many others.³⁻⁵ For these reasons, the copolymerization of polar comonomers with α -olefins is an intensively investigated research field.

A crucial prerequisite for incorporation of polar monomers is the compatibility of the polar comonomer and the catalyst. These copolymerizations of polar comonomers and ethylene are an intensively investigated research field. Early transition metal catalysts such as Ziegler and Natta type catalysts are of special interest for industrial applications due to their outstanding high activities which is why they account for the largest share of the industrially produced polyolefins. However early transition metals exhibit a high oxophilicity which limits their applicability to non-polar comonomers such as ethylene, propylene and 1-olefins. Polymerization in presence of polar compounds would lead to the formation of a stable σ -complex with the polar group or eliminations of hetero atoms in the β -position.⁶

Due to their reduced oxophilicity, late transition metal catalysts are promising candidates for copolymerizations of ethylene and polar monomers. However, their higher tendency towards β -hydride elimination still slows or even shuts down chain propagation.

A general mechanistic overview of the catalytic insertion of polar monomers with ethylene is given in Figure 5.1.

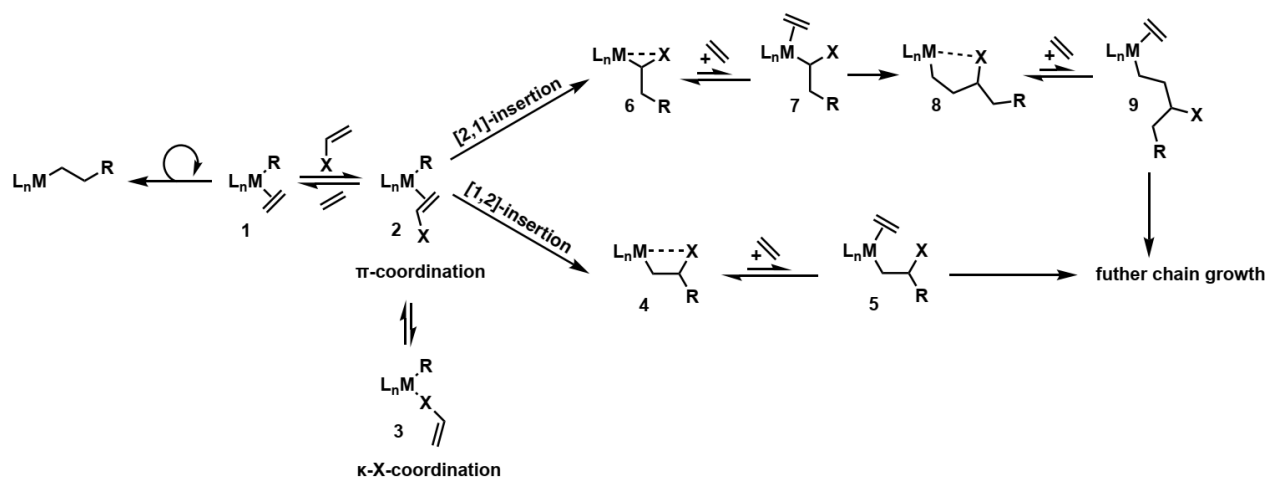


Figure 5.1. Insertion mechanism of functionalized polar vinyl monomers.

The first step towards chain growth is monomer coordination. If there is more than one monomer present, they compete with each other for the coordination to the metal center, whereby ethylene is favored because of its better σ -donor ability. Furthermore, the insertion is further slowed down by κ -X-coordination (3) that competes with the π -coordination (2) crucial for insertion. Electron-rich polar monomers favour the 1,2-insertion (4) in contrast to electron-poor polar monomers that prefer 2,1-insertion (6). Further rate decreasing factors after the incorporation of the polar monomer are the chelate opening after consecutive ethylene insertion (6, 8, 4) and the insertion into the α -substituted metal carbon bond (6 \rightarrow 7) that need to be overcome in order to get further chain growth.⁷

These limitations were overcome by ground-breaking findings by Brookhart and Drent who were able to copolymerize ethylene with some polar comonomers such as acrylates, vinyl acetate, acrylonitrile and vinyl halides producing high-molecular-weight polymers.^{8,9}

Brookhart and co-workers first introduced α -diimine palladium and nickel complexes with bulky diimine ligands.⁸ They obtained polymers which are highly branched and the polar monomers are predominantly located at the end of the chain due to their high tendency towards chain walking after insertion of the polar monomer.^{8,10-13} In 2002 Drent et al.⁹ reported on the synthesis of neutral Pd catalysts with *ortho*-phosphinobenzene sulfonate ligands. These catalysts are able to produce highly linear polyethylene and copolymerize ethylene with different polar monomers like acrylonitrile, vinyl acetate, functionalized norbornenes, and many more which are incorporated in the polymer backbone.¹⁴

Grubbs and colleagues demonstrated in 2000 that neutral salicylaldimine nickel catalysts capable of copolymerizing ethylene with polar-substituted norbornenes, providing a further contribution to this field of polymer chemistry.¹⁵ Then, employing this kind of nickel catalyst, a few other special polar monomers were effectively copolymerized with ethylene.¹⁶⁻²⁰

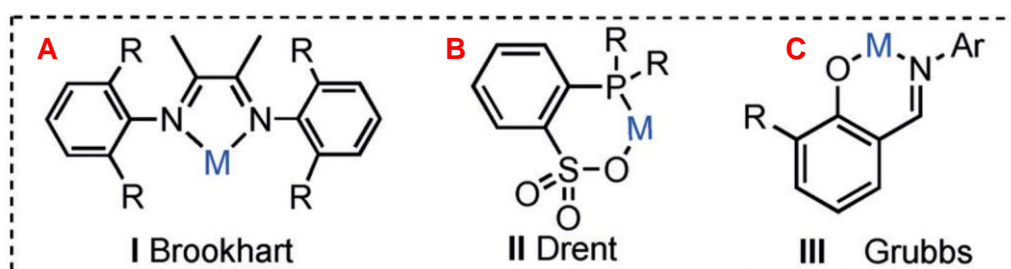


Figure 5.2. Molecular structures of Brookhart (A), Drent (B), and Grubbs (C) catalysts. M=palladium or nickel.²¹

5.2 Synthesis and characterization of novel polyethylene-based terpolymers with non-alternating in-chain keto groups.

5.2.1 Materials and Methods

Ethylene-carbon monoxide-norbornene (EtCONB) and ethylene-carbon monoxide-methyl-5-norbornene-2-carboxylate (EtCONBE) were synthesized in a high-pressure polymerization set-up consisting of a 300 mL MiniClave by BüchiGlasUster. The reactor was evacuated and purged with nitrogen three times prior to the reaction. 100 mL of dried and deoxygenated toluene were transferred into the reactor vessel by cannula and heated to the desired reaction temperature, before the precatalyst, dissolved in 4 mL of toluene and the respective amount of norbornene or methyl-5-norbornene-2-carboxylate were injected into the reactor by syringe, consecutively. The stirring rate was adjusted to 1000 rpm and the reactor was pressurized with the desired mixture of carbon monoxide and ethylene. This mixture was further fed to the reactor by the automated mass flow controllers to maintain a stable pressure (thus replenishing consumed gaseous monomer) over the course of the entire reaction. After the desired polymerization time, the reactor was vented and cooled. The obtained polymer was precipitated in methanol, filtered off, washed thoroughly with methanol and vacuum dried at 60 °C for >24 h. Reference (co-) polymerizations of ethylene, ethylene- methyl-5-norbornene-2-carboxylate, ethylene-norbornene and ethylene-CO were carried out following the same protocol.

Polymer ¹H NMR spectra were acquired in 1,1,2,2-tetrachloroethane-d₂ at 110 °C and were recorded on a Bruker Avance III HD 400 (1H: 400 MHz, 13C: 101 MHz). ¹H chemical shifts were referenced to the residual C₂H₂Cl₄: 6.00 ppm.

Size exclusion chromatography (SEC) was performed on a PolymerChar GPC-IR instrument equipped with an integrated four-capillary viscometer and an IR4 dual wavelength infrared detector (selective for methylene and methyl groups) on PSS Polefin Linear XL columns (3 × 30 cm) and with

an additional guard column at 160 °C in 1,2-dichlorobenzene. Universal calibration using narrow polystyrene standards was employed.

The calorimetric measurements were performed with a Mettler-DSC822 operating in N₂ atmosphere. The sample, typically 5 mg, was placed in a sealed aluminum pan, and the measurement was carried out from -70 to 180°C using a heating and cooling rate of 10 °C min⁻¹.

Crystallinity was calculated from both DSC curves and diffraction data. In the first case it was evaluated from the second heating DSC scans as follows: $x_c^{DSC} = (\Delta H_m^{II} / \Delta H_m^0) \times 100$, where ΔH_m^{II} is the second melting enthalpy of the sample and ΔH_m^0 thermodynamic melting enthalpy of 100% crystalline PE taken equal to 297 Jg⁻¹²², while in the second case it was calculated from the WAXS patterns of melt-crystallized samples as: $x_c^{RX} = [A_c(110) + A_c(200)] / [A_c(110) + A_c(200) + A_a] \times 100$ where A_c refers to the integrated area of the Bragg reflections from the orthorhombic PE crystal and A_a to the integrated area of the amorphous halo. A Voigt fit was used.

ATR-IR spectra of polymers were acquired on a Perkin Elmer Spectrum 100 instrument. For calculation of the carbon monoxide incorporation, the ratio of the integral of the C=O signal (integration area: band between 1692-1715 cm⁻¹ ± 65 cm⁻¹) to the integral of the C-H signal of the PE at ~2915 cm⁻¹ (integration area: 2740-3030 cm⁻¹) was calculated and referenced with linear polyketone samples with known C=O content synthesized via ADMET copolymerization and subsequent hydrogenation.²³ Methyl-5-norbornene-2-carboxylate incorporation ratios were determined by the same method, but referenced to a linear calibration with aliphatic polyesters (since the methyl-5-norbornene-2-carboxylate has an ester group in the side chain) with defined chain lengths of 18, 32 and 48 carbon atoms between ester groups²⁴ (Figure 5.3). The carbon monoxide and methyl-5-norbornene-2-carboxylate contents of EtCONBE terpolymers were calculated by deconvolution of the carbonyl region to separate C=O and ester bands. The deconvoluted bands were integrated and reference against the respective calibration.

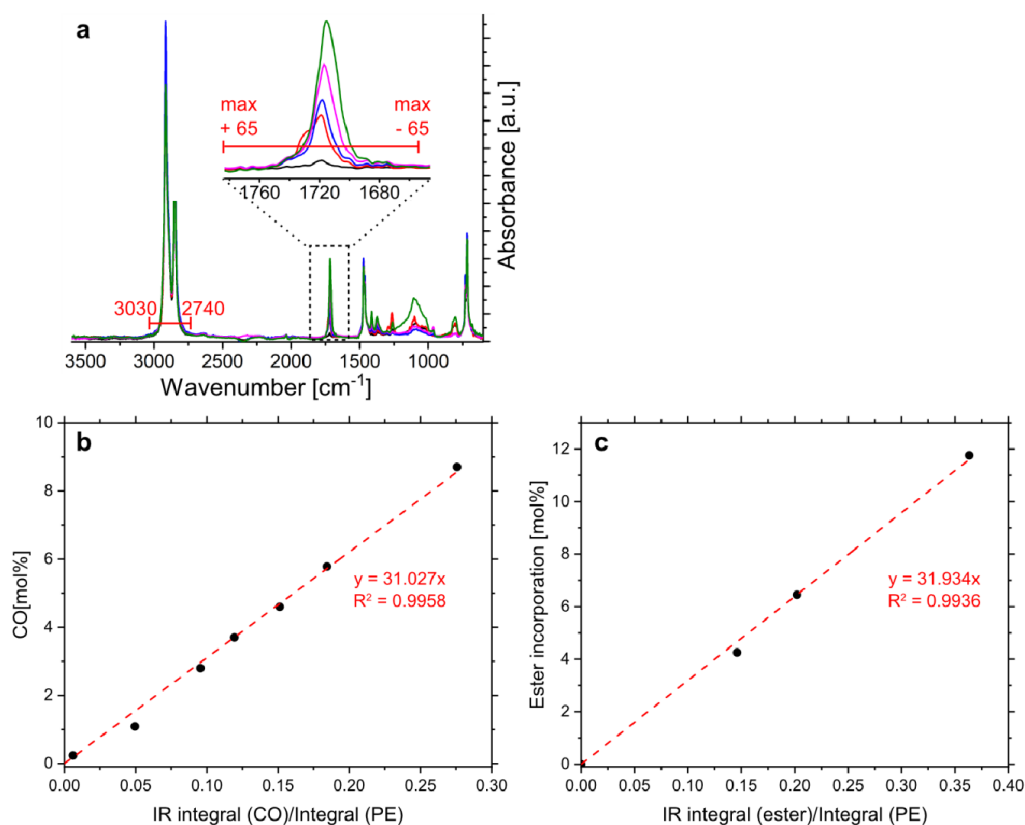


Figure 5.3. Referencing of IR spectra. **a:** Polyketones with known carbonyl contents were analyzed by ATR-IR. The samples were synthesized via ADMET copolymerization of docosa-1,21-dien-11-one and undeca-1,10-diene followed by hydrogenation.²³ The limits of integration for the determination of signal intensity ratios for carbonyl stretching vibrations (spectral position with max. absorbance ± 65 cm^{-1}) vs. the polyethylene C-H vibration (2740-3030 cm^{-1}) are depicted in red. **b:** The integral intensity ratio is directly proportional to the concentration of C=O groups in the polymer χ . That is, $\chi \approx n_{\text{CO}}/n_{\text{C}_2\text{H}_4}$ which is a valid approximation if $n_{\text{C}_2\text{H}_4} \gg n_{\text{CO}}$. **c:** Linear calibration for ester based comonomers (NBE) based on the same integration method, but referenced to aliphatic polyesters with defined chain lengths of 18, 32 and 48 carbon atoms.²⁴

Wide-angle X-ray diffraction (XRD) experiments were performed with a Malvern Panalytical (Malvern, UK) Empyrean multipurpose diffractometer using Cu K α radiation ($\lambda = 1.5418$ Å) by a continuous scan of the diffraction angle 2θ in the interval $5\text{--}40^\circ$ at a speed of $0.05252^\circ/\text{s}$.

Mechanical tests were performed on melt crystallized compression-molded films, soon after their preparation, with a universal mechanical tester Zwicky by Zwick Roell, following the standard test method for tensile properties of thin plastic sheeting ASTM D882. Rectangular specimens 100 mm long and 5 mm wide, cut from the compression-molded films by using a die-cutter, have been stretched up to the break while recording the stress-strain curves to determine mechanical tensile parameters, such as the stress and strain at breaking (σ_b and ϵ_b) and at yield point (σ_y and ϵ_y) and the tension set after breaking (t_b). The values of Young's modulus (E) have been determined in independent experiments.

The strain at break ϵ_b has been evaluated as $\epsilon_b = ((L_f - L_0)/L_0) \times 100$ where L_0 and L_f are the initial and final lengths of the specimen, respectively. The tension set after break t_b , which represents a

measurement of the elastomeric properties of the samples, has been determined following the procedure described in the ASTM D412. Ten minutes after breaking, the two pieces of the broken specimen have been fit carefully together so that they are in contact over the full area of the break and the final total length L_r has been measured. Then the tension set after breaking has been calculated as $t_b = ((L_r - L_0)/L_0) \times 100$.

5.2.2 General Introduction

Nowadays, polyethylene (PE) is the most produced and used synthetic polymer in the world. More than 70 million of PE are produced annually.²⁵

The high crystallinity and outstanding properties are made possible by its linear hydrocarbon chains.^{1,26}

However, although polyethylenes hydrocarbon backbone is the key to its success, it also represents its biggest problem.

In fact, the strong nonpolar and inert nature of the polymer chains make polyethylene resistant to degradation reactions and, thus, it accumulates in the environment contributing to environmental pollution.²⁷⁻²⁹ Consequently, being able to modify the molecular structure of polyethylene by introducing functional groups that make it degradable but do not change its excellent properties, is a key and crucial issue from both academic and industrial perspectives.^{24,30-32}

In this framework, the incorporation of small concentrations of keto groups in the PE chains could be a viable option. In fact, due to their ability to promote chain scission by Norrish type I and II reactions, in-chain keto groups are especially well suited to enhance photodegradation (Figure 5.4).³³

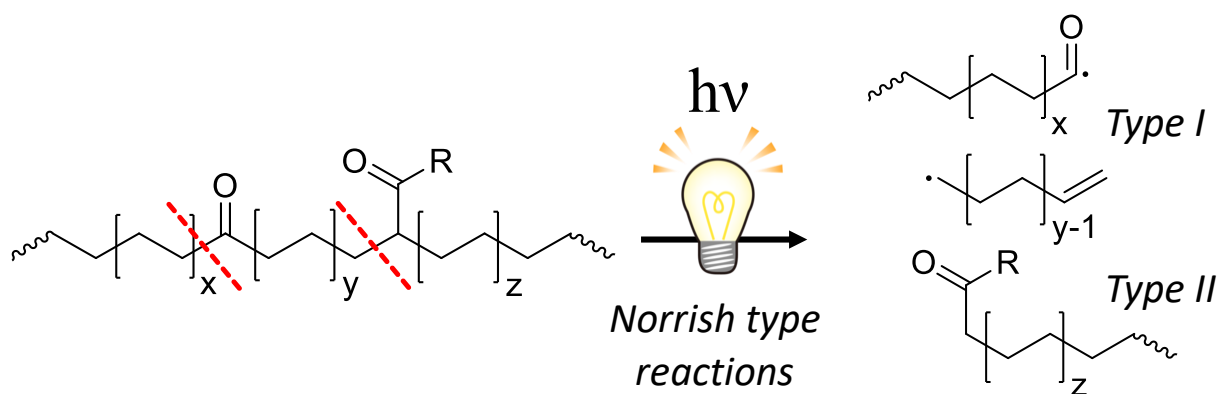


Figure 5.4. Illustrated mechanism of photolytic cleavage of Keto-polyethylenes promoted by Norrish type reactions.

However, since the catalytic ethylene-CO copolymerization typically produces alternating polyketones due to the preference for CO incorporations, it had long been sought after to find a way to produce linear HDPE-like polyethylenes with in-chain keto units by incorporating small amounts of carbon monoxide during ethylene polymerization.

Only recently, Mecking et al,³⁴ using some phosphinophenolato Ni (II) complexes, were able to synthesize high-molecular-mass polyethylenes characterized by the presence of small amounts of CO (<1 mol%) distributed in a non-alternating fashion in the polymer chain. The same authors showed that such materials (Keto-PEs) possess properties such as crystallinity, melting temperature and mechanical performances comparable to those of commercial HDPE but, unlike the latter, are photodegradable because of the presence of carbonyl groups in chain.³⁴

In the present Chapter, we will show the synthesis and characterization of novel ethylene-carbon monoxide-norbornene terpolymers, obtained by using two advanced complexes based on Ni (II) and Pd (II). The aim is to investigate the effect of the co-presence of carbon monoxide and norbornene on the crystallization and on all the other properties of KetoPEs. Actually, it is even of great interest to be able to understand the effect of decreasing crystallinity on the photodegradability of these materials. However, this aspect was not addressed in the present PhD work.

In addition, we will also focus on the synthesis of other polyethylene terpolymers with combined in-chain and side-chain functional groups from catalytic terpolymerization of carbon monoxide and methyl-5-norbornene-2-carboxylate (NBE). In this case, the goal is to obtain materials with properties on par with KetoPEs but with a higher polar nature. The incorporation of a small amount of an additional polar comonomer, such as NBE, could be beneficial to achieve a higher surface free energy and, thus, compatibility with polar materials.

All the polymers examined in this Chapter have been synthesized during my research period abroad at the University of Konstanz, Germany. The NMR, DSC, GPC and FT-IR characterization of the polymers too has been carried out in Konstanz, while their mechanical properties have been studied at the University of Naples Federico II.

5.2.3 Ethylene-CO-Norbornene Terpolymers - Synthesis and Characterization

Ethylene, CO and norbornene were polymerized in toluene by using two different catalytic systems, based on Nickel and Palladium complexes, as shown in Figure 5.5.

All the polymerization experiments performed with Ni and Pd catalysts are reported in Tables 5.1 and 5.2, respectively. Details concerning the synthetic procedures are described in section 5.2.1.

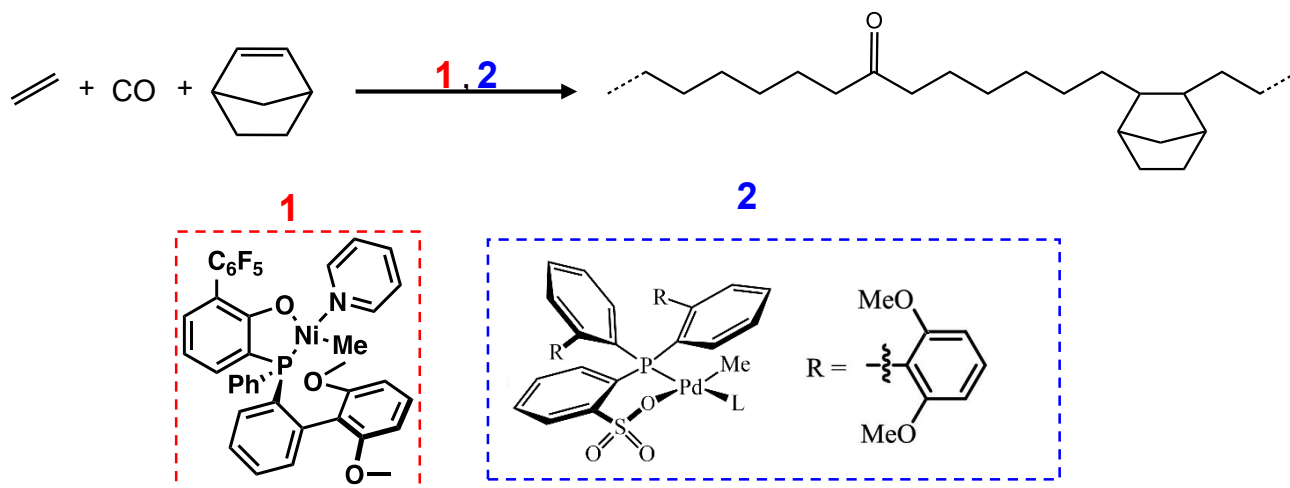


Figure 5.5. Catalytic Terpolymerization of Ethylene with CO and Norbornene using the neutral phosphinophenolato Ni (II) (1) and phosphinosulfonate Pd (II) (2) catalysts.

Table 5.1. Polymerization details and molecular characteristics of the samples synthesized using complex 1.^a

entry	CO/C ₂ H ₄ feed ^b (%)	NB ^c (mol L ⁻¹)	yield (g)	X (CO) ^d (mol%)	C=O IR ^d (cm ⁻¹)	M _n ^e (kDa)	M _w /M _n ^e
EtCO/Ni	0.6		2.2	1.3	1714	140	1.6
EtNB/Ni		0.1	3.3			84	1.7
EtCONB-1/Ni	0.8	0.1	1.4	3.4	1714	43	1.7
EtCONB-2/Ni	0.8	0.15	1.1	0.7	1714	40	1.7
EtCONB-3/Ni	0.8	0.2	1.0	0.7	1714	34	1.7
EtCONB-4/Ni	0.8	0.3	1.1	0.9	1714	38	1.8
EtCONB-5/Ni	0.8	0.4	1.1	0.5	1714	41	1.8

^aPolymerization conditions: 10 μmol precat. 1, 10 atm, 100 °C, 1000 rpm, 75 min, 100 mL toluene; ^bratio of CO in an ethylene-CO gas feed; ^cconcentration of NB in initial reaction solution. ^dFrom ATR-IR spectroscopy (see section 5.2.1); ^edetermined by SEC in 1,2-dichlorobenzene at 160 °C via universal calibration against PS standards.

Table 5.2. Polymerization details and molecular characteristics of the samples synthesized using complex **2**.^a

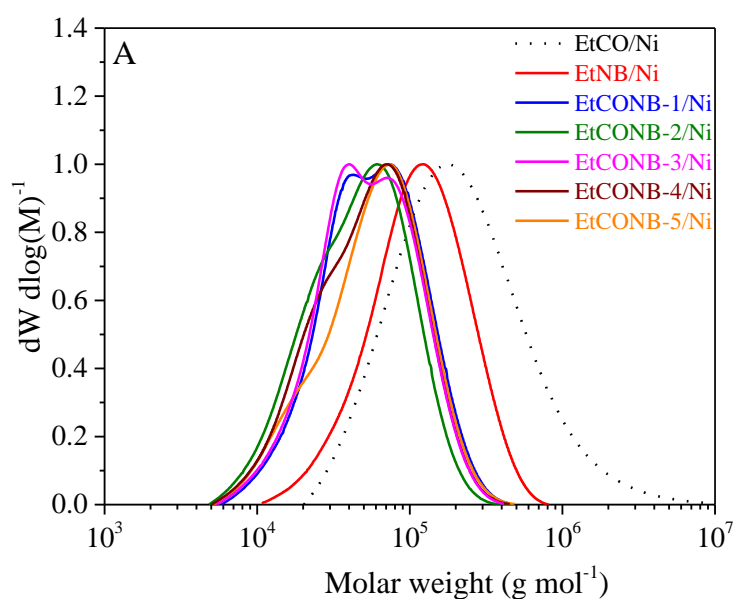
entry	CO/C ₂ H ₄ feed ^b (%)	NB ^c (mol L ⁻¹)	yield (g)	X (CO) ^d (mol%)	C=O IR ^d (cm ⁻¹)	M _n ^e (kDa)	M _w /M _n ^e
EtCO/Pd	0.6		7.5	0.4	1715	20	2.1
EtNB/Pd		0.1	9.8			51	1.7
EtCONB-1/Pd	0.8	0.1	1.1	2.6	1714	51	1.7
EtCONB-2/Pd	0.8	0.2	0.5	3.3	1710	48	1.7
EtCONB-3/Pd	0.8	0.3	0.7	1.1	1717	43	1.7
EtCONB-4/Pd	0.8	0.45	0.8	0.7	1717	42	1.7

^aPolymerization conditions: 2 μmol precat. **2**, 30 atm, 90 °C, 1000 rpm, 120 min, 100 mL toluene; ^bratio of CO in an ethylene-CO gas feed; ^cconcentration of NB in initial reaction solution. ^ddetermined from ATR-IR spectroscopy (see section 5.2.1); ^edetermined by SEC in 1,2-dichlorobenzene at 160 °C via universal calibration against PS standards.

The catalytic activity of both catalysts decreases in the presence of norbornene. In fact, in both cases, by comparing the yields of copolymers with respect to those of terpolymers, important differences can be observed. However, as the concentration of norbornene in feed increases, the activity seems to be almost constant since all the different terpolymers are obtained in comparable amounts. Details about the concentration of norbornene in the terpolymer samples are not currently available.

The CO composition was determined by ATR-IR spectroscopy, as described in section 5.2.1.

The GPC traces of all samples synthesized with catalysts **1** and **2** are shown in Figure 5.6A and 5.6B, respectively. The molecular weights values and the molecular weights distributions, extracted from the curves of Figures 5.6A and 5.6B, are listed in Tables 5.1 and 5.2, respectively.



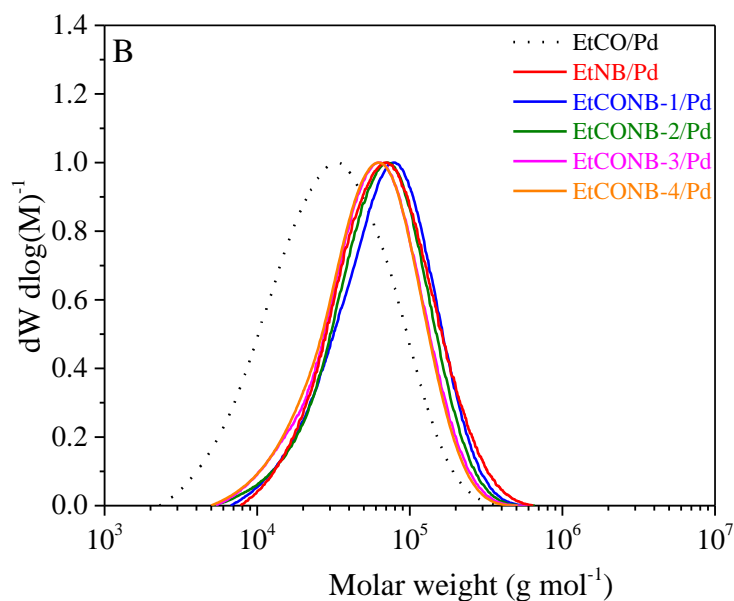


Figure 5.6. SEC traces of EtCONB terpolymers, and EtCO and EtNB copolymers synthesized with the Ni (A) and the Pd (B) catalysts.

From the data shown in Figure 5.6A, it is apparent that all ethylene-carbon monoxide-norbornene terpolymers, obtained by the Nickel-based catalyst, show significantly lower molecular weights than the two reference copolymers.

On the other hand, the EtNB copolymer and the Et-CO-NB terpolymers synthesized with the Palladium catalyst, have similar molecular weights to each other and higher than the reference ethylene-carbon monoxide copolymer (Figure 5.6B and Table 5.2).

It is worth noting that the SEC traces of terpolymers obtained by Ni are characterized by the presence of shoulders at lower molecular weights, and in some cases, the distribution appears almost bimodal (Figure 5.6A).

By contrast, all samples synthesized with the Pd catalyst show symmetrical and unimodal molecular weight distributions (Figure 5.6B). It is important to highlight that this is the first time that KetoPE-based materials, with such a high molecular weight, have been accessed with a phosphinosulfonato palladium catalyst. To date, all attempts have resulted in the formation of low-molecular weight brittle oligomers ($M_n < 3000 \text{ g mol}^{-1}$).³⁵

The ATR-IR spectra collected on all samples reported in Tables 5.1 and 5.2 are displayed in Figures 5.8 and 5.9, respectively.

In this regard, it is important to remember that the position of the relative absorption maximum of keto groups is closely related to how they are distributed in the polymer chain.^{34,35} In particular, the IR resonances of keto groups gradually shift with their spatial proximity, from 1719 cm^{-1} for isolated CO groups embedded in a polyethylene matrix to 1692 cm^{-1} for alternating polyketones (Figure 5.7).^{34,35}

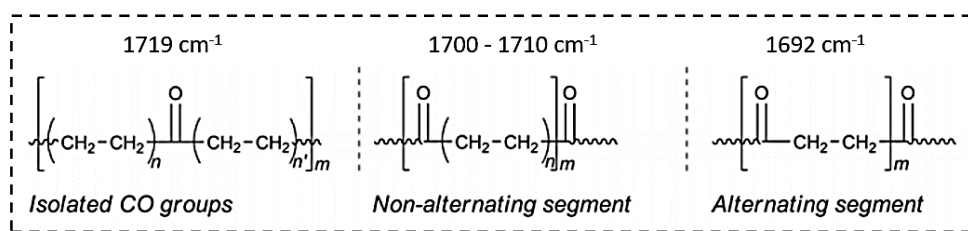


Figure 5.7. Comparison of the various molecular architectures of polyketones with the corresponding IR absorption region indicated.³⁵

As expected, the EtNB copolymer samples (EtNB/Ni, EtNB/Pd), synthesized with the two different catalysts, do not show any adsorption maxima in the carbonyl region (Figures 5.8 and 5.9).

Concerning the EtCO copolymers and the EtCONB terpolymers, the IR spectroscopic data reveal in all cases the presence of an absorption maximum at wavenumber values in the range of 1710 – 1719 cm^{-1} (Figures 5.8, 5.9 and Tables 5.1, 5.2). This is a clear indication that the keto groups incorporated into the polyethylene chains are predominantly isolated/nonalternating in terms of distribution.

As described in section 5.2.1, IR data were also used to determine the CO content by evaluating the ratio of the integral of the C=O signal and that of the C-H signal of the PE at $\sim 2915 \text{ cm}^{-1}$. The results are shown in Tables 5.1 and 5.2. Almost all samples have very similar CO contents, ranging from 0.4 to 1.0 mol%. Terpolymers EtCONB-1/Ni, EtCONB-1/Pd and EtCONB-2/Pd differ from the others since they present a CO concentration higher than 2.5 mol%.

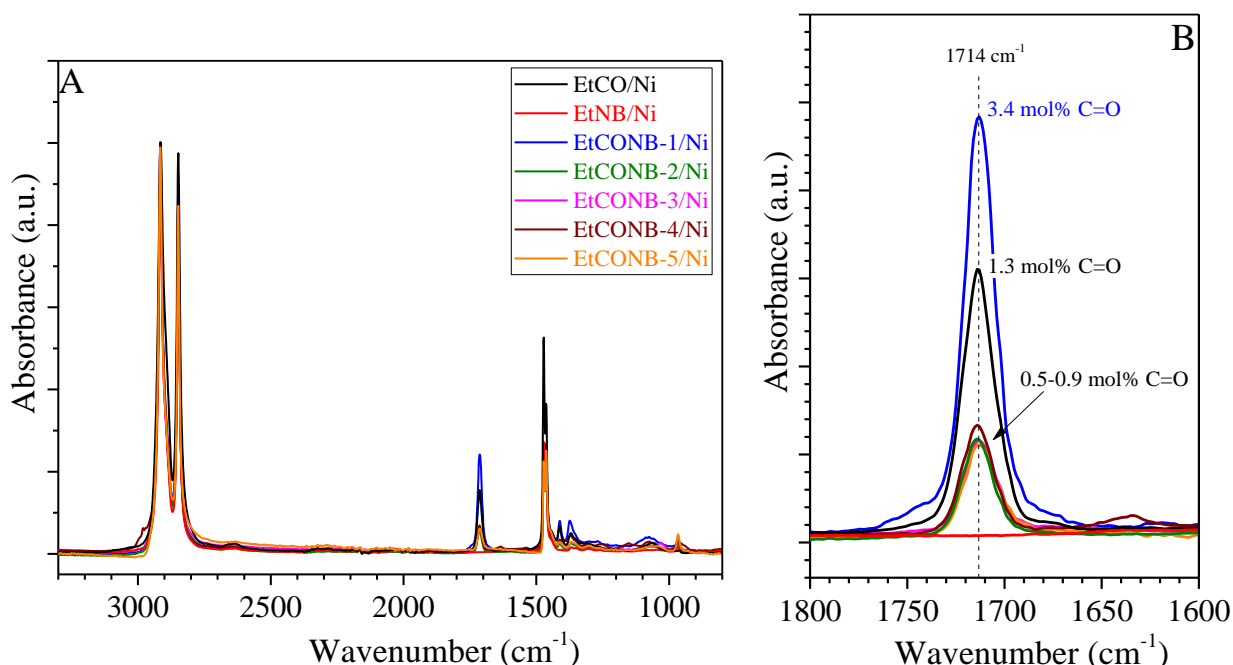


Figure 5.8. Full ATR-IR spectra of terpolymers and reference copolymers reported in Table 5.1, obtained with the Ni (II) complex (A). Expansion of the IR carbonyl region (B).

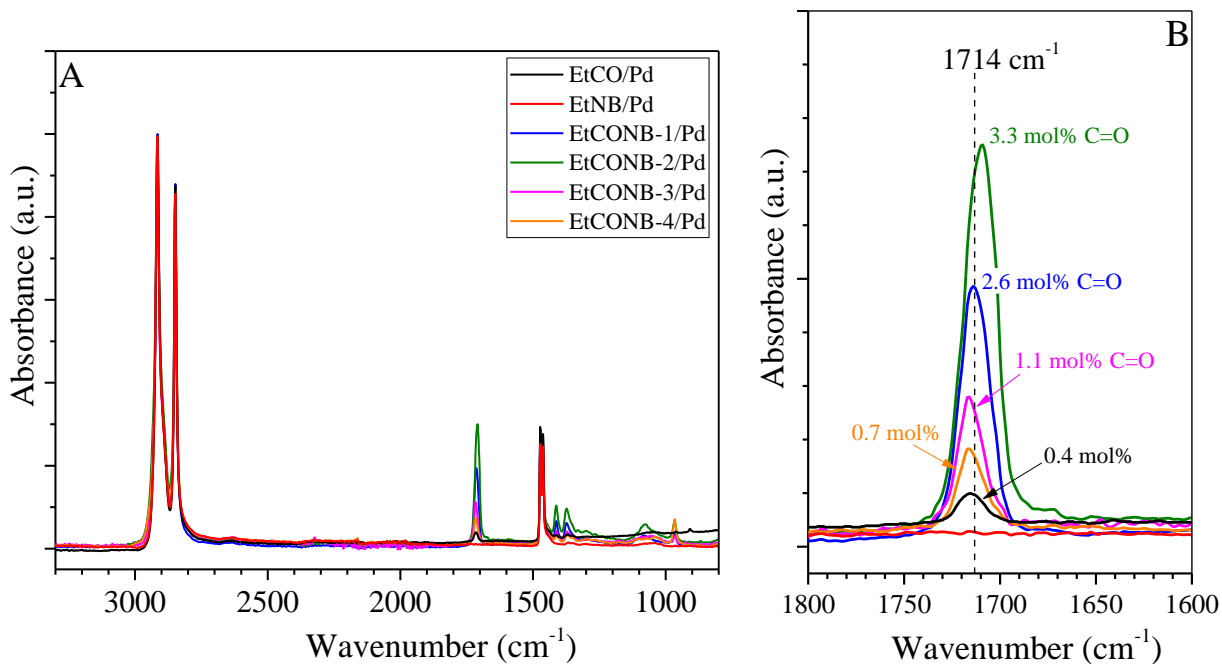


Figure 5.9. Full ATR-IR spectra of terpolymers and reference copolymers reported in Table 5.2, obtained with the Pd (II) complex (A). Expansion of the IR carbonyl region (B).

The WAXS patterns of all the samples of Tables 5.1 and 5.2 are reported in Figures 5.10 and 5.11, respectively. In particular, Figures 5.10A and 5.11A show the X-ray diffraction profiles collected on the as-prepared samples while Figures 5.10B and 5.11B those obtained on the melt-crystallized samples.

From the data reported in Figures 5.10 and 5.11, it is apparent that samples crystallize from both solution and melt in the orthorhombic form of PE with a small amount of the monoclinic form in some cases. Therefore, the incorporation of these low concentrations of carbon monoxide and norbornene, even in terpolymer synthesized with the highest amount of norbornene in feed, does not have a significant effect on the crystal packing of the polyethylene chains.

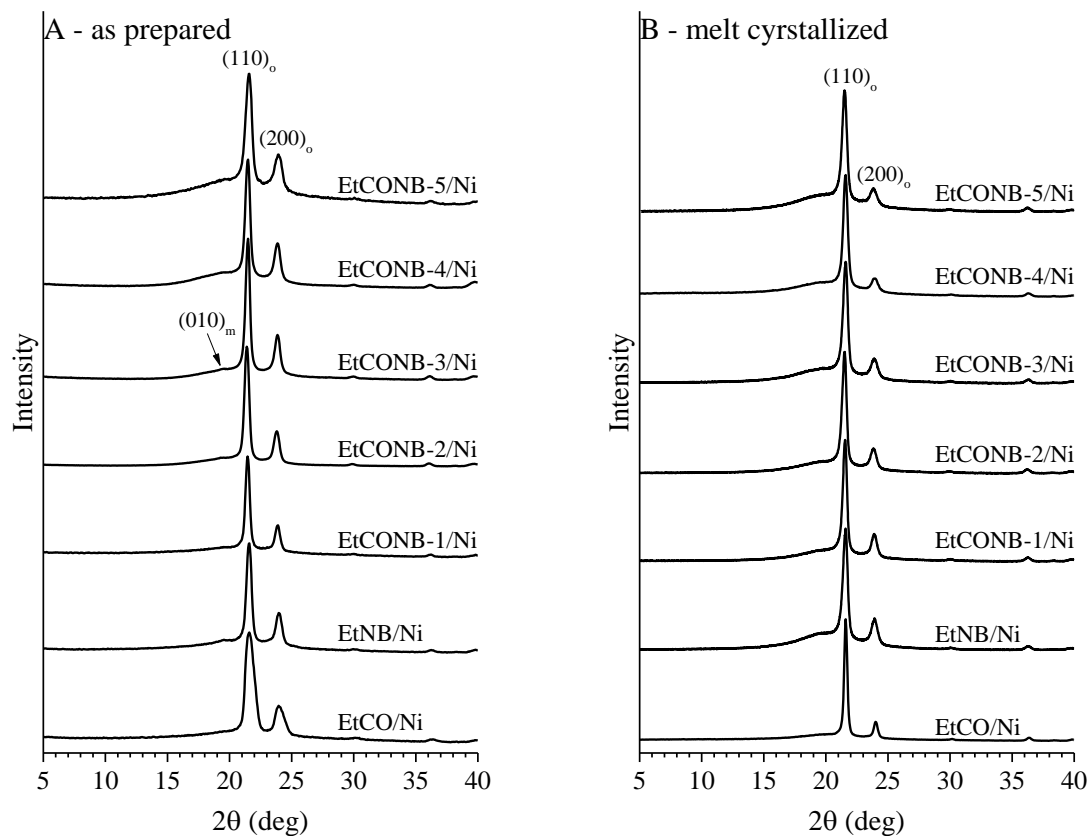


Figure 5.10. WAXS profiles of as-polymerized (A) and melt-crystallized (B) samples reported in Table 5.1.

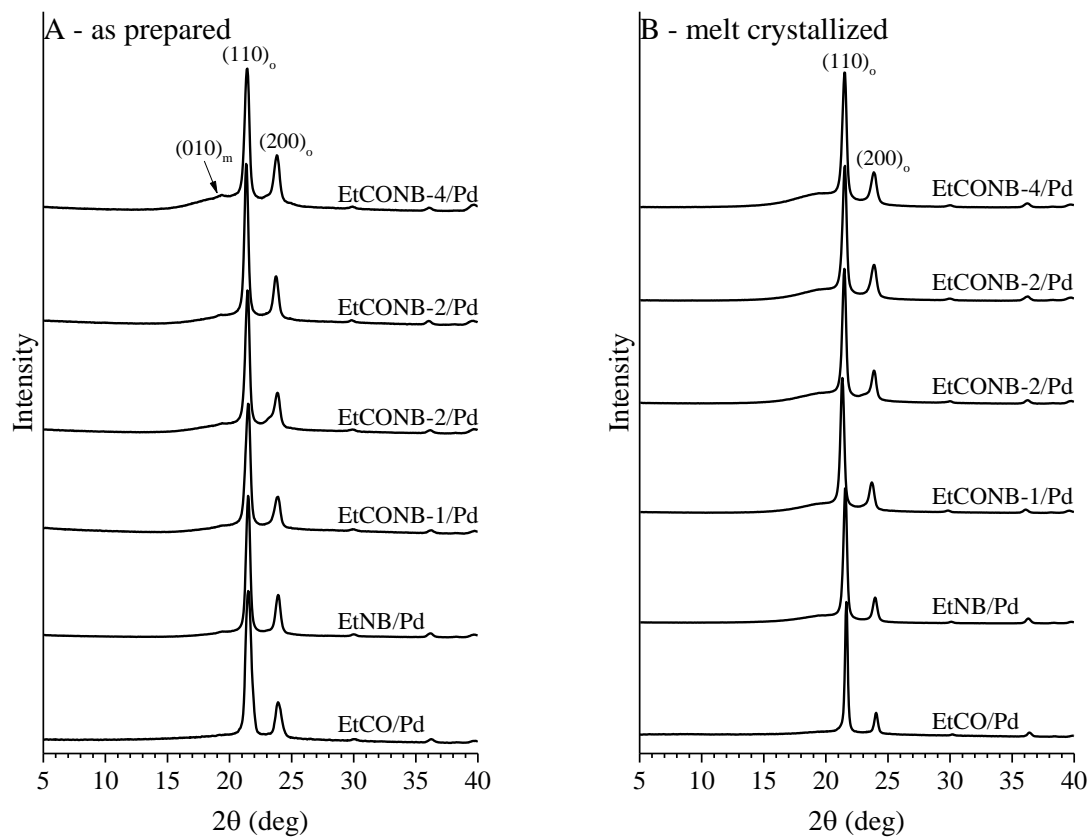


Figure 5.11. WAXS profiles of as-polymerized (A) and melt-crystallized (B) samples reported in Table 5.2.

The DSC curves of samples reported in Tables 5.1 and 5.2, recorded during first heating from 50°C to 180°C, successive cooling from the melt to -70°C, and second heating of the melt crystallized samples up to 180°C, all recorded at 10 °C/min, are reported in Figures 5.12 and 5.13, respectively. The thermal parameters extracted from the DSC curves of Figures 5.12 and 5.13, and the crystallinity evaluated as reported in section 5.2.1, are listed in Tables 5.3 and 5.4.

DSC data confirm the crystallinity already found with WAXS and clearly indicate that norbornene was successfully incorporated into all synthesized terpolymers samples. In fact, as can be observed from the second heating scans shown in Figures 5.12C and 5.13C, the melting temperatures of the EtCONB terpolymers are always lower than those of the reference EtCO copolymers and also slightly decrease as the norbornene content in feed increases.

In addition, the data in Tables 5.3 and 5.4 show that the melting enthalpy decreases as the norbornene content in feed increases, moving from 186 and 226 Jg⁻¹, for the reference EtCO copolymers to 104 and 139 Jg⁻¹ in the more norbornene-rich terpolymers, obtained with nickel and palladium catalysts, respectively.

This suggests that through the introduction of norbornene, the crystallinity of these materials has been successfully modified. This is even more evident from the graph in Figure 5.14, where the crystallinity, evaluated from the second melting enthalpy, is reported as a function of the norbornene content used in feed, for both sets of studied samples.

In both cases, crystallinity decreases as norbornene concentration increases, varying from 63 to 35% in samples produced with the Ni-based catalyst and from 78 to 45% in those obtained with the Pd-based complex.

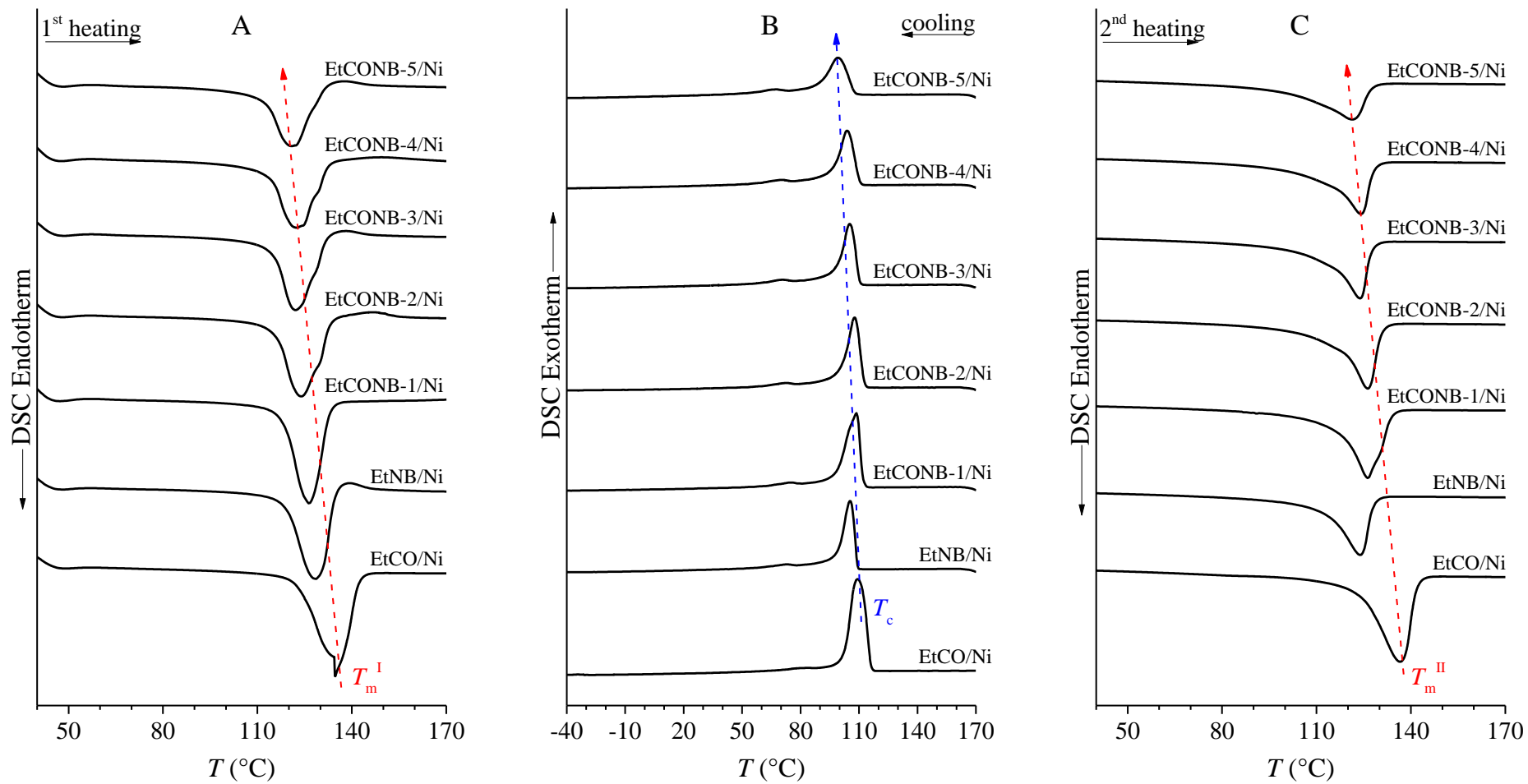


Figure 5.12. DSC thermograms of samples reported in Table 5.2 recorded at 10 °C/min during heating of as-polymerized samples (A), cooling from the melt (B) and successive heating (C).

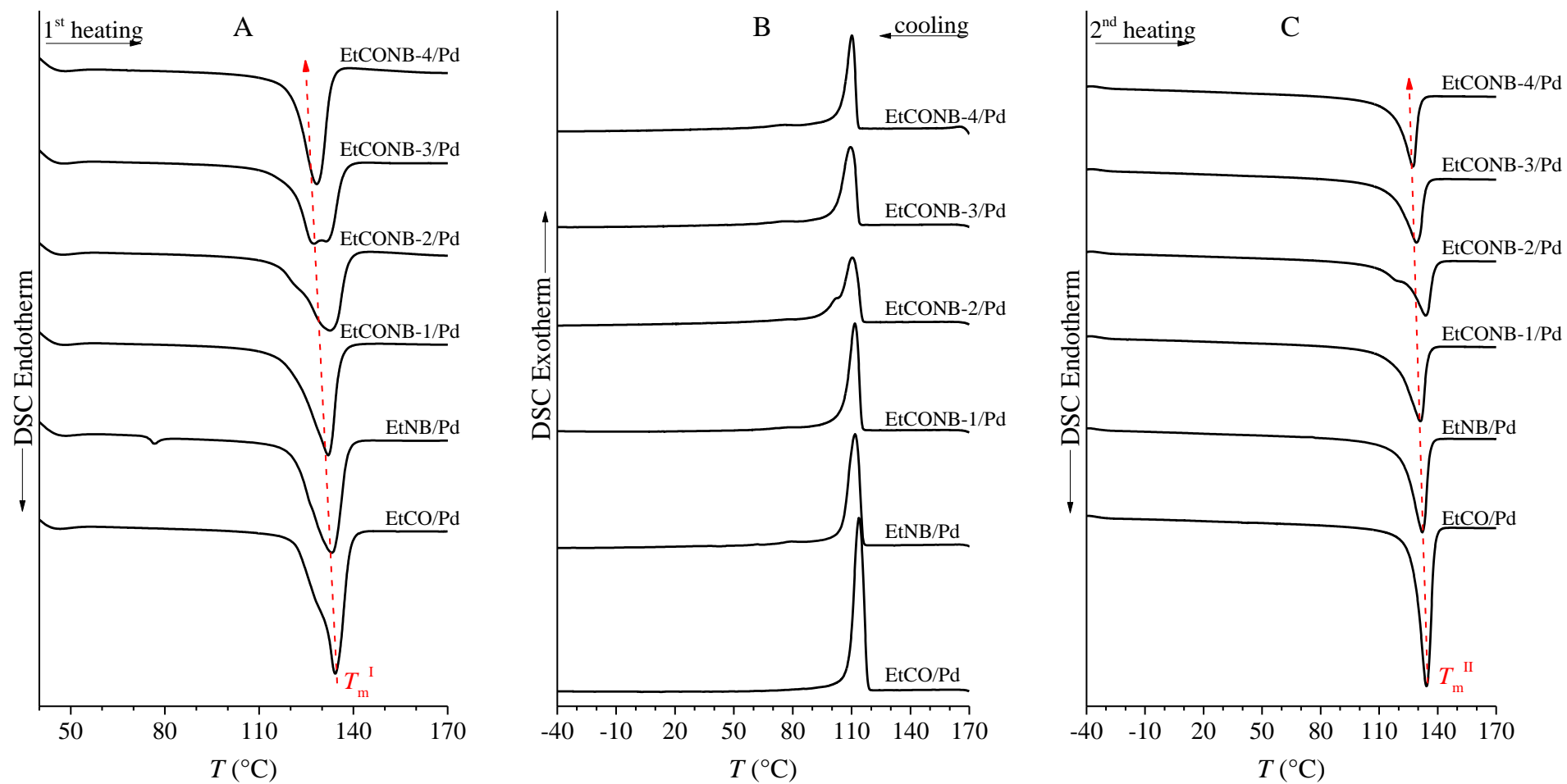


Figure 5.13. DSC thermograms of samples reported in Table 5.3 recorded at 10 °C/min during heating of as-polymerized samples (A), cooling from the melt (B) and successive heating (C).

Table 5.2. Thermal Properties of samples reported in Table 5.1.

entry	X (CO) (mol%)	NB ^a (mol L ⁻¹)	T _m ^I (°C)	ΔH _m ^I (Jg ⁻¹)	T _c (°C)	ΔH _c (Jg ⁻¹)	T _m ^{II} (°C)	ΔH _m ^{II} (Jg ⁻¹)	x _c ^{DSC b} (%)	x _c ^{RX c} (%)
EtCO/Ni	1.3		135.3	201.0	109.0	185.6	136.0	186.0	62	62
EtNB/Ni		0.1	128.7	175.6	105.4	124.5	124.0	122.3	63	56
EtCONB-1/Ni	3.4	0.1	126.4	192.5	108.5	153.7	126.3	151.6	51	58
EtCONB-2/Ni	0.7	0.15	123.8	168.4	107.7	142.2	126.3	140.0	47	51
EtCONB-3/Ni	0.7	0.2	122.2	160.1	105.2	131.9	123.8	127.5	43	49
EtCONB-4/Ni	0.9	0.3	122.3	157.9	103.9	131.9	124.2	128.0	43	47
EtCONB-5/Ni	0.5	0.4	120.9	141.0	99.2	118.1	121.5	103.9	35	38

^aconcentration of NB in initial reaction solution; ^bevaluated from the second melting enthalpy as described in section 5.2.1.; ^cevaluated from the WAXS profiles of melt-crystallized samples as described in section 5.2.1.

Table 5.3. Thermal Properties of samples reported in Table 5.2.

entry	X (CO) (mol%)	NB ^a (mol L ⁻¹)	T _m ^I (°C)	ΔH _m ^I (Jg ⁻¹)	T _c (°C)	ΔH _c (Jg ⁻¹)	T _m ^{II} (°C)	ΔH _m ^{II} (Jg ⁻¹)	x _c ^{DSC b} (%)	x _c ^{RX c} (%)
EtCO/Pd	0.4		134.2	231.6	113.8	224.5	134.3	225.6	76	78
EtNB/Pd		0.1	133.1	220.9	111.8	178.4	132.1	176.4	60	65
EtCONB-1/Pd	2.6	0.1	132.0	210.4	111.7	163.8	131.2	164.5	56	61
EtCONB-2/Pd	3.3	0.2	132.6	196.5	110.4	148.2	133.8	148.8	51	58
EtCONB-3/Pd	1.1	0.3	127.5	201.8	109.5	152.0	129.2	150.1	51	53
EtCONB-4/Pd	0.7	0.45	128.3	164.5	110.1	140.5	127.4	139.0	47	40

^aconcentration of NB in initial reaction solution; ^bevaluated from the second melting enthalpy as described in section 5.2.1.; ^cevaluated from the WAXS profiles of melt-crystallized samples as described in section 5.2.1.

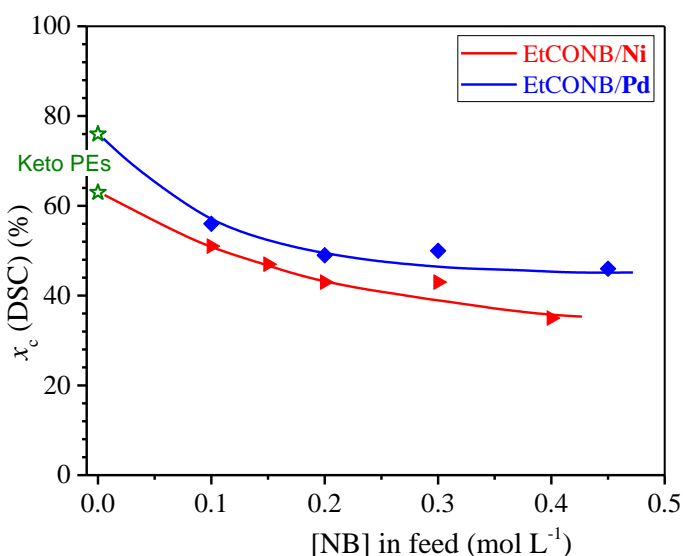


Figure 5.14. Values of the degree of crystallinity (x_c^{DSC}), evaluated from the second heating scan of Figures 5.12C and 5.13C, as a function of norbornene concentration in feed. Terpolymer samples obtained by Ni- and Pd-based catalysts are shown in red and blue, respectively.

The stress-strain curves of compression-molded films of the samples reported in Tables 5.1 and 5.2 are shown in Figures 5.15 and 5.16, respectively. The values of the mechanical parameters extracted from the stress-strain curves of Figures 5.15 and 5.16 are reported in Tables 5.5 and 5.6, respectively. All terpolymer samples exhibit deformation with necking according with high values of crystallinity and are characterized by remarkable strength, modulus, and ductility with high deformation at break. The two reference KetoPE samples (EtCO/Ni and EtCO/Pd, black curves in Figures 5.15 and 5.16), present values of Young's modulus and stress at yielding higher than those of the terpolymers in the respective series in agreement with the highest degree of crystallinity (Tables 5.2 and 5.3). By comparing the ethylene-carbon monoxide copolymers obtained with the two different catalytic systems, an important difference can be observed in terms of ductility. In fact, KetoPE synthesized with the Ni-based catalyst is much more ductile than that obtained with the Pd complex. This different behavior can be easily explained by virtue of the strong difference in molecular mass of the two samples ($M_n = 140$ kDa for EtCO/Ni vs $M_n = 20$ kDa for EtCO/Pd, Tables 5.1 and 5.2).

Concerning the samples from Nickel (Figure 5.4), the data of Figure 5.1 and Table 5.4, indicate that the co-presence of carbon monoxide and norbornene in the terpolymers produces a moderate enhancement of ductility compared to the two reference copolymers. At the same time, the simultaneous presence of both defects in the polyethylene backbone results in a decrease in the strain at yielding that gradually decreases from sample EtCONB-1/Ni to sample EtCONB-5/Ni, obtained using the lowest and highest NB concentration in feed, respectively.

For the set of samples synthesized with the Palladium-based catalyst (Figure 5.16), the same considerations can be basically made.

In all cases, the high values of t_b (Tables 5.4 and 5.5) and the low values indicate that these samples show irreversible plastic deformation with partial elastic recovery after breaking.

In conclusion, the study of mechanical properties showed that the incorporation of small norbornene content produces increased deformability compared with the original KetoPEs. This increased ductility, however, does not result in a large decrease in stiffness since the crystallinity, although partially altered, still remains high.

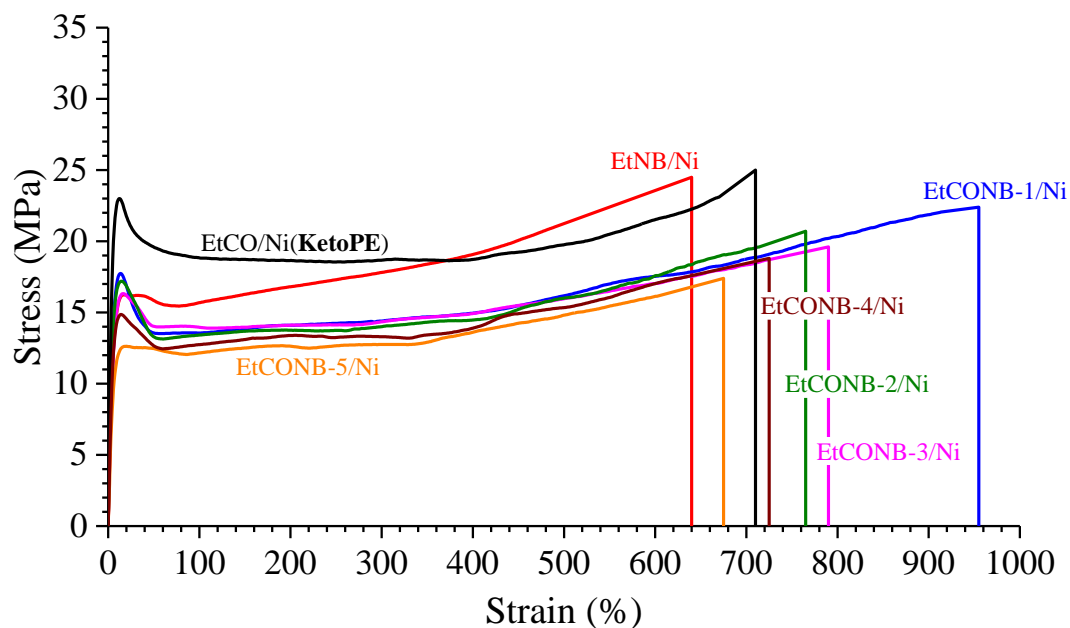


Figure 5.15. Stress-strain curves of the melt-crystallized compression molded films of the EtCO and EtNB copolymers and the EtCONB terpolymers, obtained with the Ni-based catalyst.

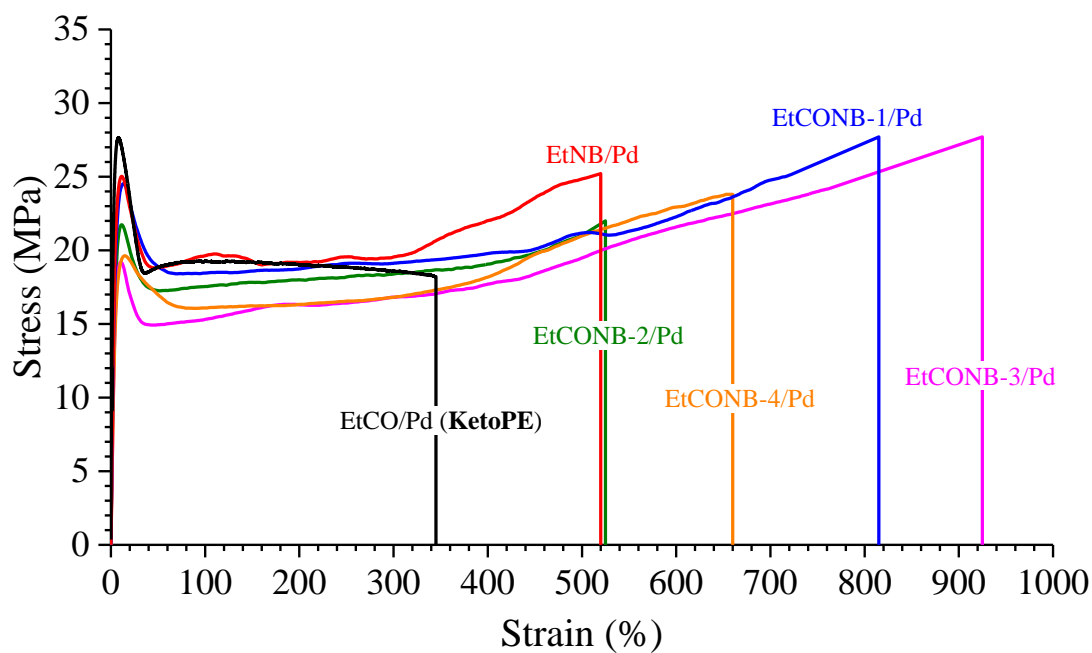


Figure 5.16. Stress-strain curves of the melt-crystallized compression molded films of the EtCO and EtNB copolymers and the EtCONB terpolymers, obtained with the Pd-based catalyst.

Table 5.4. Mechanical parameters determined from the stress-strain curve reported in Figure 5.15 recorded on compression molded films of the EtCO and EtNB copolymers and the EtCONB terpolymers, obtained with the Ni-based catalyst.

entry	X (CO) (mol%)	NB ^a (mol L ⁻¹)	E ^b (MPa)	ε _y ^c (%)	σ _y ^d (MPa)	ε _b ^e (%)	σ _b ^f (MPa)	t _b ^g (%)
EtCO/Ni	1.3		525±30	12±1	23±1	710±90	25±2	510±25
EtNB/Ni		0.1	345±30	17±2	16±3	640±50	25±5	320±50
EtCONB-1/Ni	3.4	0.1	325±12	13±1	18±1	950±30	22±1	460±40
EtCONB-2/Ni	0.7	0.15	324±3	15±1	17±1	765±2	21±2	390±20
EtCONB-3/Ni	0.7	0.2	265±20	17±2	16±1	790±50	20±2	370±10
EtCONB-4/Ni	0.9	0.3	250±15	17±3	15±1	725±60	19±1	360±50
EtCONB-5/Ni	0.5	0.4	215±6	18±1	13±1	670±50	17±1	260±30

^aconcentration of NB in initial reaction solution; ^bYoung's modulus; ^cstrain at the yield point, ^dstress at the yield point; ^estrain at break; ^fstress at break; ^g tension set at break.

Table 5.5. Mechanical parameters determined from the stress-strain curve reported in Figure 5.16 recorded on compression molded films of the EtCO and EtNB copolymers and the EtCONB terpolymers, obtained with the Pd-based catalyst.

entry	X (CO) (mol%)	NB ^a (mol L ⁻¹)	E ^b (MPa)	ε _y ^c (%)	σ _y ^d (MPa)	ε _b ^e (%)	σ _b ^f (MPa)	t _b ^g (%)
EtCO/Pd	0.4		670±40	9±1	27±1	350±10	19±1	320±10
EtNB/Pd		0.1	520±30	16±3	25±1	520±20	25±2	500±10
EtCONB-1/Pd	2.6	0.1	560±20	14±2	25±1	815±100	28±2	460±10
EtCONB-2/Pd	3.3	0.2	475±34	12±1	22±1	530±35	22±1	400±50
EtCONB-3/Pd	1.1	0.3	430±28	11±1	20±1	920±100	27±1	500±20
EtCONB-4/Pd	0.7	0.45	405±20	15±1	20±1	660±20	24±1	410±30

^aconcentration of NB in initial reaction solution; ^bYoung's modulus; ^cstrain at the yield point, ^dstress at the yield point; ^estrain at break; ^fstress at break; ^g tension set at break.

5.2.4 Ethylene-CO-methyl-5-Norbornene-2-Carboxylate Terpolymers – Synthesis and Characterization

Samples of ethylene/carbon monoxide/methyl-5-norbornene-2-carboxylate terpolymers (EtCONBE) and of ethylene/carbon monoxide (EtCO) and ethylene/methyl-5-norbornene-2-carboxylate (EtNBE) copolymers were synthesized at 90 °C using a neutral phosphinosulfonate Pd (II) catalyst, as illustrated in the Figure 5.17. Details of polymerization conditions and the main properties of the samples are summarized in Table 5.6.

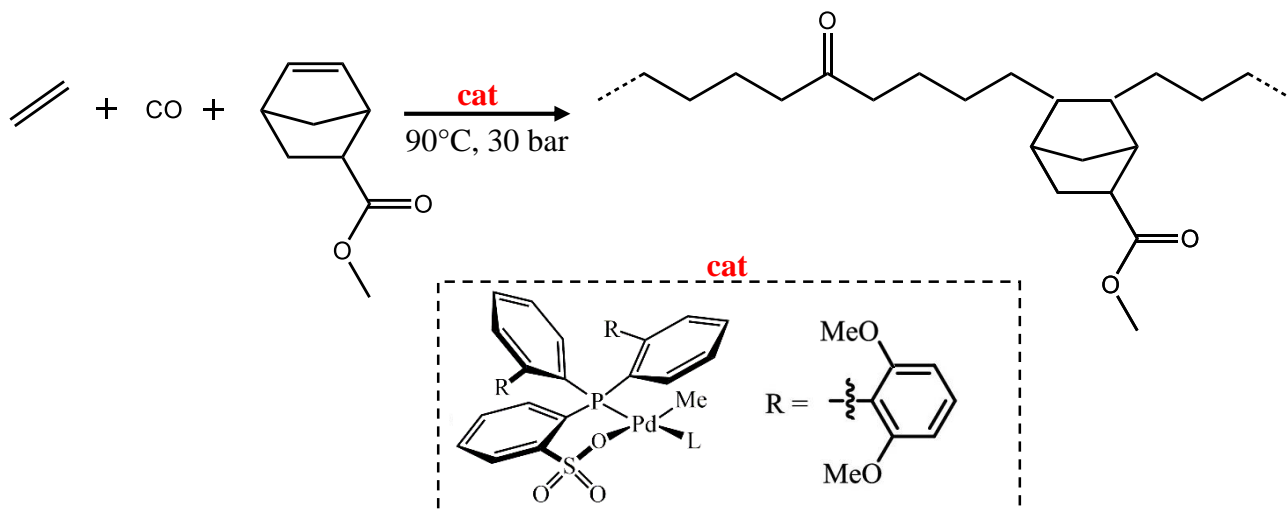


Figure 5.17. Catalytic Terpolymerization of Ethylene with CO and methyl-5-Norbornene-2-Carboxylate using the neutral phosphinophenolato Pd (II) catalyst.

Table 5.6. Polymerization details and molecular characteristics of the synthesized samples.^a

entry	CO/C ₂ H ₄ feed ^b (%)	NBE ^c (mol L ⁻¹)	yield (g)	X (CO) ^d (mol%)	X (NBE) ^d (mol%)	C=O IR ^d (cm ⁻¹)	M _n ^e (kDa)	M _w /M _n ^e
EtCO ^f	0.6		7.5	0.4 (0.5)		1715	20	2.1
EtNBE		0.1	9.6		0.4 (0.5)	1739	33	2.1
EtCONBE-1	0.6	0.1	0.20	alt	0.2 (0.3)	1739 - 1702	5.5	2.1
EtCONBE-2	0.4	0.1	0.93	3.3 (4.4)	0.2 (0.5)	1739 – 1710	44	2.3
EtCONBE-3	0.3	0.1	4.20	0.6 (1.0)	0.4 (0.8)	1739 – 1714	58	1.6
EtCONBE-4	0.2	0.1	12.6	0.3 (0.5)	0.3 (0.6)	1739 - 1716	38	1.9

^aPolymerization conditions: 2 μmol precat. 2, 30 atm, 100 °C, 1000 rpm, 60 min, 100 mL toluene. ^bRatio of CO in an ethylene-CO gas feed. ^cConcentration of NBE in initial reaction solution. ^dCalculated from ATR-IR spectroscopy (see experimental section details) In brackets: Incorporation calculated from ¹H NMR spectroscopy by integration of the ¹H signals of α-carbonyl CH₂ (CO) or OCH₃ (NBE) in relation to the overall integral. ^eDetermined by SEC in 1,2-dichlorobenzene at 160 °C via universal calibration against PS standards. ^fFirst reported in Table 5.2.

In order to reveal the presence of carbon monoxide and methyl-5-norbornene-2-carboxylate (NBE) in the terpolymer samples, ATR-IR measurements were performed.

The ATR-IR spectra collected on all as-prepared samples reported in Table 5.6 are shown in Figure 5.17.

IR spectra recorded on the reference copolymers EtCO and EtNBE show an absorption maximum in the carbonyl region centered at 1714 and 1739 cm^{-1} , respectively. The signal at 1714 cm^{-1} , as widely discussed in the previous section, is associated with the presence of in-chain carbonyl groups that characterize the EtCO copolymer, while the maximum at 1739 $^{-1}$ is related to the backbone-adjacent ester groups of the functionalized norbornene units (Figure 5.17) incorporated into the EtNBE reference copolymer.

At this point, it is easy to understand that the spectroscopic data recorded on EtCONBE terpolymers, clearly demonstrate the incorporation of CO and NBE into the four synthesized samples and, thus, the real terpolymer nature of these materials. In fact, in all cases, the presence of both maxima can be distinguished at wavenumber values similar to those observed in the reference copolymers.

In addition, the position of the keto groups adsorption band in the range 1710 - 1716 cm^{-1} in the spectra of samples EtCONBE-2, EtCONBE-3 and EtCONBE-4 indicates the predominantly isolated/nonalternating distribution of the in-chain carbonyl groups formed by CO incorporation. By contrast, sample EtCONBE-1, appears to be mainly characterized by an alternating distribution of keto groups as suggested by the absorption band at $\approx 1700 \text{ cm}^{-1}$. However, the fact that the intensities associated with the polyethylene C-H vibrations at 2740 - 3030 cm^{-1} are still very intense, indicate that long polyethylene sequences are also present in this sample (blue curve in Figure 5.17A).

As described in section 5.2.1, from the IR spectra it is possible to determine the concentration of both comonomeric units in these samples by performing the deconvolution of the terpolymer absorption bands. The results are shown in Table 5.6 and indicate that the terpolymers are characterized by very low NBE content (<1 mol%) and CO concentration ranging from 0.3 to 3.3 mol%.

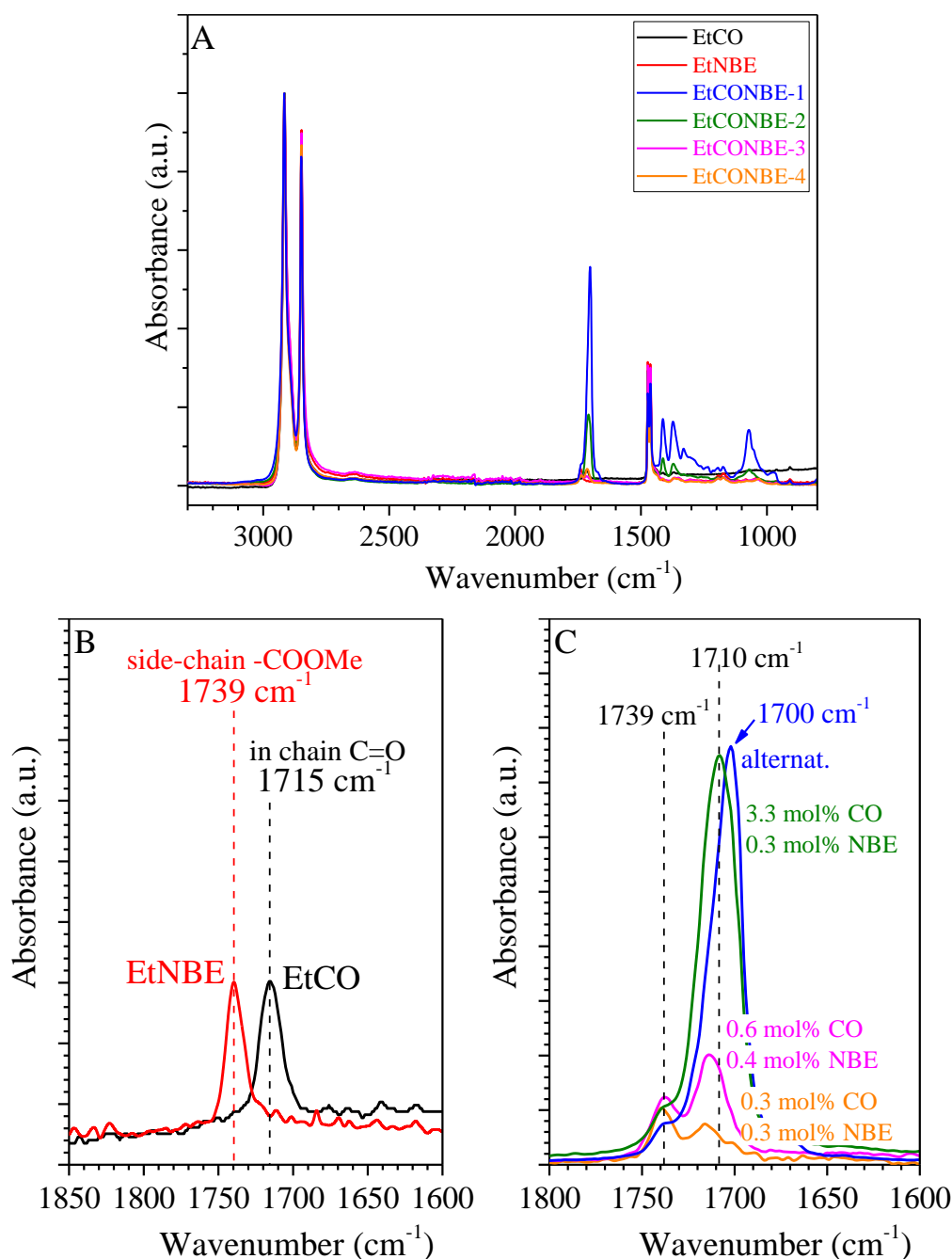


Figure 5.17. Full ATR-IR spectra of terpolymers and reference copolymers reported in Table 5.6 (A). Expansion of the carbonyl region of ATR-IR spectra of the EtCO and EtNBE reference copolymers (B) and of the EtCONBE terpolymers (C). In (C) the absorbance intensity of alternating polyketones (blu curve) is adjusted for clarity.

However, as can be noticed in the IR spectra of Figure 5.18, in some cases the ester group absorption band is partly overlapped with that of the in-chain carbonyl groups, preventing the correct evaluation of NBE concentration. Therefore, in order to confirm the estimated composition by IR, ^1H NMR spectroscopy measurements were also performed on all samples.

The ^1H NMR spectra collected on the sample EtCONB-3 is shown in Figure 5.19, as an example. The CO and NBE concentrations in the terpolymers, calculated by integration of the ^1H signals of α -carbonyl CH_2 (CO) (at ≈ 2.5 ppm) and OCH_3 (NBE) (at ≈ 3.7 ppm) in relation to the overall

integral,^{34,36} respectively, are in agreement with those evaluated by IR analysis (Table 5.6). In addition, the ¹H NMR spectrum further confirms the low content of alternating carbon monoxide-ethylene sequences and, thus, that the in-chain keto groups are predominantly isolated or at least separated by several ethylene units.

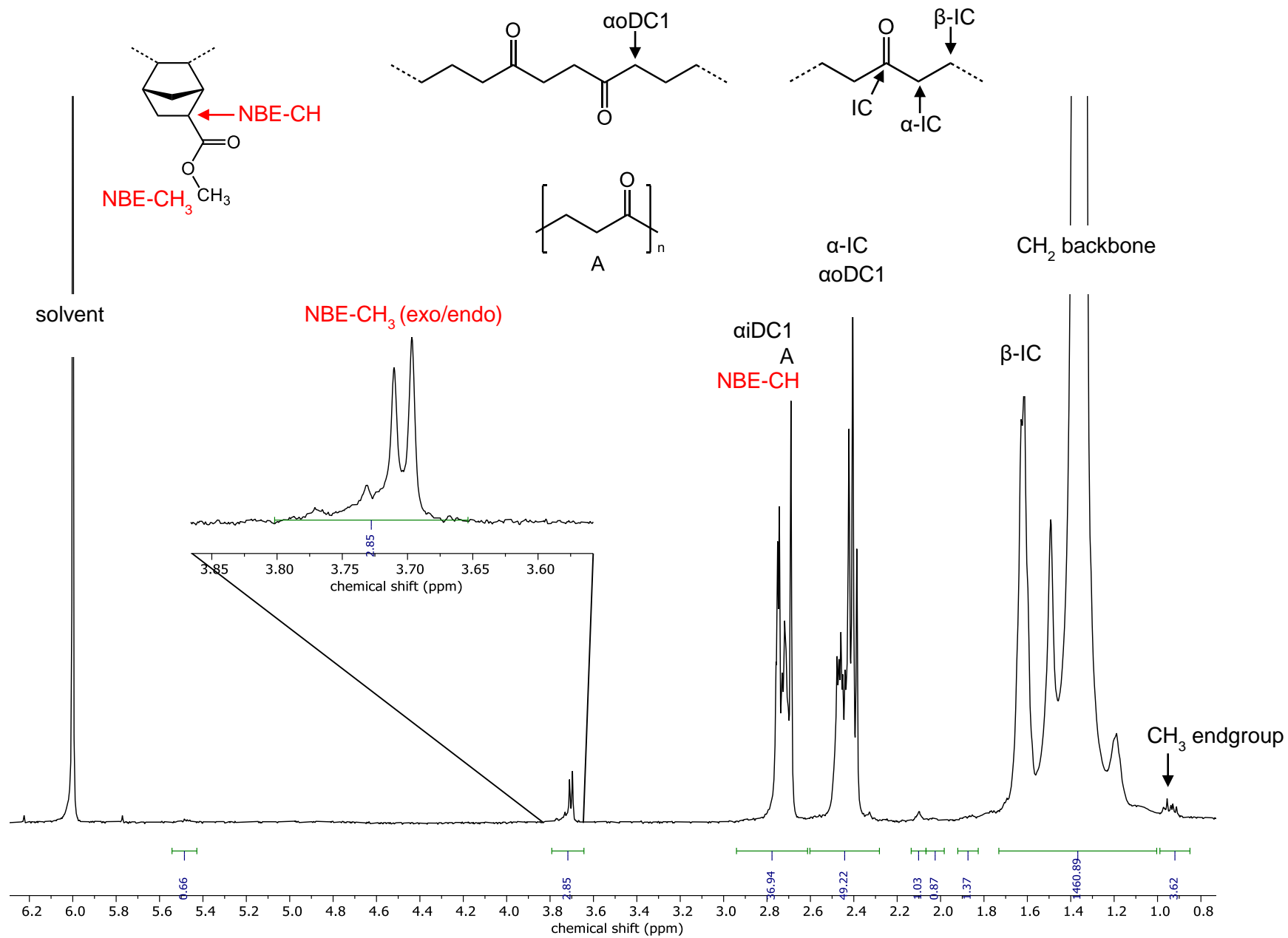


Figure 5.19. ¹H NMR spectrum of the terpolymer sample EtCONB-3 (Table 5.6) with full assignments. Acquired in tetrachloroethane-d₂ at 110 °C.

The GPC curves of all samples reported in Table 5.6 are shown in Figure 5.20.

Analysis of the data reported in Figure 5.18, indicates that EtCONBE terpolymers synthesized by using a CO/ethylene feed ratio in the range of 0.4 - 0.2%, have similar molecular weights to the ethylene/NBE reference copolymer and higher than the ethylene/CO copolymer, both produced under the same conditions at 30 bar and 90°C. In contrast, the terpolymer sample EtCONBE-1 with the predominantly alternating structure, obtained using a higher concentration of carbon monoxide in feed (CO/C₂H₄=0.6, Table 5.6), exhibits a significantly lower molecular weight (5.5 kDa, Table 5.6). In all cases, samples show unimodal and moderately narrow molecular weight distribution ($M_w/M_n = 1.6 - 2.1$, Table 5.6).

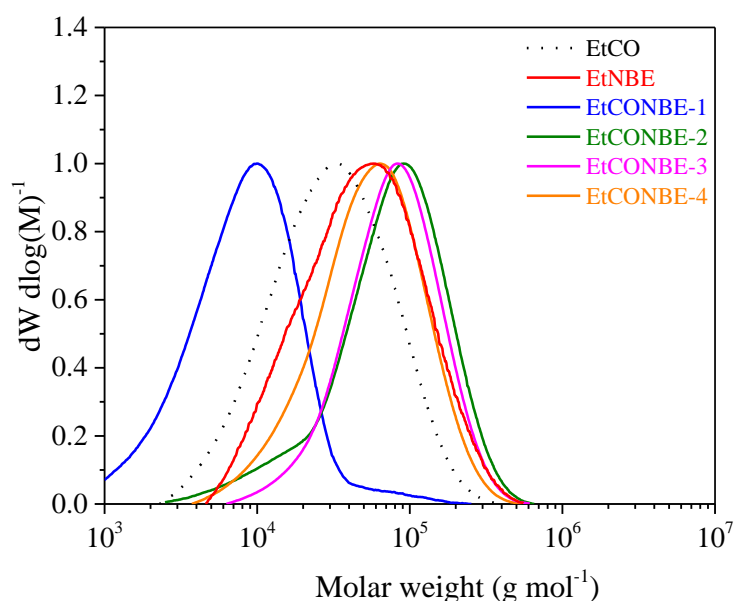


Figure 5.20. SEC traces of EtCONBE terpolymers, and EtCO and EtNBE copolymers reported in Table 5.6.

The DSC thermograms recorded on the two reference copolymers and the non-alternating EtCONBE terpolymers during first heating from 50°C to 180°C, successive cooling from the melt to -70°C, and second heating of the melt crystallized samples up to 180°C, all recorded at 10 °C/min, are reported in Figure 5.21. The DSC curves recorded on sample EtCONBE-1, characterized by the predominantly alternating keto groups distribution, are shown separately in Figure 5.22 since they were acquired in a different temperature range.

For each sample, the melting and crystallization temperatures with the associated enthalpy values are given in Table 5.7. The crystallinity, evaluated as described in section 5.2.1, is also reported in Table 5.7. DSC scans reported in Figure 5.22 indicate that all samples present similar crystallization and melting temperatures at around 110 and 137 °C, respectively, despite the differences in molecular structure and composition.

In the DSC thermogram shown in Figure 5.23, the presence of a broad endotherm centered at ≈ 200 °C during the first heating scan (curve a), in addition to that at 125 °C associated with polyethylene-like crystals, confirms the presence of alternating polyketone crystals³⁷ (APK) in the sample EtCONBE-1, according to the IR data reported in Figure 5.17. APK crystals do not crystallize during cooling (curve b) so the only exotherm of crystallization observed is related to crystals of a polyethylene nature that then melt in subsequent heating (curve c).

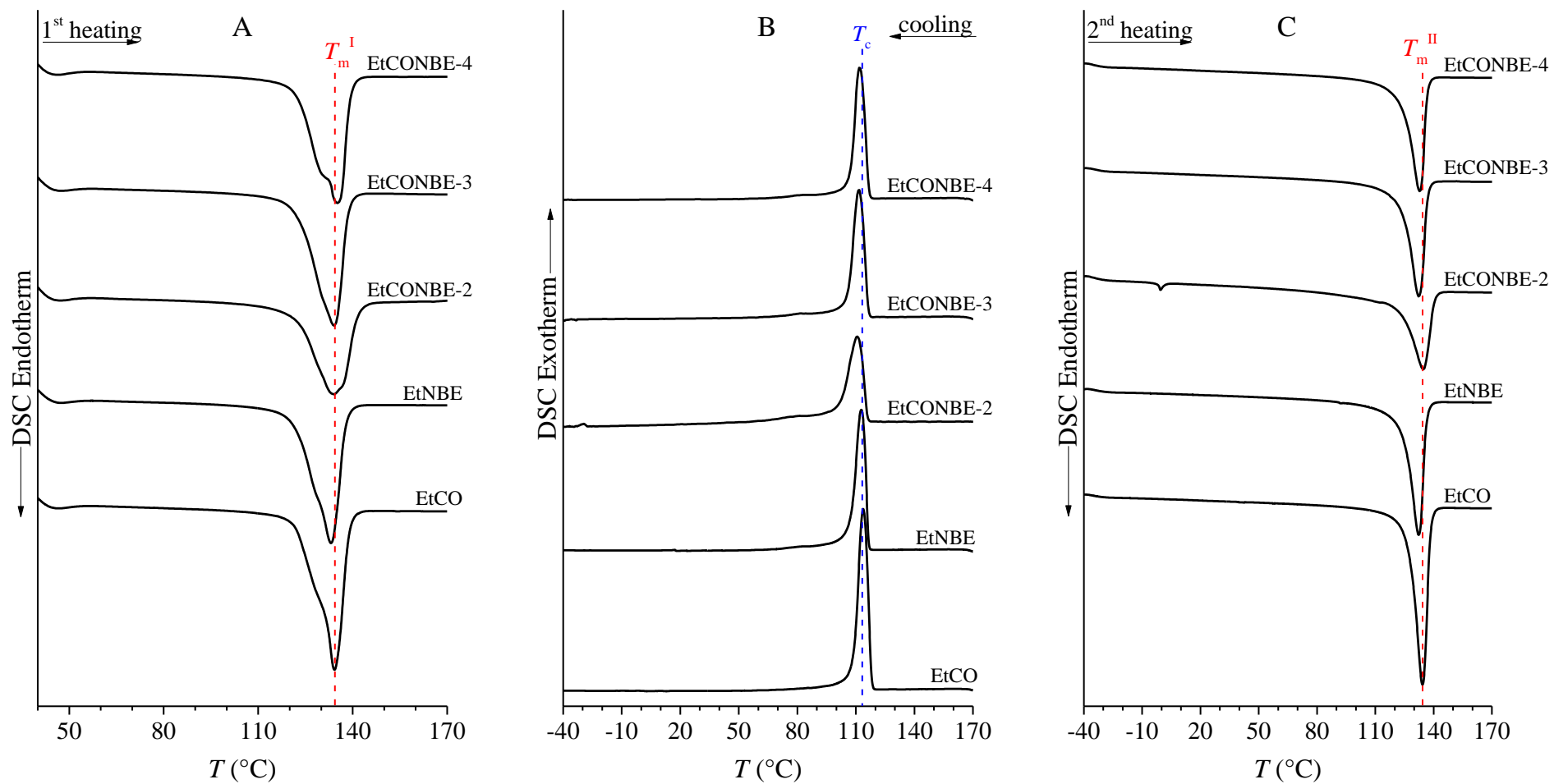


Figure 5.22. DSC thermograms recorded on the two reference copolymer samples and on the EtCONBE-2, EtCONBE-3 and EtCONBE-4 terpolymer samples at 10 $^{\circ}\text{C}/\text{min}$ during heating of as-polymerized samples (A), cooling from the melt (B) and successive heating (C).

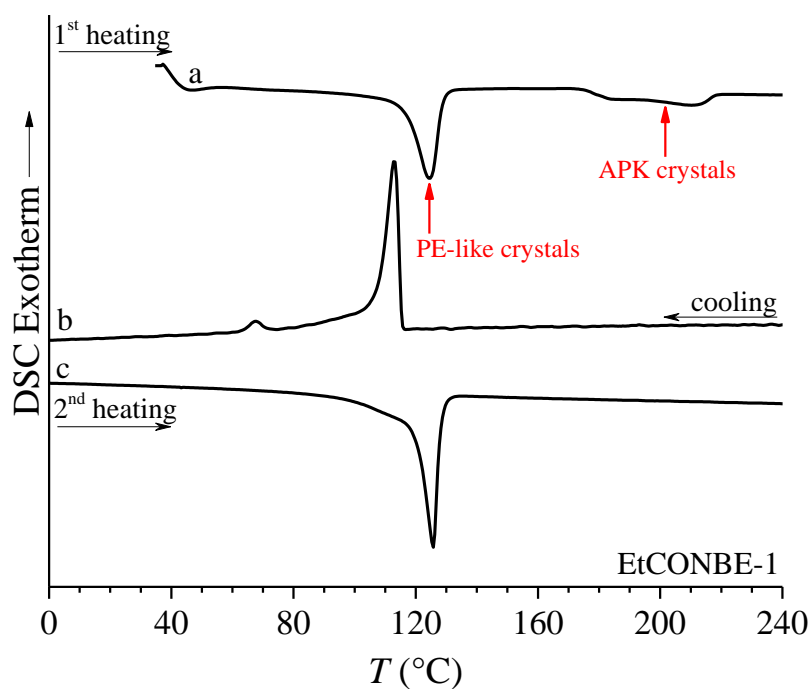


Figure 5.23. DSC thermogram recorded on the sample EtCONBE-1 at 10 °C/min during heating of the as-polymerized sample (a), cooling from the melt (b) and successive heating (c).

Table 5.7. Thermal Properties of samples reported in Table 5.6.

entry	X (CO) ^a (mol%)	X (NBE) ^a (mol%)	T_m^I (°C)	ΔH_m^I (Jg ⁻¹)	T_c (°C)	ΔH_c (Jg ⁻¹)	T_m^{II} (°C)	ΔH_m^{II} (Jg ⁻¹)	$x_c^{DSC\ b}$ (%)	$x_c^{RX\ c}$ (%)
EtCO	0.4 (0.5)		134.2	231.6	113.8	224.5	134.3	225.6	76	78
EtNBE		0.4 (0.5)	133.1	218.8	112.7	194.4	132.3	198.5	68	65
EtCONBE-1	alt	0.2 (0.3)	124.5,215	116.5	113.0	147.9	125.7	146.0	50	52
EtCONBE-2	3.3 (4.4)	0.2 (0.5)	134.2	201.8	110.7	195.1	134.7	195.7	66	67
EtCONBE-3	0.6 (1.0)	0.4 (0.8)	135.2	222.9	112.0	181.5	132.9	182.0	62	65
EtCONBE-4	0.3 (0.5)	0.3 (0.6)	134.1	213.9	111.7	191.6	132.4	190.0	65	66

^aCalculated from ATR-IR spectroscopy. In brackets: Incorporation calculated from ¹H NMR spectroscopy; ^bevaluated from the second melting enthalpy as described in section 5.2.1.; ^cevaluated from the WAXS profiles of melt-crystallized samples as described in section 5.2.1.

The X-ray diffraction profiles, recorded on all the as-prepared and melt-crystallized samples reported in Table 5.6 are displayed in Figure 5.24A and 5.24B, respectively.

The WAXS data show that samples crystallize in the orthorhombic form of PE and, thus, that the crystallinity is completely preserved in all the synthesized terpolymers, as also indicated by the similar x_c values reported in Table 5.7.

This means that the crystallinity is not considerably affected or disturbed by the incorporation of these negligible contents of side-chain ester and in-chain keto (≈ 1 mol% of each polar comonomer) groups. The diffraction profile of the as-prepared sample EtCONBE-1 further demonstrate the presence of alternating polyketone crystals, as indicated by the (110) reflection at $2\theta \approx 22.5^\circ$ related to the APK crystals³⁷ (Figure 5.24A).

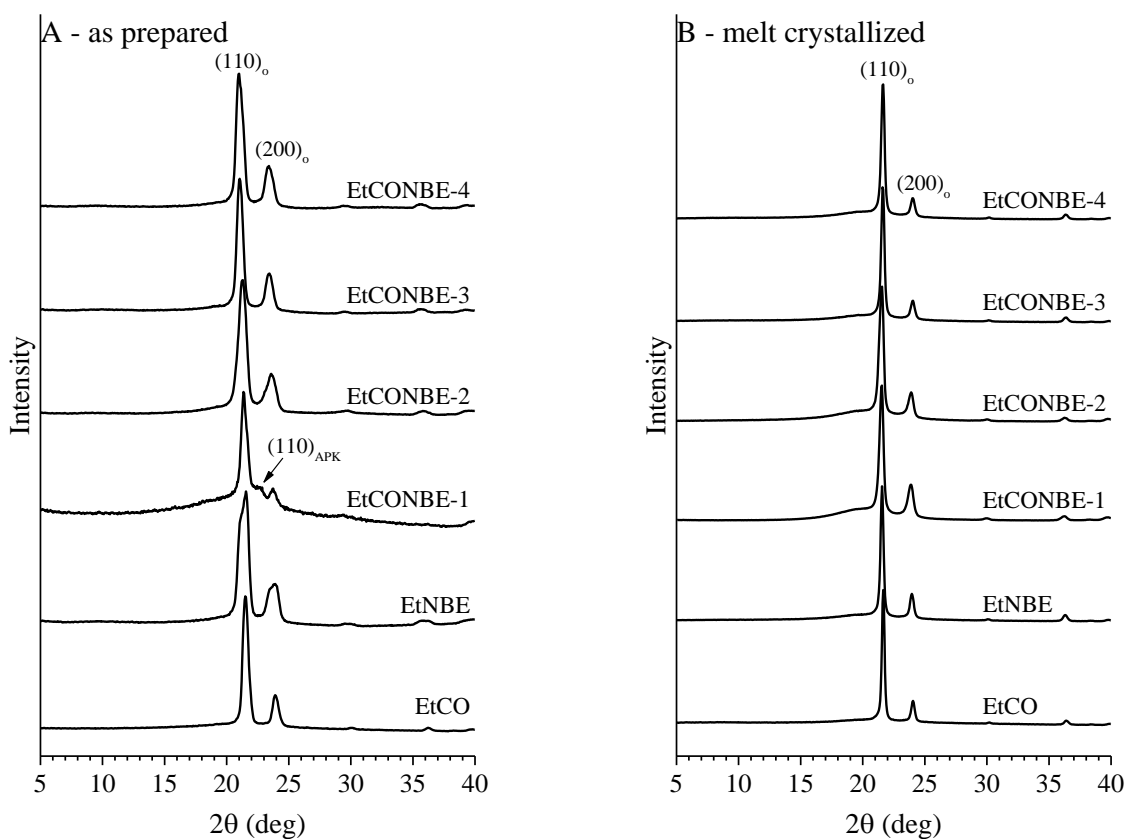


Figure 5.24. WAXS profiles of as-polymerized (A) and melt-crystallized (B) samples reported in Table 5.6.

The stress-strain curves of compression-molded films, obtained by slow cooling from the melt to room temperature, of samples reported in Table 5.6 are displayed in Figure 5.25. The values of the mechanical properties are reported in Table 5.8.

The curve of the terpolymer EtCONBE-1 is not shown since there was insufficient material to investigate the mechanical properties of this sample (see Table 5.6).

The data in Figure 5.25 and Table 5.8, clearly show that the mechanical behavior of the three analyzed terpolymers is almost on par with the reference ethylene-carbon monoxide copolymer in terms of the stresses involved both at yielding and at higher strains. This is in accordance with the high crystallinity present in the terpolymer samples, which, therefore, ensures high resistance to the plastic deformation and, in general, excellent mechanical performances despite the presence of two polar comonomeric units. In addition, all samples of the EtCONBE terpolymers and the EtNBE copolymer are characterized by much higher ductility than the EtCO copolymer. This is in agreement with the lower molecular weight of the sample EtCO, which does not guarantee a degree of entanglements high enough to achieve high strains at break.

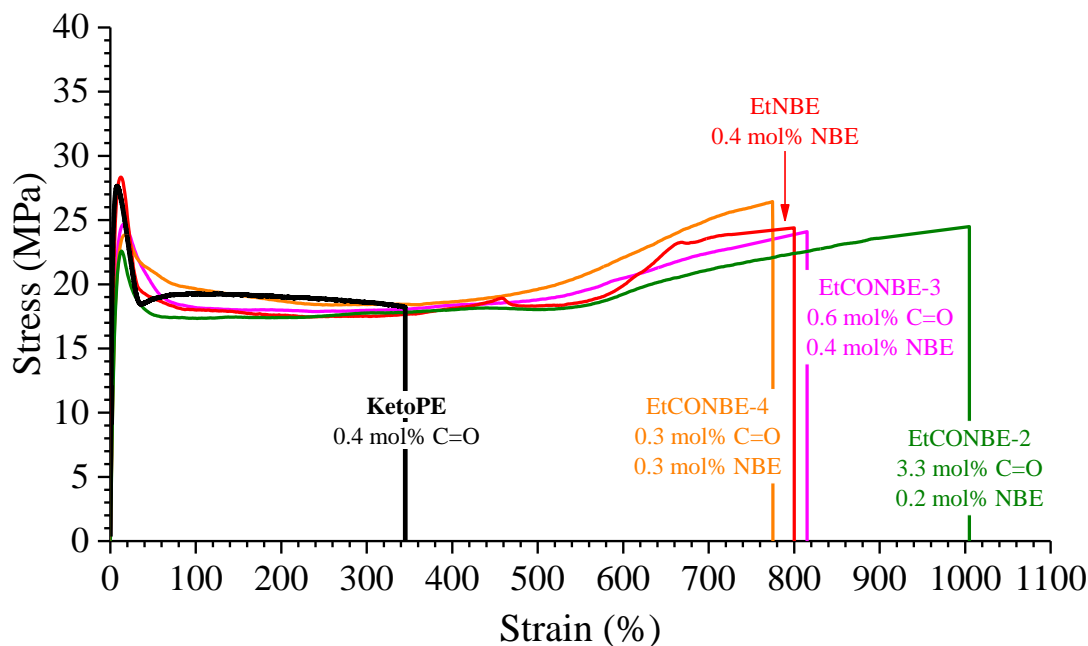


Figure 5.25. Stress-strain curves of the melt-crystallized compression molded films of the EtCO and EtNBE copolymers and the EtCONBE terpolymers reported in Table 5.6.

Table 5.8. Mechanical parameters determined from the stress-strain curve reported in Figure 5.25 recorded on compression molded films of the EtCO and EtNBE copolymers and the EtCONBE terpolymers reported in Table 5.6.

entry	X (CO) (mol%)	NB^a (mol L ⁻¹)	E^b (MPa)	ε_y^c (%)	σ_y^d (MPa)	ε_b^e (%)	σ_b^f (MPa)	t_b^g (%)
EtCO	0.4 (0.5)		670±40	9±1	27±1	350±10	19±1	320±10
EtNBE		0.4 (0.5)	590±50	13±2	28±2	800±100	25±1	760±20
EtCONBE-2	3.3 (4.4)	0.2 (0.5)	385±40	14±1	22±2	1000±90	24±2	550±10
EtCONBE-3	0.6 (1.0)	0.4 (0.8)	470±10	15±1	25±2	810±70	24±1	620±30
EtCONBE-4	0.3 (0.5)	0.3 (0.6)	460±20	17±1	24±2	770±80	27±3	650±20

^aCalculated from ATR-IR spectroscopy. In brackets: Incorporation calculated from ¹H NMR spectroscopy ^bYoung's modulus; ^cstrain at the yield point, ^dstress at the yield point; ^estrain at break; ^fstress at break; ^g tension set at break.

5.2.5 Conclusions Chapter 5

In this chapter has been described the catalytic terpolymerization of ethylene, carbon monoxide, and norbornene (EtCONB), performed by using two advanced complexes based on Ni(II) and Pd(II). Samples of random EtCO and EtNB reference copolymers, and of EtCONB terpolymers characterized by a different CO and norbornene concentration have been prepared with both catalysts. The effect of the presence of carbon monoxide and norbornene co-units on the crystallinity and mechanical properties of keto-polyethylenes has been analyzed. IR spectroscopy measurements have demonstrated the effective incorporation of carbon monoxide into polyethylene chains. In addition, in all the studied terpolymers, the observed IR absorption maximum in the range $1710 - 1719 \text{ cm}^{-1}$ has indicated the predominantly isolated/nonalternating nature of the in-chain keto groups formed by CO incorporation. The molecular weight analysis, performed by GPC, revealed that all synthesized samples are characterized by moderately high molecular masses and narrow molecular weight distributions.

The structural characterization, performed by WAXS, has shown that all the EtCONB terpolymers are semicrystalline materials and crystallize in the orthorhombic form of polyethylene.

The analysis of thermal properties has confirmed the crystallinity found with WAXS and indicated that norbornene was successfully incorporated into all synthesized terpolymer samples. In fact, the observed melting temperatures of the EtCONB terpolymers are always lower than those of the reference EtCO copolymers and also slightly decrease as the norbornene content increases. Furthermore, from the melting enthalpy values it was possible to appreciate that the crystallinity of these materials has been altered and that, specifically, it decreases as the norbornene content increases.

The study of mechanical properties showed that the incorporation of carbon monoxide and norbornene produces increased deformability compared with the reference ethylene-carbon monoxide copolymers. At the same time, the simultaneous presence of both defects in the polyethylene backbone results in modification of the strain at yielding and of the Young modulus values which gradually reduce as norbornene content increases, according to the decrease of crystallinity.

In the same Chapter it was also reported the synthesis and characterization of novel polar polyethylenes with combined in-chain and side-chain functional groups formed by Pd(II)-catalyzed terpolymerization of ethylene, carbon monoxide, and methyl-5-norbornene-2-carboxylate (EtCONBE). The results of IR and ^1H NMR analysis have indicated that both carbon monoxide and methyl-5-norbornene-2-carboxylate were successfully incorporated into PE chains in low concentrations (between 1 and 3 mol% in total). In addition, also in this case, the position of the

carbonyl groups adsorption band in the range 1710 - 1716 cm^{-1} in the spectra of all studied terpolymer samples revealed the predominantly isolated/nonalternating distribution of the in-chain keto groups. Analysis by WAXS showed that the orthorhombic structure of polyethylene is fully retained in the formed terpolymers despite the presence of the two polar comonomers. Moreover, the incorporation of these low amounts of side-chain ester and in-chain keto groups does not significantly affect the crystallization and melting temperatures, as well as the corresponding enthalpies, compared with the reference ethylene-carbon monoxide copolymer.

It was also shown that the mechanical behavior of the analyzed terpolymers is similar to those of the reference ethylene-carbon monoxide copolymer in terms of the stresses involved both at yielding and at higher strains. This is in accordance with the high crystallinity present in the terpolymer samples, which, therefore, ensures high resistance to the plastic deformation and, in general, excellent mechanical performances.

In general, the obtained terpolymers represent very interesting systems since they are characterized by the presence of small amounts of polar co-units that impart polar character and photodegradability to the material and at the same time do not compromise the desirable properties of polyethylene such as crystallinity, melting temperature and mechanical behavior.

References

- 1) M. Stürzel, S. Mihan, R. Mülhaupt *Chem. Rev.* **2016**, *116*, 1398.
- 2) M. A. Spalding, A. M. Chatterjee *Handbook of Industrial Polyethylene and Technology*, 1st ed., Wiley-VCH, Weinheim, **2017**.
- 3) J. Y. Dong, Y. Hu *Coord. Chem. Rev.* **2006**, *250*, 47.
- 4) T. Runzi, S. Mecking *Adv. Funct. Mater.* **2014**, *24*, 387.
- 5) S. Y. Dai, C. L. Chen *Macromolecules* **2018**, *51*, 6818 .
- 6) A. Nakamura, S. Ito, K. Nozaki *Chem Rev* **2009**, *109*, 5215.
- 7) A. Nakamura, T. M. J. Anselment, J. Claverie, B. Goodall, R. F. Jordan, S. Mecking, B. Rieger, A. Sen, P. W. N. M. Van Leeuwen, K. Nozaki *Accounts of Chemical Research* **2013**, *46*, 1438.
- 8) L. K. Johnson, C. M. Killian, M. Brookhart *J. Am. Chem. Soc.* **1995**, *117*, 6414.
- 9) E. Drent, R. van Dijk, R. van Ginkel, B. van Oort, R. I. Pugh *Chem. Commun.* **2002**, 744.
- 10) L. K. Johnson, S. Mecking, M. Brookhart *J. Am. Chem. Soc.* **1996**, *118*, 267.
- 11) Z. B. Guan, P. M. Cotts, E. F. McCord, S. J. McLain *Science* **1999**, *283*, 2059.
- 12) L. H. Guo, C. L. Chen, *Sci. China Chem.* **2015**, *58*, 1663.
- 13) L. H. Guo, S. Y. Dai, X. L. Sui, C. L. Chen *ACS Catal.* **2016**, *6*, 428.
- 14) N. Schuster, T. Runzi, S. Mecking *Macromolecules* **2016**, *49*, 1172.
- 15) T. R. Younkin, E. F. Connor, J. I. Henderson, S. K. Friedrich, R. H. Grubbs, D. A. Bansleben *Science* **2000**, *287*, 460.
- 16) E. F. Connor, T. R. Younkin, J. I. Henderson, S. Hwang, R. H. Grubbs, W. P. Roberts, J. J. Litzau, *J. Polym. Sci. Part A* **2002**, *40*, 2842.
- 18) M. R. Radlauer, A. K. Buckley, L. M. Henling, T. Agapie *J. Am. Chem. Soc.* **2013**, *135*, 3784.
- 19) D. Takeuchi, Y. Chiba, S. Takano, K. Osakada *Angew. Chem. Int. Ed.* **2013**, *52*, 12536.
- 20) M. P. Weberski, C. L. Chen, M. Delferro, T. Marks *Chem. Eur. J.* **2012**, *18*, 10715.
- 21) C. Tan, C. Chen *Angew. Chem. Int. Ed.* **2019**, *58*, 7192.
- 22) R. P. Quirk, M. A. A. Alsamarrie, Physical constants of polyethylene. In: *Polymer Handbook*, Eds J. Brandrup, E. H. Immergut, 3rd Ed. New York: Wiley; **1989**. p. V/19.
- 23) P. Ortmann, F. P. Wimmer, S. Mecking *ACS Macro Lett.* **2015**, *4*, 704.
- 24) M. Häußler, M. Eck, D. Rothauer, S. Mecking *Nature* **2021**, *590*, 423.
- 25) D. B. Malpass, E. I. Band “Introduction to polymers of propylene,” in *Introduction to Industrial Polypropylene: Properties, Catalysis, Processes*, Scrivener; **2012**, pp. 1–18.
- 26) G. R. Strobl *The Physics of Polymers*, Springer **2007**.
- 27) Y. Mato, T. Isobe, H. Takada, H. Kanehiro, C. Ohtake, T. Kaminuma *Environ. Sci. Technol.* **2001**, *35*, 318.

- 28) C.M. Rochman, M.A. Browne, B.S. Halpern, B.T. Hentschel, E. Hoh, H.K. Karapanagioti, L.M. Rios-Mendoza, H. Takada, S. Teh, R.C. Thompson *Nature* **2013**, *494*, 169.
- 29) R. Geyer, J.R. Jambeck, K.L. Law *Sci. Adv.* **2017**, *3*, e1700782.
- 30) J.M. Garcia, M.L. Robertson *Science* **2017**, *358*, 870.
- 31) H. Sardon, A.P. Dove, Plastics recycling with a difference, *Science* **2018**, *360*, 380.
- 32) X. Tang, E.-Y.-X. Chen *Chem* **2019**, *5*, 1.
- 33) R. G. .W. Norrish, C. H. Bamford *Nature* **1937**, *140*, 195.
- 34) M. Baur, F. Lin, T. Morgen, L. Odenwald, S. Mecking *Science* **2021**, *374*, 604.
- 35) S. Soomro, D. Cozzula, W. Leitner, H. Vogta, T. E. Muller *Polymer Chemistry* **2014**, *5*, 3831.
- 36) M. Baur, S. Mecking *ACS Macro Lett.* **2022**, *11*, 1207.
- 37) E. A. Klop, B. J. Lommerts, J. Verunik, J. Aerts, R. R. Van Puijenbroek *J. Polym. Sci. B Polym. Phys.* **1995**, *33*, 315.

Annex

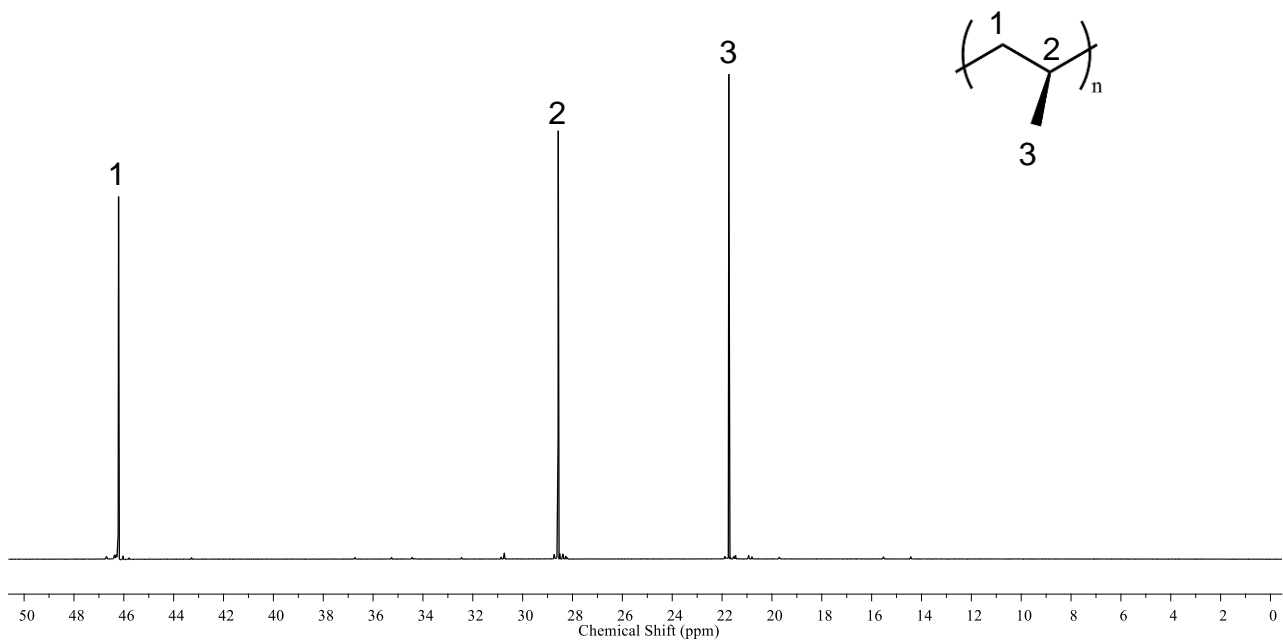


Figure A1. ^{13}C NMR spectra of the homopolymer sample iPP-Hf.

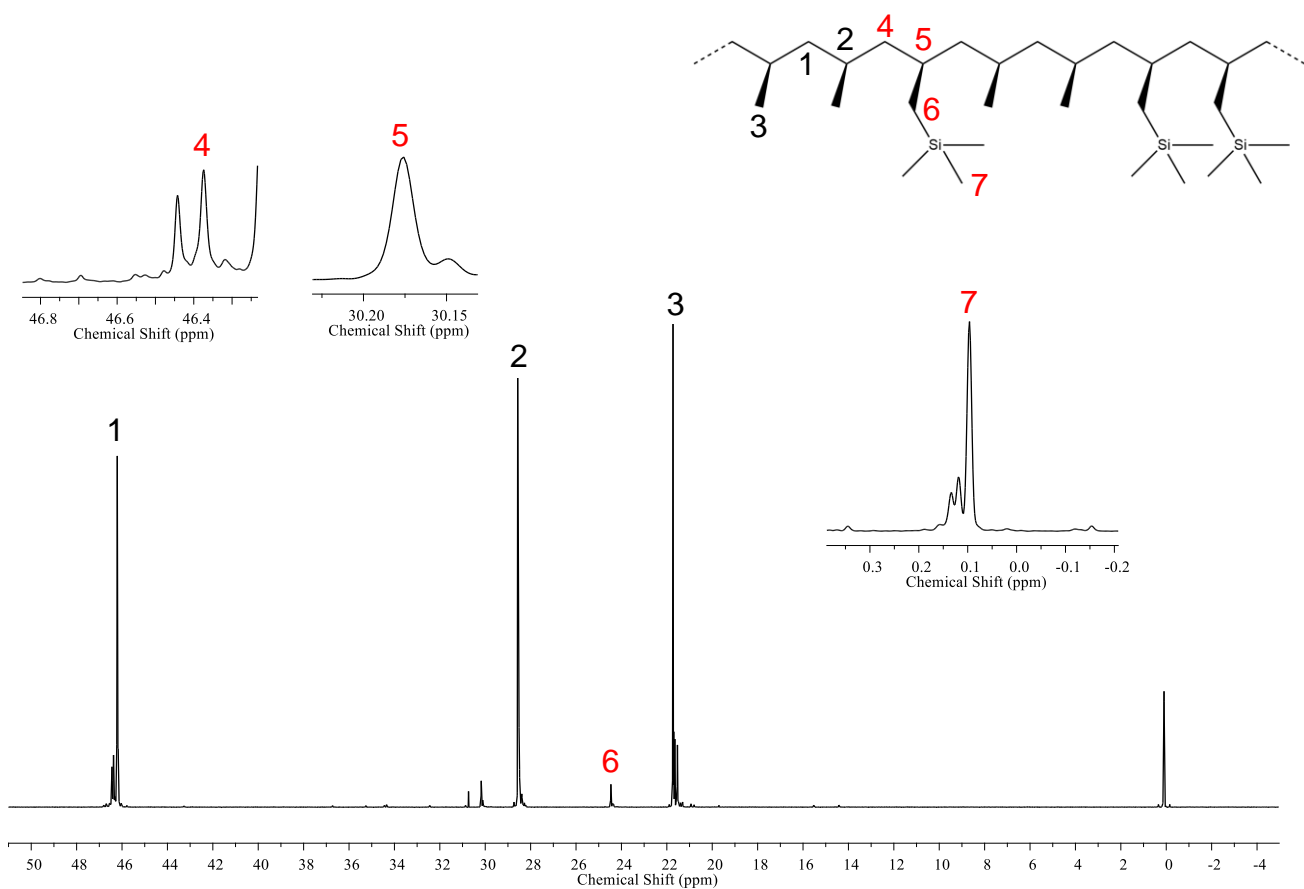


Figure A2. ^{13}C NMR spectra of the copolymer sample iPPATMS-2 with 6.5 mol% of ATMS.

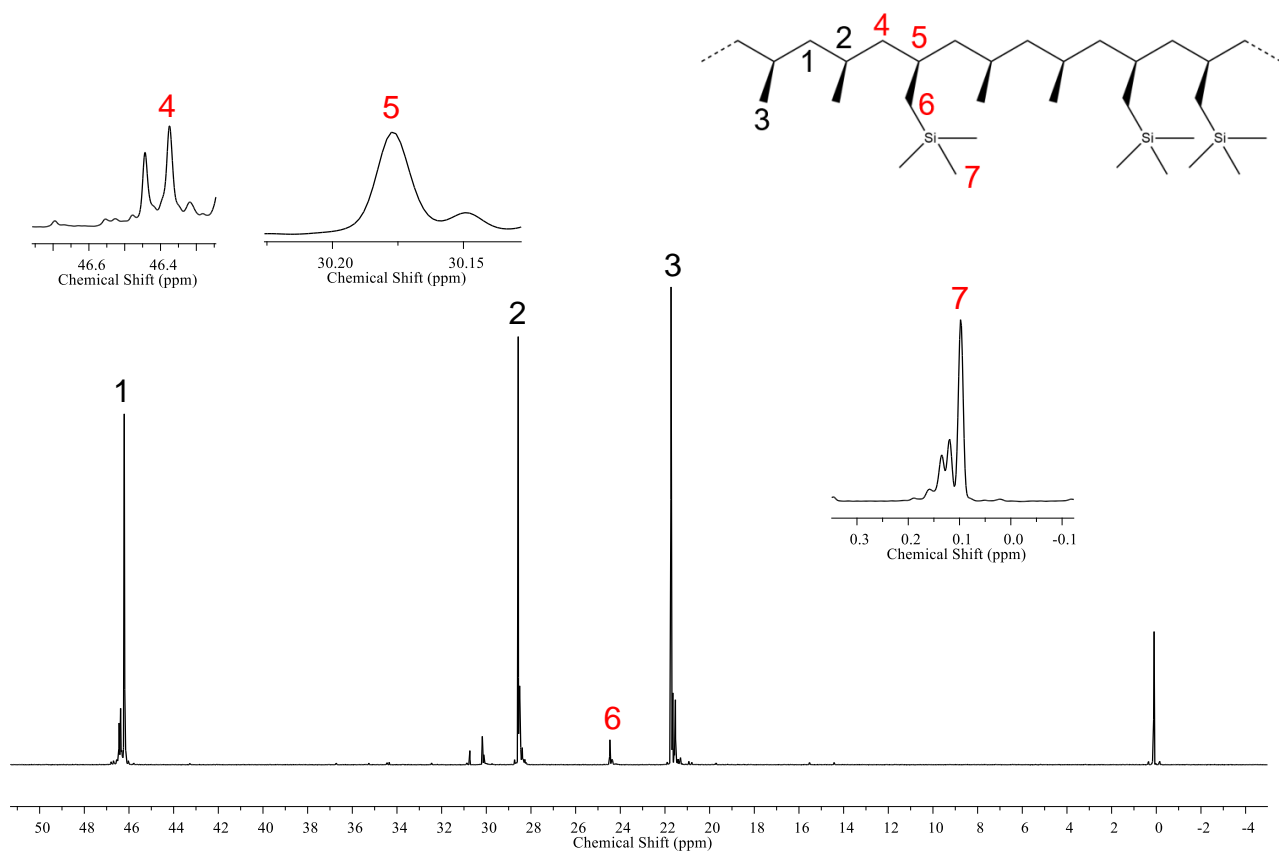


Figure A3. ^{13}C NMR spectra of the copolymer sample iPPATMS-3 with 8.3 mol% of ATMS.

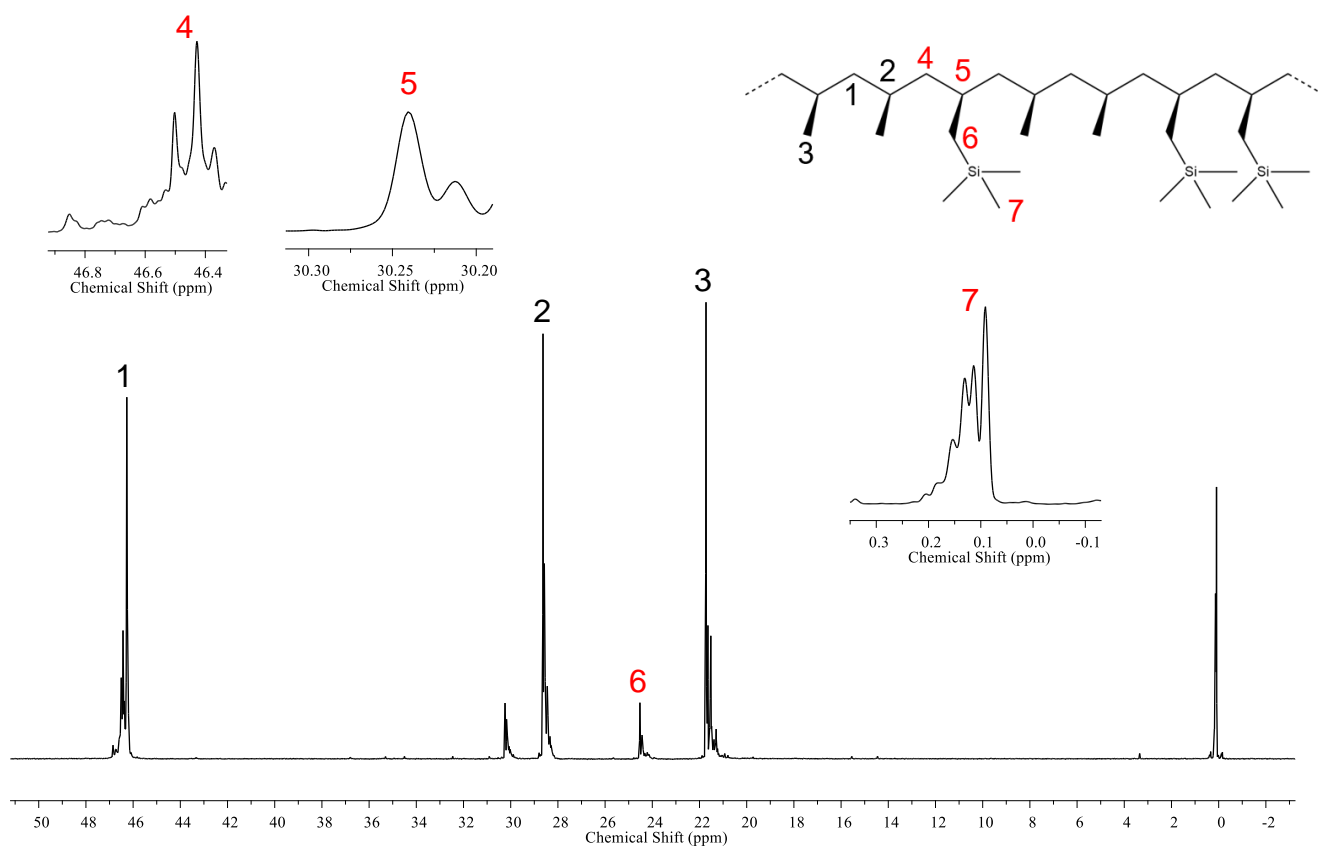


Figure A4. ^{13}C NMR spectra of the copolymer sample iPPATMS-4 with 11.5 mol% of ATMS.

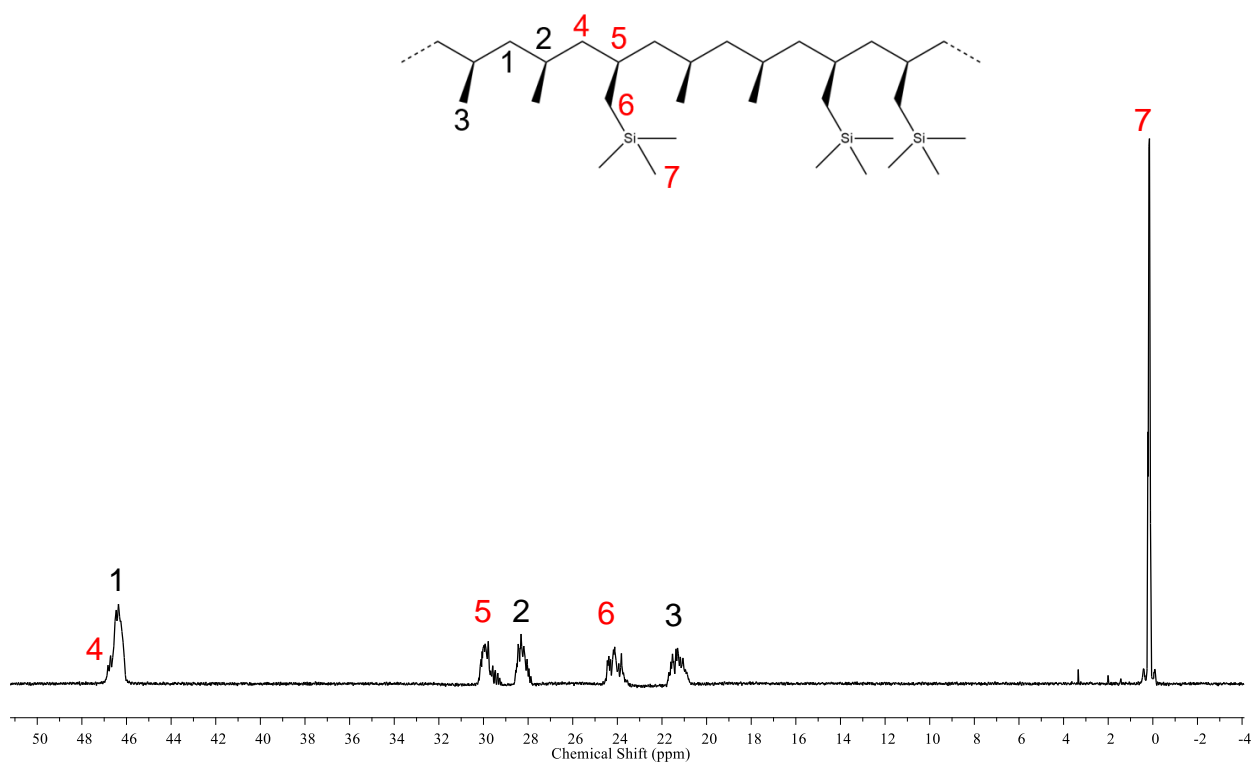


Figure A5. ^{13}C NMR spectra of the copolymer sample iPPATMS-5 with 50.5 mol% of ATMS.

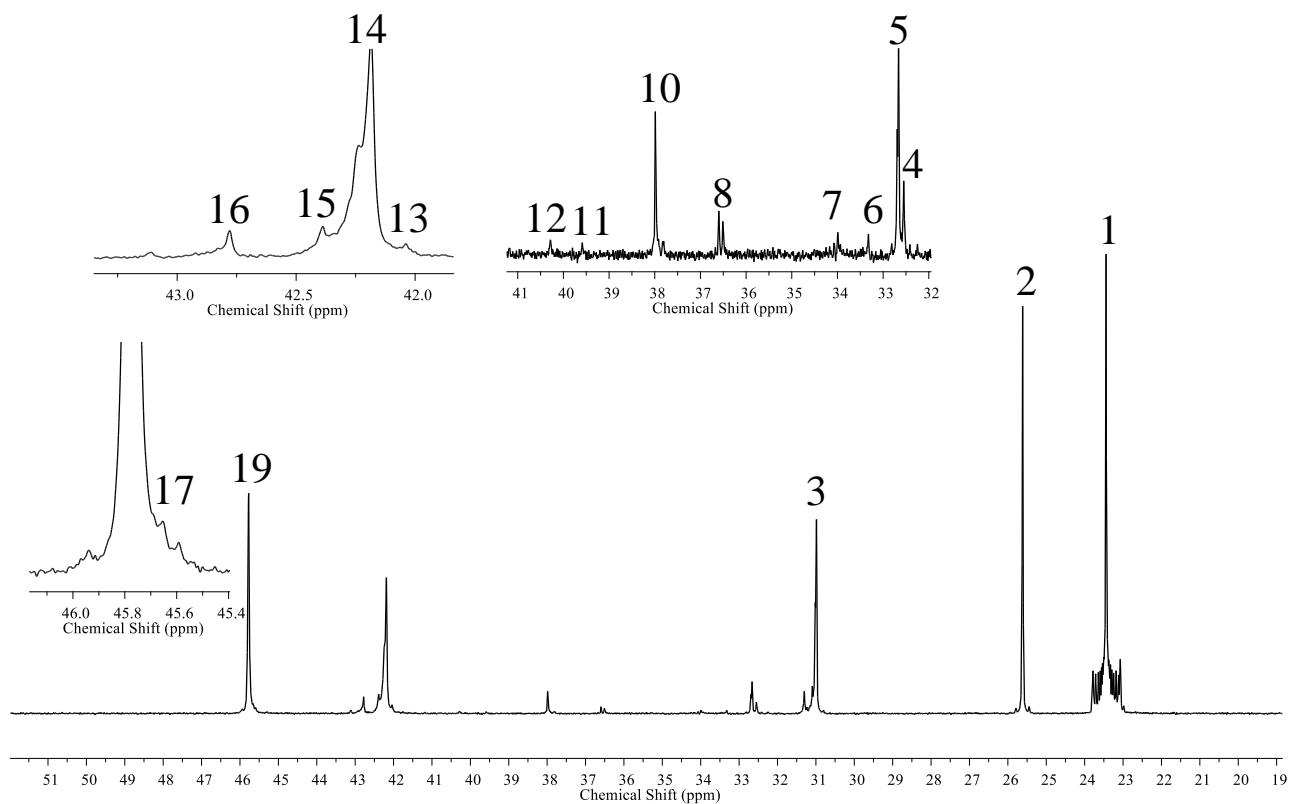


Figure A6. ^{13}C NMR spectra of the copolymer sample iP4MPHD-1 with 4.8 mol% of 1,5-HD. The assignment of all resonances observed in the spectra are reported in Table 3.6 of Chapter 3.

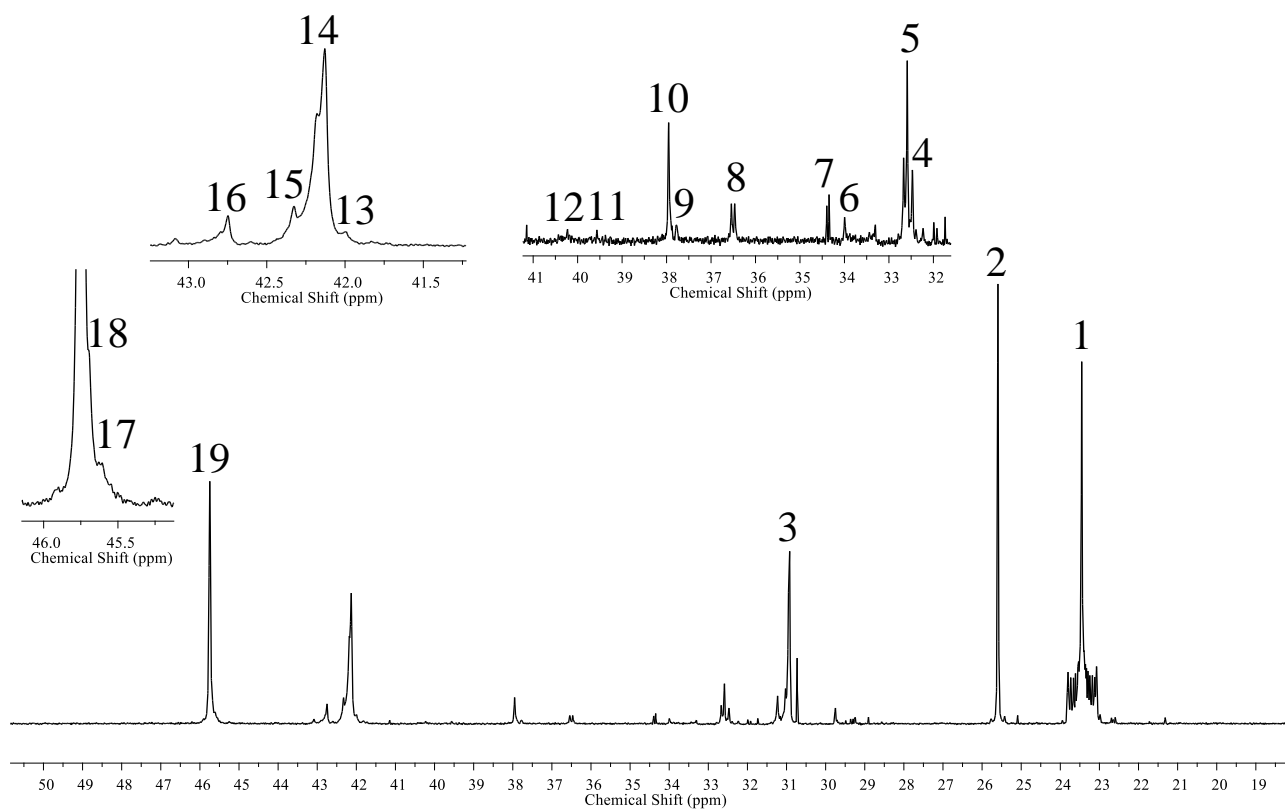


Figure A7. ^{13}C NMR spectra of the copolymer sample iP4MPHD-3 with 7.0 mol% of 1,5-HD. The assignment of all resonances observed in the spectra are reported in Table 3.6 of Chapter 3.

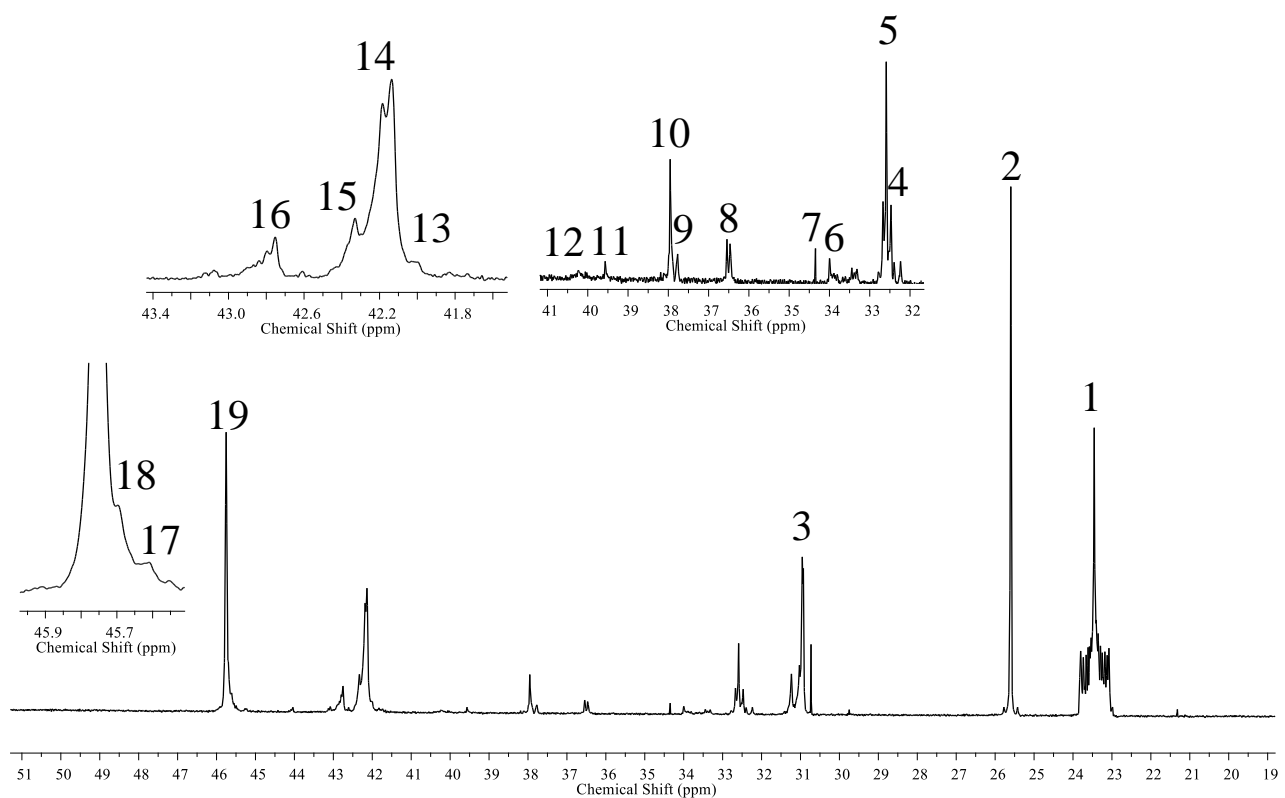


Figure A8. ^{13}C NMR spectra of the copolymer sample iP4MPHD-4 with 10.1 mol% of 1,5-HD. The assignment of all resonances observed in the spectra are reported in Table 3.6 of Chapter 3.

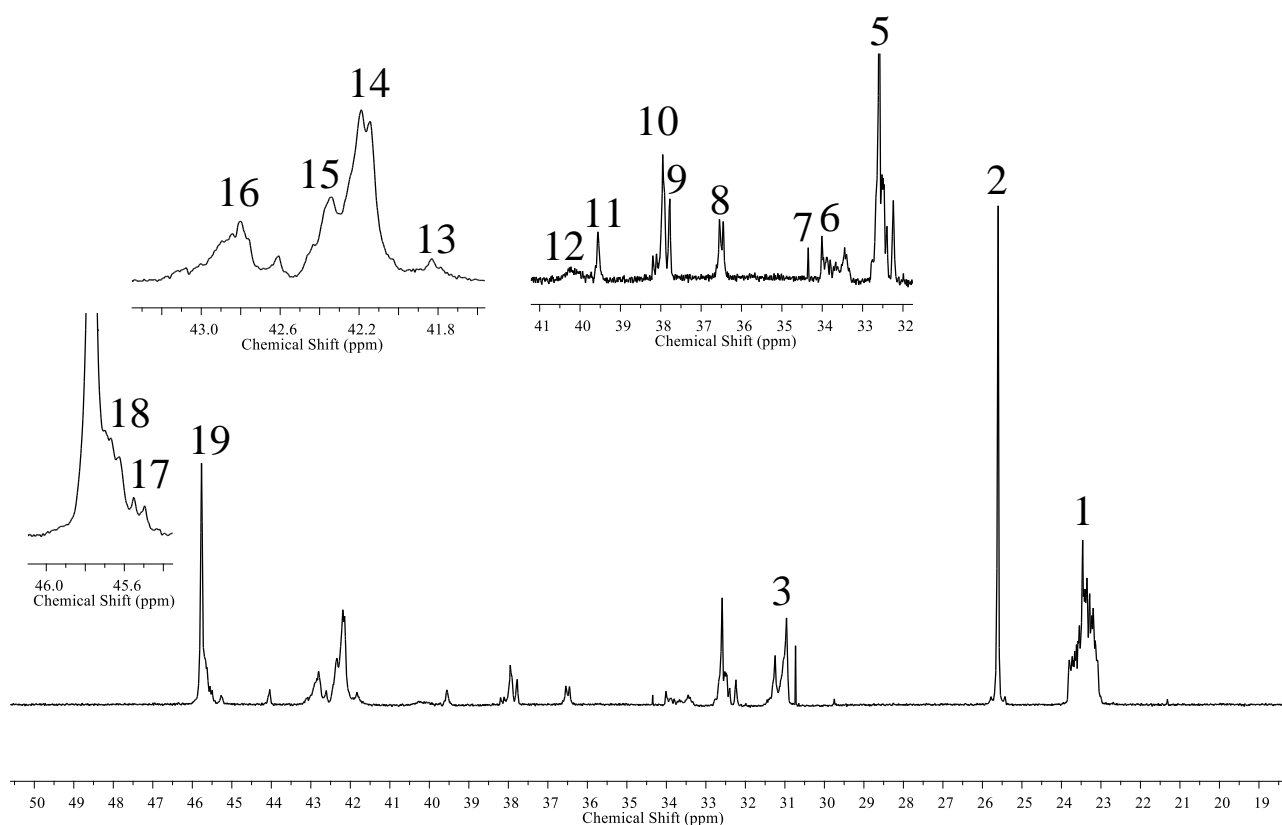


Figure A9. ^{13}C NMR spectra of the copolymer sample iP4MPHD-5 with 19.4 mol% of 1,5-HD. The assignment of all resonances observed in the spectra are reported in Table 3.6 of Chapter 3.

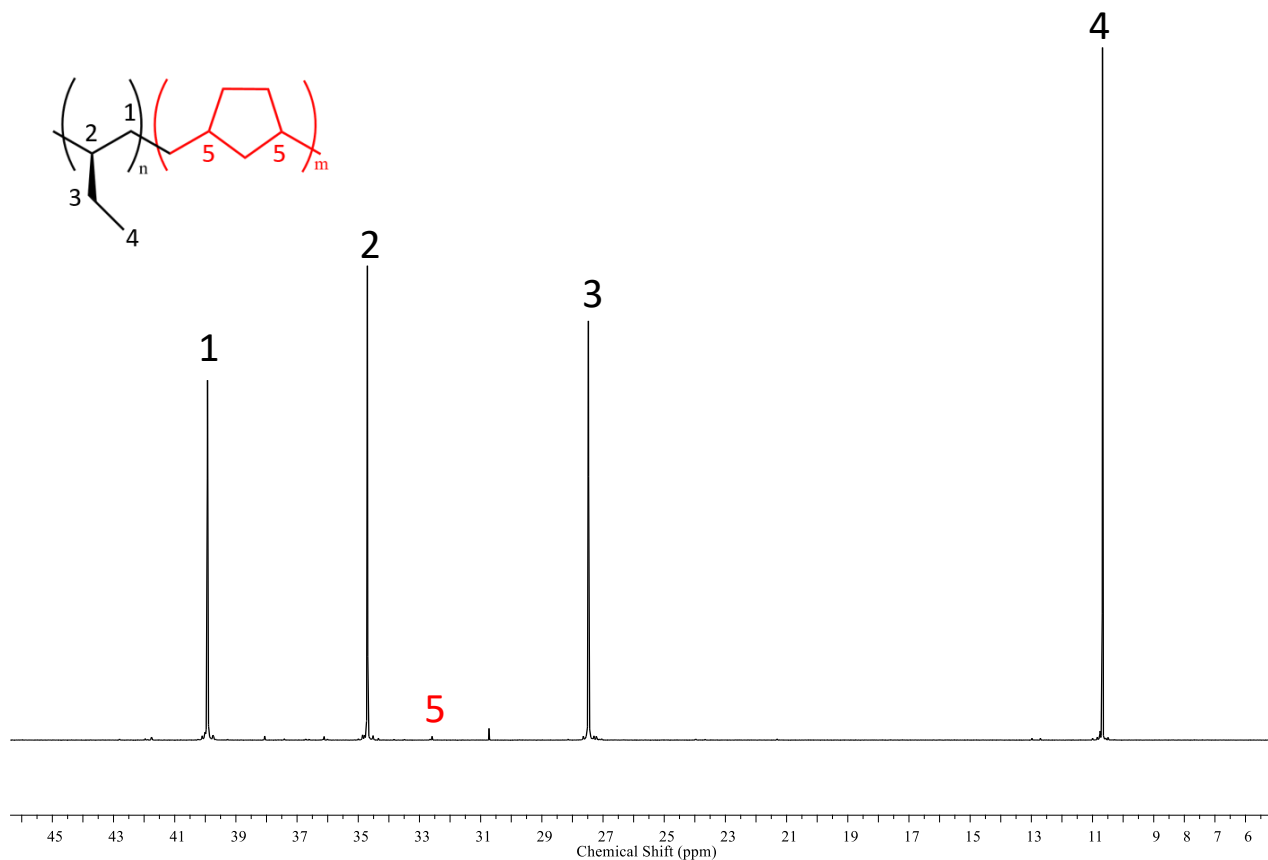


Figure A10. ^{13}C NMR spectra of the copolymer sample iP4BHD-1 with 0.47 mol% of 1,5-HD.

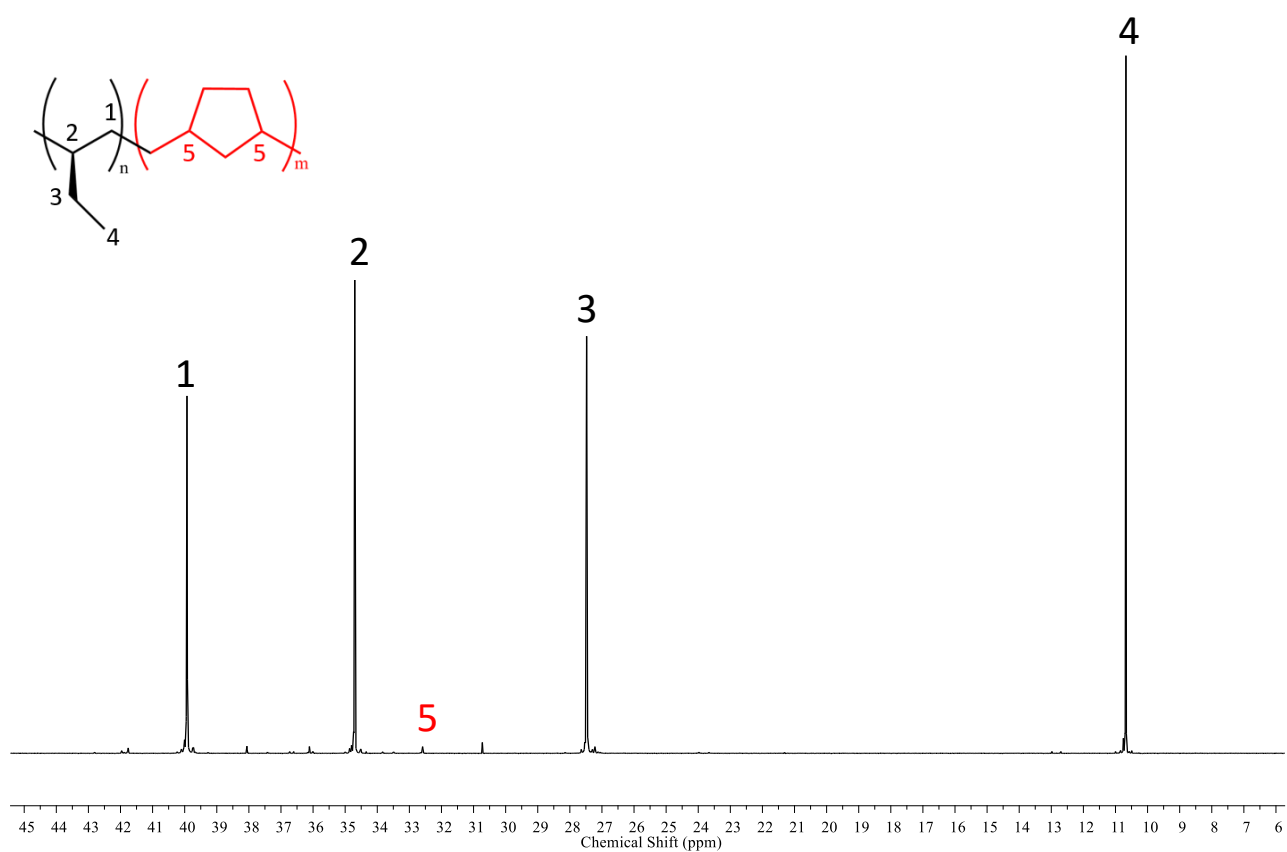


Figure A11. ^{13}C NMR spectra of the copolymer sample iPBHD-2 with 0.80 mol% of 1,5-HD.

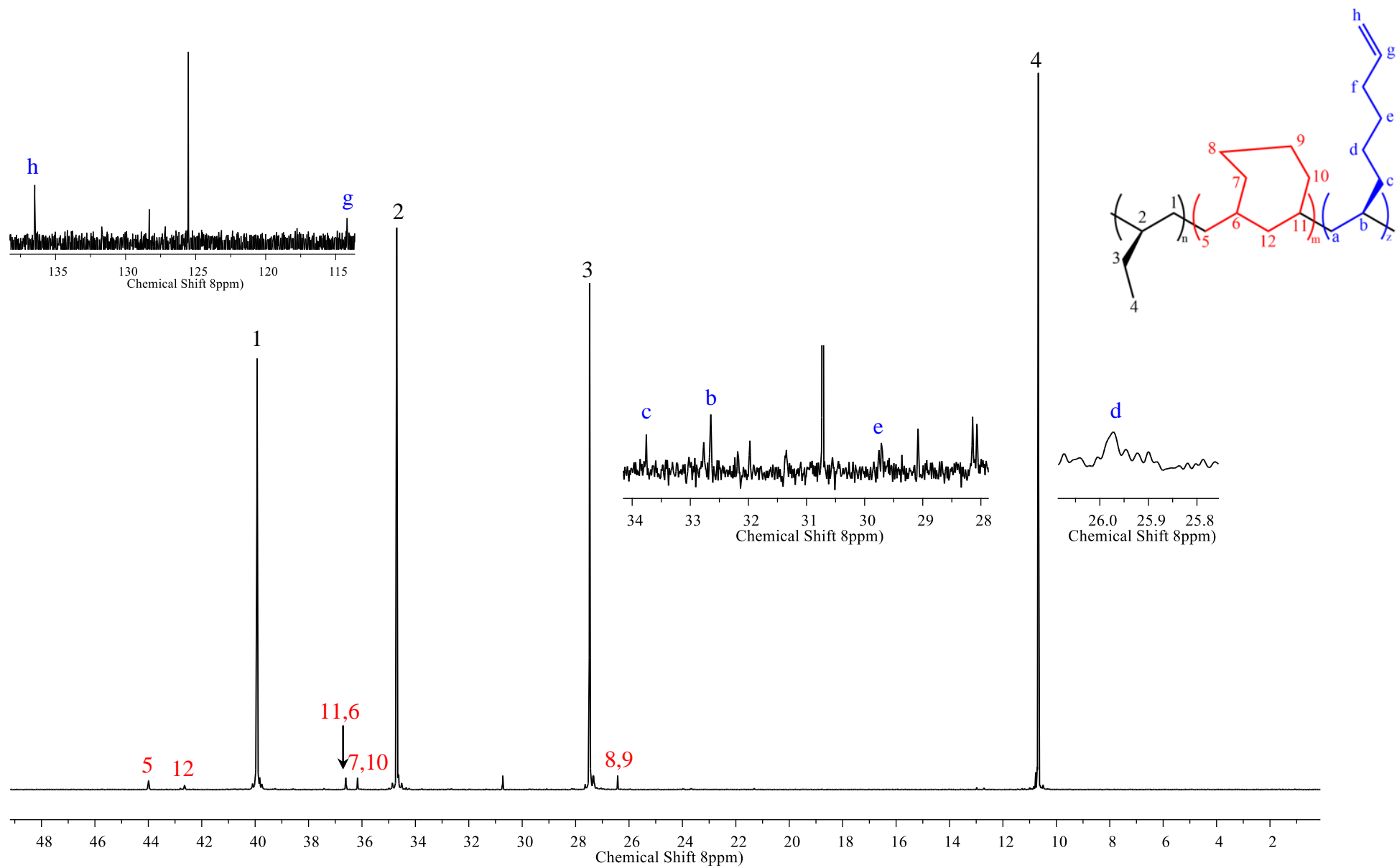


Figure A12. ^{13}C NMR spectra of the copolymer sample iPBD-1 with 1.08 mol% of 1,7-OD.

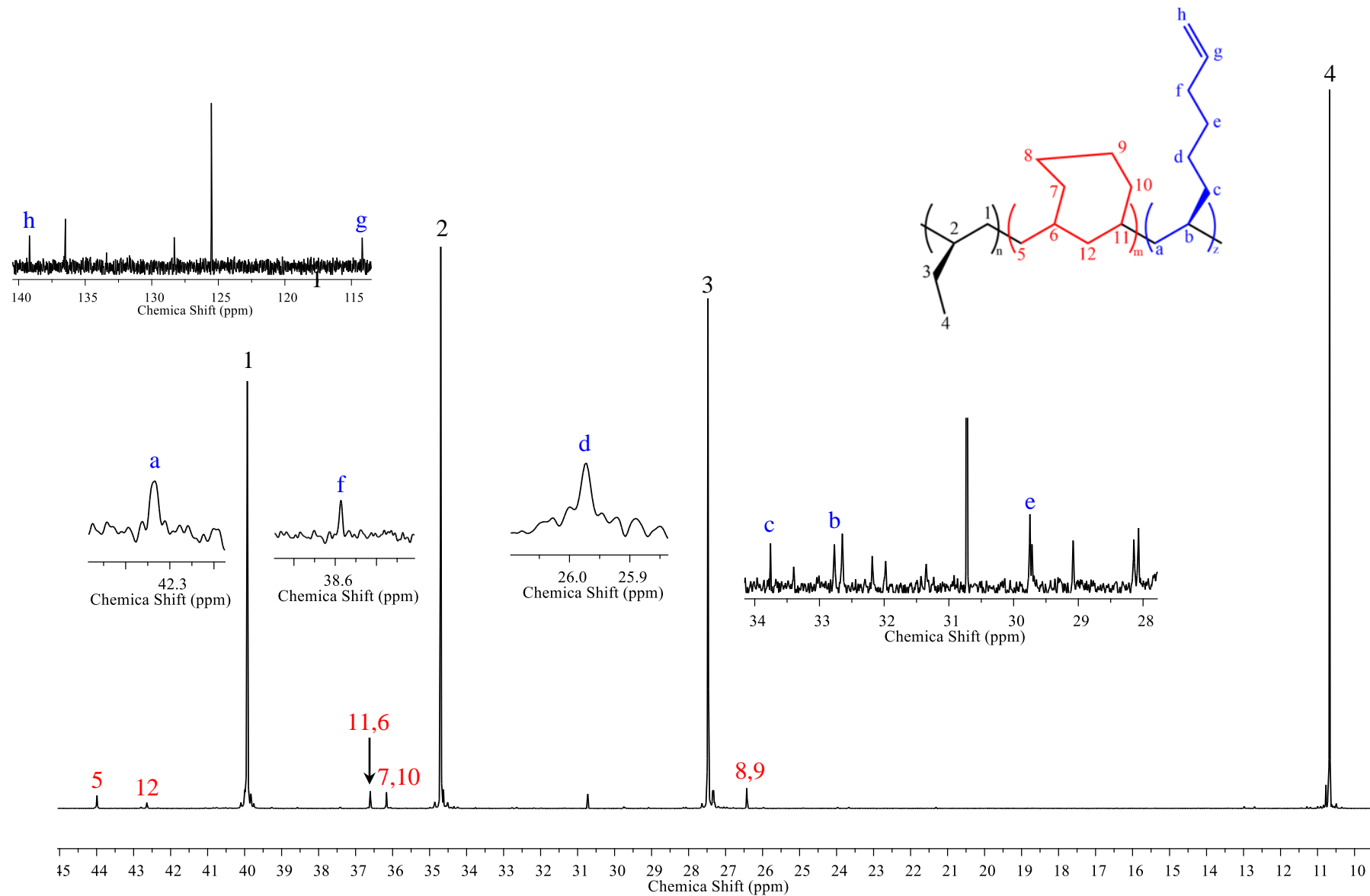


Figure A13. ^{13}C NMR spectra of the copolymer sample iPBOD-2 with 1.56 mol% of 1,7-OD.

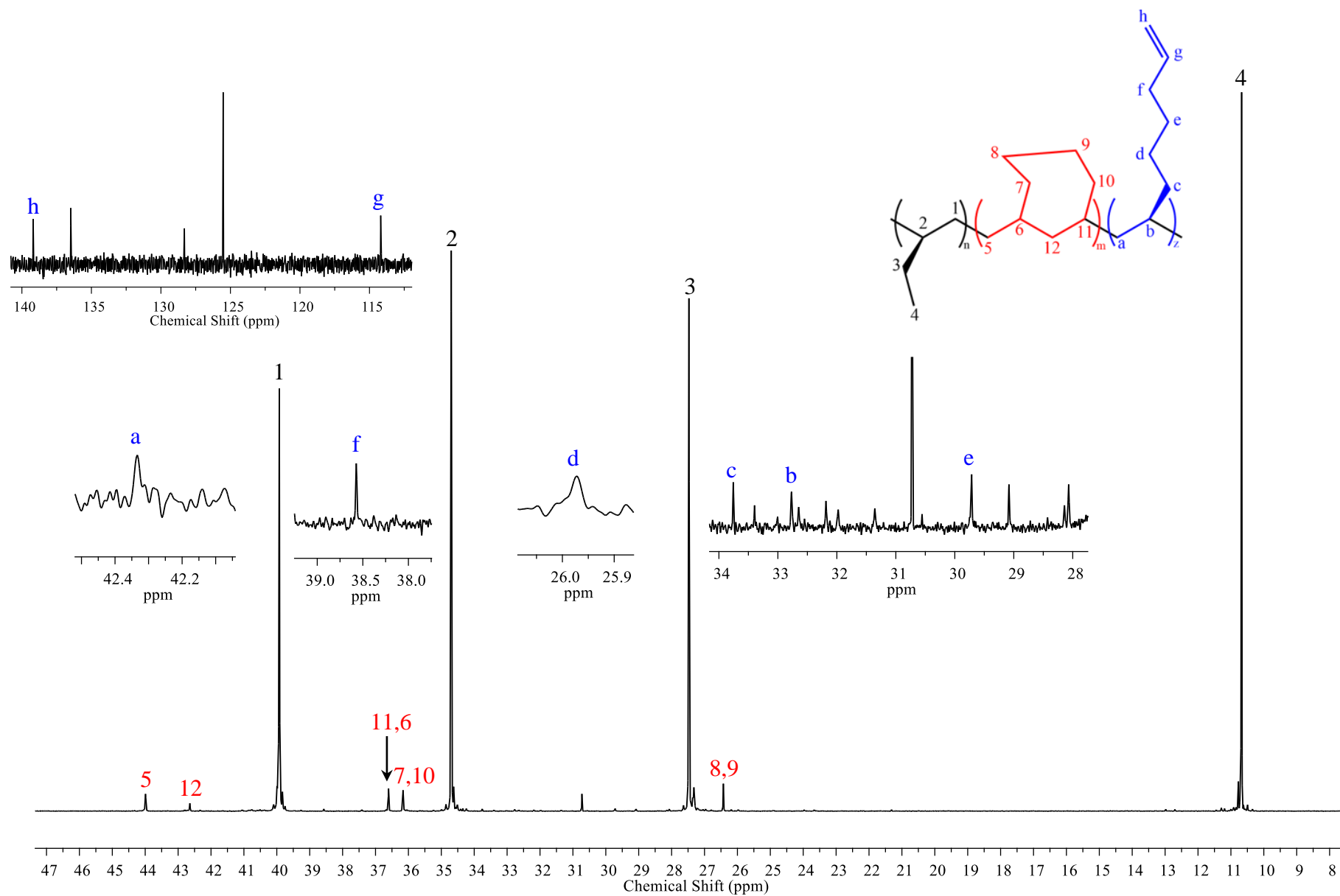


Figure A14. ^{13}C NMR spectra of the copolymer sample iPBOd-3 with 1.87 mol% of 1,7-OD.